NUREG/CR-6730
Vol. 1

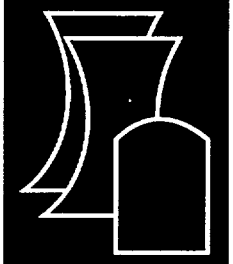

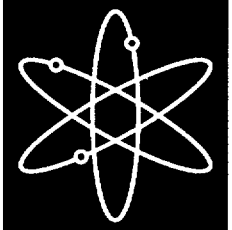

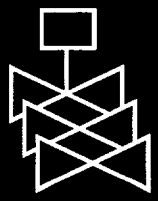

TRAC-M/F77, Version 5.5 Developmental Assessment Manual

Assessments

Los Alamos National Laboratory

U.S. Nuclear Regulatory Commission
Office of Nuclear Regulatory Research
Washington, DC 20555-0001

NUREG/CR-6730
Vol. 1

TRAC-M/F77, Version 5.5 Developmental Assessment Manual

Assessments

Manuscript Completed: June 2001
Date Published: July 2001

Prepared by
B.E. Boyack, J.F. Lime, D.A. Pimentel,
J.W. Spore, J.L. Steiner

Los Alamos National Laboratory
Los Alamos, NM 87545

F. Odar, NRC Project Manager

Prepared for
Division of Systems Analysis and Regulatory Effectiveness
Office of Nuclear Regulatory Research
U.S. Nuclear Regulatory Commission
Washington, DC 20555-0001
NRC Job Code W6245

AVAILABILITY OF REFERENCE MATERIALS IN NRC PUBLICATIONS

NRC Reference Material

As of November 1999, you may electronically access NUREG-series publications and other NRC records at NRC's Public Electronic Reading Room at www.nrc.gov/NRC/ADAMS/index.html. Publicly released records include, to name a few, NUREG-series publications; *Federal Register* notices; applicant, licensee, and vendor documents and correspondence; NRC correspondence and internal memoranda; bulletins and information notices; inspection and investigative reports; licensee event reports; and Commission papers and their attachments.

NRC publications in the NUREG series, NRC regulations, and *Title 10, Energy*, in the Code of *Federal Regulations* may also be purchased from one of these two sources.

1. The Superintendent of Documents
   U.S. Government Printing Office
   Mail Stop SSOP
   Washington, DC 20402–0001
   Internet: bookstore.gpo.gov
   Telephone: 202-512-1800
   Fax: 202-512-2250
2. The National Technical Information Service
   Springfield, VA 22161–0002
   www.ntis.gov
   1–800–553–6847 or, locally, 703–605–6000

A single copy of each NRC draft report for comment is available free, to the extent of supply, upon written request as follows:

Address: Office of the Chief Information Officer,
Reproduction and Distribution
Services Section
U.S. Nuclear Regulatory Commission
Washington, DC 20555-0001
E-mail: DISTRIBUTION@nrc.gov
Facsimile: 301–415–2289

Some publications in the NUREG series that are posted at NRC's Web site address www.nrc.gov/NRC/NUREGS/indexnum.html are updated periodically and may differ from the last printed version. Although references to material found on a Web site bear the date the material was accessed, the material available on the date cited may subsequently be removed from the site.

Non-NRC Reference Material

Documents available from public and special technical libraries include all open literature items, such as books, journal articles, and transactions, *Federal Register* notices, Federal and State legislation, and congressional reports. Such documents as theses, dissertations, foreign reports and translations, and non-NRC conference proceedings may be purchased from their sponsoring organization.

Copies of industry codes and standards used in a substantive manner in the NRC regulatory process are maintained at—

The NRC Technical Library
Two White Flint North
11545 Rockville Pike
Rockville, MD 20852–2738

These standards are available in the library for reference use by the public. Codes and standards are usually copyrighted and may be purchased from the originating organization or, if they are American National Standards, from—

American National Standards Institute
11 West 42nd Street
New York, NY 10036–8002
www.ansi.org
212–642–4900

Legally binding regulatory requirements are stated only in laws; NRC regulations; licenses, including technical specifications; or orders, not in NUREG-series publications. The views expressed in contractor-prepared publications in this series are not necessarily those of the NRC.

The NUREG series comprises (1) technical and administrative reports and books prepared by the staff (NUREG–XXXX) or agency contractors (NUREG/CR–XXXX), (2) proceedings of conferences (NUREG/CP–XXXX), (3) reports resulting from international agreements (NUREG/IA–XXXX), (4) brochures (NUREG/BR–XXXX), and (5) compilations of legal decisions and orders of the Commission and Atomic and Safety Licensing Boards and of Directors' decisions under Section 2.206 of NRC's regulations (NUREG–0750).

TRAC-M/F77, VERSION 5.5
DEVELOPMENTAL ASSESSMENT MANUAL

VOLUME I: ASSESSMENTS

by

B. E. Boyack, J. F. Lime, D. A. Pimentel, J. W. Spore, and J. L. Steiner

ABSTRACT

Los Alamos National Laboratory has developed the Transient Reactor Analysis Code (TRAC) to provide advanced, best-estimate simulations of real and postulated transients in pressurized water reactors (PWRs) and for many related thermal-hydraulic facilities. The modernized TRAC-M/F77, Version 5.5, is the latest release version. The previous release code, TRAC-PF1/MOD2, Version 5.4, was modified by removing nonstandard FORTRAN constructs to produce a standard FORTRAN 77 (F77) code. In the process, a more uniform programming style was established. TRAC-M/F77 (1) is more portable and maintainable than Version 5.4; (2) retains TRAC's essential features, a one- and/or three-dimensional, two-fluid treatment for the thermal hydraulics; (3) has other necessary modeling capabilities to model a reactor system; and (4) has a newly enhanced reflood model.

This Developmental Assessment Manual describes the TRAC-M/F77, Version 5.5, assessment calculations that were compared with analytical calculations and experimental data. The manual is issued in two volumes. Volume I contains the assessment sections, and Volume II contains the appendices. The appendices to the manual include the input listings of the assessment problems, and code-data comparision of assessments exercised with different reflood, grid spacer, and noding modeling options. The comparisons were performed to determine the accuracy and applicability of TRAC-M/F77. Based on these assessments against analytical solutions, separate-effects tests, and integral tests, we believe that TRAC-M/F77 is a viable calculational tool for analyzing PWRs during a loss-of-coolant accident and operational transients. In addition, the developmental assessment calculations demonstrate that TRAC-M/F77 is applicable to a wide range of test facilities and is accurate in terms of predicting major trends.

CONTENTS

CONTENTS (cont)

CONTENTS (cont)

CONTENTS (cont)

FIGURES

FIGURES (cont)

FIGURES (cont)

Page

FIGURES (cont)

FIGURES (cont)

FIGURES (cont)

FIGURES (cont)

Page

FIGURES (cont)

FIGURES (cont)

FIGURES (cont)

FIGURES (cont)

Page

FIGURES (cont)

Page

FIGURES (cont)

Page

FIGURES (cont)

FIGURES (cont)

FIGURES (cont)

FIGURES (cont)

Page

FIGURES (cont)

FIGURES (cont)

FIGURES (cont)

TABLES

Page

TABLES (cont)

TRAC-M/F77, VERSION 5.5
DEVELOPMENTAL ASSESSMENT MANUAL

by

B. E. Boyack, J. F. Lime, D. A. Pimentel, J. W. Spore, and J. L. Steiner

EXECUTIVE SUMMARY

Los Alamos National Laboratory has developed the Transient Reactor Analysis Code (TRAC) to provide advanced best-estimate simulations of real and postulated transients in pressurized light-water reactors and for many related thermal-hydraulic facilities. The TRAC-M/F77, Version 5.5 program is the latest released version. The previous release code, TRAC-PF1/MOD2, Version 5.4, was modified by removing nonstandard FORTRAN constructs to produce a standard FORTRAN 77 (F77) code. TRAC-M/F77 also has a new revised multi-quench-front reflood model. To validate the methodology and models used in the code, we used analytical problems, separate-effects tests, and integral-effects tests to assess the code.

The analytical assessment problems included two steady-state heat-conduction problems, a fill-and-drain hydrodynamic problem, and a U-tube manometer problem. The separate-effects tests included tests that evaluated counter-current flow limitation (CCFL), condensation, critical flow, loop-oscillatory behavior, core reflood, and downcomer emergency core cooling (ECC) flow penetration. The separate-effects core reflood assessments included a Lehigh rod-bundle test, two Full-Length Emergency Core Heat Transfer (FLECHT) Separate-Effects and System-Effects Tests (SEASET) reflood tests, a Cylindrical Core Test Facility (CCTF) test, and two Upper-Plenum Test Facility (UPTF) tests. The integral-effects test assessments included the Loss-of-Fluid Test (LOFT) L2-6 loss-of-coolant transient and the LOFT L6-1 loss-of-steam load transient, the CCTF Run 54 reflood test, and the Slab Core Test Facility (SCTF) Run 719 reflood test. In all of the reflood assessment problems, four calculations were performed to evaluate the two reflood options available in TRAC-M/F77 and to evaluate the effect of modeling grid spacers with each of the reflood options. In this developmental assessment, we found that the grid spacer model in TRAC was deficient, and we recommend that it not be used. A brief summary of the assessment results is given as follows.

Analytical Assessment Problems

The analytical heat-conduction problems showed that the TRAC finite-difference solution to the heat-conduction equations in rod geometries is accurate. The analytical hydrodynamic models showed that TRAC is accurate and stable during the filling and draining of cells. The gravity head calculated by TRAC is shown to be accurate. The U-tube manometer test problem showed that TRAC can calculate an accurate period of oscillation.

Counter-Current Flow Limitation (CCFL)

The TRAC CCFL model gave reasonable results in predicting the CCFL. The assessment is limited to air-water mixtures at atmospheric conditions. Also, we have not assessed the current code CCFL model for steam-water mixtures.

Condensation

The TRAC condensation model gave good results in predicting the liquid temperature in the stable and mist-flow regimes. The model predicted the frequency of oscillations when the plug flow is considered. The transition from stable to oscillatory flow is reasonably predicted for a steam mass flux at or below 40 $kg \cdot m^{-2} \cdot s^{-1}$. For a higher steam flux, the condensability (a measure of the maximum steam mass that the injected water can condense) is overpredicted.

Critical Flow

The critical flow tests included five Marviken tests and the Edwards blowdown experiment. The Marviken test assessments show that TRAC calculates saturated critical flow correctly but underpredicts the subcooled critical flow. It is recommended that a nonequilibrium critical-flow model, such as the Henry-Fauske Model, be implemented into the code as a user option for modeling the critical flow for small-diameter nozzles, orifices, and short tubes. With the Edwards blowdown experiment, there is much closer agreement between the TRAC calculation and test data.

Lehigh Run 02/24/80-6

Overall, the agreement between predicted and measured parameters was judged to be reasonable. The TRAC grid-spacer model replicates the behavior of the Lehigh Run 02/24/80-6, but only because the model was tuned to these data. When applied to other facilities and tests, we have found that the grid-spacer model produces excessive and nonphysical cooling rates. The TRAC grid-spacer model lacks an appropriate physical basis, and its use is not recommened. However, the Lehigh data clearly show enhanced wall cooling caused by the bundle grid spacer. Therefore, a well-based grid-spacer model definitely should be developed for TRAC.

UPTF Test 8B

TRAC does a reasonable job of predicting cold-leg plugging and thermal-hydraulic oscillation, which in the test were driven by core-simulator steam injection and cold-leg ECC injection.

UPTF Test 6

The results of this assessment indicate that the code does a reasonable job of predicting downcomer penetration of ECC flow. The predicted vessel liquid-mass inventory is in good agreement with the data.

CCTF Run 14

Minimal to reasonable agreement was found between the predicted and measured cladding temperatures for the lower half of the core. Above the core midplane, the agreement between predicted and measured cladding temperatures is minimal. The predictions of peak cladding temperature (PCT) times are in reasonable agreement with the measured values for the lower part of the core but are in only minimal agreement in the upper part of the core. The predictions of cladding quench times are in reasonable agreement with the measured times in the lower two-thirds of the core. Higher in the core, the predicted quench times are later than measured. A noding sensitivity study also was performed for this test. In general, a coarser noding of the core results in a less-accurate calculation. Lower PCTs, later PCT times, and later quench times are calculated with a coarsely noded core model rather than with a finely noded core model. Void fraction profiles and core pressure drops also are less accurate.

FLECHT SEASET Forced Reflood Test 31504

With respect to key parameters, such as cladding temperatures and coolant distribution, the agreement between code-predicted and measured values is judged to vary between minimal and reasonable.

FLECHT SEASET Gravity Reflood Test 33436

With respect to key parameters, such as cladding temperatures and coolant distribution, the agreement between code-predicted and measured values is insufficient. The predicted cladding temperatures were much higher than the test data. Much of the predicted behavior for FLECHT SEASET test 33436 is consistent with that observed for the other reflood tests. These behaviors are the prediction of (1) too-little liquid inventory in the test vessel, particularly in advance of the quench front; (2) too-little heat transfer in advance of the quench front; and (3) too-large liquid-transport rate through the test vessel.

LOFT Test L26

The TRAC-calculated parameters for LOFT test L2-6 are in either reasonable or excellent agreement with the data, with the important exception of the predicted surface cladding temperatures. The predicted surface cladding temperatures are characterized as being in the range of minimal to reasonable agreement with the data.

LOFT Test L61

In the LOFT L61 assessment, two TRAC models were developed, one with the vessel modeled with 1D components and the other with the vessel modeled with a 3D Vessel component. The calculated results of both models show that TRAC accurately predicted the pressure-sensitive behavior of the LOFT L6-1 experiment. TRAC results agreed with almost all experimental measurements within their range of uncertainty.

CCTF Run 54

Overall, the predicted core thermal-hydraulic behavior is in reasonable agreement with the data. Predictions of cladding thermal response in the lower half of the core are in better agreement with data than predictions of cladding thermal response in the upper half of the core. At each level in the core, the cladding thermal response passes through four periods: (1) adiabatic heatup, (2) slow heatup, (3) slow cooldown, and (4) quench. TRAC failed to predict the third period accurately, frequently showing either a continued heatup or a cooldown that was too slow. A core noding sensitivity study also was performed for this test. A finer renoding of the CCTF Run 54 core did not improve the calculated results.

SCTF Run 719

Overall, the predicted core thermal-hydraulic behavior is in minimal agreement with the data. Cladding temperatures calculated by TRAC-M in the lower half of the core are in reasonable agreement with the data. Cladding temperatures calculated by TRAC-M in the upper half of the core are in minimal agreement with the data.

ACKNOWLEDGMENTS

All the assessment calculations are based upon the modernized FORTRAN version of TRAC. Although he is not cited as a coauthor of this developmental assessment report, the principal investigator for the TRAC modernization effort is J. F. Dearing, who was assisted in the development effort by R. C. Johns and P. T. Giguere. The authors express their appreciation to Dr. F. Odar of the United States Nuclear Regulatory Commission, who was the Project Manager for this effort throughout. Finally, we express our appreciation to G. Mirabal and L. Rothrock for editing and A. Mascarenas for preparing the manuscript for publication.

ACRONYMS AND ABBREVIATIONS

1D	One dimensional
2D	Two dimensional
3D	Three dimensional
ACC	Accumulator
ANS	American Nuclear Society
B&W	Babcock & Wilcox
BE	Best estimate
BN	Boron nitride
BOCREC	Bottom of core recovery
CCFL	Countercurrent flow limitation
CCTF	Cylindrical Core Test Facility
CFS	Common File System
CHF	Critical heat flux
CL	Cold leg
CPU	Central Processing Unit
CSAU	Code Scaleability, Applicability, and Uncertainty
CSS	Constrained steady state
ECC	Emergency core coolant
ECCS	Emergency core-coolant system
EOCB	End of complete bypass
EM	Evaluation model
F77	FORTRAN 77
FLECHT	Full-Length Emergency Core Heat Transfer
HPIS	High-pressure injection system
HTC	Heat-Transfer Coefficient
IAF	Inverted-annular-flow
IB	Intermediate Break
IET	Integral effect test
IFDC	Interfacial-drag coefficient
JAERI	Japan Atomic Energy Research Institute
KWU	Kraftwerk Union Atiengesellschaft
LANL	Los Alamos National Laboratory
LB	Large break
L/D	Length-to-diameter
LWR	Light water reactor
LOCA	Loss-of-coolant accident
LOFT	Loss-of-Fluid Test
LOSP	Loss-of-offsite power
LPCI	Low-pressure coolant injection
LPIS	Low-pressure injection system
LRB	Lehigh University rod bundle
MgO	Magnesium oxide
MSFCV	Main steam flow control valve
NRC	Nuclear Regulatory Commission
PCT	Peak cladding temperature
PI	Principal Investigator
PORV	Pressure-operated relief valve

ACRONYMS AND ABBREVIATIONS (cont)

PWR	Pressurized water reactor
S/W	Steam/water
SB	Small break
SCTF	Slab Core Test Facility
SEASET	Separate-Effects and System-Effects Test
SETS	Stability-enhancing two-step
TRAC-M	Modernized Transient Reactor Analysis Code
UCSP	Upper-core support plate
UPTF	Upper-Plenum Test Facility
XTV	X-TRAC-View

1. INTRODUCTION

Los Alamos National Laboratory (LANL) has developed the modernized Transient Reactor Analysis Code (TRAC-M) to provide advanced, best-estimate simulations of real and postulated transients in pressurized water reactors (PWRs) and many related thermal-hydraulic facilities. The TRAC-M, Version 5.5 code is the latest released version. The code features one- and three-dimensional (1D and 3D), two-fluid treatment for the thermal hydraulics, together with other necessary modeling capabilities to describe a reactor system. This code differs from the last formally released TRAC, Version 5.4.15, in the following major features. First, standard FORTRAN 77 (F77) has been implemented throughout the code with a commensurate increase in portability and maintainability. Second, the platform-dependent binary file named TRCGRF has been replaced by the files XTVGR.b and XTVGR.t, which can be processed by the TRAC visualization and plotting tool, X-TRAC-View.[1-1] Third, this version contains a newly revised reflood model.[1-2,1-3]

The TRAC-M developmental assessment matrix includes analytical test problems that address the following models and capabilities within TRAC-M:

Analytical Test Problem	Report Section
Heat-conduction solution	3.1
Hydrodynamics and level tracking	3.2
Hydrodynamics and manometer oscillations	3.3

The TRAC-M developmental assessment matrix includes separate-effects tests that address the following models and capabilities within TRAC-M:

Separate-Effect Tests	Report Section
Countercurrent flow limitation (CCFL) model with Bankoff's test facility	4.1
Condensation model with Akimoto condensation flow test facility.	4.2
Critical flow model with Marviken critical flow tests and Edwards blowdown	4.3
Post-critical heat flux (CHF) heat transfer with the Lehigh rod-bundle test	4.4
Condensation model, interfacial drag model, and flow-regime model in full-scale downcomer with Upper-Plenum Test Facility (UPTF) Test 8B	4.5
Condensation model, interfacial drag model, and flow-regime model in full-scale cold leg with UPTF Test 6	4.6
Reflood model with Cylindrical Core Test Facility (CCTF)-14 Reflood Test	4.7
Reflood model with the Full-Length Emergency Core Heat Transfer (FLECHT) Separate-Effects and System-Effects Tests (SEASET) Forced Test 31504	4.8
Reflood model with the FLECHT SEASET Gravity Test 33436	4.9

The TRAC-M developmental assessment matrix includes integral tests that address the following models and capabilities within TRAC-M:

Integral-Effect Tests	Report Section
Blowdown, refill, and reflood hydraulics and heat transfer with the Loss-of-Fluid Test (LOFT) L2-6 Large-Break (LB) Loss-of-Coolant Accident (LOCA)	5.1
Operation transient hydraulics and heat transfer with LOFT L6-1 transient	5.2
Reflood heat transfer and hydraulics with CCTF Test 54	5.3
Reflood heat transfer and hydraulics with the Slab Core Test Facility (SCTF) Run 719	5.4

These assessment problems initially were issued in two volumes, Refs. 1-4 and 1-5. Volume I contained those assessment calculations that did not include the 2D and 3D assessments. Volume II contained the 2D and 3D assessments. Four of the assessment problems in Volume II contained modeling deficiencies that we were not able to correct before the manual was issued: UPTF Test 8B, CCTF Run 14, CCTF Run 54, and SCTF Run 719. The first three of these were corrected, and the amended assessment sections for these problems were issued in Ref. 1-6. In addition to the corrections, two core renoding sensitivity studies were conducted, as requested by the NRC. The 18-level core of the CCTF Run 14 model was renoded into 6 levels, and in the CCTF Run 54 model, the 7-level core was renoded into 17 levels. The CCTF Run 14 and Run 54 assessment sections have been amended to include the core-renoding study. The fourth assessment problem, the SCTF Run 719, subsequently was corrected for modeling deficiencies, and a draft report of corrected assessment was issued. Core flooding rates are included in each of the reflood assessment problems, as requested by the NRC.

The assessment problems now are combined into one document, with the document still being issued in two volumes. Volume I contains the assessment sections, and Volume II contains the appendices. The appendices include the input listings of the assessment problems and the code-data comparision of assessments that were exercised with different reflood, grid spacer, and noding modeling options.

REFERENCES

1-1. J. F. Dearing and R. C. Johns, "XTV Users Guide, Release 2.3c," Los Alamos National Laboratory document LA-UR-01-921 (May 1998).

1-2. R. A. Nelson Jr., D. A. Pimentel, S. Jolly-Woodruff, and J. Spore, "Reflood Completion Report, Volume I, A Phenomenological Thermal-Hydraulic Model of Hot Rod Bundles Experiencing Simultaneous Bottom and Top Quenching and an Optimization Methodology for Closure Development," Los Alamos National Laboratory report LA-UR-98-3043 (April 1998).

1-3. B. E. Boyack, J. F. Lime, D. A. Pimentel, J. W. Spore, and T. D. Knight, "Reflood Completion Report, Volume II, Developmental Assessment of a New Reflood Model for the TRAC-M/F77 Code," Los Alamos National report LA-UR-98-3043 (April 1998).

1-4. B. E. Boyack, J. F. Lime, D. A. Pimentel, J. W. Spore, and J. L. Steiner, "TRAC-M/F77, Version 5.5 Developmental Assessment Manual Volume I: Assessment Sections Not Including 2D/3D Tests," Los Alamos National Laboratory document LA-UR-99-6480 (December 1999).

1-5. B. E. Boyack, J. F. Lime, D. A. Pimentel, J. W. Spore, and J. L. Steiner, "TRAC-M/F77, Version 5.5 Developmental Assessment Manual Volume II: 2D/3D Assessment Sections," Los Alamos National Laboratory document LA-CP-99-345 (December 1999).

1-6. J. F. Lime, TRAC-M/F77, Version 5.5 Developmental Assessment Manual Amended Assessment Sections," Los Alamos National Laboratory document LA-CP-00-270 (August 2000).

2. CODE DESCRIPTION

TRAC is an advanced, best-estimate computer program for calculating the transient reactor behavior of a PWR. As such, TRAC incorporates a four-component (liquid water, liquid solute, water vapor, and noncondensable gas), two-fluid (liquid and gas) modeling of thermal-hydraulic processes involved in such transients. The complexity of the thermal-hydraulic modeling requires many additional models and correlations with logic imposed into a coherent description of a phenomenon.

TRAC-M is the latest in a series of TRAC codes, including TRAC-PD2/MOD1, TRAC-PF1, TRAC-PD2, TRAC-P1A, and TRAC-P1, the earliest publicly released version. The development history represented by these earlier code versions begins with a very fundamental and important improvement in analyzing the behavior of light water reactors (LWRs), namely, the decision to track separately the liquid and vapor fields in the reactor-coolant system. These codes required the greatly improved computer systems that were becoming available during the 1970s. They also pushed advances in numerical techniques to solve the complex equation set and to permit the large number of nodes that are required in the best-estimate analysis of some transients of interest.

A preliminary TRAC version consisting of only 1D components was completed in December 1976. Although this version was neither released publicly nor documented formally, it was used in TRAC-P1 development and formed the basis for the 1D loop-component modules. The first publicly released version, TRAC-P1, was completed in December 1977.[2-1]

The TRAC-P1 program was designed primarily for the analysis of large-break (LB) loss-of-coolant accidents (LOCAs) in PWRs. Because of its versatility, however, TRAC-P1 could be applied directly to many analyses, ranging from blowdowns in simple pipes to integral LOCA tests in multiloop facilities. A refined version, TRAC-P1A, was released to the National Energy Software Center in March 1979.[2-2] Although it still treated the same class of problems, TRAC-P1A was more efficient than TRAC-P1 and incorporated improved hydrodynamic and heat-transfer models. It was also easier to implement on various computers. TRAC-PD2 (Ref. 2-3) contained improvements in reflood, heat-transfer models, and numerical solution methods. Although a LBLOCA code, TRAC-PD2 was applied successfully to small-break (SB) problems and to the Three Mile Island accident.

TRAC-PF1 (Ref. 2-4) was designed to improve the ability of TRAC-PD2 to handle SBLOCAs and other transients. TRAC-PF1 had all the major improvements of TRAC-PD2; in addition, it used a two-fluid model with stability-enhancing two-step (SETS) numerics[2-5] in the 1D components. The two-fluid model, in conjunction with a stratified-flow regime, modeled countercurrent flow better than the drift-flux model that was used previously. The two-step numerics allowed large time steps for slow transients. A 1D core component permitted calculations with reduced dimensionality, although the 3D Vessel option was retained. A noncondensable gas field was added to the 1D and 3D hydrodynamics. Significant improvements were made to the trip logic and to the input. TRAC-PF1 was released publicly in July 1981.

The development of TRAC-PF1/MOD1 maintained the models necessary for applying the code to LBLOCAs and added or modified models as necessary to enhance the

application of the code to SBLOCAs and operational transients.[2-6,2-7] In particular, many user-convenience features to promote the application of the code to transients involving more complex control of the nuclear plant were added or enhanced. TRAC-PF1 contained generalized, reactivity-feedback models (subject to point-kinetics assumptions); generalized trip and control-system modeling; and necessary components to model the rest of the plant. The code was applicable to most transients for which large asymmetries in the power generation do not exist, for which the 1D fluid modeling in the pipe is valid, and for which thermal stratification in the liquid in the 1D components is not important (the 3D Vessel component can model thermal stratification in a coarse manner). The code maintained the capability to run in either a 1D or a mixed 1D and 3D mode, with SETS numerics in both the 1D and 3D components.

TRAC-PF1/MOD2 Version 5.4 (Ref. 2-8) is superior to all earlier versions of TRAC, both in its numerical solution schemes and its closure relationships. It provided new and state-of-the-art features for LWR safety analysis. Version 5.4 was used to perform a number of the developmental assessment calculations presented in this document. The results of these calculations were, however, never published officially.

The TRAC-M/F77, Version 5.5 code is the latest release version. This code differs from the last formally released TRAC code, Version 5.4.15, in the following major features. First, standard F77 has been implemented throughout the code with a commensurate increase in portability and maintainability. Second, the platform-dependent binary file named TRCGRF has been replaced by the files XTVGR.b and XTVGR.t, which can be processed by the TRAC visualization and plotting tool, X-TRAC-View (XTV, Ref. 2-9). Third, a newly revised reflood model is in the code (Refs. 2-10 and 2-11). TRAC-M, Version 5.5 was used to perform the developmental assessment calculations in this document. It should be noted that as the TRAC-M/F77 code was being developed, the TRAC-PF1/MOD2 code was also being updated at the same time to incorporate those code changes and fixes common to both codes. Many of the assessment calculations were also performed with an interim version of TRAC-PF1/MOD2, Version 5.4.29R9+. The 5.4.29R9+ code also included the revised top-down reflood model.

REFERENCES

2-1. Safety Code Development Group, "TRAC-P1: An Advanced Best Estimate Computer Program for PWR LOCA Analysis," Los Alamos Scientific Laboratory report LA-7279-MS, NUREG/CR-0063 (May 1978).

2-2. Safety Code Development Group, "TRAC-P1A: An Advanced Best Estimate Computer Program for PWR LOCA Analysis," Los Alamos Scientific Laboratory report LA-7777-MS, NUREG/CR-0665 (May 1979).

2-3. Safety Code Development Group, "TRAC-PD2: An Advanced Best Estimate Computer Program for Pressurized Water Reactor Loss-of-Coolant Accident Analysis," Los Alamos Scientific Laboratory report LA-8709-MS, NUREG/CR-2054 (April 1981).

2-4. "Computer Program for Pressurized Water Reactor Analysis," Los Alamos National Laboratory report LA-9944-MS, NUREG/CR-3567 (February 1984).

2-5. J. H. Mahaffy, "A Stability-Enhancing Two-Step Method for Fluid Flow Calculations," *J. Computational Physics* **46**, 329–341 (1982).

2-6. Safety Code Development Group, "TRAC-PF1/MOD1 Correlations and Models," Los Alamos National Laboratory report LA-11208-MS, NUREG/CR-5069 (December 1988).

2-7. Safety Code Development Group, "TRAC-PF1/MOD1: An Advanced Best Estimate Computer Program for Pressurized Water Reactor Thermal-Hydraulic Analysis," Los Alamos National Laboratory report LA-10157-MS, NUREG/CR-3858 (July 1986).

2-8. L. A. Guffee, S. B. Woodruff, R. G. Steinke, and J. W. Spore, "TRAC-PF1/MOD2 Code Manual, Programmer's Guide, Volume 3," Los Alamos National Laboratory report LA-12031-M, NUREG/CR-5673 (July 1992).

2-9. J. F. Dearing and R. C. Johns, "XTV Users Guide, Release 2.3c," Los Alamos National Laboratory document LA-UR-01-921 (May 1998).

2-10. R. A. Nelson, Jr., D. A. Pimentel, S. Jolly-Woodruff, and J. Spore, "Reflood Completion Report, Volume I, A Phenomenological Thermal-Hydraulic Model of Hot Rod Bundles Experiencing Simultaneous Bottom and Top Quenching and an Optimization Methodology for Closure Development," Los Alamos National Laboratory report LA-UR-98-3043 (April 1998).

2-11. B. E. Boyack, J. F. Lime, D. A. Pimentel, J. W. Spore, and T. D. Knight, "Reflood Completion Report, Volume II, Developmental Assessment of a New Reflood Model for the TRAC-M/F77 Code," Los Alamos National Laboratory report LA-UR-98-3043 (April 1998).

3. ANALYTICAL TEST PROBLEMS

This section of the Development Assessment Manual describes comparisons between the TRAC-M/F77 code and analytical test problems. In Section 3.1, TRAC-M/F77 is compared with steady-state conduction solutions for 1D radial and two-dimensional (2D) radial-axial geometries. Analytical steady-state conduction solutions are developed with fixed heat-transfer coefficients and fixed fluid conditions. Comparisons are made with the TRAC-predicted temperature distributions for the same boundary conditions.

In Section 3.2, TRAC-M/F77 is compared with a drain and fill problem. Without significant numerical instabilities, this analytical test problem demonstrates the TRAC capability to accurately calculate mixture levels and level crossings at cell boundaries. It also tests TRAC methods for the calculation of gravity heads.

In Section 3.3, TRAC-M/F77 is compared with a manometer oscillation problem with a known analytical frequency. This test problem indicates that TRAC is accurately calculating the gravity head and the oscillation in this U-tube geometry.

One additional analytical test problem comparison can be found in the TRAC-M/F77 User's Guide for the American Nuclear Society decay-heat models. Two additional analytical test problem comparisons can be found in the TRAC-M/F77 Theory Manual for the offtake model and TRAC momentum solution for single-phase flow.

3.1. Steady-State Conduction Problems

The following steady-state conduction problems were provided by the Japan Atomic Energy Research Institute (JAERI) as part of the checkout for their fully implicit axial conduction solution. These steady-state conduction problems were added to the Los Alamos standard test problem set, which is executed each time a new code version is completed. These test problems provide an analytical check to verify that the TRAC conduction solution is accurate. The results for a 1D radial steady-state conduction solution and a 2D radial and axial steady-state conduction solution will be presented and discussed.

3.1.1. 1D Radial Conduction

The 1D radial steady-state conduction was determined for a generic nuclear fuel rod, with dimensions show in Fig. 3.1-1. For this test problem, the inner material is representative of fuel that is surrounded by a gap that is, in turn, surrounded by cladding. The material from $r = 0$ to $r = r_1$ is a uniform source of 1000 W. From $r = r_1$ to $r = r_2$, a gap occurs with a conductance of 1000 $W \cdot m^{-2} \cdot K^{-1}$. From $r = r_2$ to $r = r_3$, the thermal conductivity is 13.8 $W \cdot m^{-1} \cdot K^{-1}$. The outside fluid temperature is 300 K, and the rod surface heat-transfer coefficient is 2836 $W \cdot m^{-2} \cdot K^{-1}$.

The governing differential equation is

$$\frac{1}{r}\frac{d}{dr}\left(rk\frac{dT}{dr}\right) = -q'''$$

where T is the temperature, q''' is the heat generation rate per unit volume, k is the thermal conductivity, and r is the radial coordinate.

The boundary conditions are

$$\frac{dT}{dr} = 0 \text{ @ } r = 0$$

where there is no heat conduction across the centerline of the fuel rod, and

$$\left(-k\frac{dT}{dr}\right)_3 = h_3\left(T_3 - T_f\right) = Q/(2\pi r_3 L)$$

where h_3 is the surface heat transfer coefficient, T_3 and T_f are rod surface and outside fluid temperatures, respectively, r_3 is the distance between the rod surface and its centerline, L is the height of the rod, and Q is the heat generation rate within the rod.

$$Q = \pi r_1^2 L q''' = 1000 \text{ W}$$

At steady state, all of the energy produced must appear as surface heat flux,

$$q_1 = Q/(2\pi r_1 L),\ q_2 = Q/(2\pi r_2 L), \text{ and } q_3 = Q/(2\pi r_3 L)\ .$$

The solution for this problem is

$$T = T_3 - q_1 r_1 \ln(r/r_3)/k_3 \quad \text{for } r_2 < r < r_3$$
$$T = T_1 + q_1\left(r_1^2 - r^2\right)/(2k_1 r_1) \quad \text{for } r < r_1\ ,$$

where

$T_3 = Q/(2\pi r_3 h_3 L) + T_f$,
$T_2 = T_3 - q_1 r_1 \ln(r_2/r_3)/k_3$,
$T_1 = T_2 + q_1/h_2$,
where h_2 is the gap conductance,
$Q = 1000\ W$,
$L = 0.1$ m ,
$r_1 = 6.35$ mm ,
$r_2 = 6.426$ mm ,
$r_3 = 7.239$ mm
$k_1 = 2\ \text{W}\cdot\text{m}^{-1}\cdot\text{K}^{-1}$,
$k_3 = 13.8\ \text{W}\cdot\text{m}^{-1}\cdot\text{K}^{-1}$,
$T_f = 300$ K ,
$h_2 = 1000\ \text{W}\cdot\text{m}^{-2}\cdot\text{K}^{-1}$, and
$h_3 = 2836\ \text{W}\cdot\text{m}^{-2}\cdot\text{K}^{-1}$.

A TRAC model using 18 nodes in the radial direction (input model HCOND2) was used to represent the geometry of the analytical test problem described above. A TRAC calculation with this model with the appropriate boundary conditions was set up and executed. A listing of the input model used for this developmental assessment calculation is found in Appendix A. Archival storage information for this input model is found in Section 3.5. The results are compared with the analytical model in Table 3.1-1.

The results given in Table 3.1-1 indicate that the finite-difference solutions to the heat-conduction equation are accurate in the radial direction. The surface temperature is exact to four digits of accuracy, which is the number of digits that TRAC edits. The results in Table 3.1-1 also indicate a TRAC error of 0.17% in the centerline temperature, and thus the error is associated with an error in the temperature solution across the gap, where the steepest temperature profile occurs. Inaccuracies in the finite-difference approximation would tend to occur where the temperature profile is steep. The results confirm that the radial heat-conduction solution in TRAC is accurate and more than adequate for LWR safety applications.

3.1.2. 2D Radial and Axial Conduction

The analytical solution for the 2D radial and axial heat-conduction problem was developed for a solid rod with a constant and uniform heat source, with a constant heat-transfer coefficient in the radial direction, and adiabatic boundary conditions at both ends of the rod (Fig. 3.1-2). The axial variation in the temperature profile is obtained by having one fluid temperature boundary condition on the lower half of the rod and another fluid temperature boundary condition on the upper half of the rod. This problem is solved in Ref. 3-1, and the solution is not repeated here. A listing of the input model used for this developmental assessment calculation is found in Appendix A. Archival storage information for this input model is found in Section 3.5. The analytical solution for this problem is compared with the TRAC solution in Table 3.1-2 for rod temperatures along the centerline of the rod. The TRAC results in Table 3.1-2, obtained with input model HCOND3, indicate that the 2D conduction solution in the code is accurate. Again some inaccuracies appear in the region where the temperature profile is steep. The percentage error, however, is quite small (0.05%).

The results given in Table 3.1-2 are with the fine-mesh option on. The TRAC-M/F77 fine-mesh option adds axial levels in regions where the temperature profile is steep in an attempt to reduce the finite-difference error in that region. A comparison between TRAC and the analytical solution using 21 fixed axial levels (input model HCOND1) is given in Table 3.1-3. From this comparison, it can be seen that the fine-mesh option does improve accuracy of the finite-difference approximations to the original differential equation. The maximum error for the fixed node case is 0.75%, whereas the maximum error for the fine-mesh case is 0.05%.

In Table 3.1-4, the TRAC radial solution at z = 100 mm for the 21 fixed axial heat-conduction model (HCOND1) is compared with the analytical solution at the same location. Table 3.1-4 shows that the maximum error of 0.018% along that radius occurs at the outer edge. The results indicate that the TRAC 2D heat-conduction solution is very accurate in both the axial and radial directions. The accuracy of the axial solution is significantly improved with the fine-mesh option turned on.

TABLE 3.1-1

COMPARISON BETWEEN TRAC AND ANALYTICAL SOLUTIONS FOR A 1D HEAT-CONDUCTION PROBLEM IN THE RADIAL DIRECTION AT STEADY STATE (TRAC INPUT MODEL HCOND2)

Node Location (mm)	Analytical Solution (K)	TRAC Solution (K)	Error (K)
0.000	1039.8	1038.0	−1.8
1.830	1006.7	1005.0	−1.7
2.590	973.6	972.1	−1.5
3.175	940.3	938.8	−1.5
3.670	906.9	905.4	−1.5
4.100	873.9	872.4	−1.5
4.490	840.9	839.4	−1.5
4.850	807.7	806.2	−1.5
5.185	774.5	773.0	−1.5
5.500	741.3	739.8	−1.5
5.800	707.8	706.3	−1.5
6.080	675.0	673.5	−1.5
6.350	641.9	640.4	−1.5
6.426	391.3	391.3	0.0
6.670	387.0	387.0	0.0
6.840	384.1	384.1	0.0
7.040	380.7	380.7	0.0
7.239	377.5	377.5	0.0

TABLE 3.1-2

COMPARISON BETWEEN TRAC AND ANALYTICAL SOLUTIONS ALONG A CENTER LINE OF A ROD IN A 2D HEAT-CONDUCTION PROBLEM WHILE AT STEADY STATE WITH FINE MESH (TRAC INPUT MODEL HCOND3)

Node Location (mm)	Analytical Solution (K)	TRAC Solution (K)	Error (K)
0	658.1	658.1	0.0
10	658.1	658.1	0.0
20	658.1	658.1	0.0
30	658.1	658.1	0.0
40	658.1	658.1	0.0
50	658.1	658.1	0.0
60	658.1	658.1	0.0
70	658.1	658.1	0.0
80	658.2	658.2	0.0
90	662.7	662.7	0.0
100	758.1	758.5	+0.4
110	853.9	853.6	–0.3
120	857.5	857.9	+0.4
130	858.1	858.1	0.0
140	858.1	858.1	0.0
150	858.1	858.1	0.0
160	858.1	858.1	0.0
170	858.1	858.1	0.0
180	858.1	858.1	0.0
190	858.1	858.1	0.0
200	858.1	858.1	0.0

TABLE 3.1-3

COMPARISON BETWEEN TRAC AND ANALYTICAL SOLUTIONS ALONG A CENTER LINE OF A ROD IN A 2D HEAT-CONDUCTION PROBLEM WHILE AT STEADY STATE WITH FIXED NODING (TRAC INPUT MODEL HCOND1)

Node Location (mm)	Analytical Solution (K)	TRAC Solution (K)	Error (K)
0	658.1	658.1	0.0
10	658.1	658.1	0.0
20	658.1	658.1	0.0
30	658.1	658.1	0.0
40	658.1	658.1	0.0
50	658.1	658.1	0.0
60	658.1	658.1	0.0
70	658.1	658.2	+0.1
80	658.2	658.8	+0.6
90	662.7	667.7	+5.0
100	758.1	758.1	0.0
110	853.9	848.5	–5.4
120	857.5	857.4	–0.1
130	858.1	858.0	–0.1
140	858.1	858.1	0.0
150	858.1	858.1	0.0
160	858.1	858.1	0.0
170	858.1	858.1	0.0
180	858.1	858.1	0.0
190	858.1	858.1	0.0
200	858.1	858.1	0.0

TABLE 3.1-4

COMPARISON BETWEEN TRAC AND ANALYTICAL SOLUTIONS ALONG A RADIUS AT MIDPLANE OF A ROD IN A 2D HEAT-CONDUCTION PROBLEM AT STEADY STATE (TRAC INPUT MODEL HCOND1)

Node Location (mm)	Analytical Solution (K)	TRAC Solution (K)	Error (K)
0.0	758.1	758.1	0.0
0.5	756.1	756.1	0.0
1.0	750.1	750.1	0.0
1.5	740.2	740.2	0.0
2.0	726.3	726.3	0.0
2.5	708.4	708.4	0.0
3.0	686.5	686.5	0.0
3.5	660.6	660.6	0.0
4.0	630.8	630.8	0.0
4.5	596.9	597.0	+0.1
5.0	559.1	559.2	+0.1

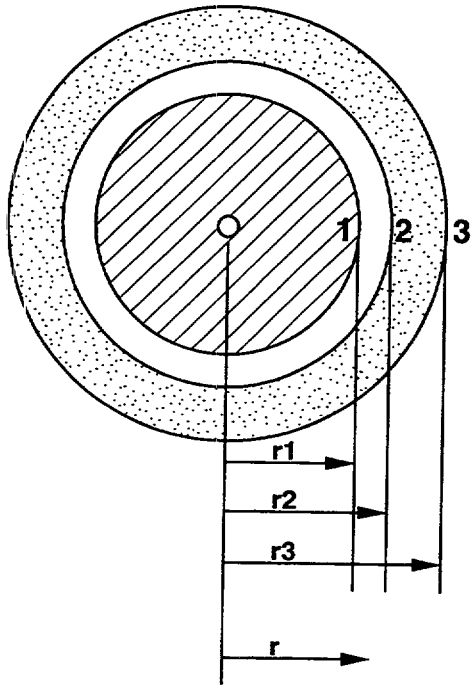

Fig. 3.1-1. Boundary conditions of a 1D heat-conduction problem in the radial direction.

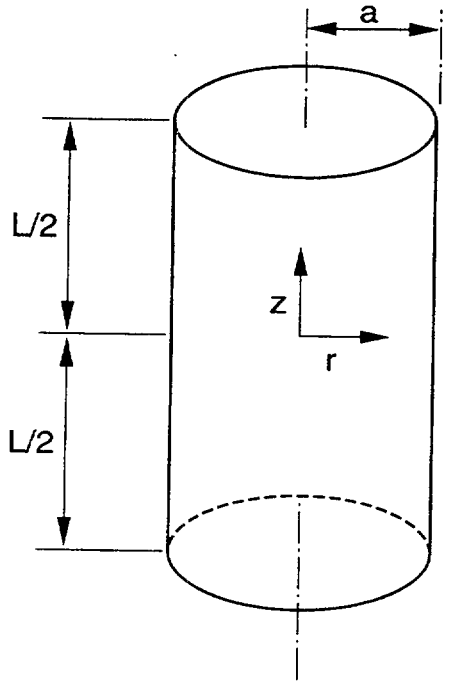

Fig. 3.1-2. Sketch of the 2D radial and axial heat-conduction problem.

3.2. 1D Drain and Fill Test Problem

The drain test problem consists of a vertical Pipe component that is partially filled with water, a Fill component, and a Break component, as shown in Fig. 3.2-1. The Break component provides a constant-pressure-boundary condition (1.0e+05 Pa) for the top of the pipe. The Fill component slowly drains water from the pipe and then refills the pipe to the original level. The purpose of this test problem is to verify that (1) TRAC does not calculate numerical instabilities as the cells in a Pipe component slowly drain or slowly fill, and that (2) TRAC accurately calculates the gravity head. A listing of the input model used for this developmental assessment calculation is found in Appendix A. Archival storage information for this input model is found in Section 3.5.

Figures 3.2-2 and 3.2-3 show the void fraction and mass flow rate within the pipe as the pipe drains and fills. These plots show that no numerical problems appear as the level crosses the cell boundaries. In Fig. 3.2-4, the pressure in cell 1 is plotted for the drain-fill transient. No significant pressure oscillations occur as the pipe drains and fills.

The Pipe component is made up of 15 cells with each cell being 1.0 m long. The Pipe component initially is full of 10 m of water. Therefore, the cell-center pressure of the first cell should be the 1.0e+05 Pa plus 9.5 m of water or,

$$p = p(break) + rho \cdot g \cdot h$$

$$= 1.0e+05 + 997.4 \cdot 9.8 \cdot 9.5 = 1.929e+05 \text{ Pa} .$$

TRAC calculates the initial cell 1 pressure before the drain starts as 1.92e+05 Pa and the final cell 1 pressure at the end-of-fill transient as 1.93e+05 Pa. The minimum level during this calculation is 4 m of water above the cell 1 center. The pressure, based on the static head above cell 1, would be

$$p = p(break) + rho \cdot g \cdot h$$

$$= 1.0e+05 + 997.4 \cdot 9.8 \cdot 4.0 = 1.391e+05 \text{ Pa} .$$

TRAC calculated a minimum pressure in cell 1 of 1.387e+05 Pa.

From this calculation and Figs. 3.2-3 and 3.2-4, it is apparent that TRAC accurately calculates gravity head as the cells slowly drain and fill. It is also apparent that TRAC encounters no significant numerical problems when a liquid level crosses a cell boundary.

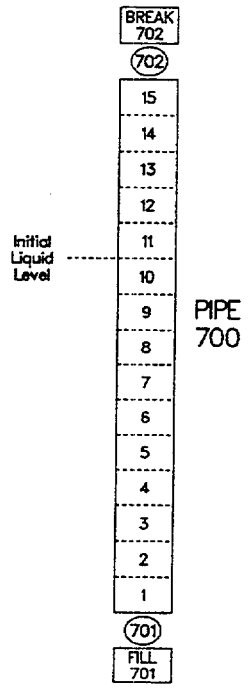

Fig. 3.2-1. TRAC model of the DRAIN test problem.

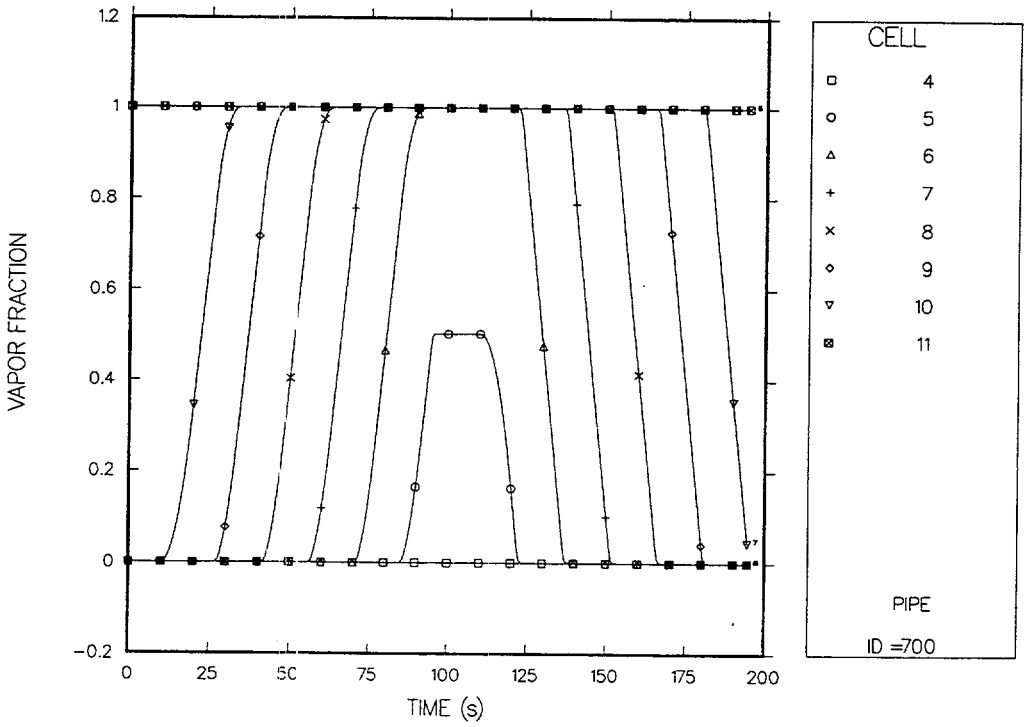

Fig. 3.2-2. Void fraction for the 1D drain and fill test problem.

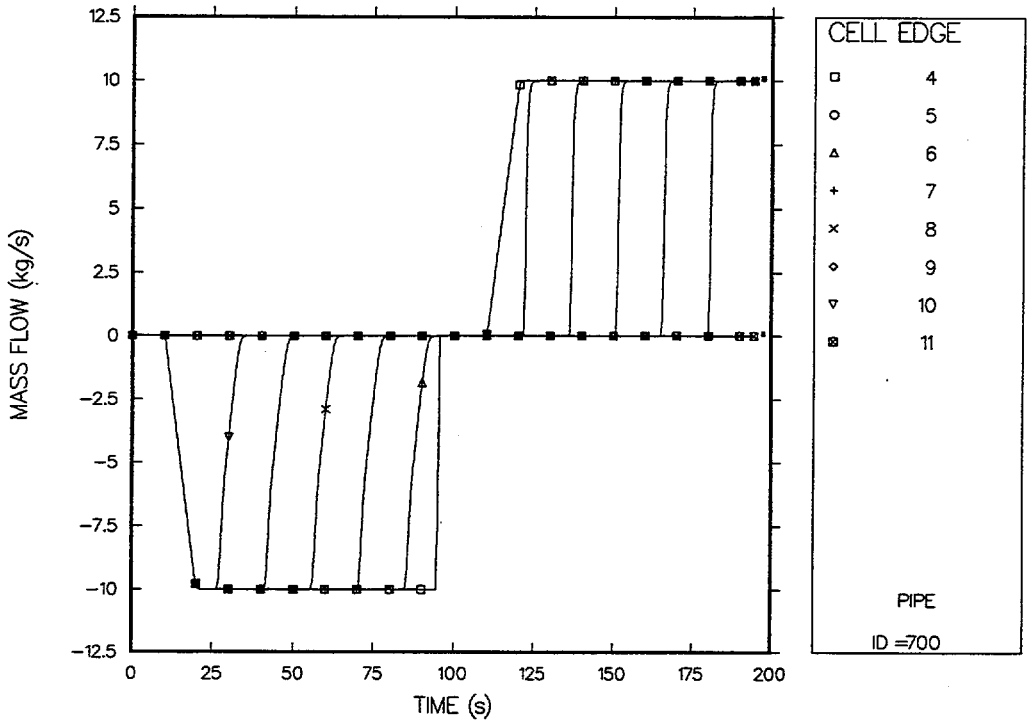

Fig. 3.2-3. Mass flow rate for the 1D drain and fill test problem.

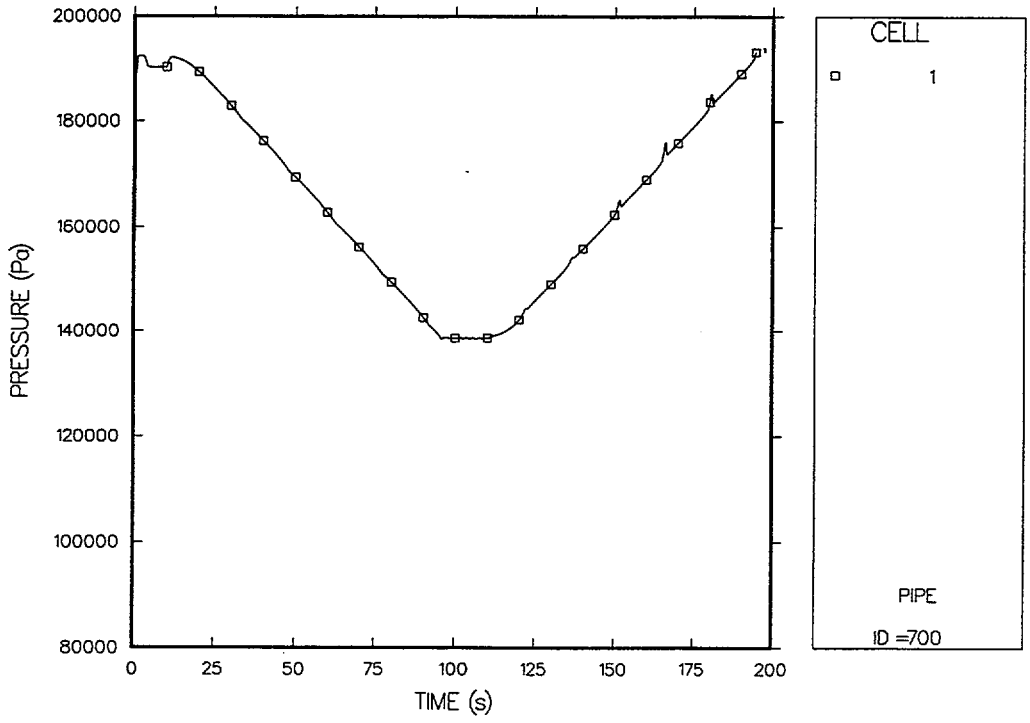

Fig. 3.2-4. Cell 1 pressure for the 1D drain and fill test problem.

3.3. U-Tube Test Problem

This test problem (Fig. 3.3-1) consists of a single pipe that represents a U-tube ~6.8 m high. Both legs of the U-tube are connected to constant pressure Break components. A listing of the input model used for this developmental assessment calculation is found in Appendix A. Archival storage information for this input model is found in Section 3.4. At initial conditions, the liquid level in one leg is 0.3 m higher than the liquid level in the other leg. This results in a U-tube oscillation that, from Ref. 3-2, has a period of

$$\tau = 2\pi\sqrt{L/2g} = 2.945 \text{ s} \quad .$$

Figure 3.3-2 shows the TRAC-calculated period for the U-tube oscillation to be ~3.1 s. In addition, it is apparent that the gas-volume-fraction oscillation in cell 6 is the same as the gas-volume-fraction oscillation in cell 10, except that their oscillations are out of phase. When the cell 6 gas volume fraction peaks high, the cell 10 gas volume fraction peaks low, and vice versa. Because of wall friction in the pipe, the amplitude of the gas-volume-fraction oscillation should decay to zero. In the TRAC calculation, the gas-volume-fraction oscillation doesn't completely dampen out because of the time and spatial averaging used to calculate interfacial shear for the momentum cells between cells 6 and 7 and between cells 9 and 10. For relatively large time-step sizes, the time-averaging model for the interfacial shear tends to move closer to the new time interfacial shear. Some time averaging of the interfacial shear is required for stability. The oscillations can be reduced through finer noding, reduced maximum time-step size, or increased wall drag. Figure 3.3-3 shows the effect of reducing the maximum time-step size from 0.05 s to 0.01 s.

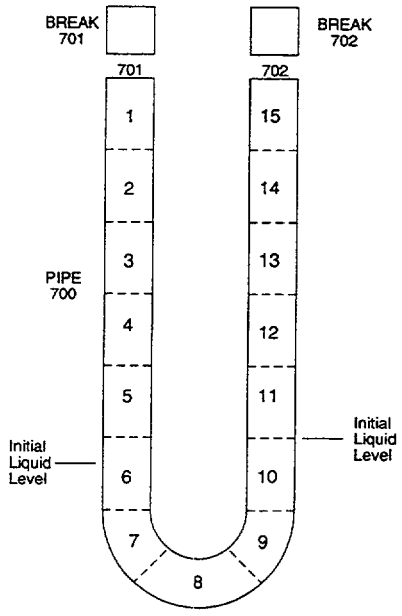

Fig. 3.3-1. TRAC model of the UTUBE test problem.

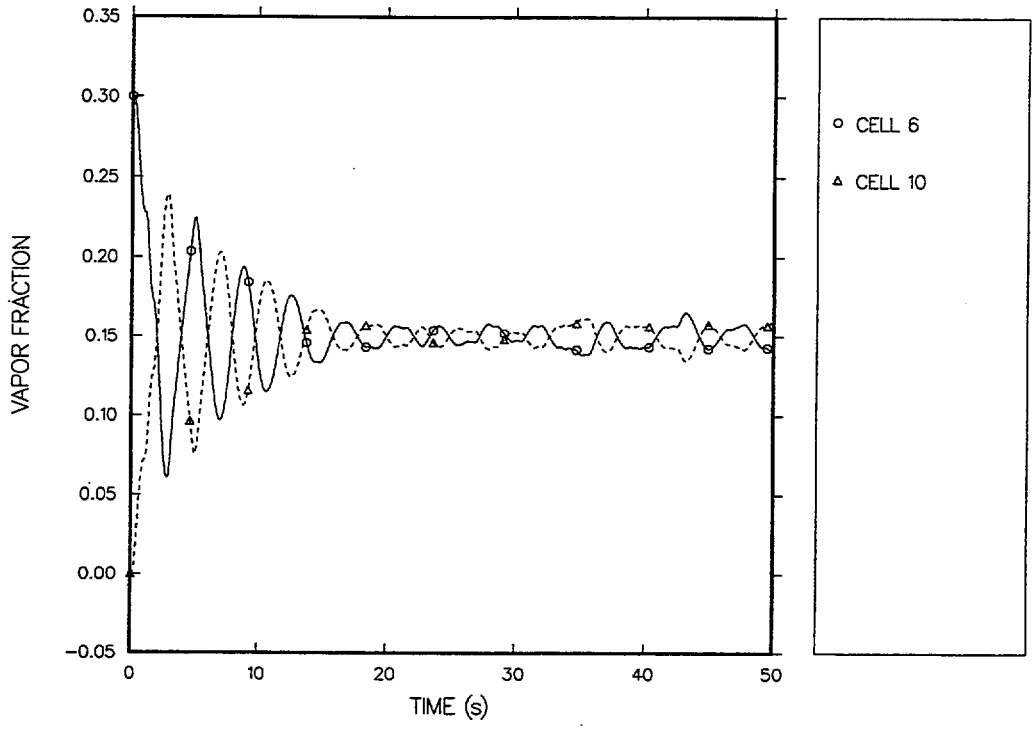

Fig. 3.3-2. Void fractions in cells 6 through 10 for the U-tube pipe.

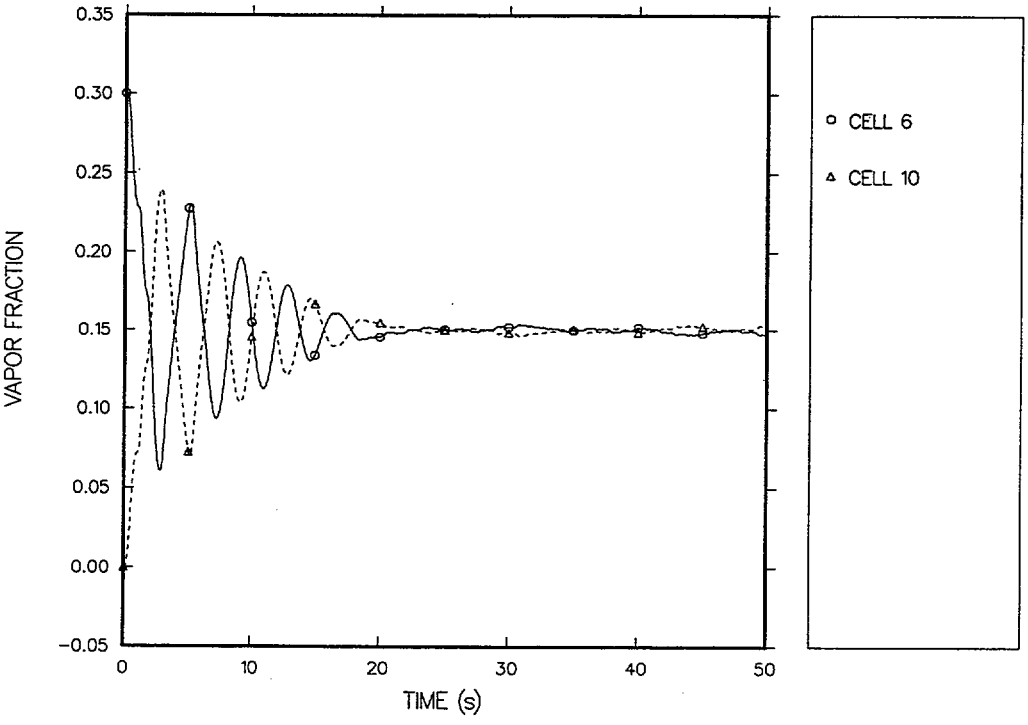

Fig. 3.3-3. Void fractions in cells 6 through 10 for the U-tube pipe with reduced time-step size.

3.4. Conclusions

We determined from the analytical-test-problem comparisons in this report that the TRAC finite-difference solution to the heat-conduction equations in rod geometries is accurate. The hydro models were found to be accurate and stable during the filling and draining of cells.

3.5. Code Performance

The Analytical assessment calculations were run on TRAC-M/F77 code Version 5.5. The run performance information and other pertinent comments follow.

1D radial steady-state conduction

Platform	Sun UltraSparc
Total Central Processing Unit (CPU) time (s)	2.68
Archive location of input model	CFS /tida/f77da_decks/hcond2
Archive location of calculation	CFS /trac-da/F77DA/nonreflood/ hcond.tar.gz

2D radial and axial steady-state conduction

Platform	Sun UltraSparc
Total CPU time (s)	13.6
Archive location of input model	CFS /tida/f77da_decks/hcond3
Archive location of calculation	CFS /trac-da/F77DA/nonreflood/ hcond.tar.gz

1D drain and fill

Platform	Sun UltraSparc
Total CPU time (s)	52.8
Archive location of input model	CFS /tida/f77da_decks/indrain
Archive location of calculation	CFS /trac-da/F77DA/nonreflood/ drain.tar.gz

U-tube test problem

Platform	Sun UltraSparc
Total CPU time (s)	45.8
Archive location of input model	CFS /tida/f77da_decks/inutube
Archive location of calculation	CFS /trac-da/F77DA/nonreflood/ utube.tar.gz

U-tube test problem with reduced time-step size

Platform	Sun UltraSparc
Total CPU time (s)	95.7
Archive location of input model	CFS /tida/f77da_decks/inutube.dt
Archive location of calculation	CFS /trac-da/F77DA/nonreflood/ utube.dt.tar.gz

REFERENCES

3-1. H. S. Carslaw and J. C. Jaeger, *Conduction of Heat in Solids* (Clarendon Press, Oxford, 1959).

3-2. Victor L. Streeter and E. Benjamin Wylie, *Fluid Mechanics* (McGraw-Hill Book Company, New York, 1975).

4. SEPARATE-EFFECT TESTS

4.1. Countercurrent Flow Limitation Model

The countercurrent flow limitation (CCFL) (or flooding) is defined when the downward flowing liquid in a countercurrent flow is about to change its direction and flow upward. This condition can be obtained if the steam flow rate is increased while keeping the liquid flow rate constant in a countercurrent flow. Depending upon the geometry of the equipment used, the occurrence of the CCFL could vary. In reactor applications, CCFL can occur at flow area restrictions when liquid flows downward through rising gas or vapor. For example, in the tie-plate region of a PWR during reflood, the upward flow of steam can prevent or limit the downflow of liquid. In TRAC-M, a special model allows the user to invoke characteristic CCFL correlations at specific locations. Rather than try to develop a new mechanistic CCFL model that could predict the complex behaviors in a variety of geometrical configurations, in TRAC we used the vast amount of correlated data already available. Therefore, the TRAC CCFL correlation provides the option to implement a CCFL correlation for a specific geometry and apply it at specific locations. We assessed the CCFL model in TRAC against the data of Bankoff et al.[4.1-1]

4.1.1. The Test Facility

The experimental apparatus of Bankoff et al. was a vertical channel with a flow area of 31 cm^2. The schematic of the test section is shown in Fig. 4.1-1. The air was introduced below a perforated plate. The water was introduced to the upper-plenum chamber and overflowed to drain. After testing various tie-plate geometries, we assessed TRAC with the 15-hole geometry corresponding to a small segment of the upper tie plate of a PWR. The air-water experiments were used to determine CCFL independent of the effects of phase change.

Pressure and temperature measurements were available at various places. Air and water flow rates were measured by rotameters. The test procedure used in air-water tests consisted of establishing the water inlet flow rate and then increasing the air flow rate, determining the water delivery rate at each step. Finally a point of essentially zero downwards delivery was obtained. This point is defined as the end of complete bypass (EOCB), which corresponds to the CCFL.

4.1.2. TRAC Model for Bankoff's Tests

The test section is modeled with a 1D Vessel component with 11 axial cells. A sketch illustrates the TRAC model in Fig. 4.1-2. The rectangular perforated plate was located at the interface of the fifth and sixth cells. The flow area of all 15 holes is specified at this interface. The hydraulic diameter of 10.5 mm was the same as that of the hole diameter. The water injection Pipe is connected to the middle of the water pool that existed initially in Cells 6 to 9. The height of this pool of water was controlled by the drain tube. The water-drain tube, modeled by a Pipe component, was connected horizontally to Cell 9. The other side of the drain tube was connected to an atmospheric Break component. Downward flowing water was collected at the bottom of the vessel, which connected to a zero Fill boundary condition. The volume of the bottom level of the Vessel was sufficient for water flowing through the tie plate to accumulate. The air flowed through an air outlet pipe to a Break component. A listing of the input model used for this developmental assessment calculation is found in Appendix B. Archival

storage information for this input model is found in Section 4.1.6.

The TRAC CCFL model allows the user to input the characteristic flooding curve parameters for a specific geometry applied at a particular location. Typically, these parameters have been developed from experimental data for the geometry of interest or for hardware of at least similar dimensions. Bankoff et al. have shown that the data correlate well with the relationship

$$H_g^{1/2} + M H_\ell^{1/2} = C \quad , \tag{4.1-1}$$

where

H_g is the dimensionless gas flux,

H_l is the dimensionless liquid delivery,

C is the abscissa intercept, and

M is the slope.

The Bankoff relationship is sufficiently general that either Wallis scaling for diameter dependence, Kutaleladze scaling for surface-tension dependence, or a combination of the two can be implemented. The scaling is performed by defining a variable-length scale in the determination of the dimensionless flux:

$$H_k = j_k \left(\frac{\rho_k}{g_c w \Delta\rho} \right)^{\frac{1}{2}} \quad , \tag{4.1-2}$$

$$w = HD^{1-B} L^B \quad , \tag{4.1-3}$$

and

$$L = \left(\frac{\sigma}{g_c \Delta\rho} \right)^{\frac{1}{2}} \quad , \tag{4.1-4}$$

where

k refers to the phase (gas or liquid),

j is the superficial velocity,

HD is the hydraulic diameter,

g_c is the gravitational constant,

σ is the surface tension,

ρ is the density,

$\Delta\rho$ is the difference between the phasic densities, and

B is a factor between 0 and 1.

For $B = 0$, the correlation reverts to the Wallis scaling and reverts to the Kutateladze scaling for $B = 1$. For B between 0 and 1, the user can input the scaling proposed by Bankoff et al., which can be used for tie-plate geometry even if no experimental data are available.

4.1.3. Comparison of Predicted and Measured Results

We varied both liquid and air mass flow. Figures 4.1-3 and 4.1-4 show the liquid and air mass flow at the perforated plate. A smoothing function was applied to the mass flows, and the smoothed mass flows were then used to calculate the dimensionless fluxes $H_l^{1/2}$ and $H_g^{1/2}$. The dimensionless fluxes are shown in Fig. 4.1-5.

Figure 4.1-6 shows the TRAC results for flow of air and water at 1 atm along with the correlation of the Bankoff data. The TRAC input parameters for the Bankoff data are B = 0.884, M = 1, and C = 1.92. As demonstrated, the TRAC results are in very good agreement with the experimented data of Bankoff. Thus, it is expected that when the TRAC flooding option is used at a given location, the liquid down flow will be predicted reasonably well for the plates similar to those used in the Bankoff experiment as well as the other types of plates.

4.1.4. Conclusions

The TRAC CCFL model allows the user to input the characteristic flooding curve parameters for a specific geometry applied at a particular location. This model, when used to predict the air-water CCFL data obtained by Bankoff et al., gave reasonable results in predicting the CCFL. The assessment is limited to air-water mixtures at atmospheric conditions. Also, we have not assessed the current code CCFL model for steam-water mixtures.

4.1.5. Code Performance

The Bankoff assessment calculations were run on TRAC-M/F77 code Version 5.5. The run performance information plus other pertinent comments follow.

Bankoff CCFL Test

Platform	Sun Sparc20
Total CPU time (s)	587.9
Archive location of input model	CFS /tida/f77da_decks/inbankoff
Archive location of calculation	CFS /trac-da/F77DA/nonreflood/ bankoff.tar.gz

REFERENCES

4.1-1. S. G. Bankoff, R. S. Tankin, M. C. Yuen, and C. L. Hsieh, "Countercurrent Flow of Air/Water and Steam/Water Through a Horizontal Perforated Plate," *Int. J. Heat Mass Transfer* **24** (8), 1381–1395 (1981).

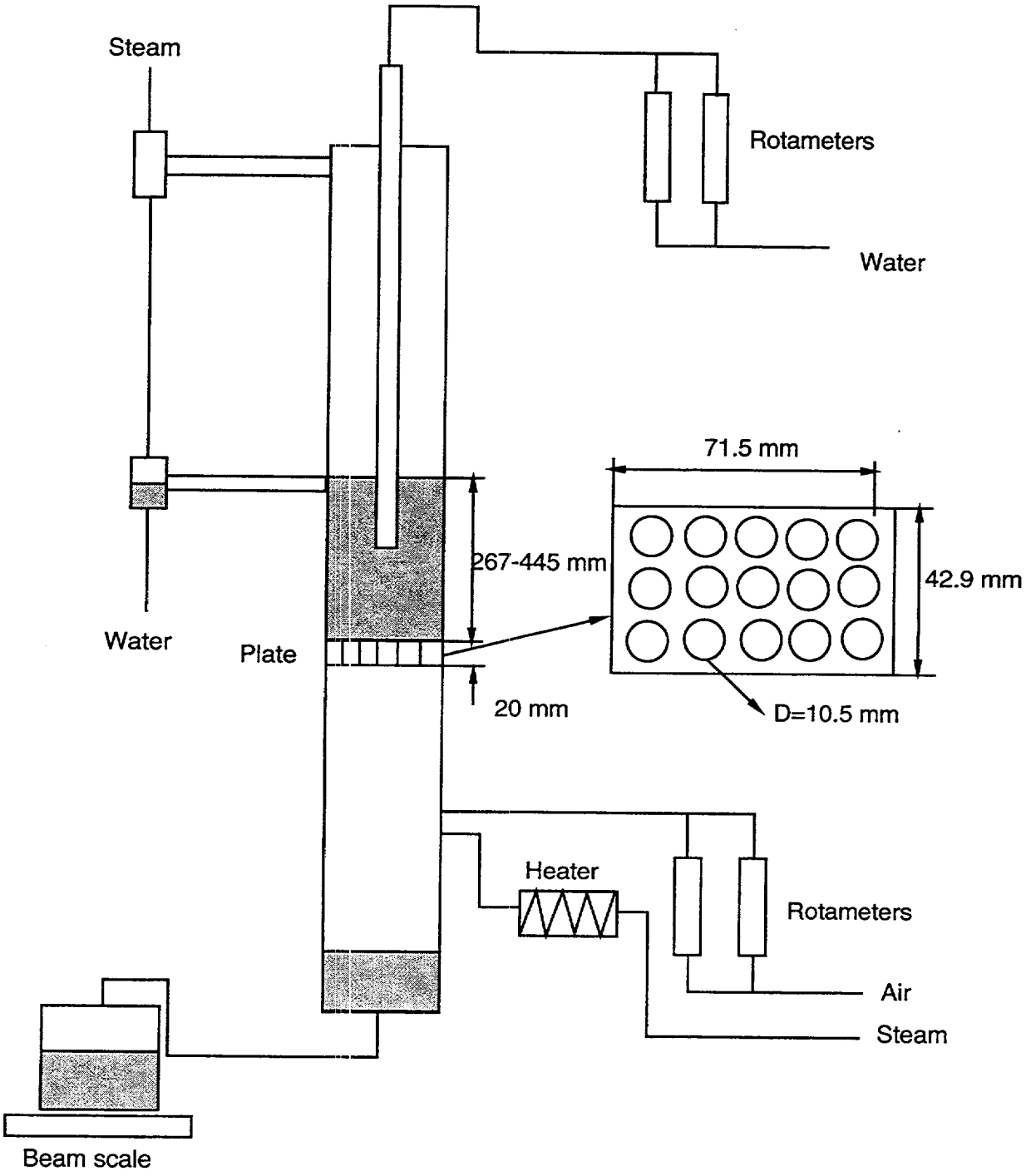

Fig. 4.1-1. Schematic of the perforated plate air-water countercurrent flow system used by Bankoff et al. (from Ref. 4.1-1).

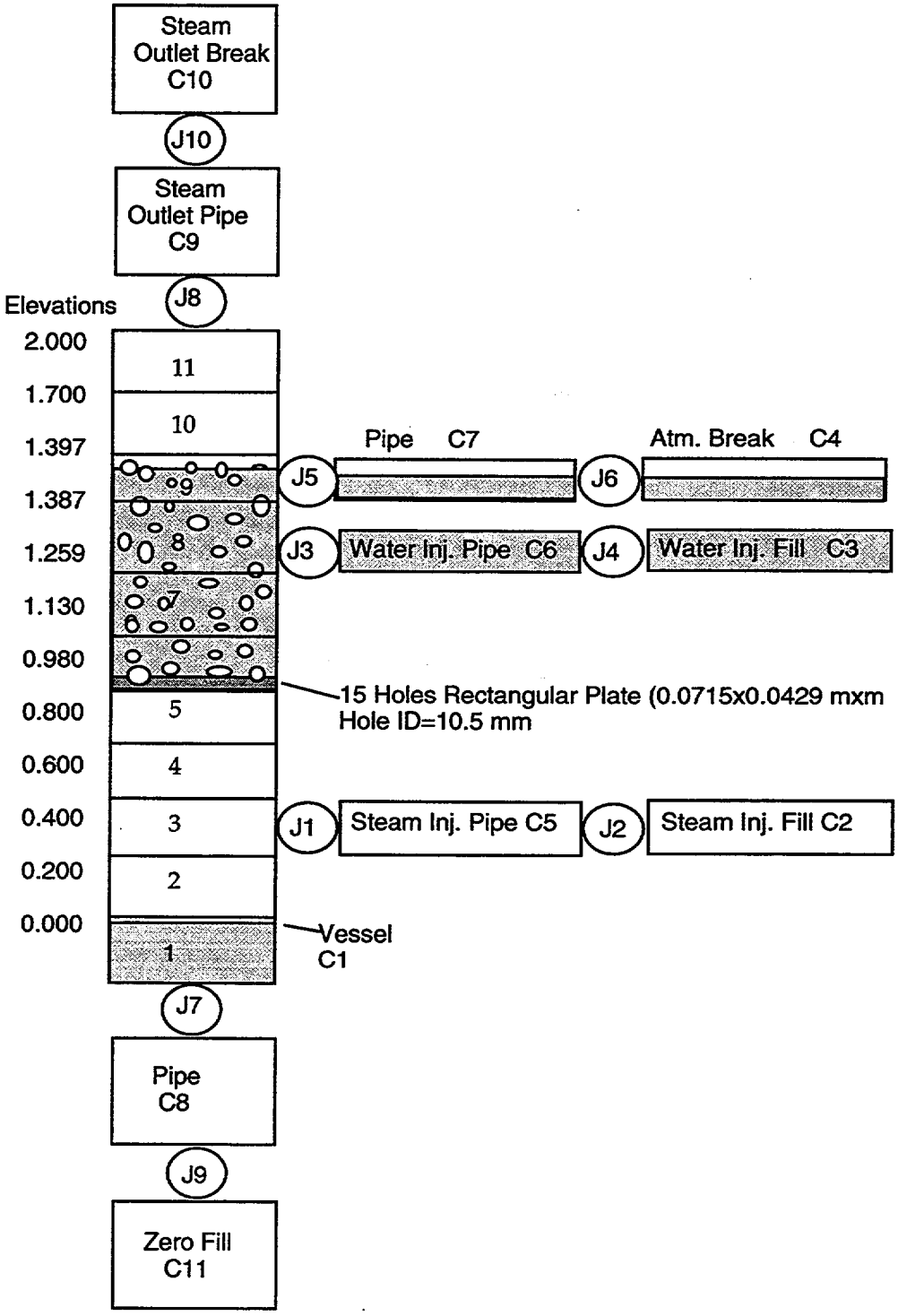

Fig. 4.1-2. TRAC model for the test apparatus of Bankoff et al.

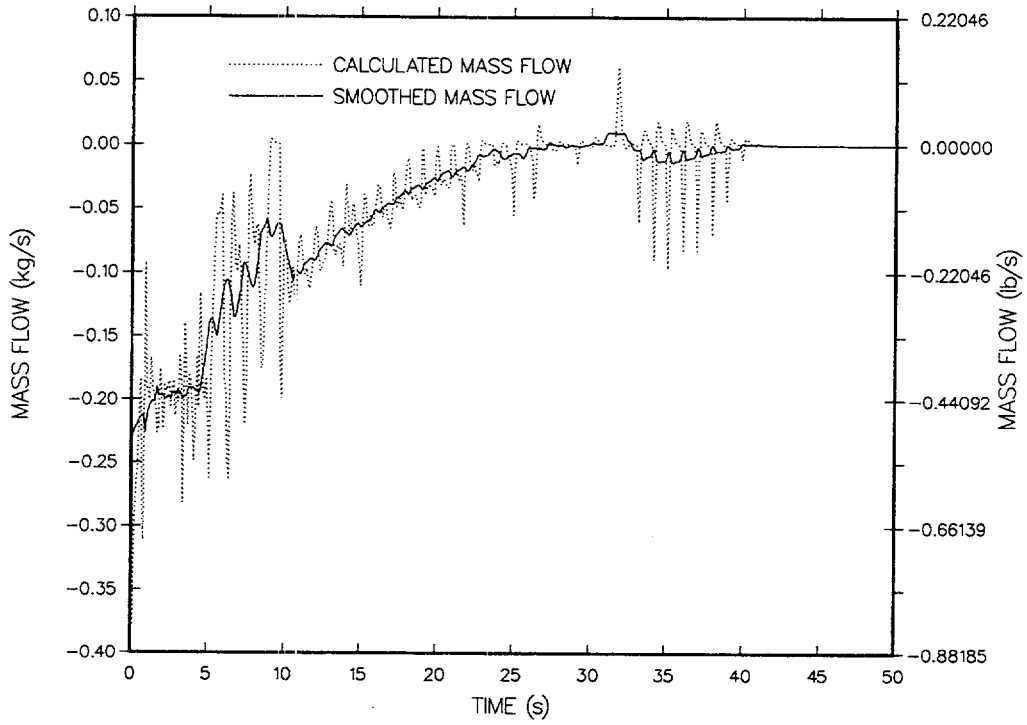

Fig. 4.1-3. Liquid mass flow at the perforated plate.

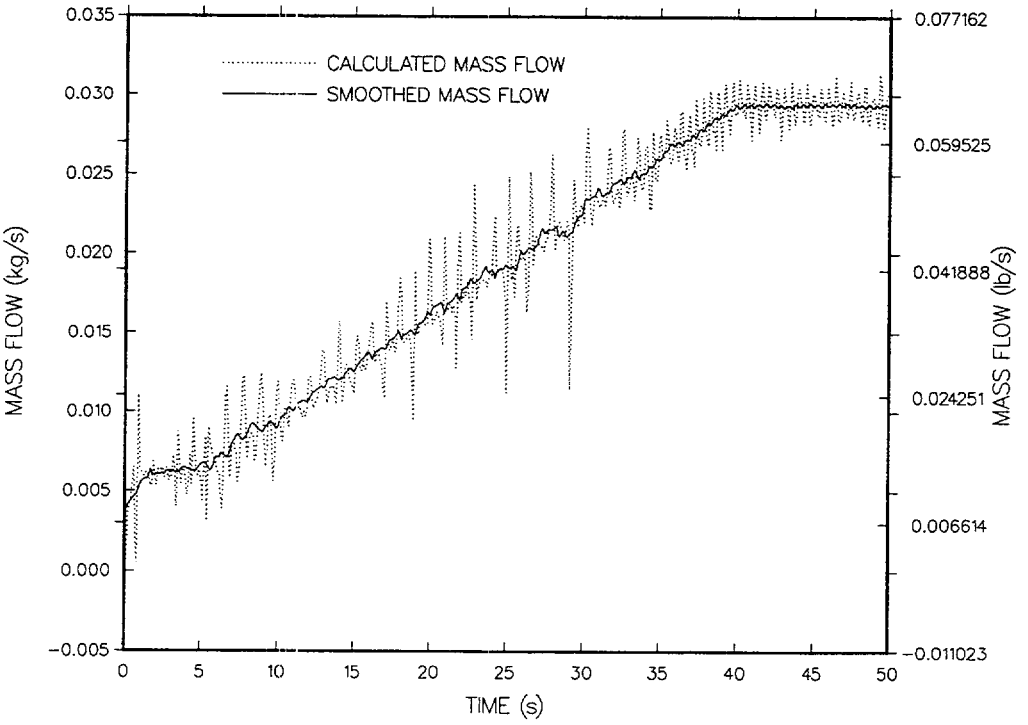

Fig. 4.1-4. Vapor mass flow at the perforated plate.

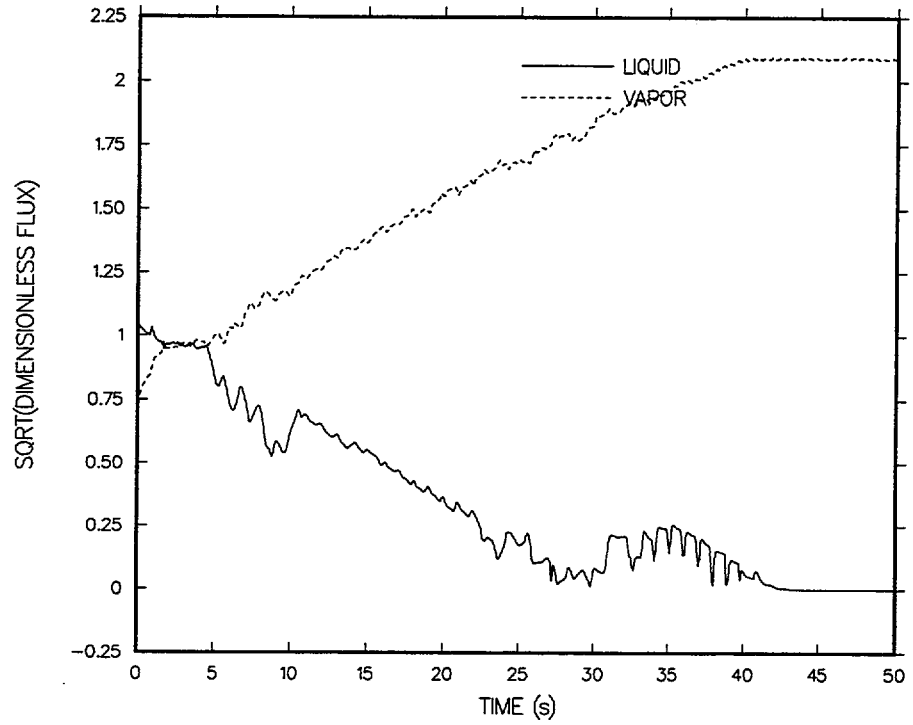

Fig. 4.1-5. Liquid and vapor dimensionless fluxes at the perforated plate.

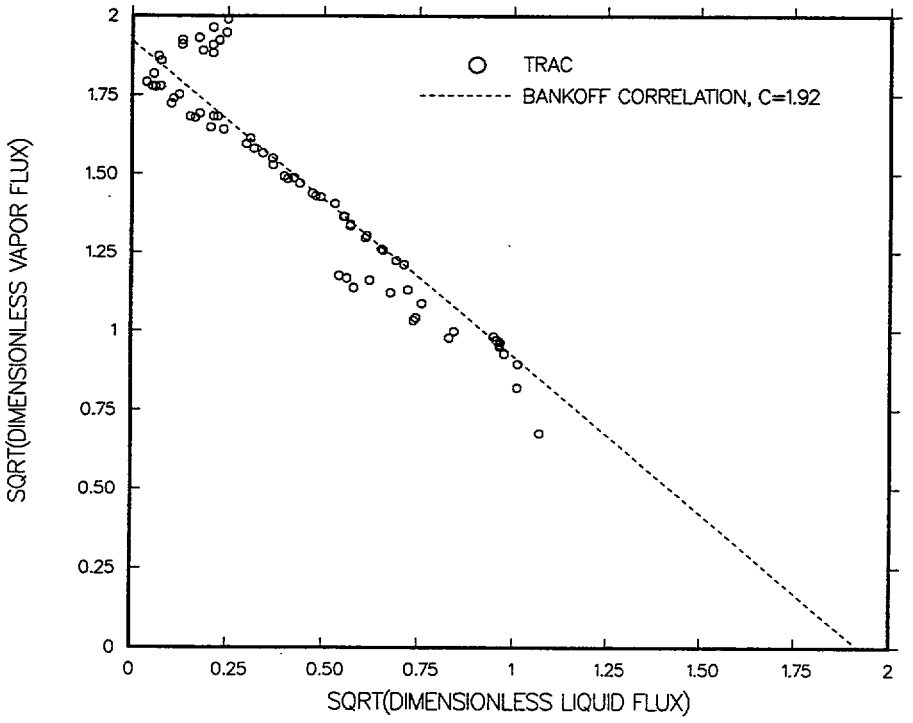

Fig. 4.1-6. Comparison of TRAC results with Bankoff correlation.

4.2. Condensation Models

When a thermal-hydraulic analysis of PWRs under an SB- or LBLOCA is of concern, a direct contact of subcooled liquid with steam occurs after the emergency injection system is turned on, causing a violent pressure transient and a water-hammer-type phenomenon. The prediction of the correct interfacial condensation rate for a variety of flow regimes is very important for LOCA analyses. The condensation model used in TRAC-PF1/MOD2 is based upon the Chen-Mayinger condensation correlation. The detail of the model with its limitations and applicability range is already discussed in the TRAC-PF1/MOD2 Theory Manual. The assessment of the model against small-scale, separate-effect data will be discussed in the following section.

4.2.1. Condensation Experiments and Test Facility

The data and correlations for this assessment are taken from Akimoto et al.[4.2-1,4.2-2] The same test section was used in all experiments. A sketch of the experimental facility is shown in Fig. 4.2-1. The test section was horizontal (3.35 m long) and 0.02 x 0.05 m in rectangular cross section. The steam produced by a steam generator was injected at one end of the test section after it was metered. The subcooled water was injected 1.5 m downstream of the steam entrance with an injection tee that transversed the entire width of the test section. The test section was transparent, which allows flow visualizations. The two-phase fluid was emptied to an exit tank that was exhausted to the atmosphere.

Akimoto et al. observed two distinct flow regimes—oscillatory and stable—where the frequency and amplitude of the oscillations changed with the steam injection rate. The water was injected after the steam flow rate was established. Oscillatory flow consisted of a liquid plug that traveled back and forth from the liquid injection point to the channel exit because of changing condensation rates, which depend on the location of the plug interface. When the liquid injection point was fully exposed to the steam, rapid condensation caused the local pressure to drop below that of the channel exit forcing the liquid plug to flow toward the channel entrance. When the plug moved upstream of the liquid injection point, this movement insulated the injected liquid from the steam. The decreasing condensation rate caused the local pressure to increase until the plug moved toward the channel exit, and a new oscillation began. When the steam flow rate was sufficiently large relative to the liquid injection rate, a mist flow with no oscillation occurred.

Akimoto et al.[4.2-1,4.2-2] reported the following simple relation for the boundary between the oscillatory and stable flow regimes:

$$M_v = 0.84 M_{c,\max} \tag{4.2-1}$$

and

$$M_{c,\max} = \frac{C_{pl}\left\{T_{sat}(P_{exit}) - T_{li}\right\}}{h_{tg}} M_{li} \quad , \tag{4.2-2}$$

where M_v is the mass flux of the injected steam, M_{ti} is the mass flux of the injected liquid through the steam flow channel, C_{pl} is the specific heat of the injected liquid, h_{tg} is

the injected-liquid's latent heat of vaporization, $T_{sat}(P_{exit})$ is the saturation temperature at atmospheric pressure, T_{li} is the injected-liquid's subcooled temperature, and $M_{c,max}$ is defined by Akimoto et al. as the condensability* of the injected water.

4.2.2. TRAC Model of Akimoto's Test Facility

The TRAC input model for this facility is shown in Figs. 4.2-2 and 4.2-3. Two Tee components were used to simulate the horizontal test section and the exit tank. The rectangular cross section is considered as a circular geometry with a hydraulic diameter of 0.286 m and actual flow area of 0.001 m^2. The node sizes are selected in such a way that the length-to-diameter ratio is similar to that used in full plant analyses. Listings of the input models used for this developmental assessment calculation are found in Appendix C. Archival storage information for the input models is found in Section 4.2.6.

4.2.3. Comparison of Measured and Predicted Results.

We will discuss the assessment results and the analysis of three types of flow: mist flow, plug flow, and the transition from stable to oscillatory flows.

4.2.3.1. Mist Flow. When the steam flow rate is high, Akimoto et al.[4.2-1,4.2-2] observed that the injected liquid was quickly atomized into droplets immediately downstream of the injection nozzle. The mixing process in the injection region was described as very rapid and complicated. Some coalesced droplets eventually reattached to the wall and formed a liquid annular film.

The liquid film temperature is determined by the condensation rate of steam. The liquid film temperature was measured as a function of distance from the injection nozzle. For the purpose of assessment, we chose the test results given in Fig. 4 of Ref. 4.2-1. The test conditions were

- steam mass flux = 40 $kg \cdot m^{-2} \cdot s^{-1}$
- injected-liquid mass flux = 330 $kg \cdot m^{-2} \cdot s^{-1}$
- injected-liquid temperature = 323 K

The predicted and measured liquid film temperatures are plotted in Fig. 4.2-4 as a function of the distance from the injection nozzle; the predicted temperatures correspond to t = 150 s because they remain constant. As it enters the test section, the liquid is subcooled to 323 K. Shortly downstream (0.1 m), experimental data indicate that the liquid is heated up to 361.6 K; whereas, the calculated liquid temperature at this location is 358.0 K, indicating a disagreement of only 3.6 K between calculated and measured data. The predicted and measured values at 0.2 m downstream of the injection point are almost the same, 366.4 and 365.7 K, respectively. At 0.3 m downstream of the injection point, the predicted and measured values, 369.6 and 368.8 K, also agree very well. The correct prediction of the liquid film temperature indicates that the TRAC condensation model (including the heat-transfer coefficient and the interfacial area) for the mist flow adequately predicts the rate of condensation and is expected to predict a reasonably correct rate of condensation for the mist-flow regime encountered in LOCA situations.

---

* The condensability is a measure of the maximum mass that the injected water can condense before reaching thermal equilibrium assuming the complete mixing of water with steam (Ref. 4.2-2).

4.2.3.2. Oscillatory Plug Flow. Unstable flow with regular oscillations occurred when the liquid injection rate was increased. Akimoto et al.[4.2-1,4.2-2] classified the oscillatory flow regime into two subregimes: type A and type B. Type-A flow included very-well-defined oscillatory behavior. We therefore considered the test reported in Fig. 5 of Ref. 4.2-1, which was performed with a 20 $kg \cdot m^{-2} \cdot s^{-1}$steam and 600 $kg \cdot m^{-2} \cdot s^{-1}$water mass fluxes.

The predicted pressure trace at the injection location shown in Fig. 4.2-5 indicates that the pressure oscillated between 36.8 to 335.8 kPa. As listed in Table 4.2-1, the measured pressure oscillation between 40 and 150 kPa indicates that the predicted pressure peak was too high. A count of the number of oscillations between 15 and 40 s yielded a predicted oscillation frequency of 1.73 s^{-1}, which agrees reasonably well with the measured data of 1.67 s^{-1}.

As seen in Figs. 4.2-6 and 4.2-7, a pressure increase near the liquid injection point (Cell 4) corresponds to both a decrease of the void fraction in Cell 4 and an increase of the void fraction in Cell 13, clearly indicating that a plug of water is moving toward the steam injection point. When the plug moves upstream of the injection point, the condensation at the liquid-steam interface continues, heating up the liquid and eventually reducing the condensation rate. The pressure then continues to rise and causes the plug movement to be reversed, exposing the injection point to the steam. When the injection point is exposed to the in-flowing steam, a rapid condensation occurs and the pressure drops below that of the exit tank. The plug of water will then start to move toward the injection point again. A new oscillation follows the same history.

Despite the complexity of the phenomenon described above, the TRAC-predicted frequency and minimum pressure agree reasonably well with the measured data. The overprediction of the maximum pressure can be explained if the condensation rate is underpredicted when the liquid-steam interface passes the liquid-injection point, where the condensation rate should reach a maximum. Therefore, the modeled steam pressure is not limited by removing enough of its energy, which allows for extreme pressure excursions, while the channel is plugged with liquid. Inadequate modeling of the pressure losses could be another reason for the overpredicted maximum pressure. Further investigation is needed to identify the correct cause.

4.2.3.3. Stable-to-Oscillatory Flow Transition. In this section, we will assess TRAC's ability to predict oscillatory condensation by comparing its calculated results with the transition correlation of Akimoto et al.[4.2-1,4.2-2] When a liquid flow rate for a given steam flow rate in the stable flow region is increased, the flow starts to show some oscillations. During this transition, it was assumed that oscillatory flow occurs when the amplitude of the pressure oscillations is >±15% of the exit tank's exhaust pressure (i.e., 1 atm.). Figures 4.2-8 through 4.2-10 contain the pressure oscillation traces for the various steam and injected-liquid mass fluxes. Table 4.2-2 shows the times at which the pressure oscillation amplitudes exceed the ±15% criterion. The predicted results and the experimental observations are presented in Fig. 4.2-11, which plots an averaged steam mass flux as a function of an averaged condensability, as given by Eq. (4.2-1). The values and the standard deviation error bars shown in Fig. 4.2-11 were generated by averaging the calculated steam mass flux and the calculated condensability of nine timesteps surrounding the time at which the aforementioned pressure oscillation amplitude criterion was determined. When the ratio $M_v/M_{c,\max}$ becomes smaller than

the experimental value of 0.84, at a given liquid flow rate, the liquid completely plugs the channel because the steam provided is not enough to overcome the condensate energy of the injected liquid, which causes oscillations. The transitions do not occur at the ideal thermodynamic ratio of $M_v/M_{c,\max}=1$ because of thermal nonequilibrium between the fluid phases.[4.2-2]

As shown in Fig. 4.2-11, the experimental constant of 0.84 in Eq. (4.2-1) is reasonably predicted for the stable-to-oscillatory flow transition for lower mass fluxes. However, for the higher steam flux, TRAC overpredicts the condensability. This may be the result of a feedback effect of the large liquid mass flux that simultaneously reduces the steam mass flux very rapidly and increases the generated drop diameter,[4.2-2] which effectively reduces the interfacial area between the liquid and vapor. The condensation rate depends upon the predicted condensation heat-transfer coefficient (HTC) and the interfacial area; unfortunately, no experimental data are available from Akimoto's tests to determine whether either the heat-transfer coefficient or the interfacial area is underpredicted.

4.2.4. Conclusions

The following conclusions can be drawn from the foregoing assessment work. In both stable and mist-flow regimes, the TRAC condensation model gave good results when predicting the liquid temperature along the test section measured by Akimoto et al.[4.2-1,4.2-2] The results indicated that the rate of condensation in the mist-flow regime was predicted reasonably well; therefore, it is expected that the model will also give reasonable results for a similar range of operating parameters in the mist-flow regime (i.e., lower steam mass flux) when it is used in full-plant simulations.

The model predicted the frequency of oscillations when the plug flow is considered. The motion of the plug in the predictions was similar to that described by Akimoto et al.[4.2-1,4.2-2] The pressure variation disagreed with the measured data. The maximum peak pressure was overpredicted, whereas the minimum pressure agreed reasonably well with the data. The overpredicted maximum pressure could be due to the overprediction of the condensation rate when the steam-water interface was at the upstream of the injection point

The transition from stable to oscillatory flow is reasonably predicted for a steam mass flux at or below 40 $kg \cdot m^{-2}s^{-1}$. For a higher steam flux, the condensability is overpredicted because of the possible feedback effect of increased drop size, which reduces interfacial heat transfer and possibly causes a severe pressure transient in full-plant-LOCA simulations for higher steam and injected-liquid mass fluxes.

4.2.5. Code Performance

The Akimoto condensation assessment calculation[4.2-1,4.2-2] was run on TRAC-M/F77 code Version 5.5. The run performance information and other pertinent comments follow.

Mist Flow Calculation

Platform	Sun Enterprise 3000
Total CPU time (s)	163.6
Archive location of input model	CFS /tida/f77da_decks/inakimoto.mist
Archive location of calculation	CFS /trac-da/F77DA/nonreflood/ akimoto.tar.gz

Oscillatory Plug Flow Calculation

Platform	Sun Enterprise 3000
Total CPU time (s)	291.9
Archive location of input model	CFS /tida/f77da_decks/inakimoto.plug
Archive location of calculation	CFS /trac-da/F77DA/nonreflood/ akimoto.tar.gz

Stable-to-Oscillatory Flow Transition Calculation

Platform	Sun Enterprise 3000
Total CPU time (s)	104.1
Archive location of input model	CFS /tida/f77da_decks/inakimoto.trans
Archive location of calculation	CFS /trac-da/F77DA/nonreflood/ akimoto.tar.gz

REFERENCES

4.2-1. H. Akimoto, Y. Tanaka, T. Kozwa, A. Inoue, and S. Aoki, "Oscillatory Flows Induced by Direct-Contact Condensation of Flowing Steam with Injected Water," *J. Nucl. Sci. Tech.* **22**(4), 269–283 (1985).

4.2-2. H. Akimoto, Y. Kozawa, A. Inoue, and S. Aoki, "Analysis of Direct Contact Condensation of Flowing Steam onto Injected Water with Multifluid Model of Two-Phase Flow," *J. Nucl. Sci. Tech.* **20** (12), 1006–1022, (1983).

TABLE 4.2-1

DATA COMPARISON IN THE JUNCTION CELL OF THE TEST SECTION

Type	Experiment	TRAC-PF1/MOD2
Oscillation Frequency (s^{-1})	1.67	1.73
Maximum Pressure (kPa)	140	335.8
Minimum Pressure (kPa)	40	36.8

TABLE 4.2-2

CALCULATED PRESSURE OSCILLATION START TIMES AND INJECTED-LIQUID CONDENSABILITY FOR A GIVEN STEAM MASS FLUX

Steam Mass Flux (±1 Std Dev) ($kg \cdot m^{-2} \cdot s^{-1}$)	Liquid Condensability (±1 Std Dev) ($kg \cdot m^{-2} \cdot s^{-1}$)	Oscillation Start Time (s)
19.59 (±4.45)	22.87 (±0.29)	20.92
40.56 (±8.12)	46.71 (±0.65)	70.13
60.24 (±3.41)	85.52 (±1.04)	122.98

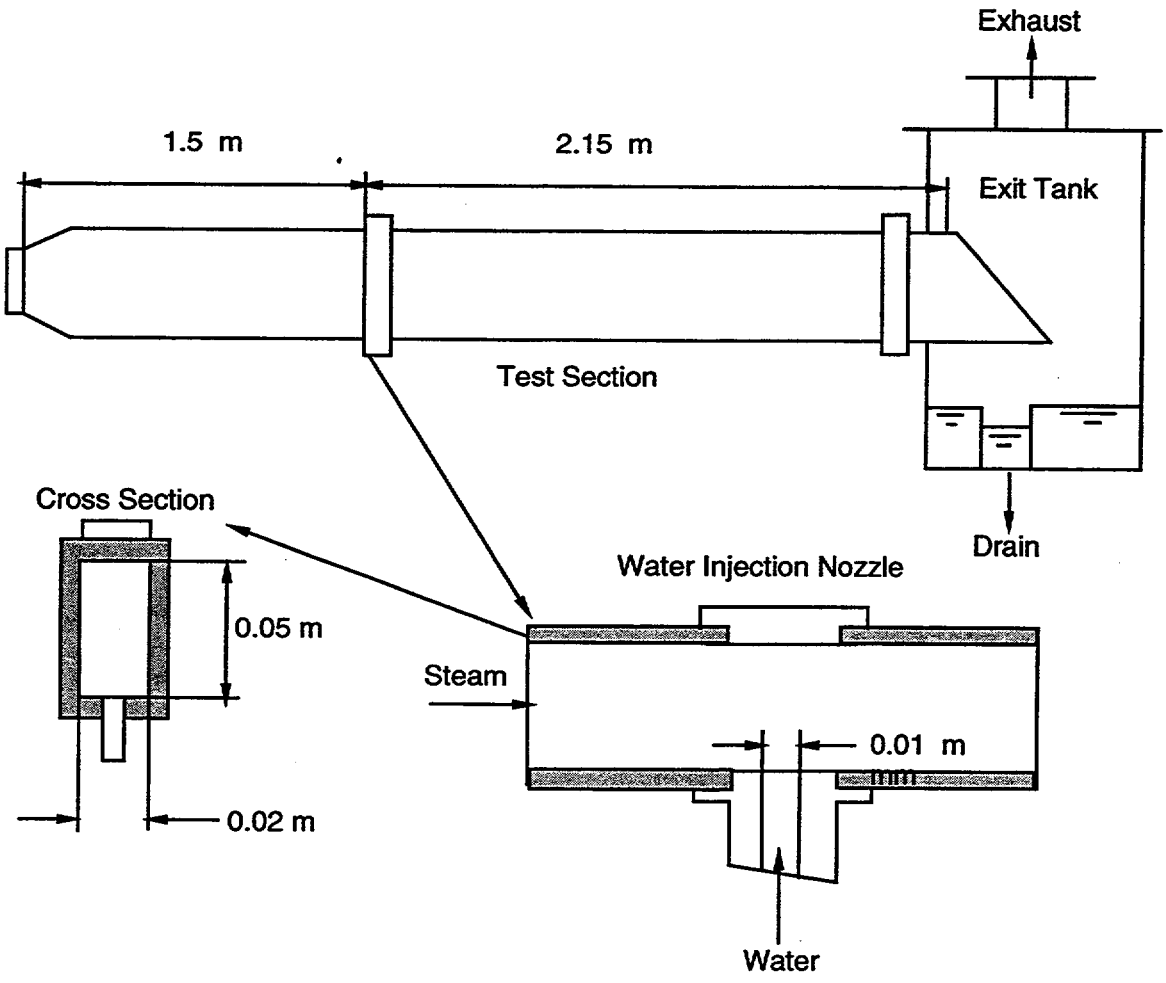

Fig. 4.2-1. The experimental apparatus of Akimoto et al. (from Ref. 4.2-1).

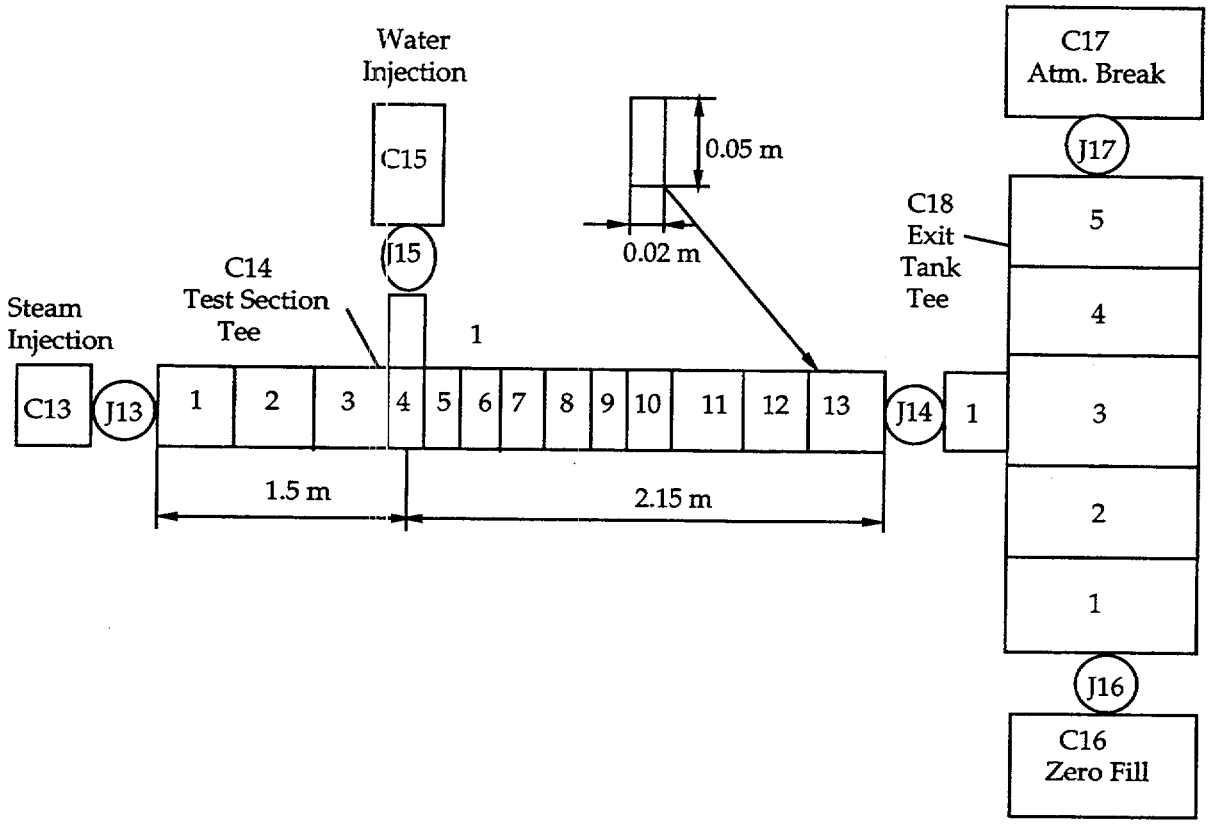

Fig. 4.2-2. TRAC input model.

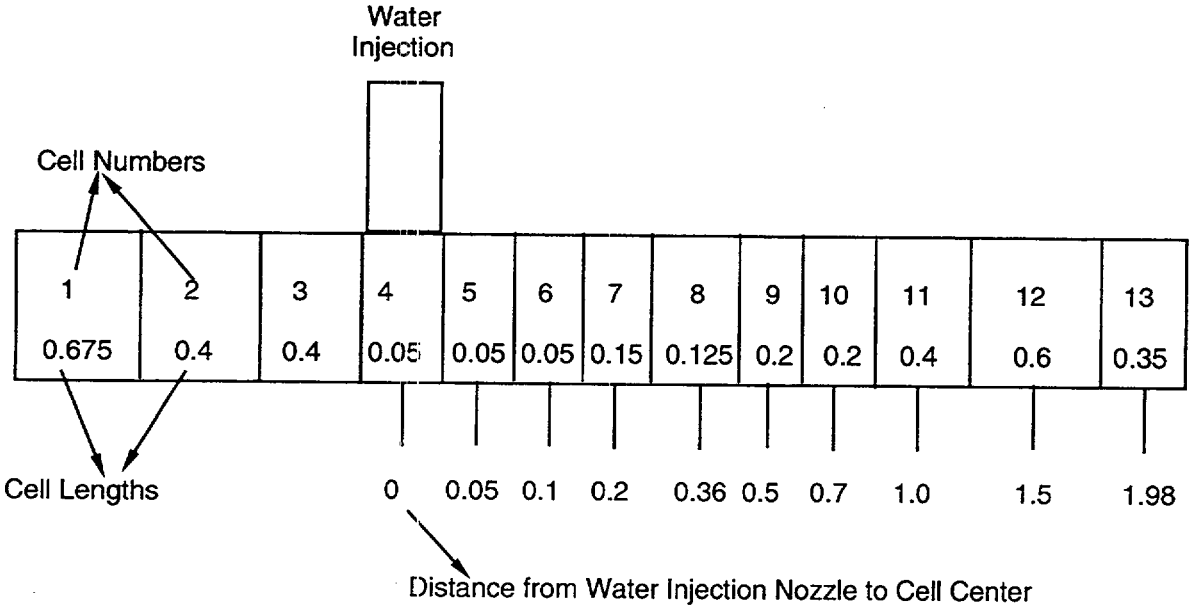

Fig. 4.2-3. Noding cell lengths of the test section.

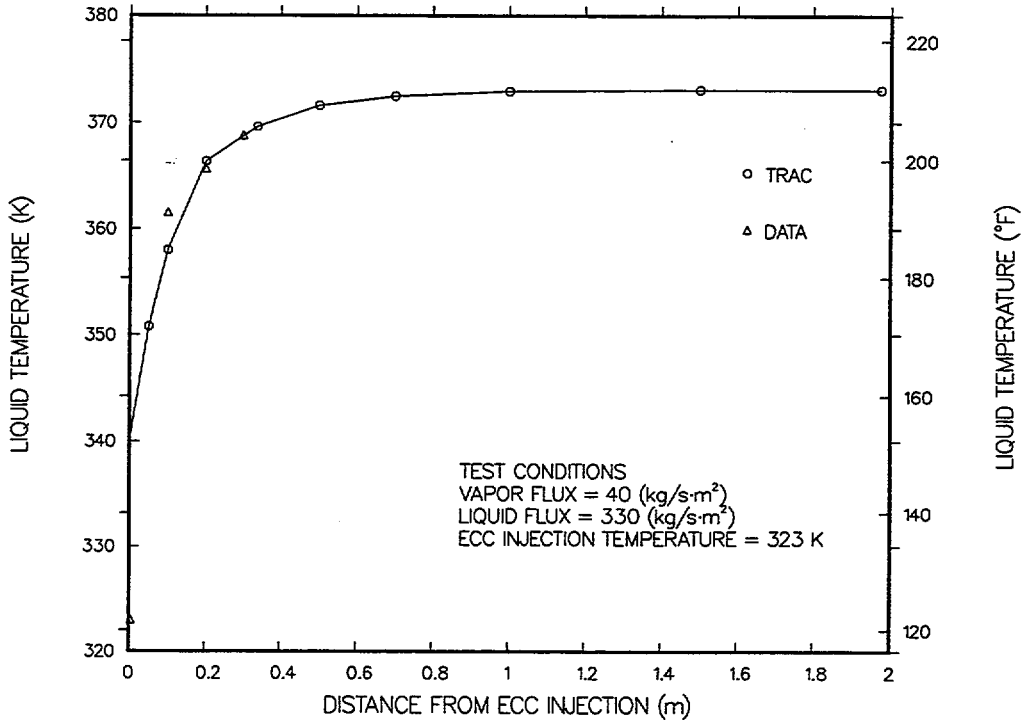

Fig. 4.2-4. Predicted and measured liquid film temperatures for the mist flow.

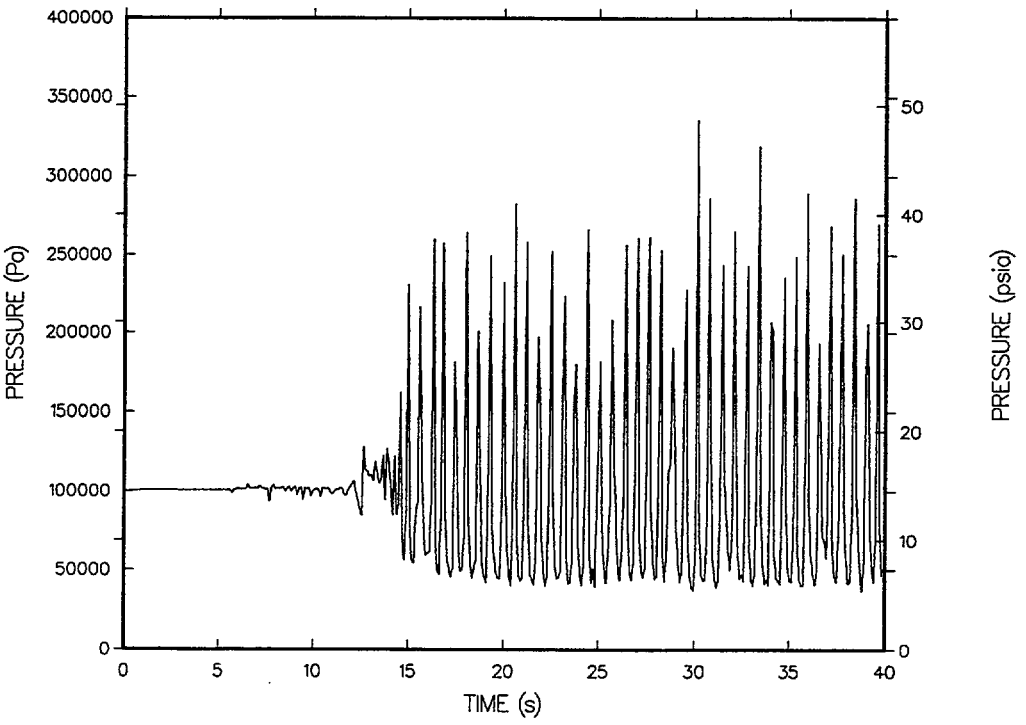

Fig. 4.2-5. Predicted pressure trace at the injection location for the oscillatory plug flow.

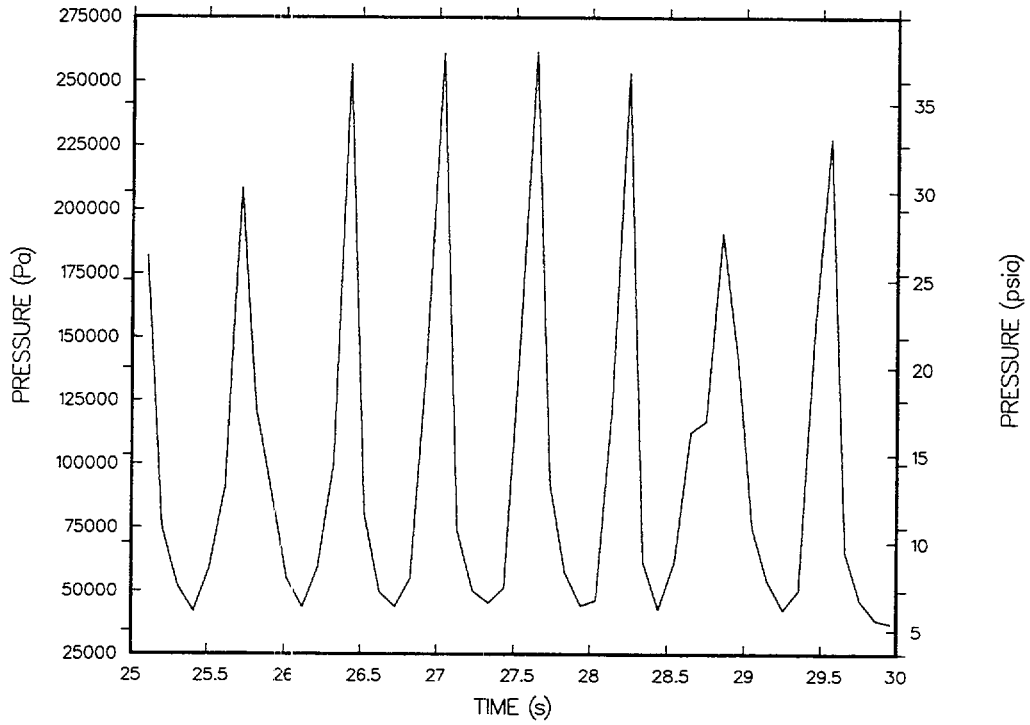

Fig. 4.2-6. Partial trace of the predicted pressure at the injection location for the oscillatory plug flow.

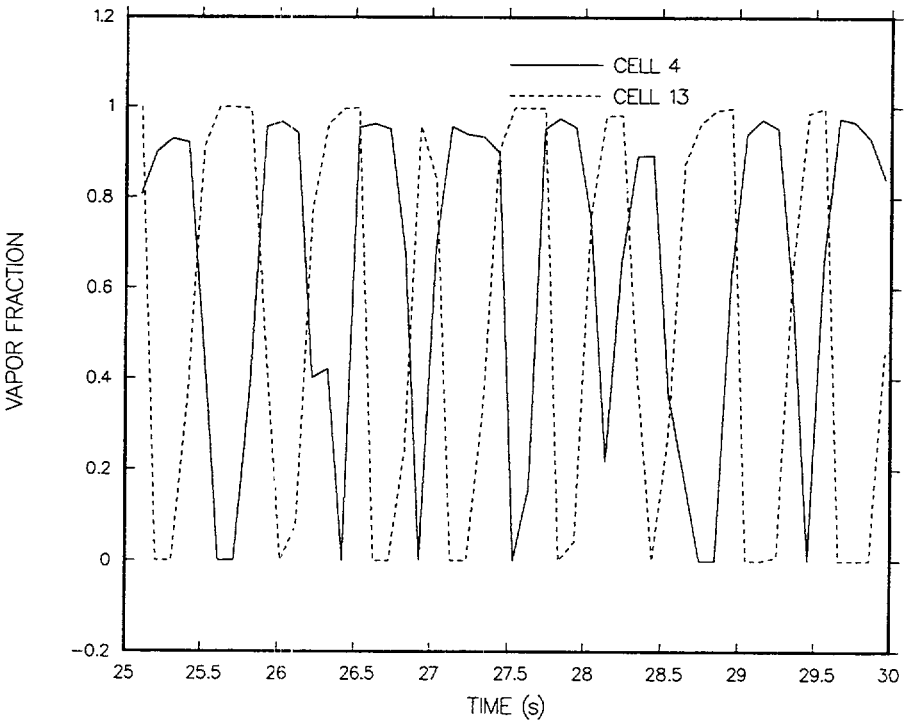

Fig. 4.2-7. Void fractions in cells 4 and 13 for the oscillatory plug flow.

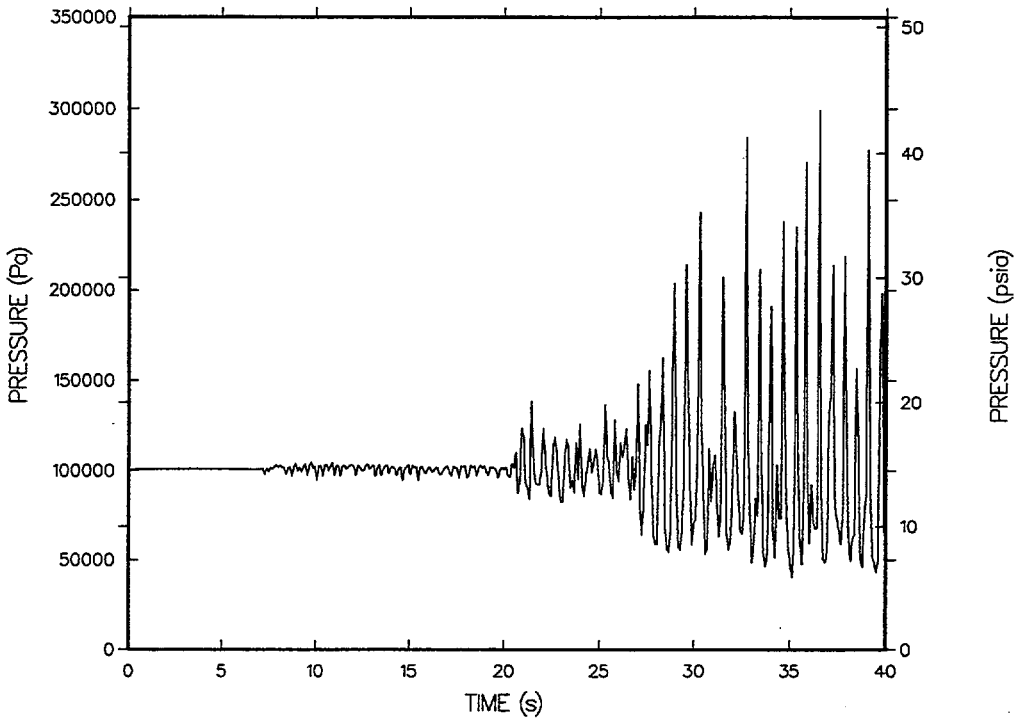

Fig. 4.2-8. Predicted pressure trace at the liquid injection location for the steady-to-oscillatory transition flow ($M_v = 20$ kg·m^{-2}·s^{-1}).

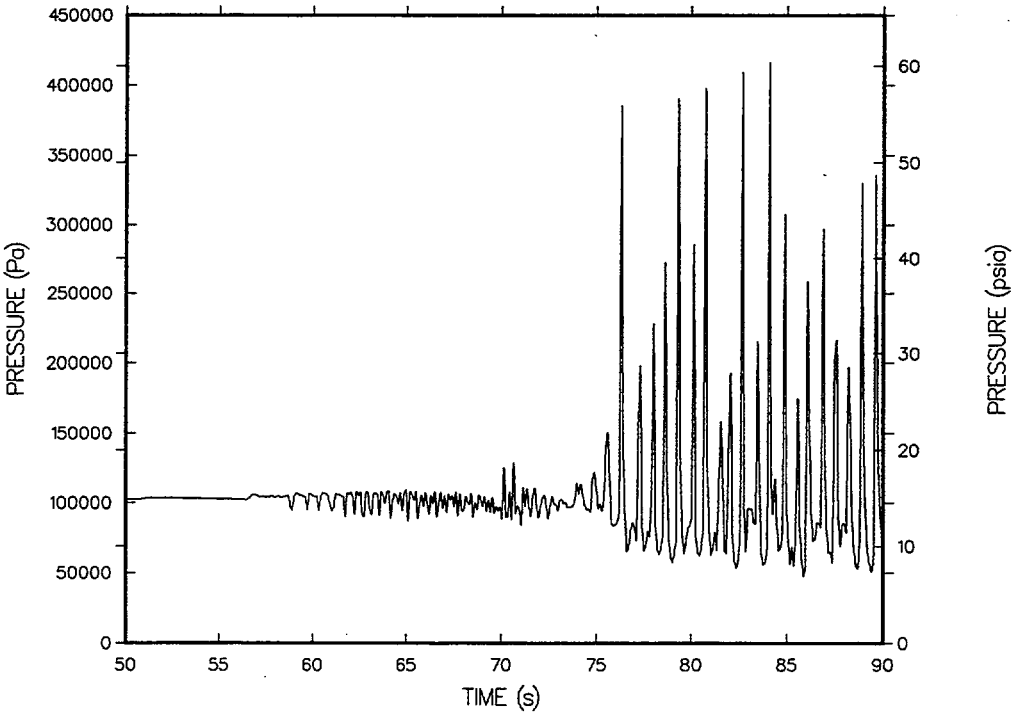

Fig. 4.2-9. Predicted pressure trace at the liquid injection location for the steady-to-oscillatory transition flow ($M_v = 40$ kg·m^{-2}·s^{-1}).

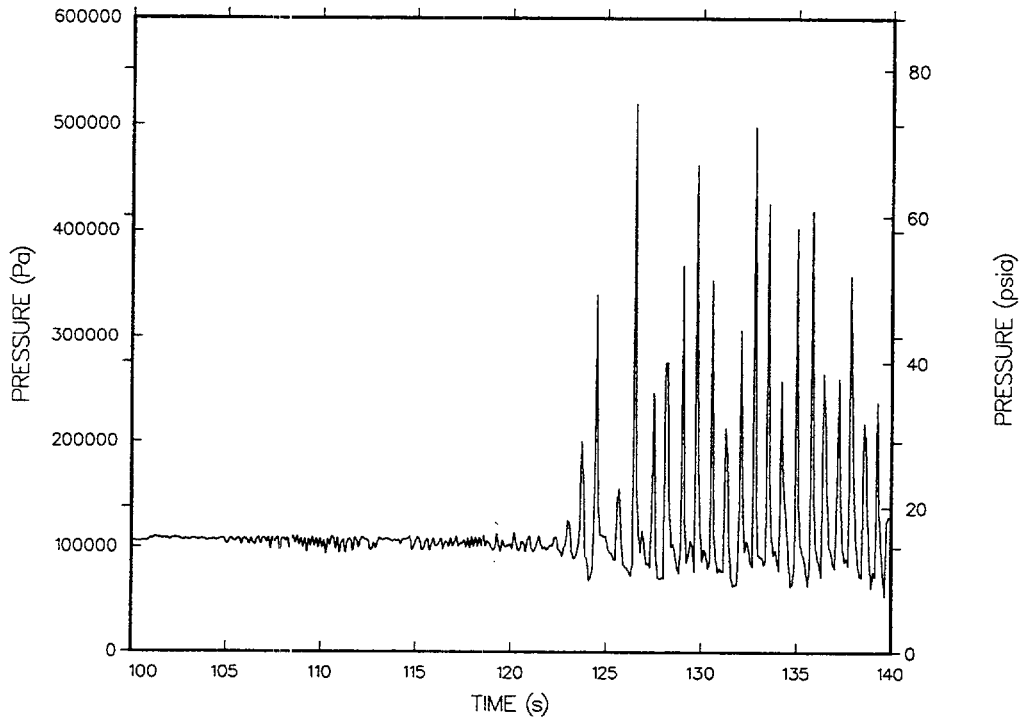

Fig. 4.2-10. Predicted pressure trace at the liquid injection location for the steady-to-oscillatory transition flow (M_v = 60 kg·m^{-2}·s^{-1}).

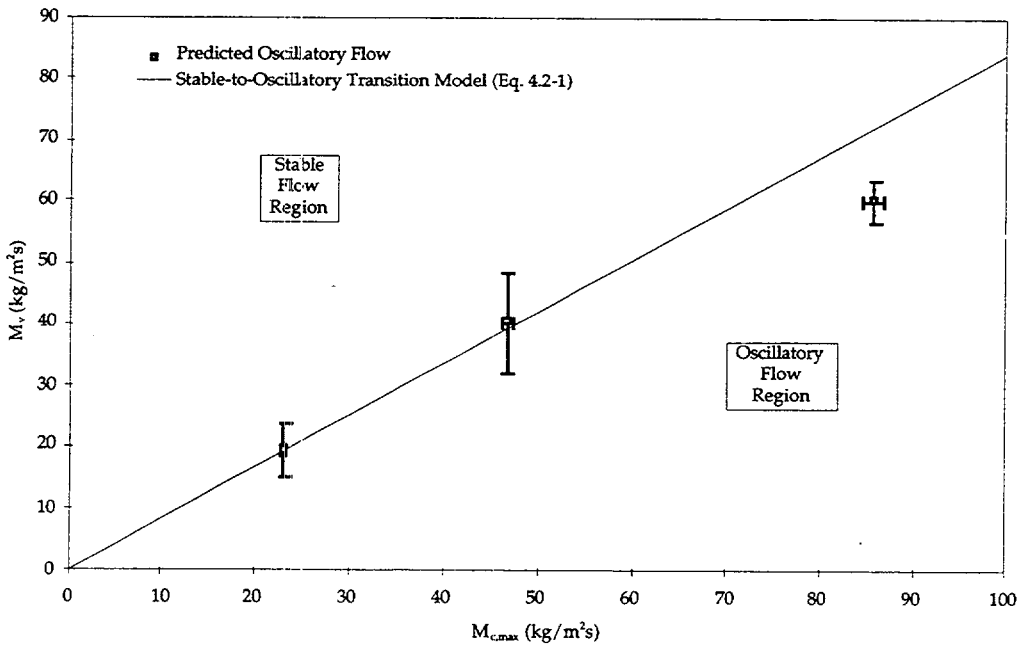

Fig. 4.2-11. Averaged steam flow rate as a function of averaged condensability, with error bars of ± one standard deviation, for the steady-to-oscillatory transition flow.

4.3. Critical-Flow Tests

This section assesses the TRAC critical-flow modeling. The section includes five Marviken critical-flow tests and the Edwards Blowdown Experiment Test 1. Only coarse-mesh models are evaluated. Previous TRAC critical-flow assessments have included fine-mesh models as well as coarse-mesh models. The fine-mesh models predate TRAC-PF1/MOD2 and were used to obtain choked-flow conditions when TRAC did not have a choked-flow model.

4.3.1. Description of TRAC Critical-Flow Model

The TRAC critical-flow model is described in Section 4.1 of the TRAC-M Theory Manual.[4.3-1] The 1D, critical-flow model was programmed in TRAC-PF1 in 1979–80 to evaluate choked-flow conditions with a coarse spatial mesh. Without the critical-flow model, a fine mesh is required to evaluate natural choking accurately from the hydrodynamic equations. Evaluating natural choking with a fine mesh is accurate only for smooth flow-area changes between upstream mesh cells. Whereas the critical-flow model improves computational efficiency by allowing a coarse mesh, it also allows upstream abrupt flow-area changes to be modeled while accurately predicting choked-flow conditions.

The critical-flow model comprises three separate models: a single-phase subcooled-liquid choked-flow model, a two-phase liquid and gas choked-flow model, and a single-phase gas, choked-flow model. The subcooled-liquid choked-flow model is a modified form of the Burnell model[4.3-2] for an upstream gas volume fraction <0.01. The subcooled-liquid choked-flow model also incorporates a nucleation-delay model developed by Jones.[4.3-3] The two-phase choked-flow model is an extension of the model developed by Ransom and Trapp[4.3-4] based on first principles and a characteristic-analysis approach for an upstream gas volume fraction between 0.1 and 0.999. Thermal equilibrium between the gas and liquid phases is assumed. Because there is a discontinuity in the sound speed during the transition from liquid to two-phase flow, linear interpolation is used between the subcooled-liquid and two-phase models for an upstream gas volume fraction between 0.01 and 0.1. The gas choked-flow model assumes ideal-gas isentropic expansion for an upstream gas volume fraction >0.999.

4.3.2. Description of Critical-Flow Assessment Models

Six critical-flow experiments from the Marviken and the Edwards blowdown test facilities were selected for assessment calculations. Marviken Tests 4, 13, 20, 22, and 24 were selected for developmental assessment calculations along with Edwards Blowdown Test 1. The selected Marviken and Edwards blowdown tests have all been used to assess earlier versions of TRAC,[4.3-5,4.3-6] so there was a previously developed input model for each of the tests. The existing model for Marviken Test 4 was already in current MOD2 format; the model for Marviken Test 24 was in early MOD2 format. The input models for Marviken Tests 13, 20, and 22, and the Edwards Blowdown Test 1 were for TRAC-PD2 and had to be converted to TRAC-PF1/MOD2 format. TRAC-PD2 did not have a critical flow model, and a fine-mesh noding was typically used upstream of the break to calculate choked flow through the break nozzle. When the Marviken and Edwards PD2 input models were converted to MOD2, the small cells upstream of the break were combined into larger cells approximately the same size as the cells in the rest of the model.

4.3.3. Marviken Tests

4.3.3.1. Facility Description. The Marviken facility is located in Sweden and was originally designed to be part of a nuclear plant, making the facility full scale. The Marviken blowdown tests provide data for assessing the ability of computer codes to predict subcooled and saturated critical flow in large diameter pipes.

The Marviken test facility consists of a pressure vessel and a discharge pipe. The discharge pipe contains a test nozzle with the minimum flow area, a rupture disk assembly, and a ball valve used to isolate the vessel after testing. The pressure vessel and discharge pipe are shown in Figs. 4.3-1 and 4.3-2. The vessel includes part of the core superstructure and three gratings to limit vortex formation. Pressure and temperature transducers are located in the vessel and discharge pipe, as shown in Figs. 4.3-1 and 4.3-2. The break flow is measured with a pitot tube and is also calculated from vessel differential pressure measurements. The data uncertainties (from Ref. 4.3-1) are 90 kPa for the pressure data, 2 K for the temperatures, 10% and 15% for subcooled and saturated break flow determined by the pitot-static method, and 15% and 20% for subcooled and saturated break flow derived from vessel differential pressure.

4.3.3.2. Model Description. The TRAC model of the Marviken facility has four components. Two Pipe components are used to represent the vessel and discharge pipe, a Break component provides the pressure boundary condition downstream of the break, and a zero-velocity Fill closes the top of the vessel. The original PD2 input models for the five Marviken tests generally used different nodalizations for the two Pipes because of differences in test conditions. The differences in the test conditions were large enough so that different nodalizations were also used among the coarsely noded MOD2 input models. The vessel, discharge pipe, and break nozzle noding for Test 4 are typical of the MOD2 input models and are shown in Figs. 4.3-3 and 4.3-4. The internally-set default subcooled and saturated break flow multipliers of 1.0 were used for all calculations.

The initial and boundary conditions were varied in the remaining Tests 13, 20, 22, and 24, and different nodalizations were used in the PD2 input models for these tests. Table 4.3-1 summarizes the differences in the Marviken tests and the TRAC models. Listings of the MOD2 input models are provided in Appendix D. Archival storage information for this input model is found in Section 4.3.7.

4.3.3.3. Comparison of Predicted and Measured Results for Test 4. The calculated pressures, fluid temperatures, and break flow were in reasonable agreement with measured data from Test 4; calculated values were within the data uncertainties for most of the 50-s test duration. The calculated values were in close agreement with the previous calculated results.

The calculated break flow is compared with the break flows from the pitot tube and vessel differential pressure measurements in Fig. 4.3-5. The break flow derived from vessel differential pressure is not valid for the first ~5 s because of momentum effects on the measured pressures. The TRAC break flow underpredicts the subcooled critical flow for the first 19 s of the test and was in reasonable agreement with the test data during the saturated blowdown after 19 s. The underprediction of the break flow

results when the flow conditions at the nozzle become saturated even though the upstream incoming flow is subcooled.

The vessel pressure comparison is shown in Fig. 4.3-6. Except for the initial pressure dip in the test data caused by delayed nucleation, the calculated pressure is just under the lower uncertainty limit until ~27 s, and is then within the uncertainty for the rest of the test. A similar comparison was obtained for the discharge line pressure shown in Fig. 4.3-7. Again, the calculated pressure was very close to the lower uncertainty of the measured pressure for most of the test. Both the calculated and measured fluid temperatures were very close to saturation for most of the test.

The fluid temperature comparison in the lower vessel shown in Fig. 4.3-8 is very similar to comparisons in the middle of the vessel and in the discharge pipe. An increase in temperature occurs in the first 20 s as warmer fluid from the upper vessel drains into the lower vessel. The calculated temperature increase is smoother because of the averaging of liquid temperature within a hydraulic cell. The fluid temperature comparison in the upper vessel is very similar to the pressure comparison because both the measured and calculated fluid temperatures are very close to saturation.

4.3.3.4. Comparison of Predicted and Measured Results for Test 13. The Test 13 nozzle was shorter and had a smaller throat diameter than in Test 4, and Test 13 also had more initial subcooling at the nozzle inlet. The lower velocities and pressure drops upstream of the nozzle, along with the higher subcooling, were sufficient to prevent vapor formation from reducing the subcooled break flow in the calculation for Test 13. Figure 4.3-9 shows that in the first 75 s, when the break flow was subcooled, the calculated flow was generally within the data uncertainty. Voiding at the nozzle exit remained below 0.01, which allowed delayed nucleation in the subcooled critical-flow model to take effect. As warmer liquid from the vessel entered the discharge line, the calculated break flow was reduced by vapor formation, and the break flow was underpredicted for the remainder of the test. As suggested in Ref. 2, the nonequilibrium effects in Test 13 were more pronounced during saturated flow because of the short nozzle length. There is a large underprediction of the flow because the TRAC two-phase critical-flow model assumes thermal equilibrium between phases.

The upper-vessel pressure comparison for Test 13 is shown in Fig. 4.3-10. Except for the initial dip in pressure caused by delayed nucleation in the test, the calculated pressure is within the data uncertainty. Similar comparisons were obtained at lower vessel elevations and in the discharge pipe.

The fluid temperature comparison in the upper vessel was virtually the same as the pressure comparison, i.e., the calculation was within the data uncertainty except for the initial dip caused by delayed nucleation in the test, and both the measured and calculated fluid temperatures followed saturation closely. As with Test 4, the calculated lower vessel fluid temperature for Test 13 increased to saturation more smoothly than the data, as shown in Fig. 4.3-11.

4.3.3.5 Comparison of Predicted and Measured Results for Test 20. The break nozzle in Test 20 was shorter than in Test 4 but had the same throat diameter. Test 20 also had less initial subcooling in the bottom of the vessel. With the reduced initial subcooling, the subcooled break flow was again underpredicted during the first 7 s of the test, as

shown in Fig. 4.3-12. The predicted saturated break flow, however, was within the data uncertainty for the remainder of the test after 7 s.

Figure 4.3-13 shows the upper-vessel pressure comparison for Test 20. The calculated pressure is within the measurement uncertainty except for the initial pressure dip because of delayed nucleation in the test. Calculated pressures at lower vessel elevations and in the discharge pipe compared similarly with measured data from Test 20. The fluid temperature comparisons for Test 20 were much like those of the other Marviken tests with the following results: (1) the predicted temperatures in the vessel were generally within the data uncertainty except for the initial dip in the data, and (2) the discharge line temperatures increased to saturation more smoothly in the calculation and were within the uncertainty afterward.

4.3.3.6 Comparison of Predicted and Measured Results for Test 22. Test 22 had the same break nozzle as Test 20, which was shorter than the Test 4 nozzle but had the same throat diameter as the Test 4 nozzle. Test 22 had the maximum initial subcooling both in the bottom of the vessel and in the discharge pipe. The subcooled break flow was prolonged until ~30 s in Test 22 (Fig. 4.3-14) because of the initial subcooling. Figure 4.3-14 shows that the code underpredicts portions of the subcooled break flow and is consistently within the data uncertainty during the saturated blowdown after 30 s.

The vessel pressure comparison for Test 22 is shown in Fig. 4.3-15. The initial dip in the pressure was not predicted because the code does not have delayed nucleation in the vapor-generation model. After the initial pressure dip, the pressure was generally underpredicted for the remainder of the subcooled blowdown. During the saturated blowdown after 30 s, the break flow and nonequilibrium effects are reduced, and the predicted pressure was within the data uncertainty. Calculated pressures at lower vessel elevations and in the discharge pipe compared similarly with measured data from Test 22. Fluid temperature comparisons for Test 22 were very much like those of the other Marviken tests.

4.3.3.7 Comparison of Predicted and Measured Results for Test 24. Test 24 had the shortest break nozzle, but its throat diameter was the same as the Test 4 nozzle. Test 24 also had the same initial subcooling in the bottom of the vessel as Test 4 and more subcooling in the discharge pipe. The short nozzle increases the acceleration and magnitude of nonequilibrium effects upstream of the throat. The nonequilibrium effects were not calculated correctly, and the subcooled break flow was thus underpredicted most for this test, as shown in Fig. 4.3-16. The calculated break flow was within the data uncertainty during the saturated blowdown after 30 s, but the vessel emptied ~15 s late in the calculation because of the underpredicted subcooled break flow.

Figure 4.3-17 shows the upper vessel pressure comparison for Test 24. Again, the initial dip in pressure was not predicted, and the pressure was underpredicted during much of the subcooled blowdown. The pressure comparison was closer after the transition to saturated break flow at ~30 s. Similar pressure comparisons were obtained in the lower vessel and discharge pipe. Fluid temperature comparisons for Test 24 were very much like those of the other Marviken tests.

4.3.4 Edwards Blowdown Test

4.3.4.1 Facility Description. The Edwards blowdown test facility[4.3-7] is a separate-effects facility that was built in England in the late 1960s to study depressurization phenomena of initially stagnant subcooled water. The facility is much smaller than any component of a full-scale reactor system.

The Edwards blowdown test apparatus shown in Fig. 4.3-18, consisted of a horizontal pipe that was sealed at one end, an orifice at the pipe exit, and a glass rupture disk. The pipe, initially filled with subcooled liquid, was electrically heated and insulated with asbestos. Pressures were measured at four locations along the pipe, and the void fraction and fluid temperature were measured at a point near the middle of the pipe. The break flow rate and pipe wall temperatures were not measured.

4.3.4.2 TRAC Model Description. The TRAC-PF1/MOD2 model of the Edwards facility has three components as shown in Fig. 4.3-19. A Pipe component represents the blowdown pipe, a zero-velocity Fill terminates the closed end of the blowdown pipe, and a Break component provides the pressure boundary condition downstream of the break.

The original TRAC-PD2 model of the Edwards facility[4.3-2] used two Pipe components for the blowdown pipe so that the fully implicit numerical option could be used in the pipe adjacent to the break, while using the faster semi-implicit option in the other Pipe representing the rest of the blowdown pipe. Also, the smaller Pipe adjacent to the break used a fine noding upstream of the break to calculate the choked flow through the break. The two Pipes in the PD2 model were combined into a single Pipe with a more uniform noding for the MOD2 model. The model was also renoded to more accurately model the instrumentation locations. The default subcooled, and saturated break-flow multipliers of 1.0 were used in the MOD2 model for the Edwards blowdown test. A listing of the input model used for this developmental assessment calculation is found in Appendix D. Archival storage information for this input model is found in Section 4.3.6.

4.3.4.3 Comparison of Predicted and Measured Results for the Edwards Test. The calculated pressures, fluid temperature, and void fraction in the middle of the blowdown pipe were in reasonable agreement with measured data from the test. Although the calculated parameters were sometimes outside the data uncertainty, the major trends in the data were predicted. The calculated values were also very close to the previous PD2 calculation for the Edwards blowdown test reported in Ref. 4.3-2.

The pressure comparisons at the closed end and at the break end of the blowdown pipe are shown in Figs. 4.3-20 and 4.3-21, respectively. Measurement uncertainties were not given in the original publications for the Edwards blowdown test; however, an uncertainty of ~0.3 MPa has been suggested in Ref. 4.3-4. Figures 4.3-20 and 4.3-21 show that the initial subcooled depressurization lasted ~0.1 s in both the test and the calculation. However, the prediction was frequently outside the data uncertainty during the saturated blowdown after 0.01 s. The pressure comparisons for the other two pressure measurements, in the midsection of the pipe, were very similar to Figs. 4.3-20 and 4.3-21.

The fluid temperature measured near the center of the pipe is compared with the corresponding calculated temperature in Fig. 4.3-22. After ~0.1 s, the liquid and vapor temperatures in the calculation were equal to the saturation temperature. The fluid temperature comparison is thus very similar to the pressure comparisons in Figs. 4.3-20 and 4.3-21 after this time. The void fraction was measured at the same location as the fluid temperature, and the void fraction comparison is shown in Fig. 4.3-23. The overall trend in the void fraction was captured in the calculation; however, there were significant differences between the measured and calculated void fractions in the first half of the test when the flows and depressurization rate were higher. Also, the oscillations in the measured void fraction from 0.15 to 0.25 s did not occur in the calculation.

4.3.5 Conclusions

Calculations were performed and compared with test data to assess the critical flow model in TRAC. Results of the comparisons for the Marviken tests with larger nozzle diameters showed that the code generally predicts saturated critical flow correctly but sometimes predicts an early transition from subcooled to saturated critical flow. For Marviken Test 13, which had a smaller nozzle diameter, the code underpredicted saturated critical flow. The early transition to saturated critical flow is a result of the TRAC vapor-generation model, which does not have delayed nucleation. The depressurization and break flow rates were both adversely affected by the early transition in the calculations for the Marviken tests. The comparisons were best for the tests with higher initial subcooling, longer break nozzle inlet sections, and larger nozzle diameters.

Comparisons of the MOD2 results with the Marviken tests indicate that whereas the code generally calculates saturated break flow correctly, the absence of nucleation delay in the vapor-generation model over most of the two-phase flow regime can cause differences in break flow and depressurization rate during subcooled break flow. The differences seem to correspond to nonequilibrium conditions just upstream of the break and result in a brief period when both the break flow and pressure are underpredicted. For the short-nozzle and small-diameter tests, Marviken Test 13 and Test 24, nonequilibrium effects become dominant. In these tests, during the period where the measured flow was highly underpredicted by TRAC, the measured mass-flux agreed in general with that predicted by the Henry-Fauske Critical-Flow Model.[4.3-9] This can be seen in Table 4.3-2, which compares the TRAC-calculated and measured critical mass fluxes at selected test times to the mass fluxes calculated by three different critical flow models: (1) Homogeneous Equilibrium Model, (2) Moody Model, and (3) Henry-Fauske Model. For Tests 13 and 24, the measured mass fluxes agrees more closely to that predicted by the Henry-Fauske model. It is recommended that a nonequilibrium critical-flow model, such as the Henry-Fauske Model, be implemented into the code as a user option for modeling the critical flow for small-diameter nozzles, orifices, and short tubes.

The magnitude of the initial pressure dip in the Marviken tests, which was not calculated, seemed to depend on the rate of depressurization more than any other single parameter. Comparisons were generally better for the tests with slower depressurization rates. Also, inasmuch as TRAC was not able to predict the initial pressure dip in the Marviken tests, it is clear that additional modeling of nonequilibrium effects is needed. Plausible solutions might be to extend the Jones nucleation-delay

model to higher void fractions and/or to implement thermal nonequilibrium modeling into the two-phase choked-flow model of Ransom and Trapp.

The calculated parameters for the Edwards blowdown test followed the same trends as the test data and predicted the timing of major events correctly. However, there were periods when the calculated parameters differed noticeably from the measured values, and oscillations in the measured void fraction were not captured in the calculation. Sparse data from the facility and the lack of data uncertainty information make it difficult to determine which models in the code contribute most to differences in the test and prediction, or whether the differences are due to incorrect initial conditions in the input model.

The Edwards blowdown test comparison shows that although the major trends and timing of events in the test data were captured in the calculation, the calculated parameters did not always match the measured values during the test. Oscillations in the measured pressure upstream of the break and in the void fraction in the middle of the pipe were not completely captured in the calculation. Uncertainties in the initial temperature distribution and the lack of break flow and pipe wall temperature measurements make it difficult to attribute calculation/test differences to a specific model in the code.

4.3.6 Code Performance

The Marviken and Edwards blowdown tests were calculated with TRAC-M/F77 code Version 5.5. The run performance information plus other pertinent comments follow.

Marviken Run 4

Platform	Sun Sparc20	
Total CPU time (s)	13.4	
Archive location of input model	CFS	/tida/f77da_decks/inmarv4
Archive location of calculation	CFS	/trac-da/F77DA/nonreflood/ critflow.tar.gz

Marviken Run 13

Platform	Sun Sparc20	
Total CPU time (s)	93.1	
Archive location of input model	CFS	/tida/f77da_decks/inmarv13
Archive location of calculation	CFS	/trac-da/F77DA/nonreflood/ critflow.tar.gz

Marviken Run 20

Platform	Sun Sparc20	
Total CPU time (s)	68.5	
Archive location of input model	CFS	/tida/f77da_decks/inmarv20
Archive location of calculation	CFS	/trac-da/F77DA/nonreflood/ critflow.tar.gz

Marviken Run 22

Platform	Sun Sparc20
Total CPU time (s)	74.0
Archive location of input model	CFS /tida/f77da_decks/inmarv22
Archive location of calculation	CFS /trac-da/F77DA/nonreflood/ critflow.tar.gz

Marviken Run 24

Platform	Sun Sparc20
Total CPU time (s)	18.2
Archive location of input model	CFS /tida/f77da_decks/inmarv24
Archive location of calculation	CFS /trac-da/F77DA/nonreflood/ critflow.tar.gz

Edwards Blowdown

Platform	Sun Sparc20
Total CPU time (s)	7.78
Archive location of input model	CFS /tida/f77da_decks/inedwards
Archive location of calculation	CFS /trac-da/F77DA/nonreflood/ critflow.tar.gz

REFERENCES

4.3-1. J. Spore, J. S. Elson, S. Jolly-Woodruff, T. K. Knight, J-C. Lin, R. A. Nelson, K. O. Pasamehmetoglu, R. G. Steinke, and C. Unal. of Los Alamos National Laboratory and J. Mahaffy and C. Murray of Pennsylvania State University, "TRAC-M/Fortran 90 (Version 3.0) Theory Manual," Los Alamos National Laboratory document LA-UR-00-910 (July 2000).

4.3-2. "RELAP/MOD1 Code Manual, Volume 1: System Models and Numerical Methods," Idaho National Engineering Laboratory report EGG-2070 draft, Rev. 1, NUREG/CR-1826 (March 1981).

4.3-3. O. C. Jones, "Flashing Inception in Flowing Liquids," Brookhaven National Laboratory report BNL-NUREG-51211 (1980).

4.3-4. V. H. Ransom and J. A. Trapp, "The RELAP5 Choked Flow Model and Application to a Large Scale Flow Test," in *ANS/ASME/NRC International Topical Meeting on Nuclear Reactor Thermal-Hydraulics* (Saratoga Springs, New York, 1980), pp. 799–819.

4.3-5. C. Booker, B. Boyack, G. Cort, K. Duerre, J. Gilbert, T. Knight, J. Meier, and M. Sahota, "TRAC-PD2 Independent Assessment," T. Knight, Comp., Los Alamos National Laboratory report LA-10166-MS, NUREG/CR-3866 (December 1984).

4.3-6. T. Bott, J. Gilbert, D. Mandell, J. Meier, and J. Sicilian, "TRAC-PD2 Developmental Assessment," T. Knight and V. Metzger, Comp., Los Alamos National Laboratory report LA-9700-MS, NUREG/CR-3208 (January, 1985).

4.3-7. A. R. Edwards and T. F. O'Brien, "Studies of Phenomena Connected with the Depressurization of Water Reactors," *Journal of British Nuclear Energy Society* **9**, 125–135 (April 1970).

4.3-8. R. W. Garner, "Comparative Analyses of Standard Problems—Standard Problem One (Straight Pipe Depressurization Experiments)," Aerojet Nuclear Company report I-212-74-5.1 (October 1973).

4.3-9. R. E. Henry and H. K. Fauske, "The Two-Phase Critical Flow of One-Component Mixtures in Nozzles, Orifices, and Short Tubes," *Journal of Heat Transfer, Transactions* **93** (May 1971).

TABLE 4.3-1

MARVIKEN TESTS AND TRAC NODING

	Test 4	Test 13	Test 20	Test 22	Test 24
Nozzle straight section length (m)	1.500	0.590	0.731	0.731	0.166
Nozzle diameter (m)	0.509	0.200	0.500	0.500	0.500
Length-to-diameter ratio	2.95	2.95	1.46	1.46	0.33
Initial pressure (MPa)	4.94	5.09	4.987	4.93	4.96
Initial subcooling near vessel bottom (K)	37	31	7	52	33
Initial subcooling at nozzle inlet (K)	63	95	77	95	83
Initial liquid level above vessel bottom (m)	17.59	17.52	16.65	19.64	19.88
Number of cells in PIPE representing vessel	15	15	38	38	15
Number of cells in PIPE representing lower vessel and discharge pipe	17	13	14	14	17

TABLE 4.3-2

COMPARISON OF MEASURED MASS FLUXES TO THE MASS FLUX CALCULATED BY TRAC-M/F77 AND DIFFERENT CRITICAL-FLOW MODELS

Marviken Test No.	4	13	20	22	24
Test Time (s)	41	100	40	40	15
Measured Mass Flux (pitot)	15971	34841	21279	17045	40881
($kg/(s\text{-}m^2)$* (Δp)	16428	34364	18640	14860	41767
TRAC-M/F77 Calculation					
Exit Pressure (MPa)	3.281	3.963	3.676	2.394	2.855
Exit Void Fraction	0.2941	0.0608	0.3321	0.2581	0.0448
Mass Flux ($kg/(s\text{-}m^2)$)	18466	23130	21448	15854	30805
Mass Flux ($kg/(s\text{-}m^2)$) determined from:					
HEM	14782	17679	15851	11910	14022
Moody Model	26635	29558	27978	22982	25233
Henry-Fauske Model	27668	35641	28391	24285	30549

*The first value given is the mass flux determined from measured pitot tube data. The second value is the mass flux determined from vessel differential pressure measurements.

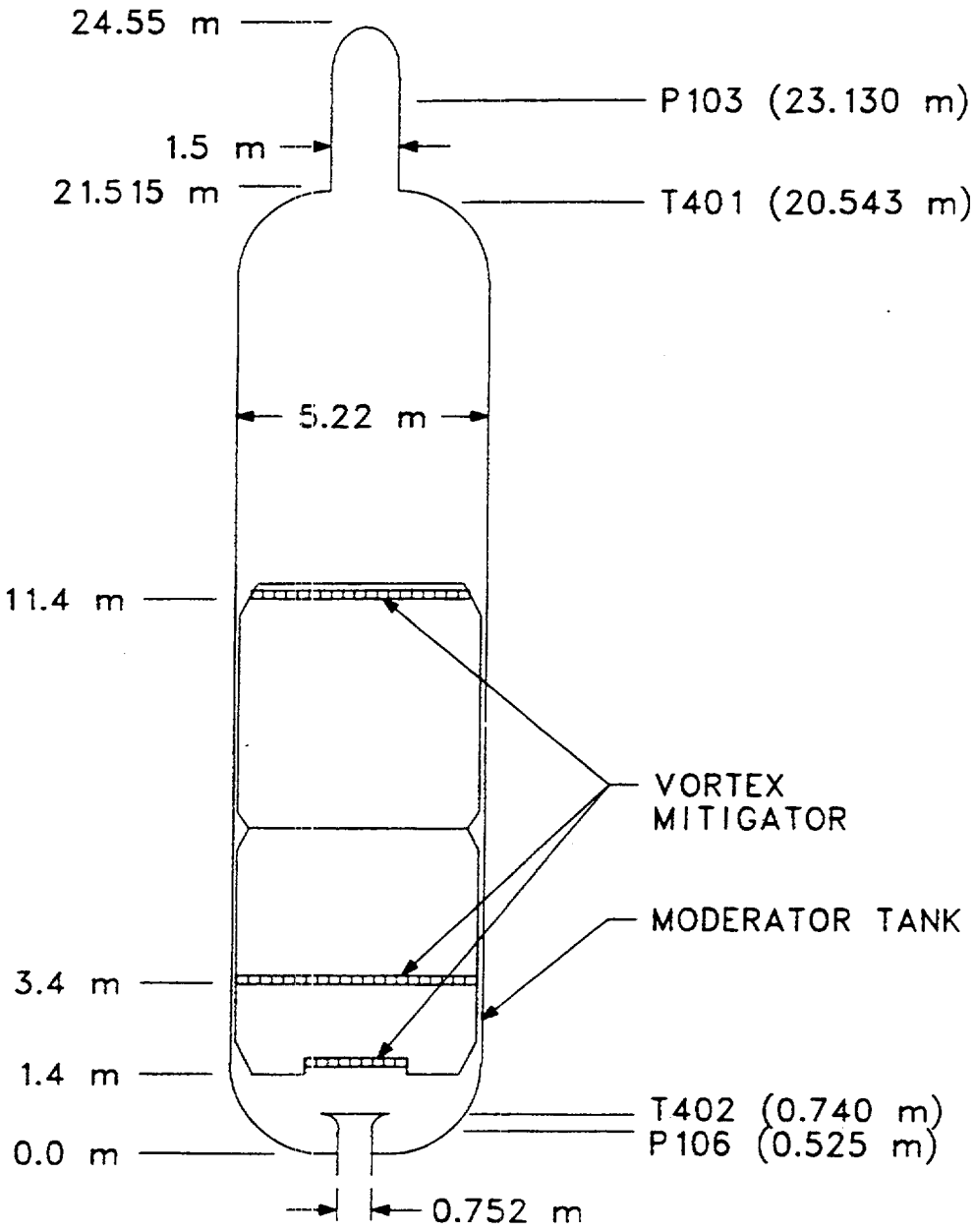

Fig. 4.3-1. Marviken pressure vessel.

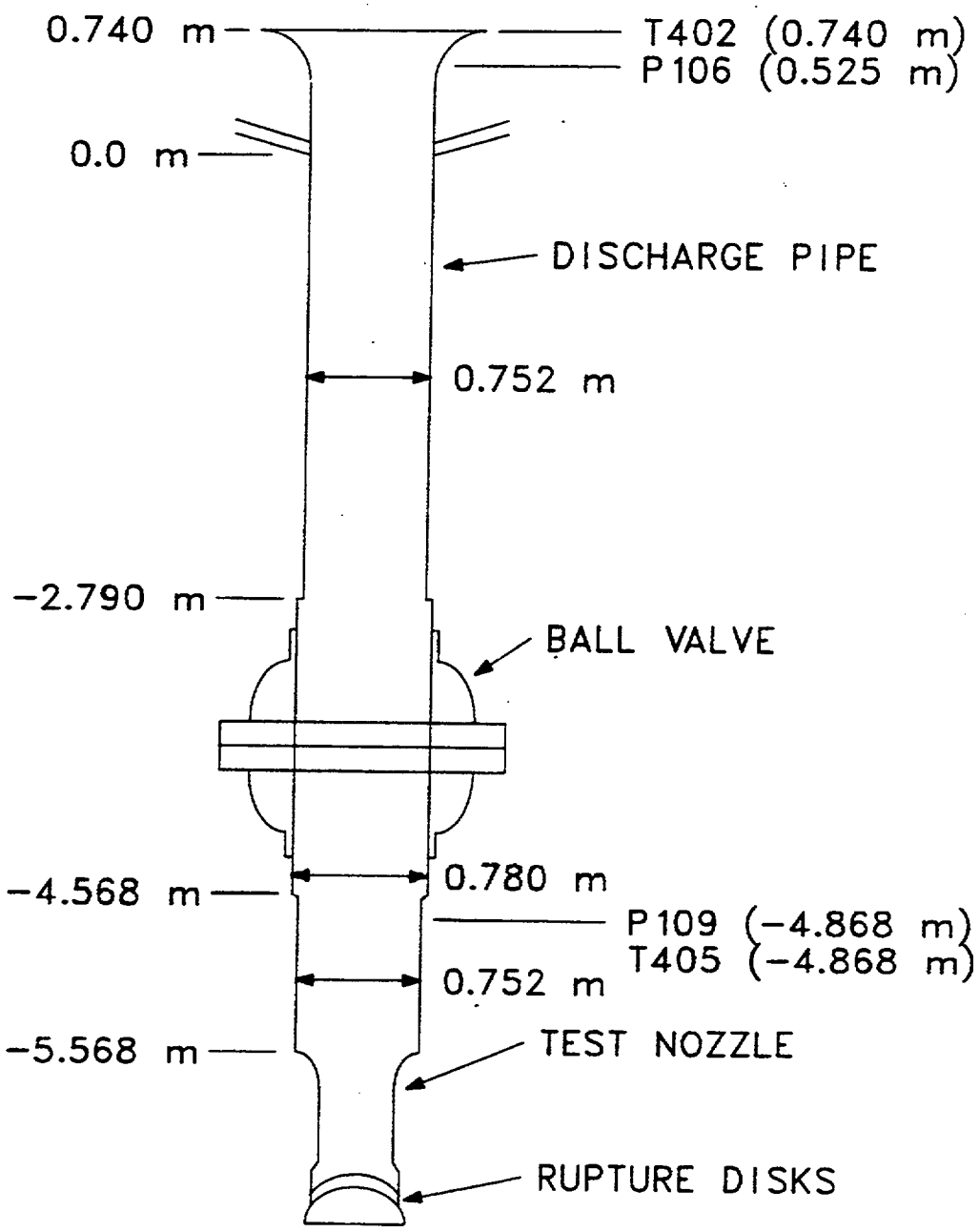

Fig. 4.3-2. Marviken discharge pipe, test nozzle, and rupture-disk assembly.

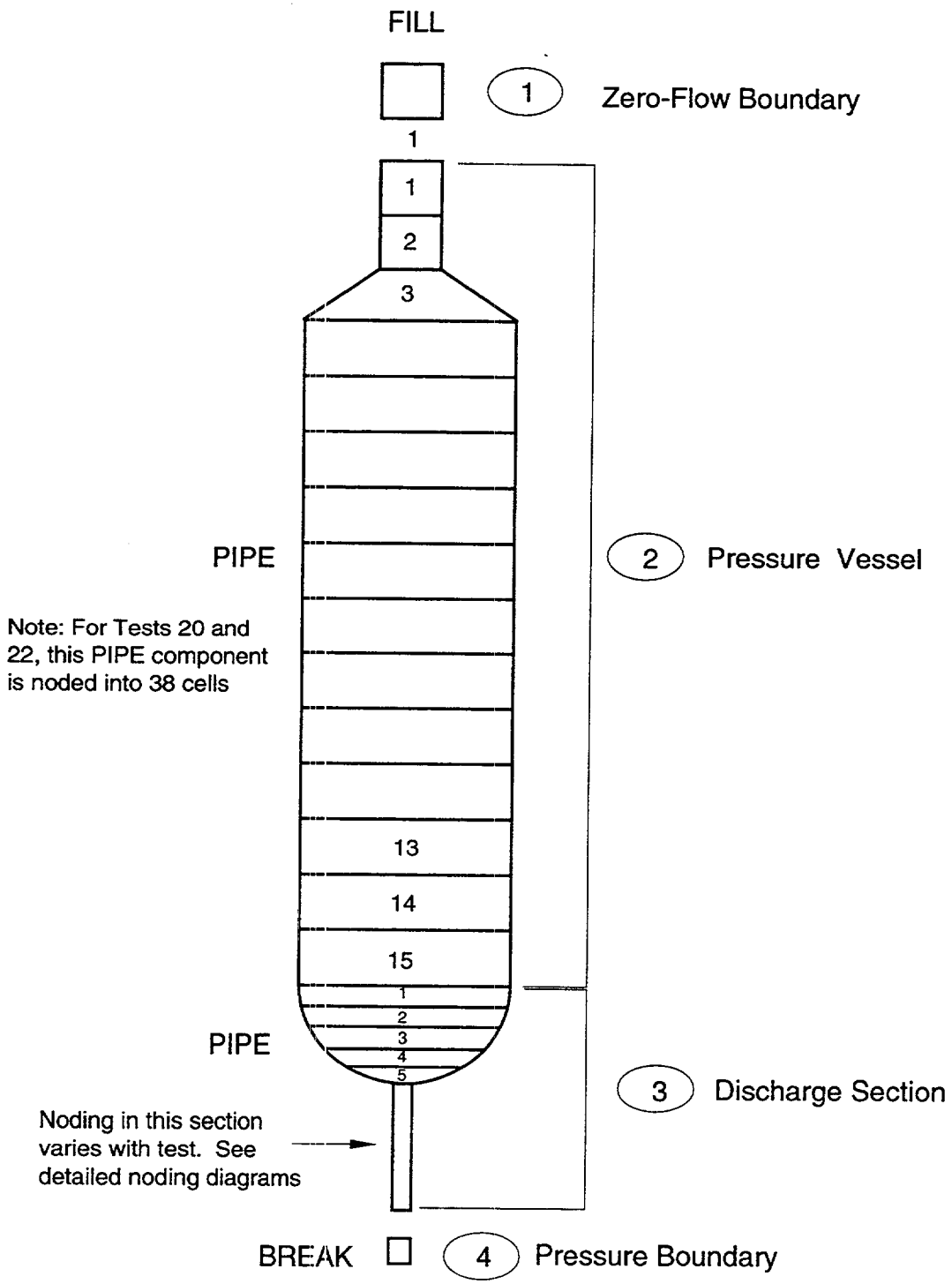

Fig. 4.3-3. Pressure-vessel and discharge-pipe noding.

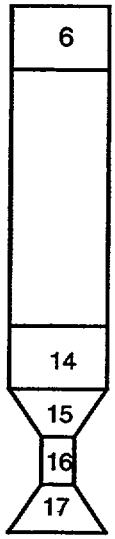

(a) Test 4

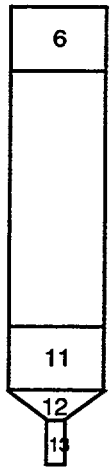

(b) Test 13

Note: Not to scale

(c) Tests 20 and 22

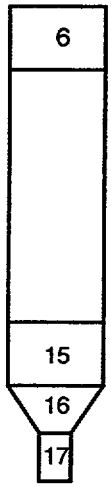

(d) Test 24

Fig. 4.3-4. Nozzle and rupture-disk assembly noding for Marviken tests.

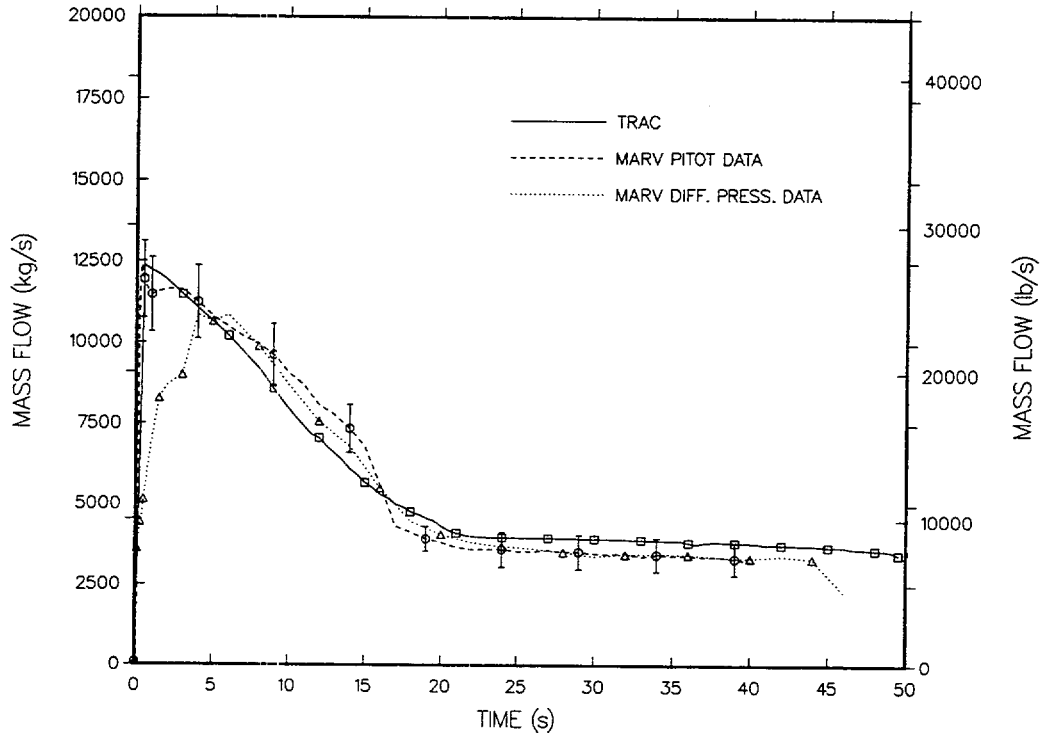

Fig. 4.3-5. Break flow comparison for Marviken Test 4.

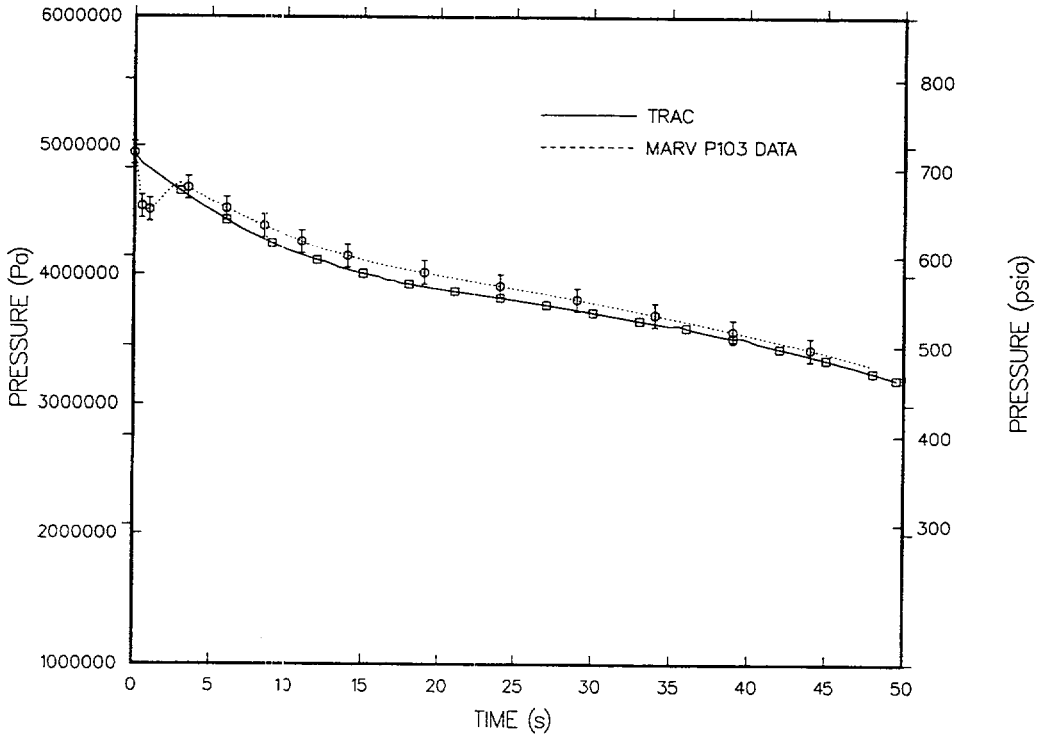

Fig. 4.3-6. Upper-vessel pressure comparison for Marviken Test 4.

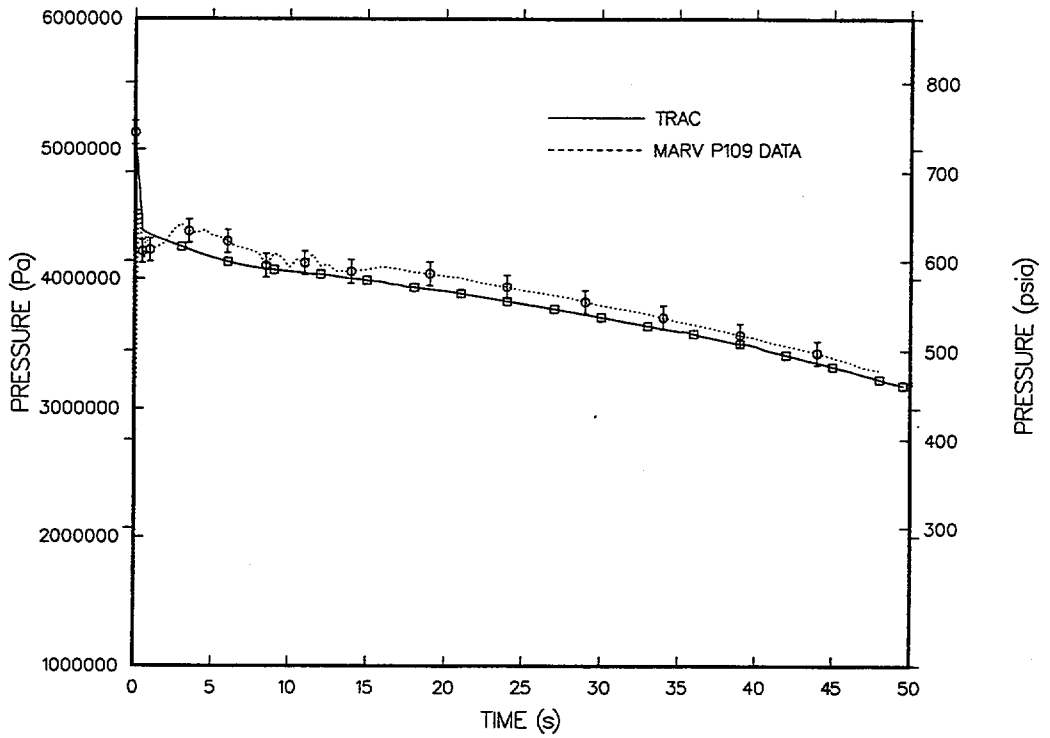

Fig. 4.3-7. Discharge line pressure comparison for Marviken Test 4.

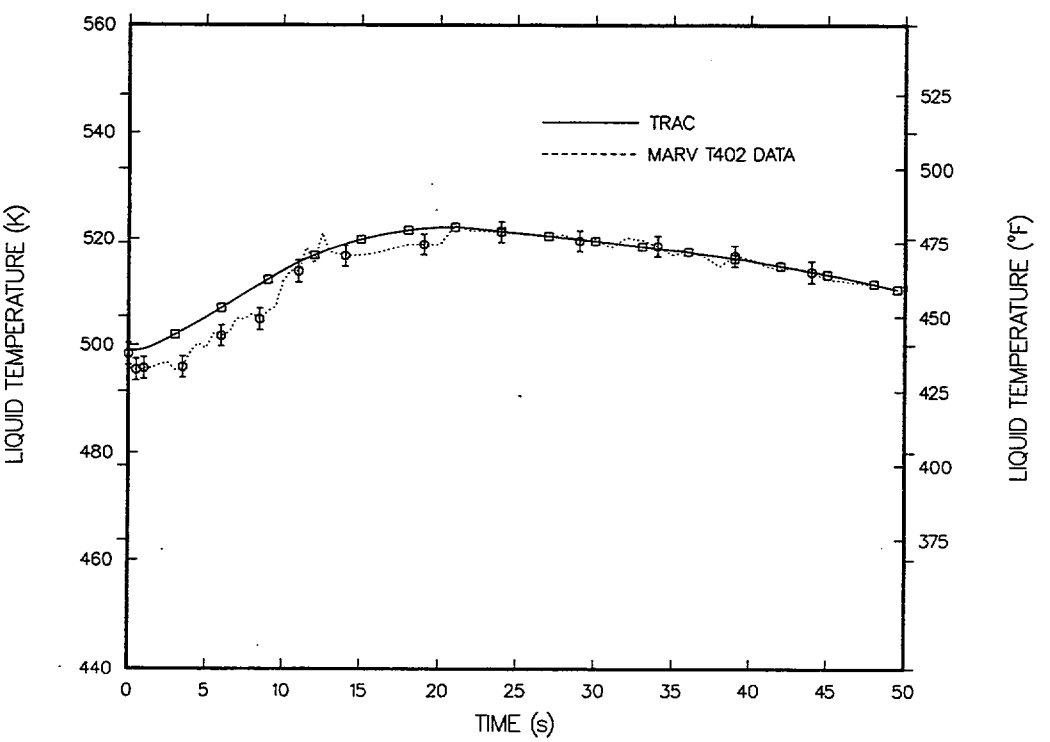

Fig. 4.3-8. Lower-vessel fluid temperature comparison for Marviken Test 4.

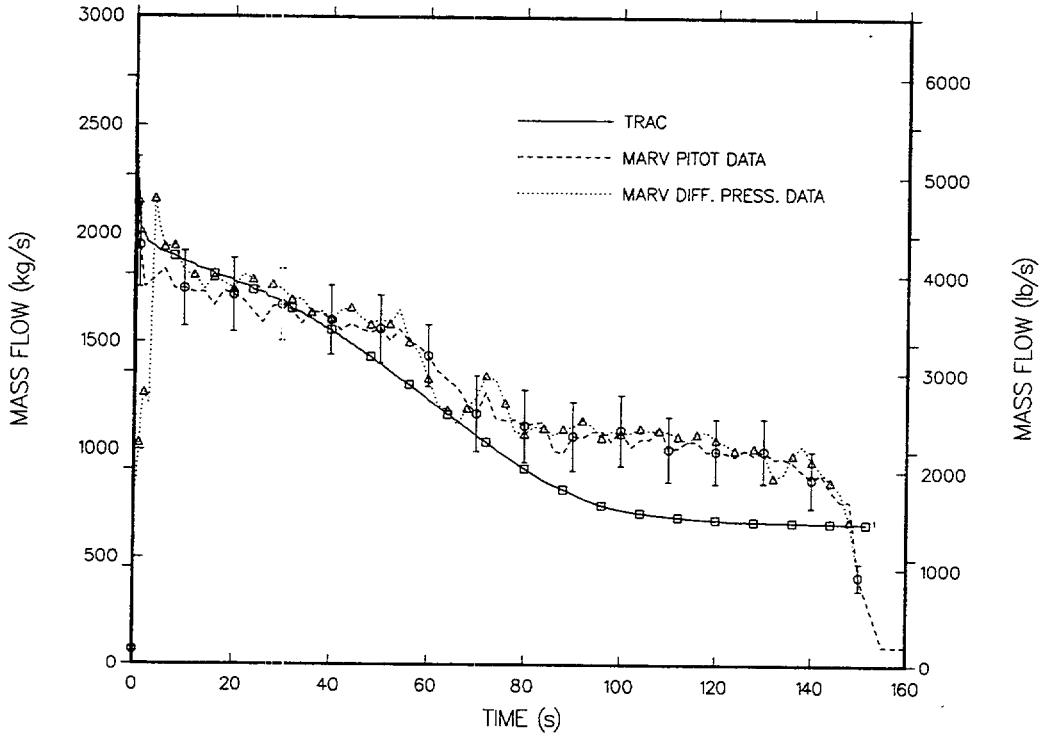

Fig. 4.3-9. Break-flow comparison for Marviken Test 13.

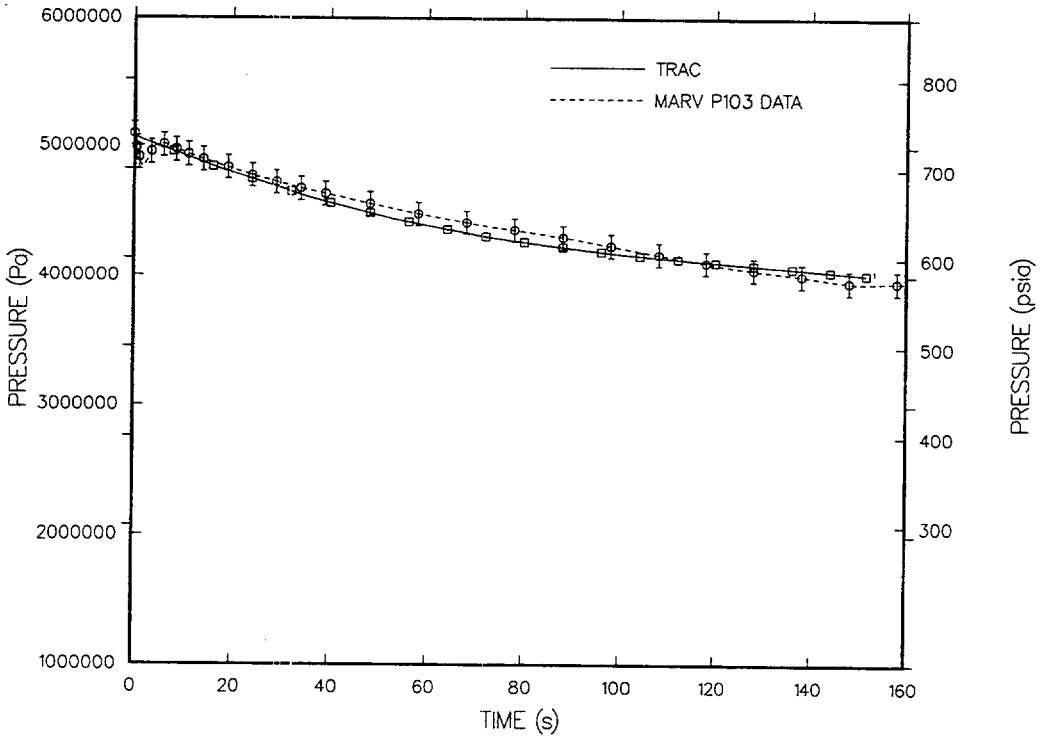

Fig. 4.3-10. Upper-vessel pressure comparison for Marviken Test 13.

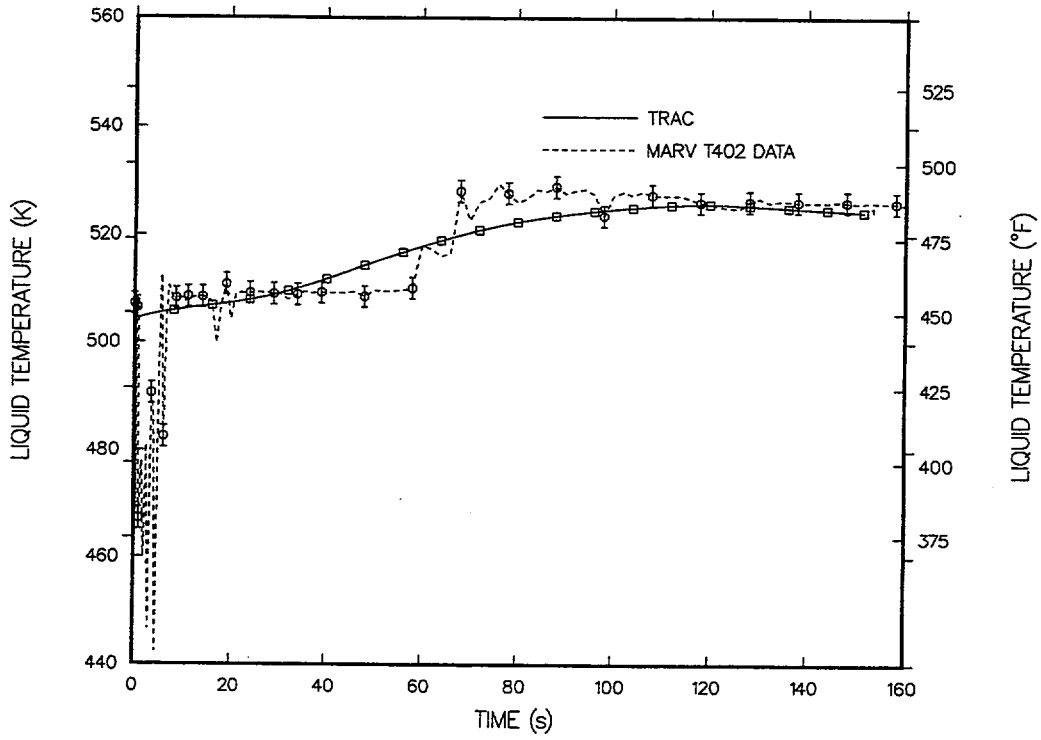

Fig. 4.3-11. Lower-vessel fluid temperature comparison for Marviken Test 13.

This space is intentionally left blank

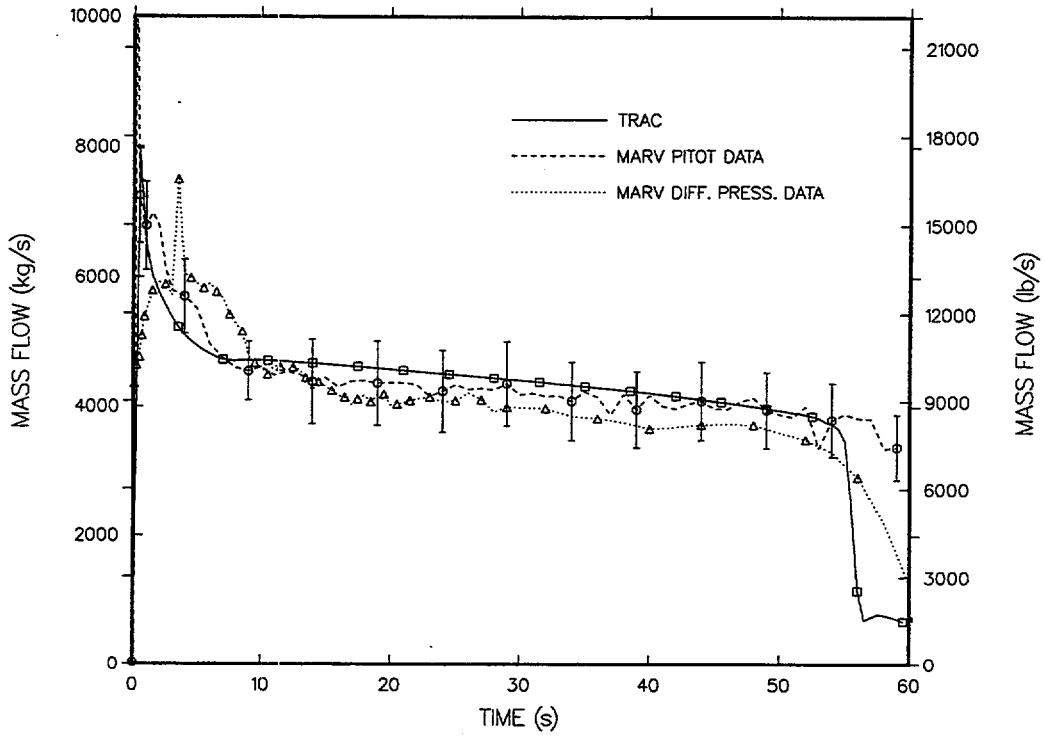

Fig. 4.3-12. Break-flow comparison for Marviken Test 20.

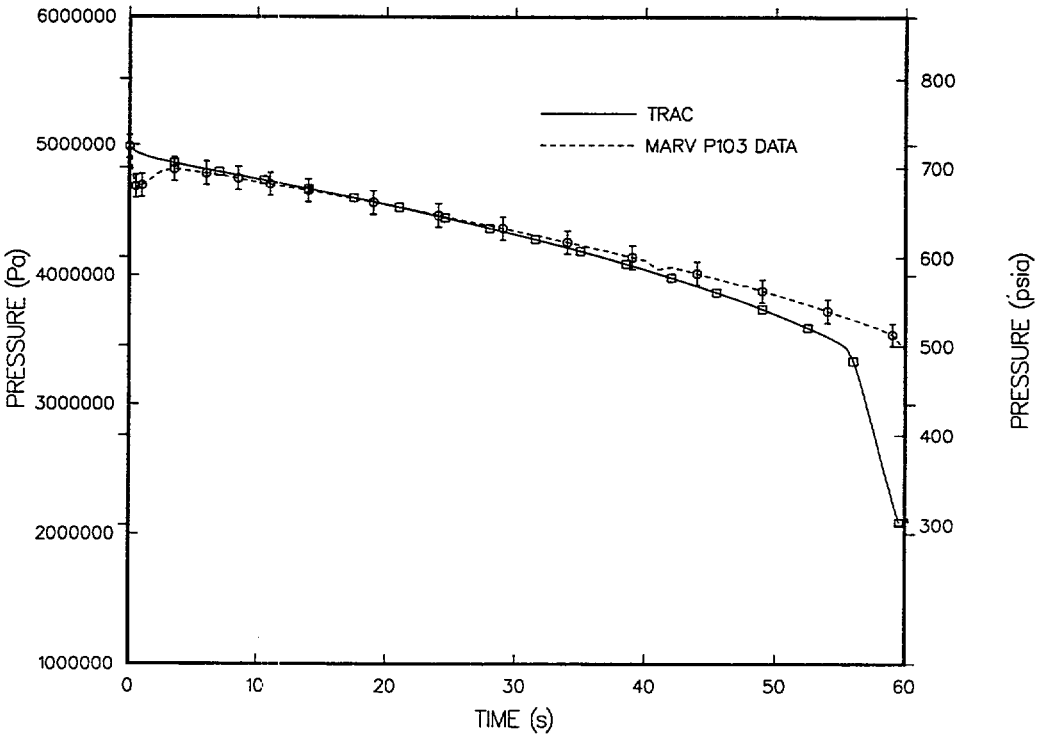

Fig. 4.3-13. Upper-vessel pressure comparison for Marviken Test 20.

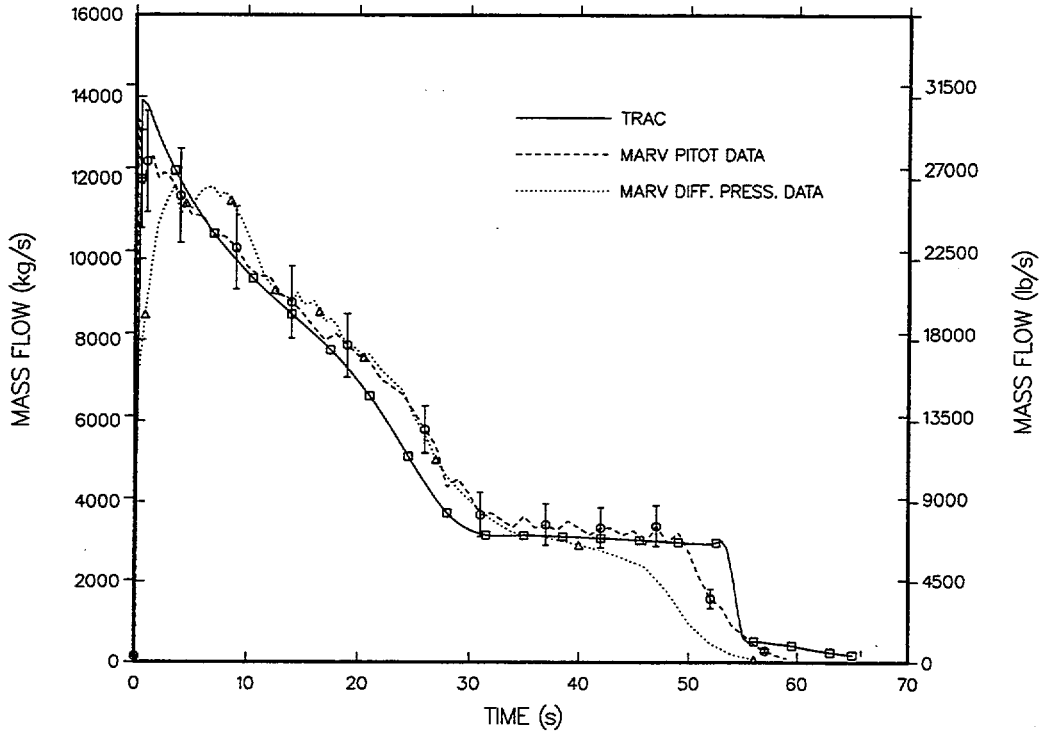

Fig. 4.3-14. Break-flow comparison for Marviken Test 22.

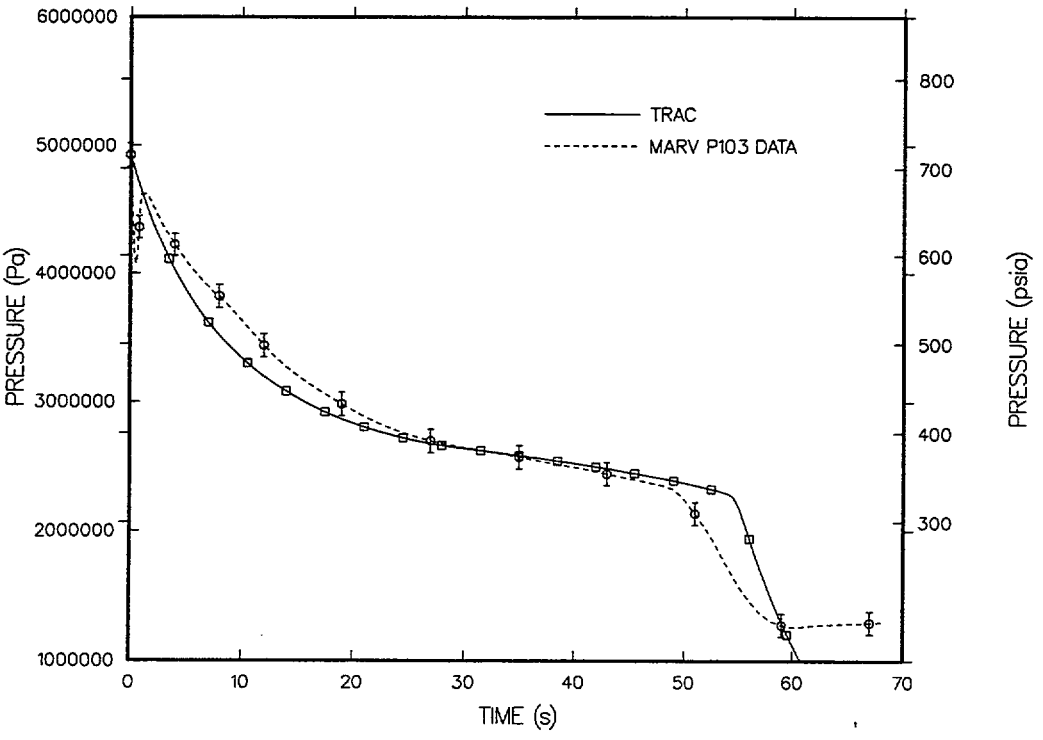

Fig. 4.3-15. Upper-vessel pressure comparison for Marviken Test 22.

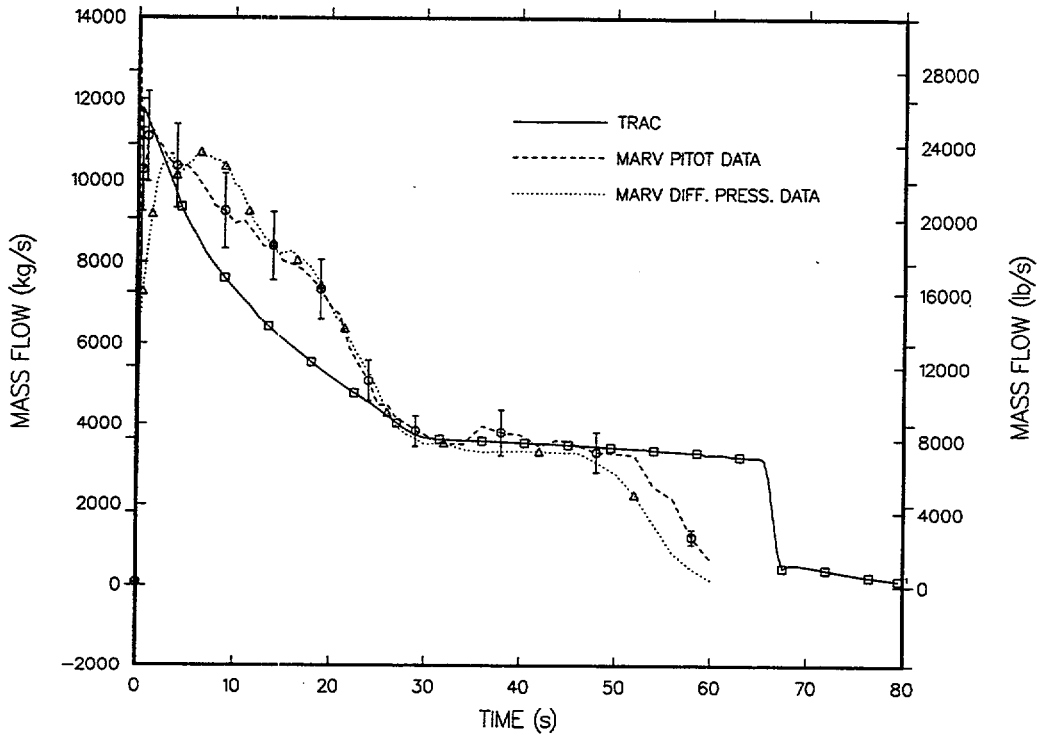

Fig. 4.3-16. Break-flow comparison for Marviken Test 24.

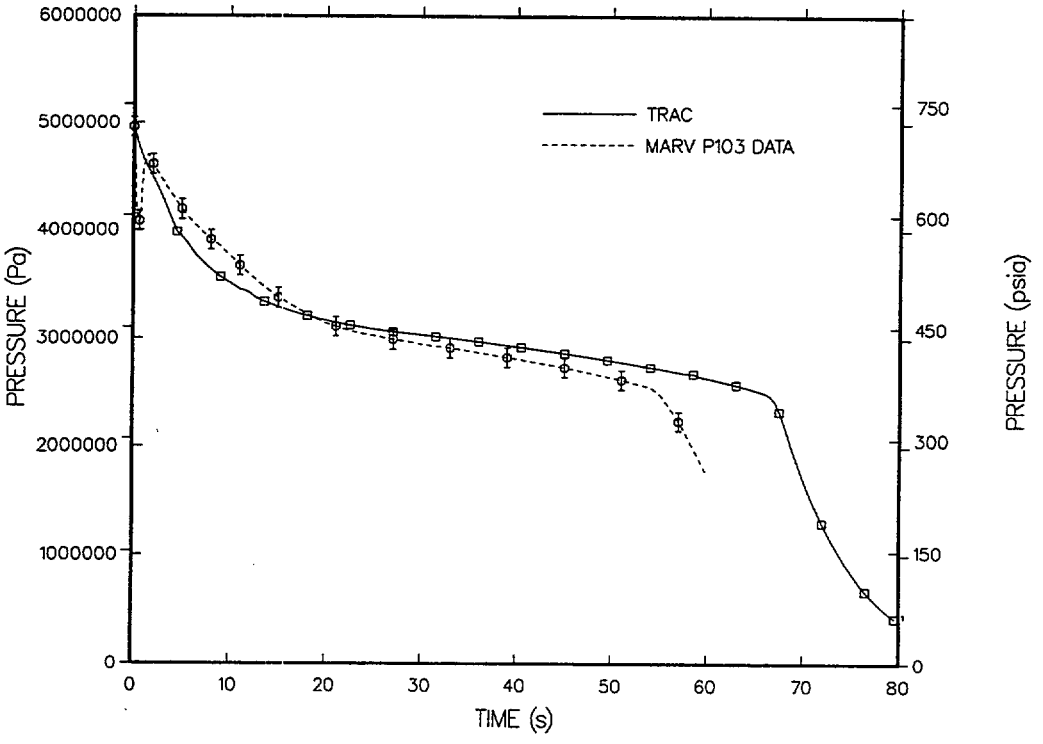

Fig. 4.3-17. Upper-vessel pressure comparison for Marviken Test 24.

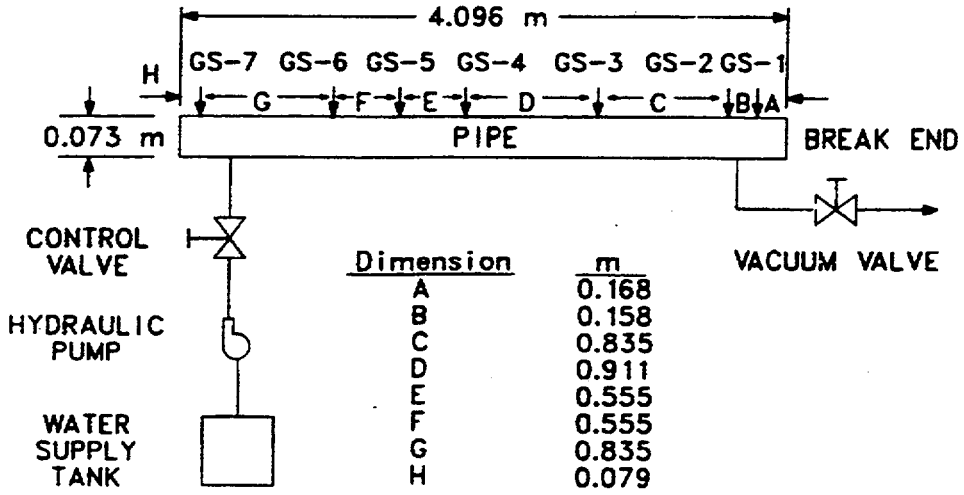

Fig. 4.3-18. Edwards blowdown test apparatus.

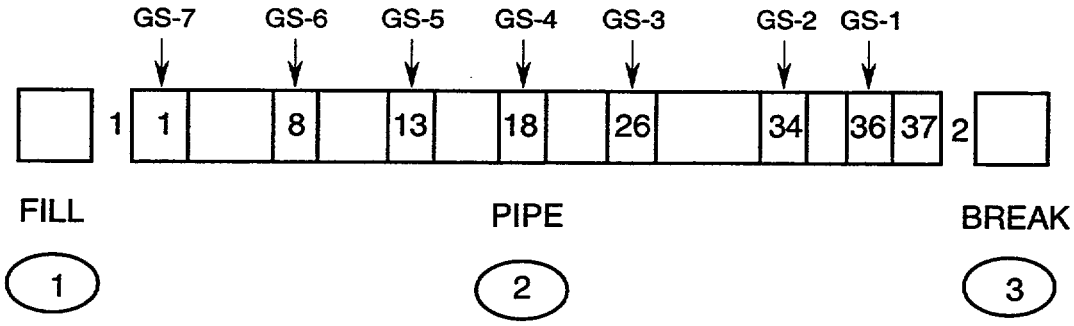

Fig. 4.3-19. TRAC model for Edwards blowdown test.

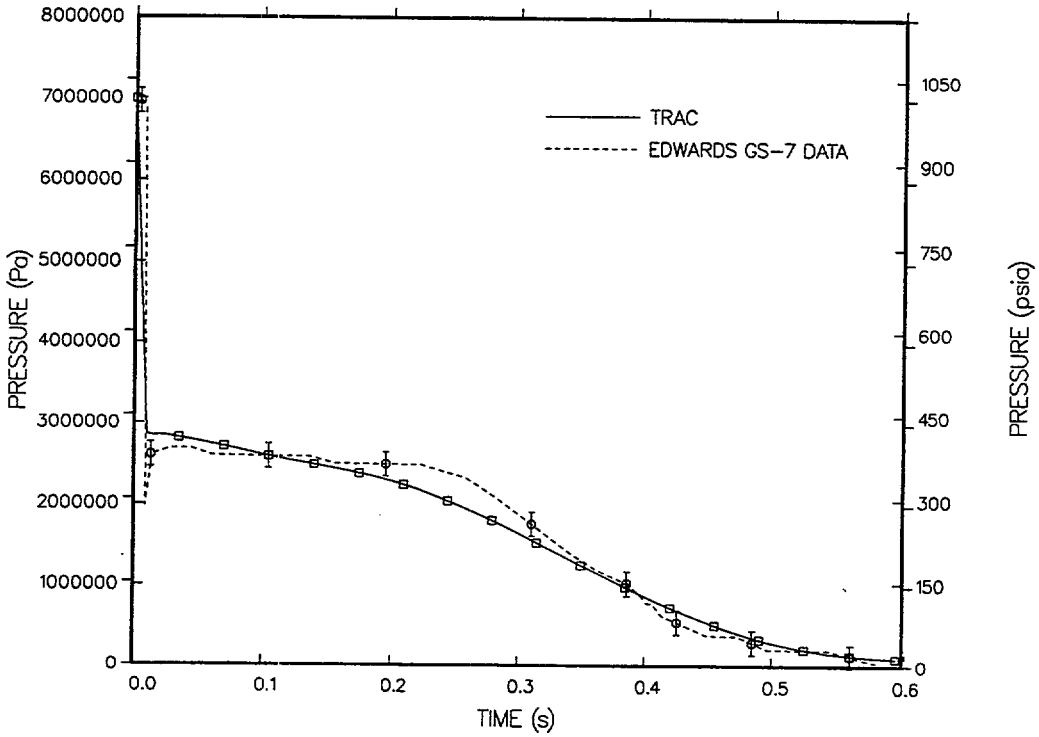

Fig. 4.3-20. Pressure comparison at closed end of pipe for Edwards blowdown test.

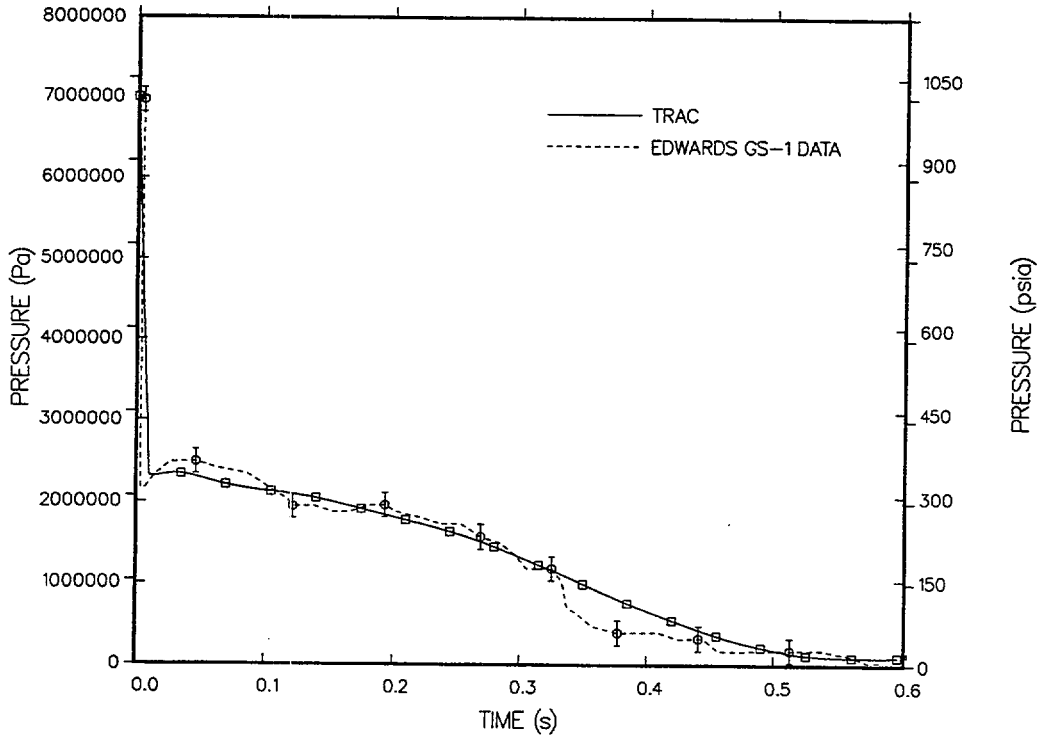

Fig. 4.3-21. Pressure comparison at break end of pipe for Edwards blowdown test.

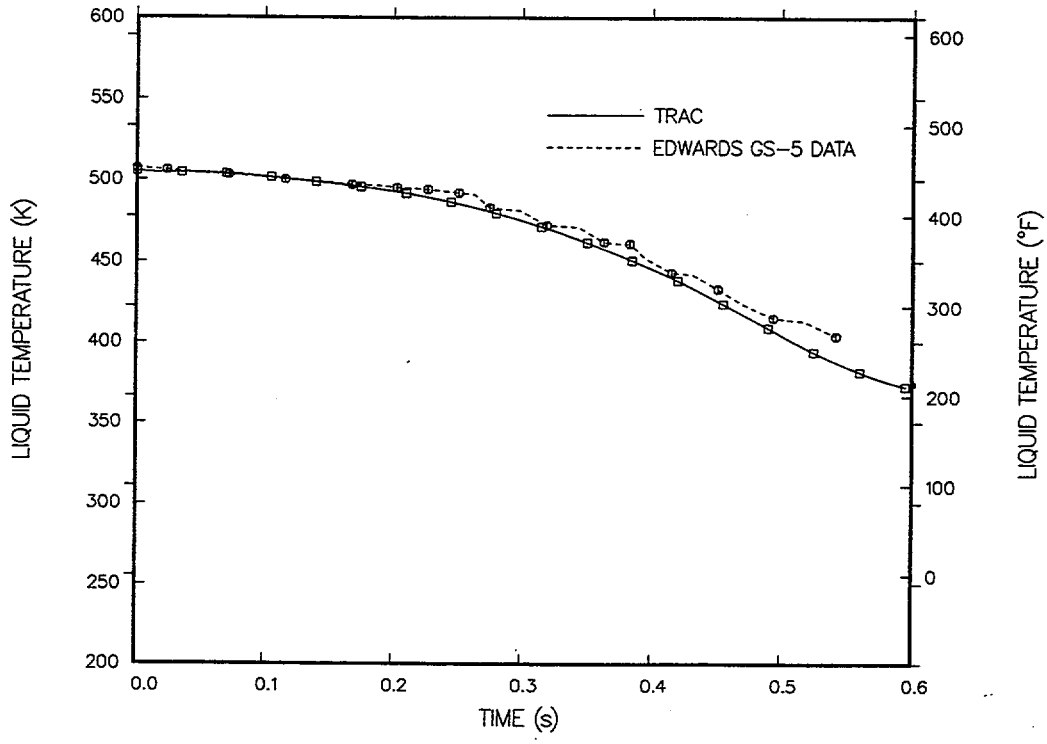

Fig. 4.3-22. Fluid temperature comparison for Edwards blowdown test.

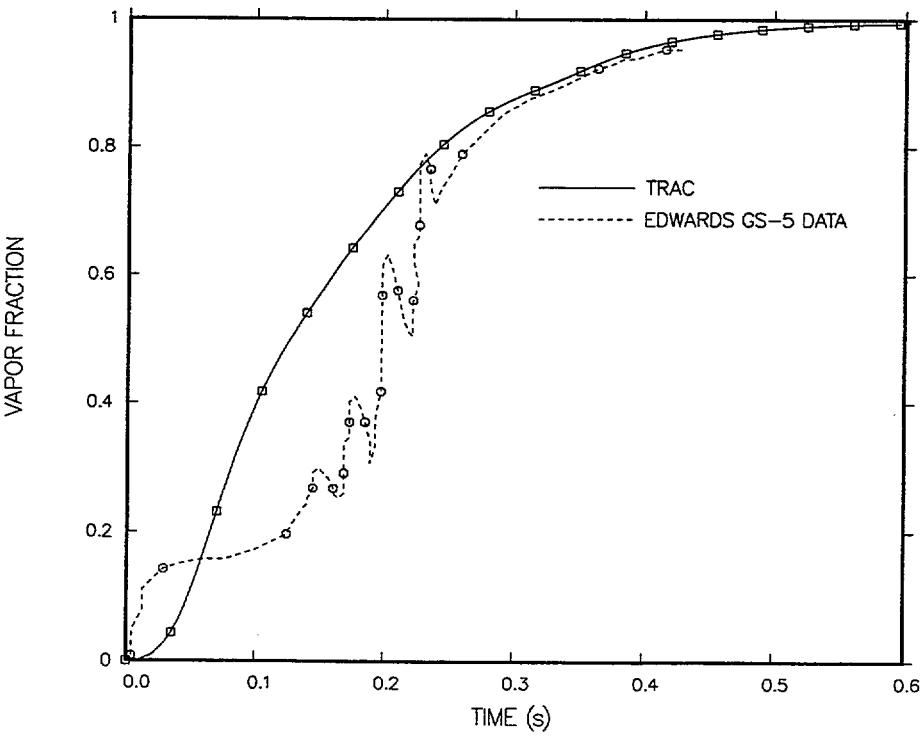

Fig. 4.3-23. Void fraction comparison for Edwards blowdown test.

4.4. Lehigh Rod Bundle Run 02/24/85-20

The Lehigh University rod bundle (LRB) test facility was designed, built, and operated by Lehigh University. The LRB test facility was designed to provide post- CHF under nonequilibrium conditions in a rod bundle at low mass fluxes, low-to-moderate vapor qualities, and near-atmospheric pressures. A total of 467 data points were generated from 144 experimental runs, which were executed with the following range of conditions:

Coolant mass flux	0.1 to 26 $kg \cdot m^{-2} \cdot s^{-1}$
Inlet quality	40°C subcooled to 0.4
Pressure	105 to 120 kPa
Heat Flux	5 to 43 $kW \cdot s^{-1}$

Post-CHF experiments were conducted in three different modes: (a) steady-state experiments with a fixed CHF location, (b) reflood experiments with slowly advancing CHF locations (propagating quench front), and (c) boiloff experiments with retreating CHF locations. The test used for this assessment, LRB Run 02/24/85-20, was one in a series of advancing quench front tests conducted in the LRB test facility.

4.4.1. Facility Description

The LRB test facility was designed and built for convective-boiling, heat-transfer studies using steam-water mixtures. The purpose of this research was to obtain post-CHF heat-transfer data with nonequilibrium vapor-temperature measurements at two axial and several radial positions downstream of a fixed or advancing CHF point. A detailed facility description is provided in Ref. 4.4-1. Much of the descriptive information that follows was taken directly from Ref. 4.4-1.

Water was drawn from a surge tank and pumped to a vertical boiler (after passing through filters to remove solid impurities) and through a flow metering station. The boiler produced the desired flow quality to the test section. After passing through the test section, the fluid passed to a tank where the water and steam were separated. A regulating valve on the steam outlet was varied to produce the desired test-section pressure. The two-phase fluid was condensed and cooled by a water-cooled condenser and returned to the surge tank.

The test section consisted of a heated shroud containing a 3 x 3 rod bundle assembly. The rod bundle was representative of a PWR rod bundle. A cross section of the bundle is shown in Fig. 4.4-1. Dimensions of the rods and the shroud were selected to provide equal hydraulic diameters in all subchannels. The shroud, made of 2-mm-thick Inconel 625 alloy, was heated by radiation from a tubular furnace with three independently controlled zones. The shroud heat flux was to be equal to the test-rod heat flux. Twelve chromel alumel thermocouples were brazed onto the outside surface of the shroud at different axial locations. The test section had a length of 1.220 m and incorporated four ports for vapor temperature, pressure probes, and a rod spacer located 762 mm from the test section inlet, as shown in Fig. 4.4-2. The inlet to the test section contained a strainer to provide uniform flow across the bundle cross section.

The test rods (9.5-mm o.d.) were heated internally by electric resistance ribbons embedded in boron nitride. The rod clad was made of stainless steel. Each rod was equipped with 12 internal thermocouples at different axial elevations. A hot patch was also available to condition the thermal state of the inlet two-phase flow and to stabilize the quench front for those tests where a fixed CHF point was desired. The hot-patch technique was used to produce dryout at the inlet of the test section. The bottom hot patches consisted of an outer copper block surrounding the shroud and 9 short hot rods, each acting as an individual hot patch for one of the nine bundle test rods. The hot rods were similar to test rods in construction but provided higher heat fluxes and were individually temperature controlled.

The test section had 108 thermocouples on the test rods. Each test rod had 10 thermocouples at 15-cm intervals. There were also 2 thermocouples in the aspirated vapor probes to measure the vapor superheat temperature. Because the clearance between test bundle rods was only 3 mm, the probes were of a small size (2.13-mm-diameter outer tube) to minimize disruption of the flow as it passed the vapor probe. The probe was traversable in the cross-sectional plane to enable the measurement of lateral variations in vapor superheat. Absolute pressure in the test bundle was measured, as well as pressure drop between the 4 taps on the shroud walls. Flow rates were measured with variable area flow meters. Power fed to all components of the test loop was measured by power transducers. The loop was designed and instrumented to collect the desired data on flow conditions.

4.4.2. Test Procedure and Description

For a typical reflood run, the test section was preheated to a selected post-CHF state with the shroud and rods at substantial superheats. A steady two-phase flow, with desired flow rate, pressure, and inlet mixture enthalpy, was established using a bypass around the test section during the preheating stage. During this initial preheating period, the test section was cooled to temperatures <450°C by flowing steam. For the quenching runs, the inlet hot patches were maintained as adiabatic sections at the fluid saturation temperature. Upon obtaining the desired initial condition, the test rods were powered to the desired heat flux, the cooling steam line was closed, the data acquisition system was started, and the two-phase flow was switched from the bypass line to the test section. The experiments were generally terminated when the quench front passed the first vapor probe location.

4.4.3. TRAC Model

Only the test section of the Lehigh University two-phase flow facility and LRB Run 02/24/85-20 was modeled because the thermal-hydraulic conditions in the other components of the two-phase loop were not of interest. Also, it was possible to specify the necessary boundary-condition time histories using experimental data. This approach permits a more direct assessment of the core thermal-hydraulic models used in TRAC. A component schematic of the model is shown in Fig. 4.4-3. The model consisted of 7 components, including 13 fluid cells. For reference to the test section schematic presented in Fig. 4.4-2, the entrance to the component 1 model in Fig. 4.4-3 corresponds to the bottom of the test section, i.e., the interface between the copper block/hot patch and the test section.

A 1D vessel model (component 1) was used to simulate the heated test section. The heated test section was divided into 11 fluid cells between 0.1 and 0.11-m (3.9 to 4.3-in.) node sizes to facilitate detailed modeling of the grid spacer and the locations of vapor probes. The fine axial noding used in the LRB Run 02/24/85-20 model is not consistent with the noding used in standard full-plant models. Core nodes in an AP600 model, for example, are ~0.6 m high. The superheated vapor temperatures were measured at locations corresponding to the middle of the sixth and ninth cells in this model. A grid spacer 0.79 cm (2 in.) long was located in cell 8. The constant power-generation option was used to simulate the electrically heated test rods. The radiation-heated square shroud was modeled with a cylindrical slab having the same perimeter as the shroud. The energy transfer from the radiation furnace was modeled by specifying a proper heat-transfer coefficient and a sink temperature at the outside of the cylindrical slab.

A Pipe (component 2) was connected to the lower end of the vessel for modeling the unheated part of the test section (hot patch). This extension Pipe consisted of only one fluid cell and is considered to be very well insulated against heat losses to the environment. At the inlet end of this Pipe component, a Fill (component 3) was used to model the constant mass injection to the test section. The upper end of the test section was open to a plenum. A Break (component 5) was connected to the upper end via an exit Pipe to specify the boundary conditions at this location.

The boundary conditions input to the model were the test section inlet mass flux, void fraction, inlet temperature (Fill component 3), and the outlet pressure (Break component 5). The initial wall temperatures were also specified for the Heat-Structure component.

A listing of the input model used for this assessment is provided in Appendix E. Archival storage information for this input model is provided in Section 4.4.8.

4.4.4. Comparison of Predicted and Test Results

This calculation was performed with TRAC-M/F77, Version 5.5. These results are for newrfd=3, which activates the newly extended reflood model with explicit top-down reflood modeling.[4.4-2] An identical set of graphical code-data comparisons with newrfd=1 is presented, without analysis, in Appendix F. Setting newrfd=1 activates the bottom-up reflood model of the TRAC-PF1/MOD2 code.

We have run Lehigh Rod Bundle Test 02/24/85-20 calculations both with and without the grid-spacer model. We have determined that the grid-spacer model should not be used because it results in excessive and nonphysical heat-transfer processes in the upper portions of the core. However, for this assessment calculation, and this assessment calculation only, we have chosen to treat the calculation with the grid-spacer model as the base case because the grid-spacer model was developed for LRB Test 02/24/85-20. We are recommending that the TRAC grid-spacer model not be used for future calculations (see Section 4.4-5 for details).

Lehigh Rod Bundle Test 02/24/85-20 was one of a series of advancing quench front tests conducted in the LRB facility. This was a subcooled reflood experiment with a slowly moving quench front. The inlet mass flux was 25.13 kg/m^2-s, and the inlet temperature coolant temperature of 351.9 K was 21.1 K subcooled relative to the

saturation temperature of 373 K at 101.3 kPa. Figure 4.4-4 shows the core inlet mass flow for this test and Fig. 4.4-5 shows the core flooding rate, defined as the time-averaged core inlet mass flow divided by the core flow area and the density of the core inlet mass flow.

The clad temperatures and the rate of the quench front propagation (two significant parameters in nuclear reactor safety analyses) are predicted as a result of the code-predicted solution for the coupled differential equations of the fluid mechanics and the heat conduction, as discussed in the TRAC Theory Manual.[4.4-3] The prediction of the clad cooling rate throughout the core strongly depends upon the prediction of the correct void-fraction distribution. The void-fraction distribution is determined primarily by the core-reflood interfacial-drag coefficient (IFDC) model. The IFDC model was developed from the inverted-annular-flow (IAF) regime map suggested by Ishii and his coworkers.[4.4-4] The IAF regimes along the core are determined from a capillary number defined at the quench-front location. In addition to the criteria suggested by Ishii, TRAC also forces IAF regimes to occur within certain void fraction ranges.[4.4-3] In some IAF regimes, the core-reflood IFDC model uses weighting functions as well as empirical constants to make transitions between them. The empirical constants are used because the experimental pressure-drop or void-fraction data for each IAF regime are not available in the literature to assess each IFDC model. The available information is usually the pressure drop over a certain length of the core that may experience several IAF regimes, depending upon the distance between the pressure taps. The pressure-drop data of Cylindrical Core Test Facility (CCTF) Run 14 (Ref. 4.4-5) was used to determine the above-mentioned empirical constants.

The Lehigh reflood tests included some limited pressure-drop data.[4.4-6] A trace of the measured pressure drop between axial locations at 406 and 609 mm above the core inlet is shown in Fig. 4.4-6 (from Ref. 4.4-6). The frequency of the reading is 40 data points per second. A decrease in the pressure-drop data indicates an increase in the vapor fraction in the region between the pressure taps. When the amount of liquid increases within this region, the pressure drop increases. As shown by points 2 and 3 in Fig. 4.4-6, the average maximum and minimum pressure drops are 310 and 213 Pa, respectively. The pressure drop, however, could also increase to as high as 531 Pa or as low as 106 Pa. At points marked by A, B, C, D, and E in Fig. 4.4-6, the pressure drop decreases to low values. The low pressure drop in this region indicates a high average void fraction, implying that the region is filled basically with vapor. The frequency of this phenomenon is about 5 to 10 s (time between points A, B, C, D, and so on).

In Fig. 4.4-7, the predicted pressure drop between the axial locations at 406 and 609 mm, based on the predicted void fraction distribution between these two locations, is plotted against time at a plotting frequency of two data points per second. The average predicted pressure drop over the first 100 s is ~110 Pa, about one-third the experimental value seen in Fig. 4.4-6. The predicted pressure drop increases with time because the quench front progresses toward the upper elevations. The predicted and measured frequency and amplitude of pressure-drop oscillations show different characteristics—the frequency and amplitude of the predicted values are much higher than the measured values. The measured and predicted average pressure drops are in minimal agreement. Furthermore, the fundamental character of the two traces differ as the Lehigh trace shows the averaged pressure drop at a relatively constant 300 Pa,

whereas the TRAC-predicted result increases with time (the latter seeming more physically realistic). In Figs. 4.4-8 to 4.4-10, the predicted and measured wall temperatures at elevations 0.15, 0.3, and 0.45 m above the core inlet are plotted against the transient time. The temperature at the elevation of 0.15 m heats up a few seconds and then starts to decrease (see Fig. 4.4-8). For the first 25 s, the predicted- and measured-cladding temperatures track each other. However, the predicted cooling rate slows relative to the data between 25 and 40 s, but increases thereafter, resulting in a quench about 13 s earlier than in the test.

At 30 cm, the predicted wall temperature (Fig. 4.4-9) shows reduced heater-rod cooling relative to the data beginning at 30 s. Thereafter, the predicted cooling rate is less than experienced in the test, and this level of the bundle is predicted to quench about 18 s later than observed in the test.

The predicted wall temperature at 45 cm (Fig. 4.4-10), although following the experimental trend line of the data early, experiences a small heatup beginning at 25 s. Beginning at 115 s, the heat-transfer rate is underpredicted so that the wall temperature remains much higher than the measured value until it is quenched. This level of the bundle is predicted to quench about 45 s later than observed in the test.

The predicted and measured wall and vapor temperatures at an elevation of 60 cm are shown in Fig. 4.4-11. This is the elevation of the first vapor-temperature probe (see Figs. 4.4-2 and 4.4-3). The predicted wall temperature tends to increase until ~70 s, whereas the measured data show an immediate decrease at a very small rate. The wall temperature is overpredicted by ~80 K. The vapor temperature at this location is variably underpredicted by ~200 to 300 K. Note that the measured vapor temperatures are the maximum possible values and are obtained by drawing a tangent to the peak values of the recorded trace.

At the axial level of 96 cm, the vapor temperature is also underpredicted as shown in Fig. 4.4-12. After 65 s, the predicted vapor temperature comes close to the saturation temperature of the fluid, well below the measured vapor temperature, which remains between 800 to 900 K. The predicted wall temperatures are less than the measured temperatures and indicate the predicted cooling rate is higher than in the test at this elevation. Whereas the wall temperature is overpredicted at the 60-cm level, it is underpredicted at the 96-cm level. The change from undercooling at the 60-cm level to overcooling at the 96-cm level is caused by the TRAC grid-spacer model implemented at the 76.2-cm level.

We have used the measured and predicted quench times at three levels to calculate an average quench-front velocity over the time intervals (Table 4.4-1). At earlier times (lower elevations), the predicted average quench front velocity is higher than the measured value. The higher predicted rate of quench front advancement can also be inferred from Fig. 4.4-8, which shows that quenching of the rod surface at the 15-cm level is predicted to occur ~20-s earlier than observed in the test. However, at later times (i.e., the 30 and 45-cm elevations) the test rods quench earlier than predicted (Figs. 4.4-9 and 4.4-10), indicating that the quench front advanced faster in the test than predicted. These results are summarized in Table 4.4-1. The quench-front velocity is not predicted correctly, and is first overpredicted at lower elevations and then

underpredicted at upper elevations. The main controlling mechanism in determining the rate of quench-front propagation is the axial-distance-dependent transition model. From this assessment, it seems that the empirical constants used in the transition boiling correlation should be reviewed.

In Figs. 4.4-13 through 4.4-20, we present a more comprehensive comparison of the measured[4.4-1] and predicted axial temperature profiles at 8 times (40, 53, 74, 94, 108, 129, 149, and 170 s). Each figure presents a snapshot along the length of the heater rods of both the test and predicted heater-rod thermal state at the specified time. For the test rods, the measured temperatures are presented for 6 different rods (numbers 1, 3, 4, 6, 7, and 8, as designated in Fig. 4.4-1). The TRAC model consolidates all 9 test heater rods into a single, average, computational rod. Dimensional effects were clearly evident in the thermal responses of the different heater rods. For example, at each time there was a range of quench times and peak cladding temperatures (PCTs). The data report,[4.4-1] in addition to providing the thermocouple readings along each of the six heater rods listed above, also provides a single-value quantification of the position of the quench front. A single number does not appear to be fully consistent with the positional variability of the quench front, as evidenced by the temperature profiles of the individual rods.

The single grid spacer in the Lehigh rod bundle facility is modeled. Its position is 0.762 m above the test section inlet, the same axial position as in the test facility.

At 40 s, the predicted and measured quench front positions are 0.10 and 0.034 m from the test section inlet (Fig. 4.4-13). Ahead of the quench front, the predicted and measured axial temperature profiles are in reasonable agreement. The predicted cladding temperature lies within the measured temperatures for the six rods for a distance of 0.05 m ahead of the quench front. For the next 0.5 m, the cladding temperature is overpredicted. The effect of the grid-spacer model is to reduce the predicted temperature, and the predicted cladding temperature lies within the measured temperatures for the final 0.55 m of the heater rods.

At 53 s, the predicted and measured quench front positions are 0.11 and 0.073 m from the test section inlet (Fig. 4.4-14). Ahead of the quench front, the predicted and measured axial temperature profiles are in reasonable agreement. The predicted cladding temperature lies within the measured temperatures for the six rods for a distance of 0.19 m ahead of the quench front. The cladding temperature is overpredicted for the next 0.43 m. The effect of the grid-spacer model is to reduce the predicted temperature, and the predicted cladding temperature lies within the measured temperatures for the final 0.47 m of the heater rods.

At 74 s, the predicted and measured quench front positions are 0.17 and 0.134 m from the test section inlet (Fig. 4.4-15). Ahead of the quench front, the predicted and measured axial temperature profiles are in reasonable agreement. However, the difference between predicted and measured temperatures at any axial location before the grid spacer is greater than at the earlier two times. The predicted temperature is always higher, ~65 K being the largest difference at this time. The predicted and measured impact of the grid spacer on cladding temperatures is more pronounced than at earlier times. The variability in the position of the quench front for the various heater rods in the test is clearly evident from this time forward.

At 94 s, the predicted and measured quench front positions are 0.22 and 0.19 m from the test section inlet (Fig. 4.4-16). Ahead of the quench front, the predicted and measured axial temperature profiles are in reasonable agreement, but the predicted temperature is always higher until the enhanced heat transfer associated with the grid-spacer model causes a sufficient reduction in predicted cladding temperature so that the predicted temperature lies with the behavior measured. The peak difference between the predicted and measure cladding temperatures is 70 K. The variability in the position of the quench front for the various heater rods is evident.

The predicted and measured cladding thermal behaviors follow the same pattern at 108 s (Fig. 4.4-17), 129 s (Fig. 4.4-18), 149 s (Fig. 4.4-19), and 170 s (Fig. 4.4-20). At 108 s, the axial elevations of the predicted and measured quench fronts are 0.25 and 0.228 m, respectively. At 129 s, the axial elevation of the predicted and measured quench fronts are 0.28 and 0.283 m, respectively. At 149 s, the axial elevation of the predicted and measured quench fronts are 0.31 and 0.33 m, respectively. At 170 s, the axial elevation of the predicted and measured quench fronts are 0.36 and 0.383 m, respectively. At each of these times, the predicted cladding temperature between the advancing quench front and the grid spacer is greater than the measured cladding temperature; the differences in PCT vary between 74 and 91 K. Throughout the transient, the differences between the predicted and measured PCT grow.

4.4.5. Comparison of Predicted and Test Results (without Grid Spacers)

The calculation results presented in Figs. 4.4-8 through 4.4-20 were for Run 02/24/85-20 with the grid spacers modeled. In this section we present the same code data comparisons for this test with the grid-spacer model eliminated. The equivalent figures are shown in the following tabulation.

With Grid Spacers	Without Grid Spacers
4.4-8	4.4-21
4.4-9	4.4-22
4.4-10	4.4-23
4.4-11	4.4-24
4.4-12	4.4-25
4.4-13	4.4-26
4.4-14	4.4-27
4.4-15	4.4-28
4.4-16	4.4-29
4.4-17	4.4-30
4.4-18	4.4-31
4.4-19	4.4-32
4.4-20	4.4-33

As a result of this and other assessments reported in this document, we determined that the TRAC grid-spacer model is seriously flawed. The grid-spacer model for interfacial heat transfer comes on when the code finds that a grid spacer is located within a hydro cell, the hydro cell is above the transition boiling regime for bottom-up reflood or below

the transition boiling regime for top-down reflood, and the vapor temperature in this hydro cell is above the saturation temperature. The TRAC grid-spacer model for interfacial heat transfer is:

$$h_{ig}A_i = C_s H_D/(vol(T_v - T_{sat}))$$

where,

h_{ig} = interfacial heat transfer coefficient from the vapor phase to the interface.

A_i = interfacial area.

C_s = correlation constant = 10^6.

H_D = hydraulic diameter.

vol = volume of the hydro cell.

T_v = vapor temperature.

T_{sat} = saturation temperature.

When a grid spacer has been modeled and the conditions governing its initiation are satisfied, the grid-spacer model for interfacial heat transfer is actuated.

A constant interfacial heat-transfer rate from the vapor phase to the interface continues until the vapor temperature reaches approximately the saturation temperature. The TRAC grid-spacer model for interfacial heat transfer in the TRAC reflood model is ad hoc; it was developed based on the Lehigh test rod surface temperatures that showed significant levels of cooling in the vicinity of the grid spacer.

The absence of the grid-spacer model can most easily be observed in the vapor-superheat comparisons beyond the grid spacer location and in all the axial cladding temperature comparisons. As discussed above, the grid-spacer model, when activated, reduces the vapor temperature to near saturation (Fig. 4.4-12). Without the grid-spacer model, the predicted superheat temperature, although fluctuating, is near the measured value (Fig. 4.4-25). With the grid-spacer model, the vapor superheat varies between values near measured to saturation for the first 70 s with the saturation temperatures resulting from the grid-spacer model. In addition, the wall temperature is significantly higher when the grid-spacer model is absent.

The impact of the grid-spacer model on the wall temperatures is more graphically illustrated in the series of wall axial temperature profiles with and without the grid-spacer model (Figs. 4.4-13 through 4.4-20 and Figs. 4.4-25 through 4.4-33, respectively). Without the grid-spacer model, the predicted wall temperatures remain much higher than measured.

We have concluded that the TRAC grid-spacer model is severely flawed and are, therefore, recommending that it not be used. However, the LRB Test 02/24/85-20 results clearly show that the grid spacer is a highly significant component and a good grid-spacer model is clearly needed. As shown in recent TRAC code assessment activities, the impact of the grid spacer varies from facility to facility. However, in both the LRB Test 02/24/85-20 just reported and in the FLECHT SEASET 33436 results

reported in Section 4.10, the grid spacers have a first-order impact on the measured cladding temperature

4.4.6. Conclusions

Overall, the agreement between predicted and measured parameters, with the flawed TRAC grid-spacer model activated, are judged to be reasonable. There are, however, important differences, and these must be analyzed.

The snapshots of predicted and measured cladding thermal characteristics along the length of the heater rods show that the code is predicting all important behaviors including the cooldown behavior, quenching, and impact of the grid spacer. Downstream of the grid spacer, the predicted cladding temperatures always lie within the range of measured temperatures for the six test rods plotted. Between the quench front and the grid spacer, and after 74 s, the predicted temperatures are always higher than measured. For the 40- and 53-s snapshots, the predicted cladding temperatures lay within the range of measured cladding temperatures for the six test rods plotted for a short distance in advance of the quench front.

Early in the transient, the code predicted a too-rapid advancement of the quench front. However, the predicted rate of quench front advancement slowed as the transient progressed and the predicted and measured axial locations of the quench front were identical by 149 s. Subsequently, the predicted position of axial quench front fell behind the measured position.

The snapshot plots of predicted and measured cladding axial temperature profiles proved helpful in understanding several of the transient plots, particularly those at the locations of the steam probes. For example, the comparison of predicted and measured cladding temperatures at 0.6 m (Fig. 4.4-11) shows that the predicted cladding temperature is always greater than measured. This is consistent with the results in each of the snapshots at the 0.6-m elevation. Clearly, the heat transfer between the quench front and the grid spacer is underpredicted by the current model. At the 0.965-m level, however, the predicted cladding temperature is shown to always be less than the measured cladding temperature (Fig. 4.4-12). With the aid of the snapshots, the reason is clear; the grid-spacer model enhances heat transfer, and the predicted cladding temperature always lies within the range of measured temperatures for the six test rods plotted. We infer that the measured cladding temperatures plotted are the maximum rod temperatures.

With the grid-spacer model activated, the vapor temperatures are underpredicted throughout the transient. Further, the predicted vapor superheats are highly variable with short periods of high superheat temperatures approaching the measured superheated vapor temperatures, interspersed with intervals during which the steam is at saturation temperatures. This behavior is directly related to the TRAC grid-spacer model.

The TRAC grid-spacer model replicates the behavior of the Lehigh Run 02/24/80-6, but that is because the model was tuned to this data. When applied to other facilities and tests, we have found that the grid-spacer model produces excessive and nonphysical cooling rates. The TRAC grid-spacer model lacks an appropriate physical basis and its

use is, therefore, discouraged. However the Lehigh data clearly shows enhanced wall cooling caused by the bundle grid spacer. Therefore, it is clear that a well-founded grid-spacer model should be developed for TRAC.

4.4.7. Code Performance

Lehigh Rod Bundle Run 02/24/85-20 was run on code Versions 5.5 and 5.4.29R9+; the run performance information plus other pertinent comments follow.

Code Version 5.5

Platform	Sun Enterprise 3000
Total CPU time (s)	741.7
Archive location of input model	CFS /tida/f77da_decks/inlehigh
Archive location of calculation	CFS /trac-da/F77DA/1.11Rrfd3/ LEHIGH.tar.gz

Code Version 5.4.29R9+

Platform	Sun Enterprise 3000
Total CPU time (s)	721.7
Archive location of input model	CFS /tida/f77da_decks/inlehigh
Archive location of calculation	CFS /trac-da/F77DA/5429R9rfd3/ LEHIGH.tar.gz

The same input model was used for both codes with no changes required for either to facilitate running.

REFERENCES

4.4-1. K. Tuzla, C. Unal, O. Badr, S. Neti, and J. C. Chen, "Thermodynamic Nonequilibrium in Post-Critical-Heat-Flux Boiling in a Rod Bundle," US Nuclear Regulatory Commission document NUREG/CR-5094, Vols. 1–4 (July 1987).

4.4-2. R. A. Nelson, Jr., D. A. Pimentel, S. Jolly-Woodruff, and J. Spore, "Reflood Completion Report, Volume I, A Phenomenological Thermal-Hydraulic Model of Hot Rod Bundles Experiencing Simultaneous Bottom and Top Quenching and an Optimization Methodology for Closure Development," Los Alamos National Laboratory document LA-UR-98-3043 (April 1998).

4.4-3. J. W. Spore, J. S. Elson, S. Jolly-Woodruff, T. K. Knight, J.-C. Lin, R. A. Nelson, K. O. Pasamehmetoglu, R. G. Steinke, and C. Unal of Los Alamos National Laboratory; and J. H. Mahaffy and C. Murray of Pennsylvania State University, "TRAC-M/Fortran 90 (Version 3) Theory Manual," Los Alamos National Laboratory document LA-UR-00-910 (July 2000).

4.4-4. N. T. Obot and M. Ishii, "Two-Phase Flow Regime Transition Criteria in Post-Dryout Region Based on Flow Visualization Experiments," Argonne National Laboratory document NUREG/CR-4972, ANL-87-27 (June 1987).

4.4-5. K. Hirano, et. al., "Data Report on Large Scale Reflood Test-14, CCTF Test CI-5 (Run 014)," Japan Atomic Energy Research Institute document JAERI-memo 57-214 (August 1982).

4.4-6. C. Unal, K. Tuzla, and J. C. Chen, "Comparison of TRAC-PF1/MOD1 Post-Test Calculation to Data Obtained From Lehigh University 3 x 3 Rod Bundle Bottom-Reflood Test," Institute of Thermo-Fluid Engineering and Science, Lehigh University document TS-862 (February 1989).

TABLE 4.4-1

PREDICTED AND MEASURED QUENCH TIMES AND QUENCH FRONT VELOCITIES

Location (m)	Quench Time (s)		Quench Front Velocity (mm/s)	
	Experimental	Predicted	Experimental	Predicted
0.15	65.5	54.	2.3	2.8
0.30	114.7	133.	3.0	1.9
0.45	178.0	221.	2.4	1.7

Note: The quench front velocity is predicted between locations listed in the table and indicates average values over a 0.15-m distance.

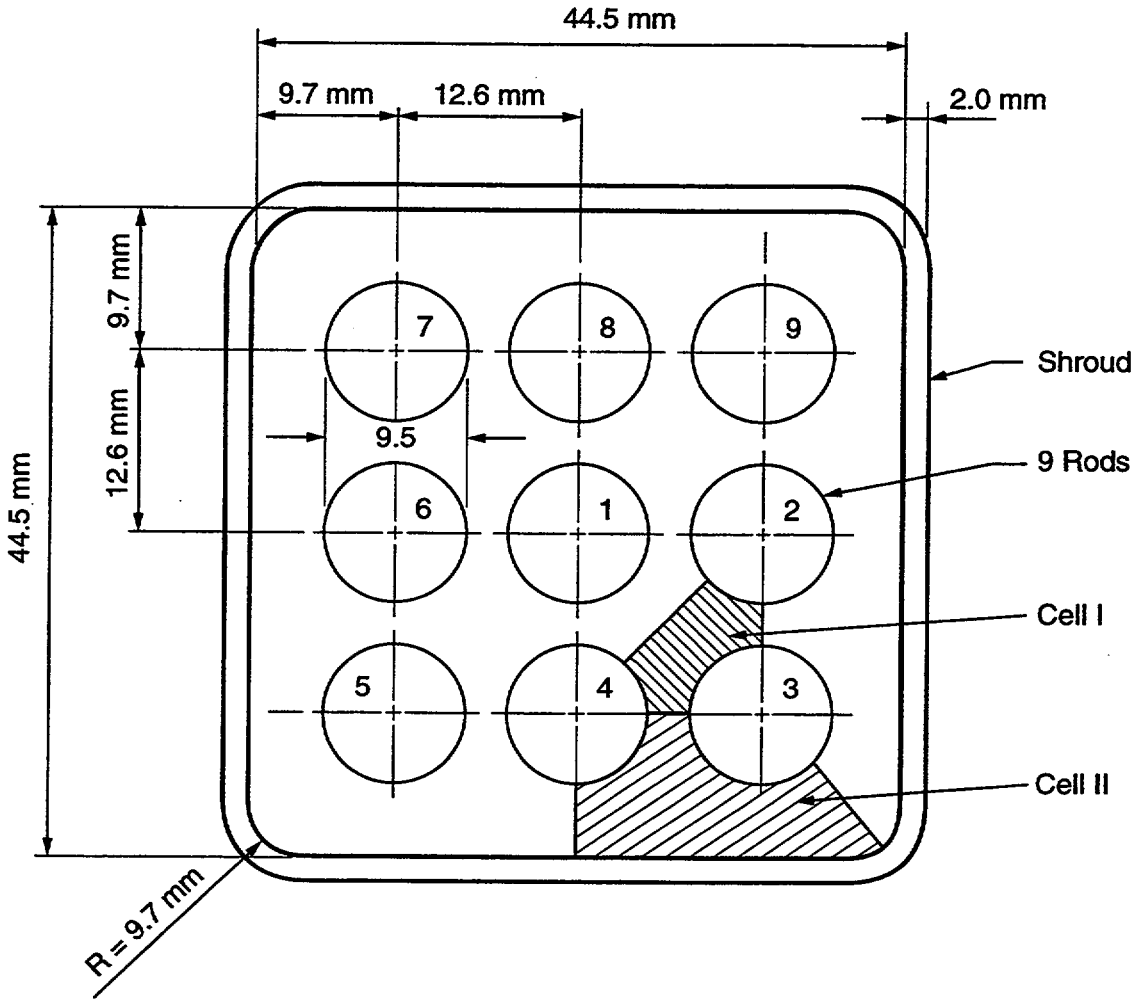

Fig. 4.4-1. Cross-sectional view of the Lehigh test bundle.

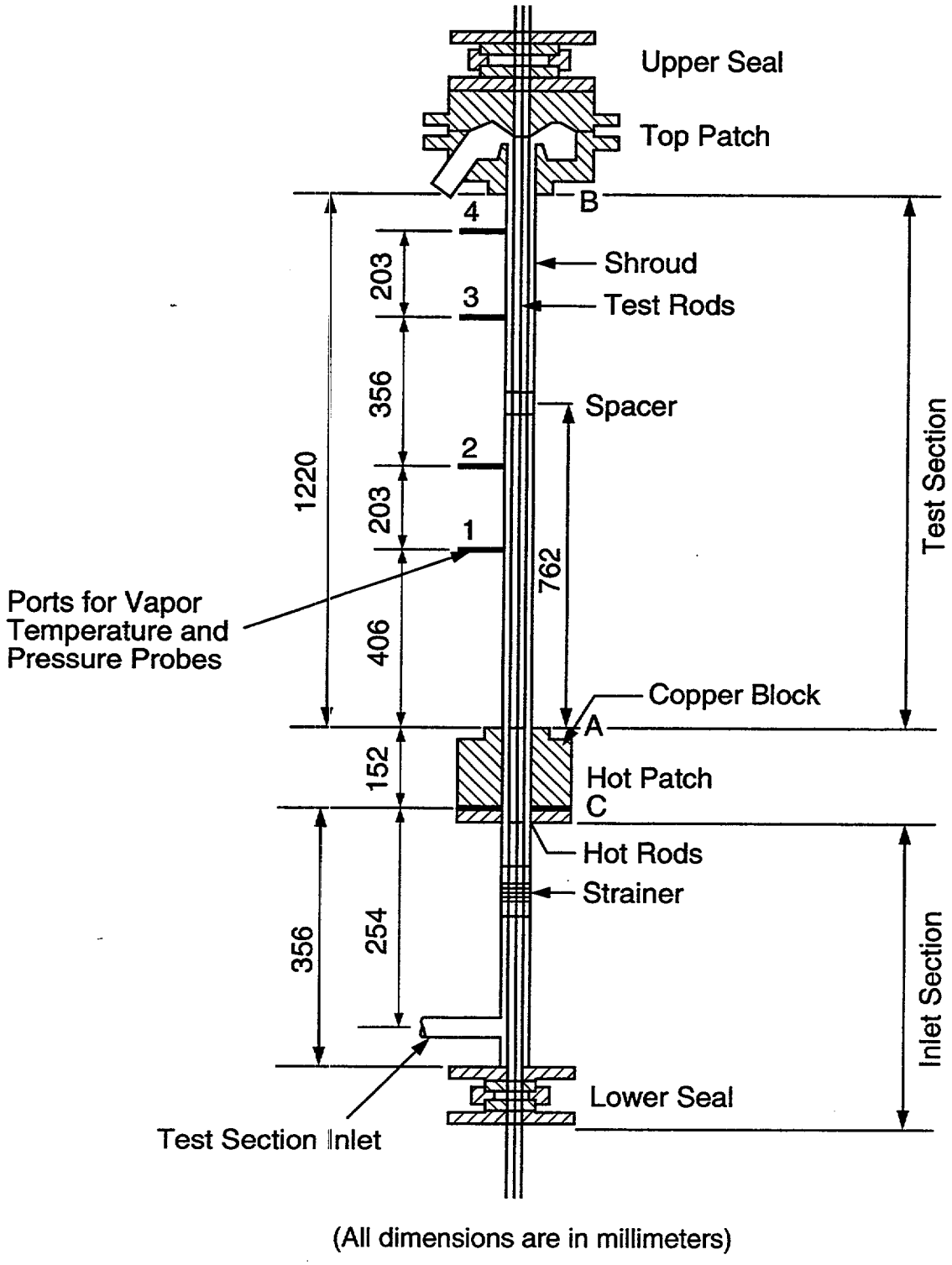

Fig. 4.4-2. Lehigh rod bundle test-section schematic.

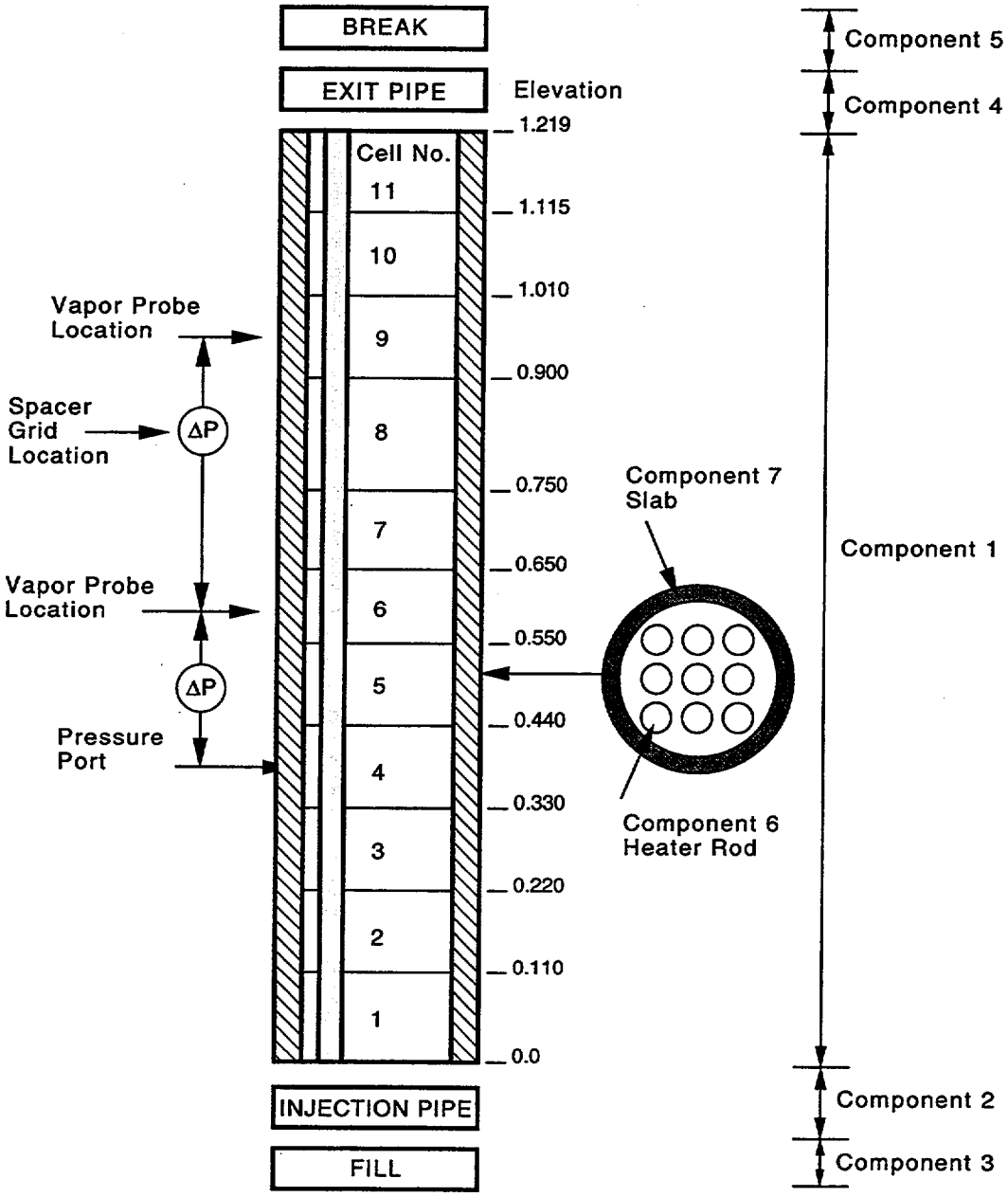

Fig. 4.4-3. Lehigh Rod Bundle Facility input model schematic.

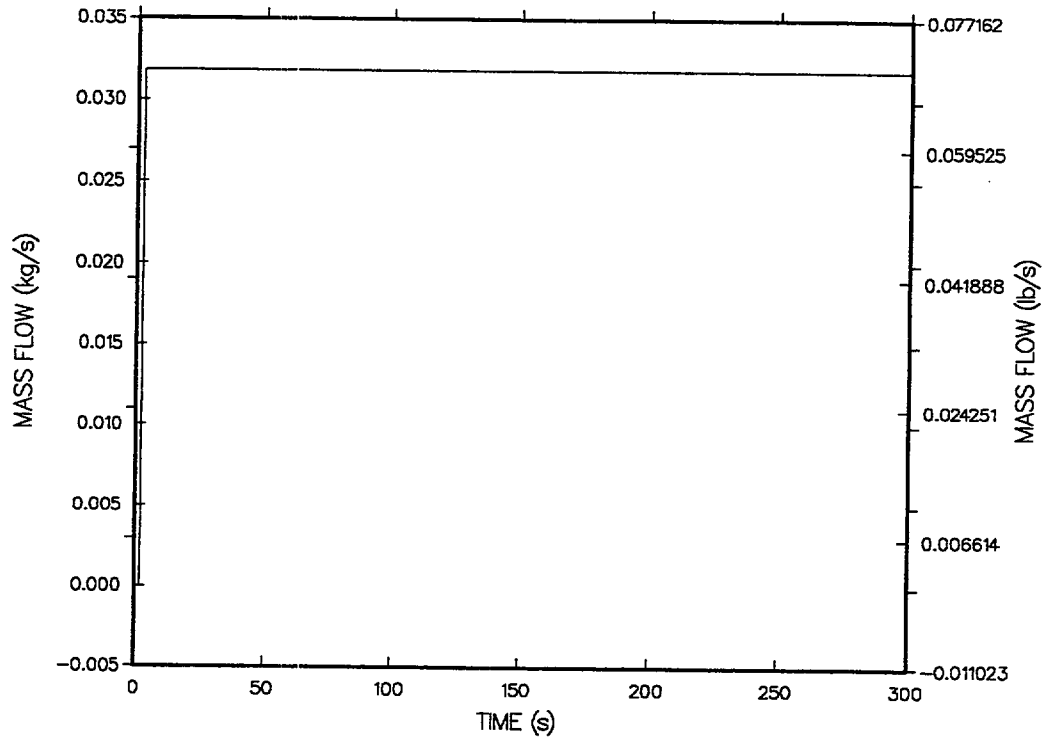

Fig. 4.4-4. Core inlet mass flow.

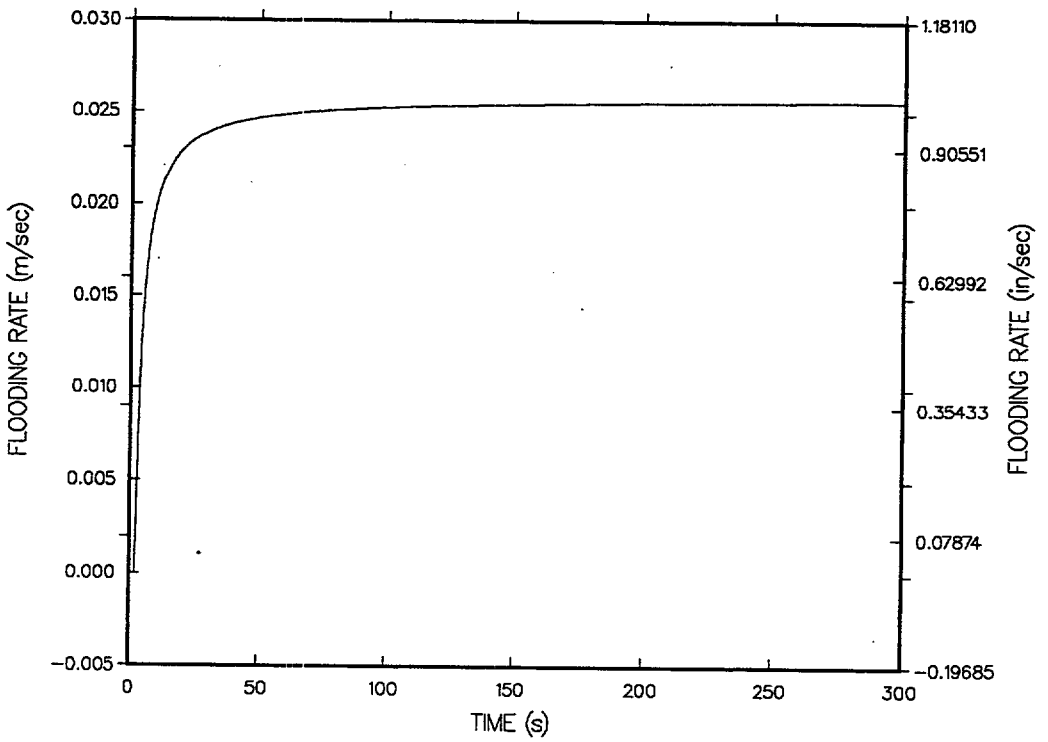

Fig. 4.4-5. Time-averaged core flooding rate.

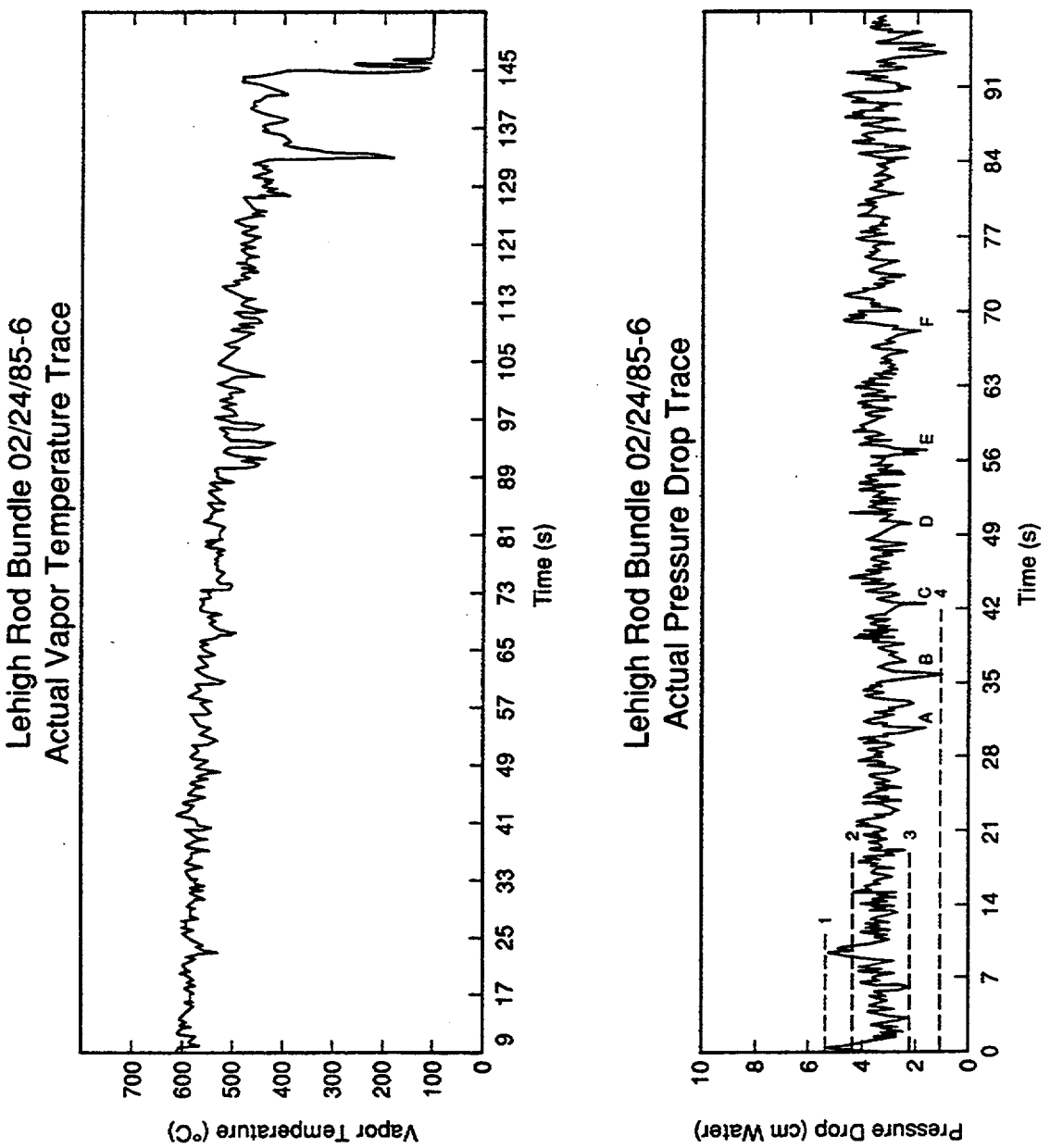

Fig. 4.4-6. The measured vapor temperature and core pressure drop between the vapor probes at 406 and 609 mm.

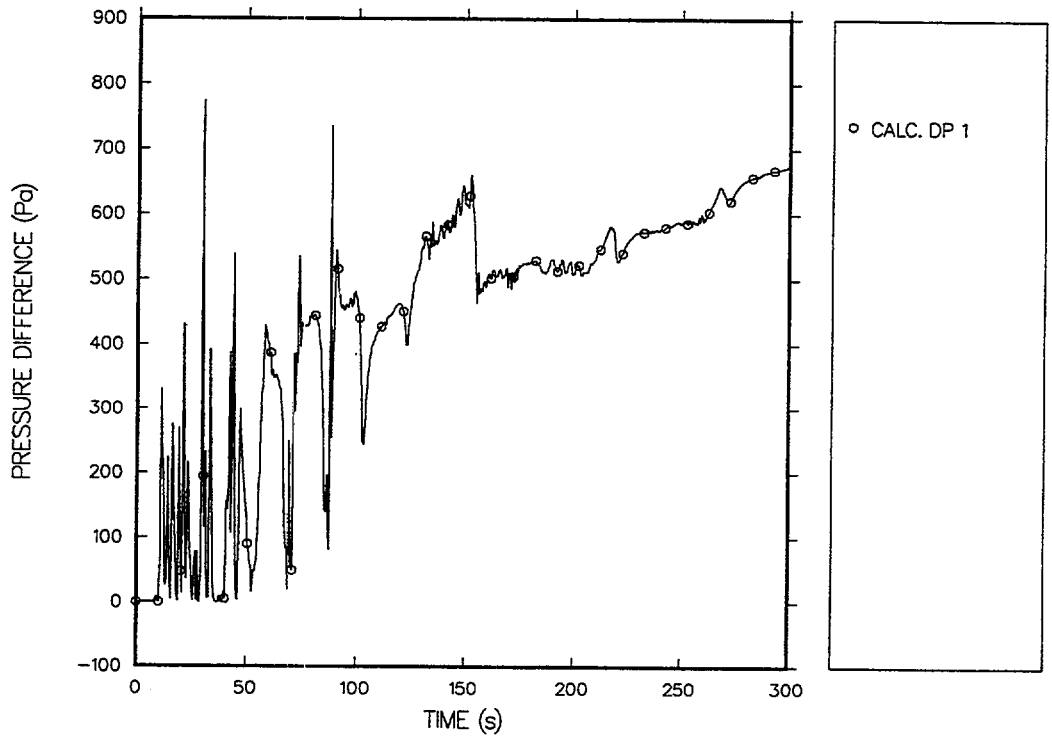

Fig. 4.4-7. Predicted trace of pressure drop between axial locations of 406 and 609 mm above the core inlet.

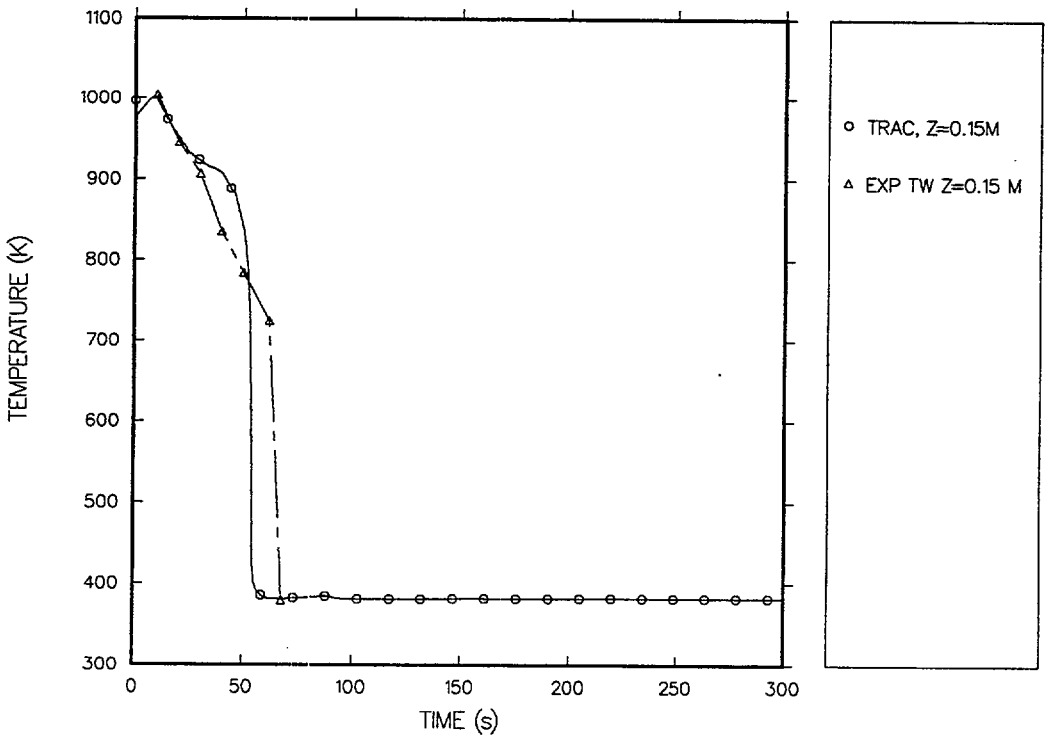

Fig. 4.4-8. Predicted and measured wall temperature, 0.15-m elevation.

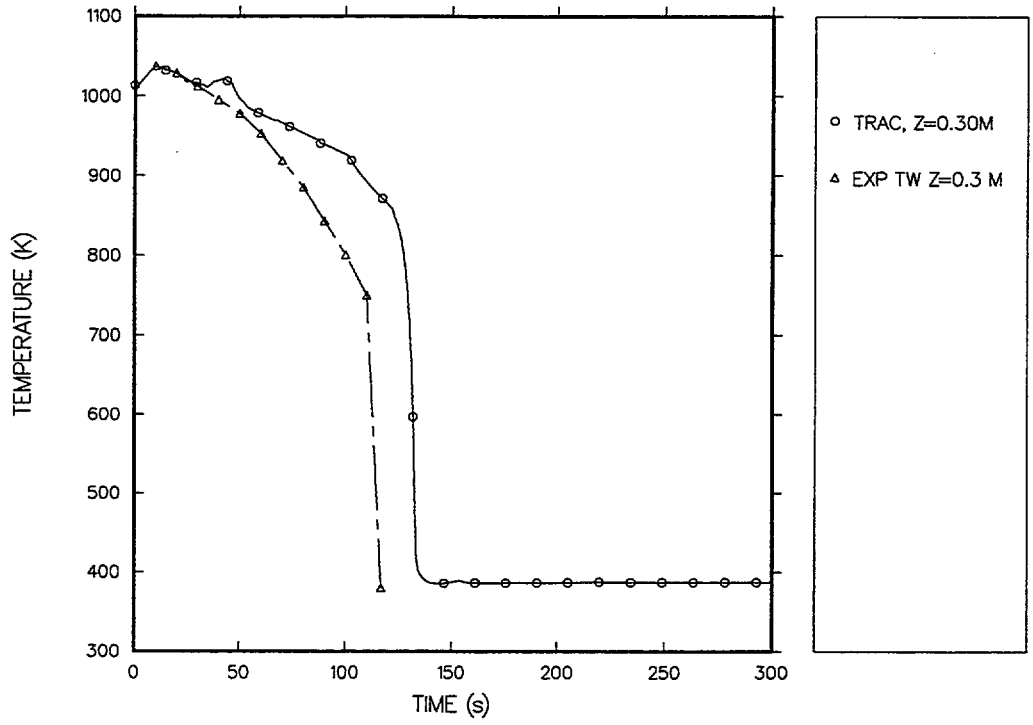

Fig. 4.4-9. Predicted and measured wall temperature, 0.3-m elevation.

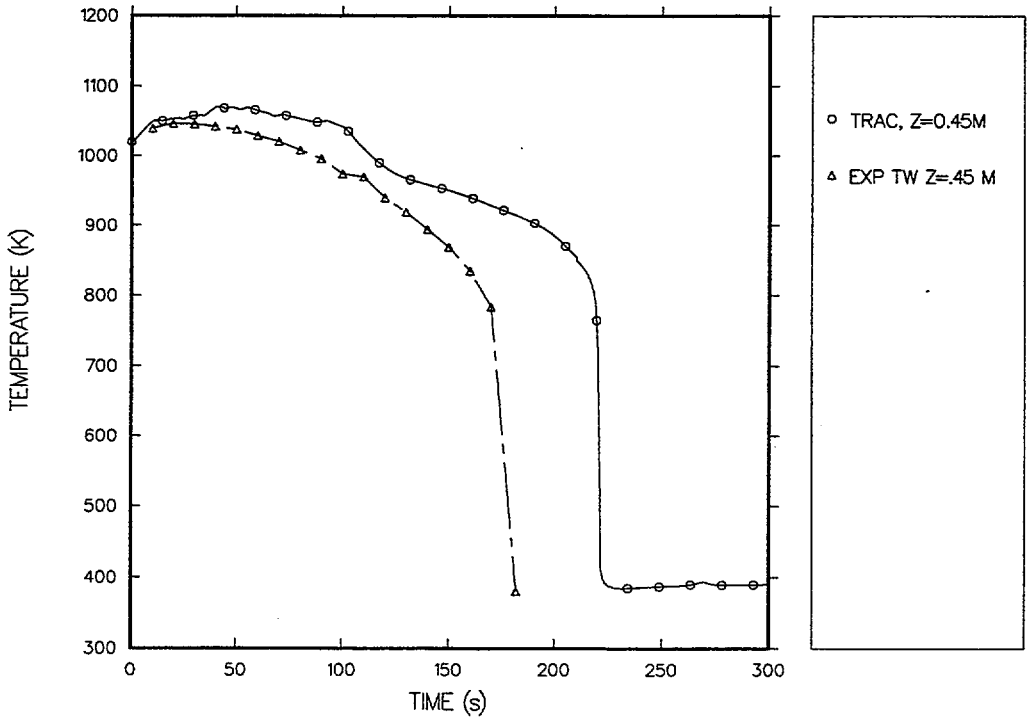

Fig. 4.4-10. Predicted and measured wall temperature, 0.45-m elevation.

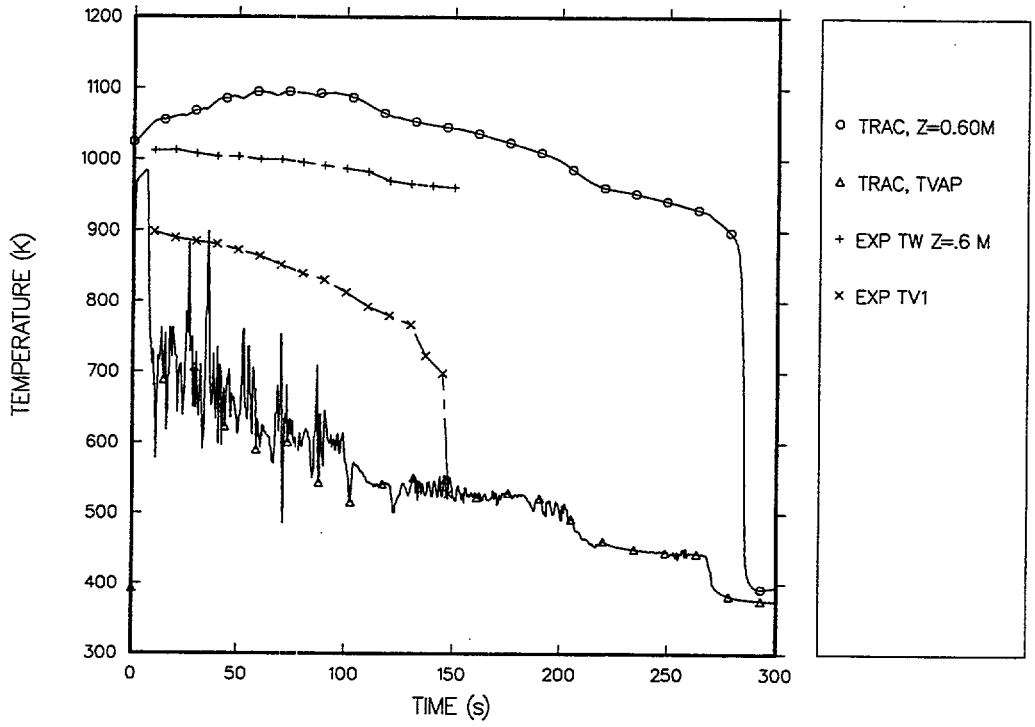

Fig. 4.4-11. Predicted wall and vapor-temperature histories at 60 cm.

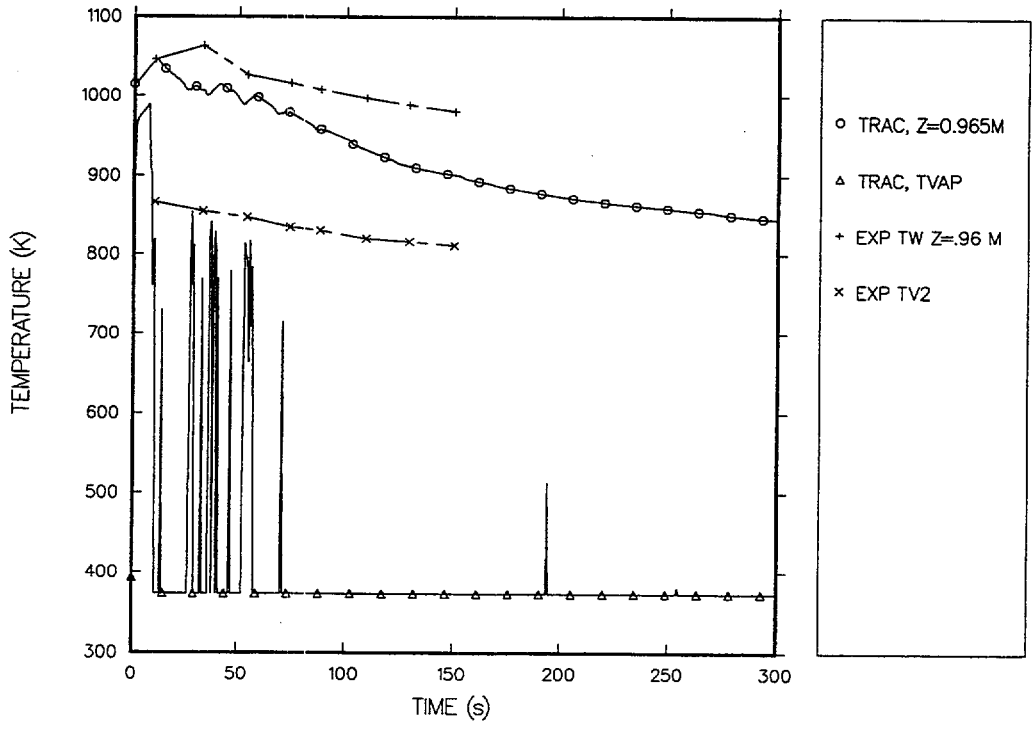

Fig. 4.4-12. Predicted wall and vapor-temperature histories at 96 cm.

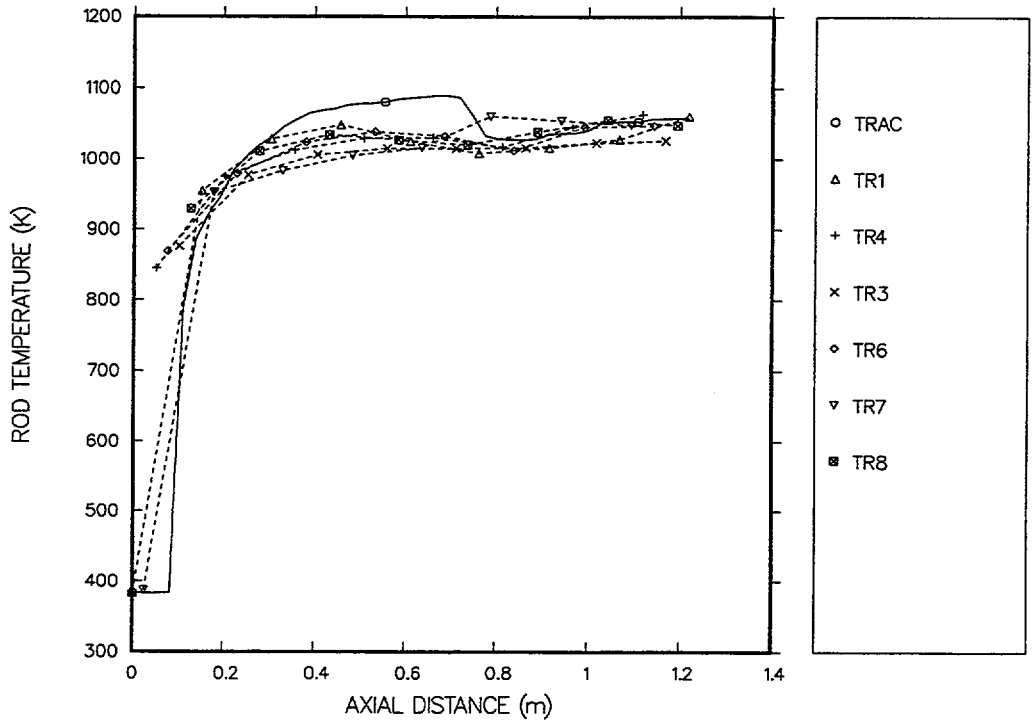

Fig. 4.4-13. Comparison of predicted and measured axial temperatures at 40 s.

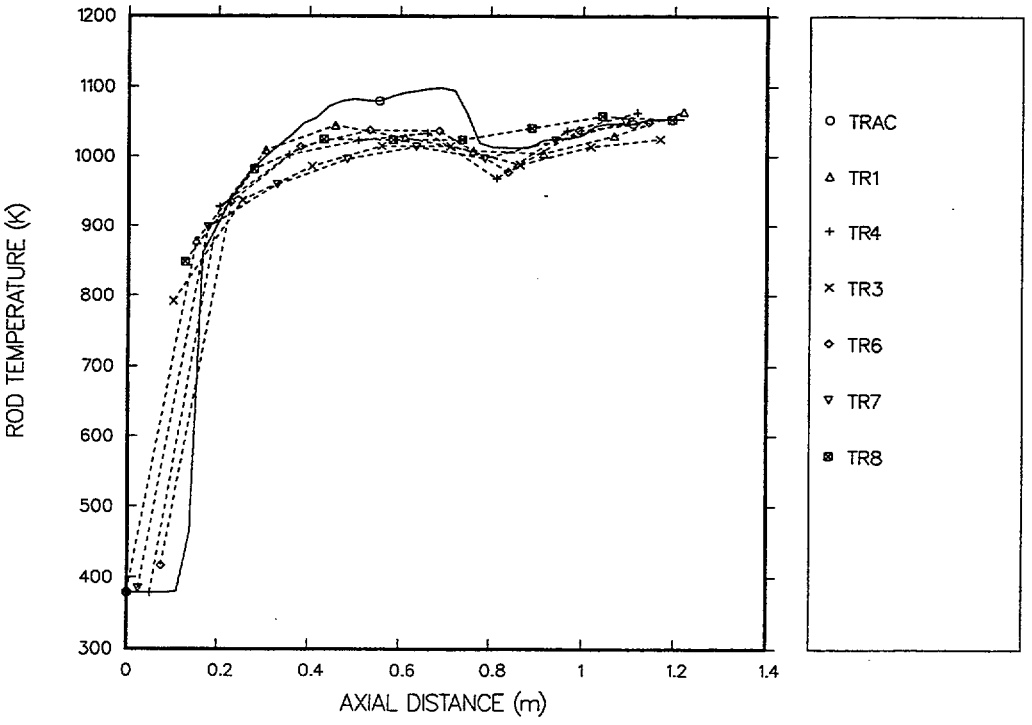

Fig. 4.4-14. Comparison of predicted and measured axial temperatures at 53 s.

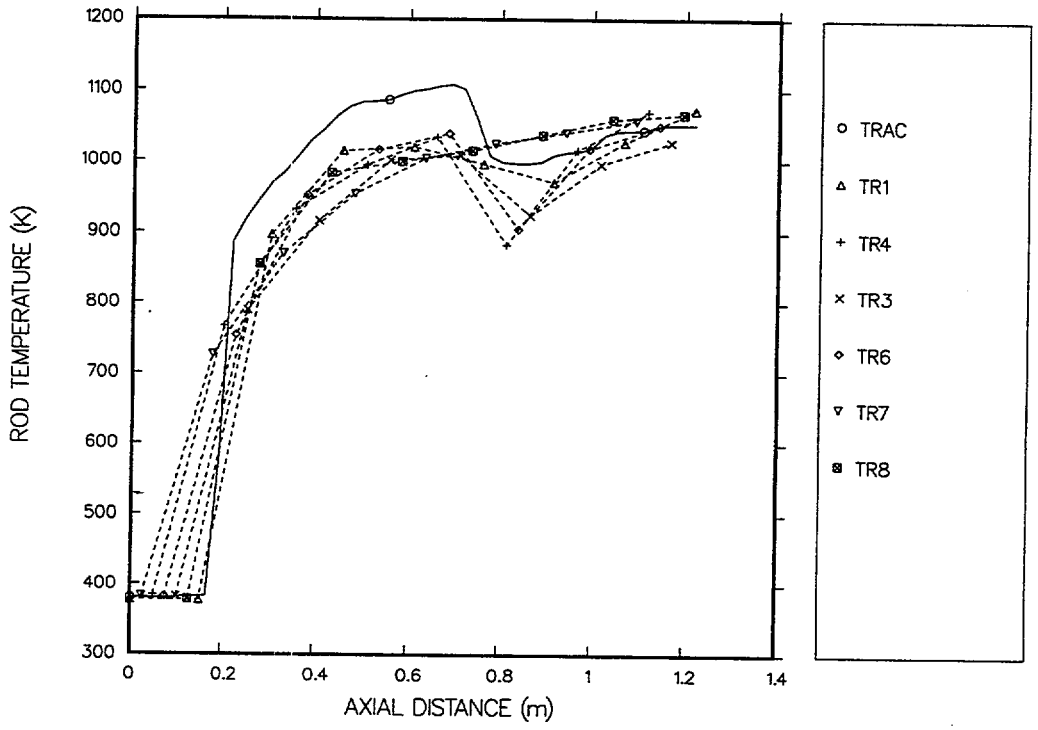

Fig. 4.4-15. Comparison of predicted and measured axial temperatures at 74 s.

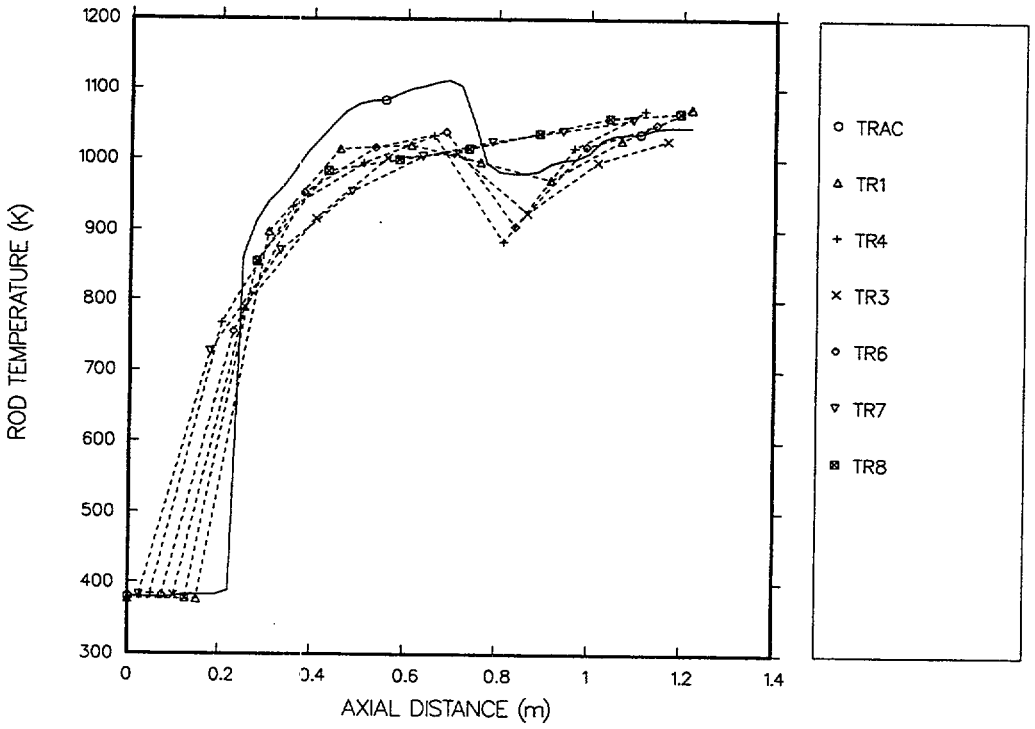

Fig. 4.4-16. Comparison of predicted and measured axial temperatures at 94 s.

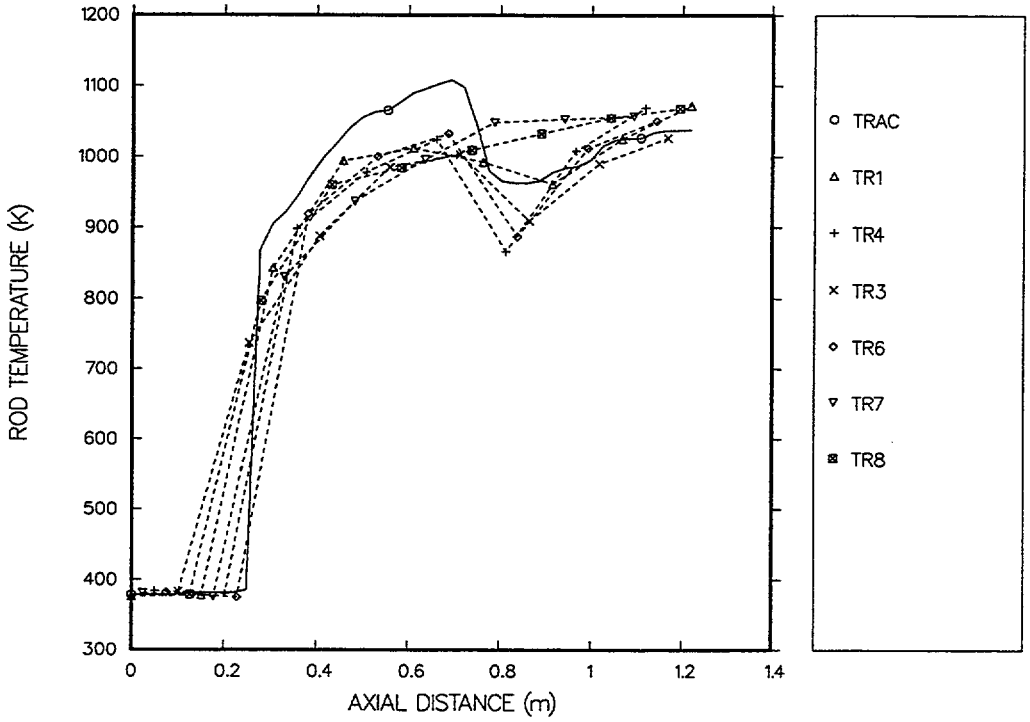

Fig. 4.4-17. Comparison of predicted and measured axial temperatures at 108 s.

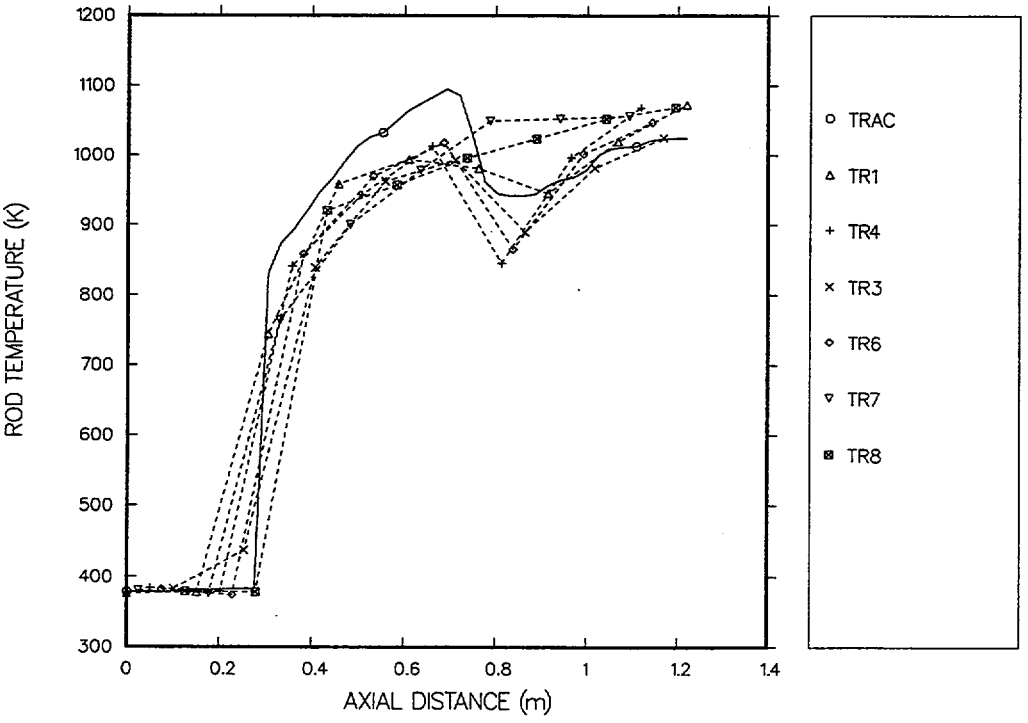

Fig. 4.4-18. Comparison of predicted and measured axial temperatures at 129 s.

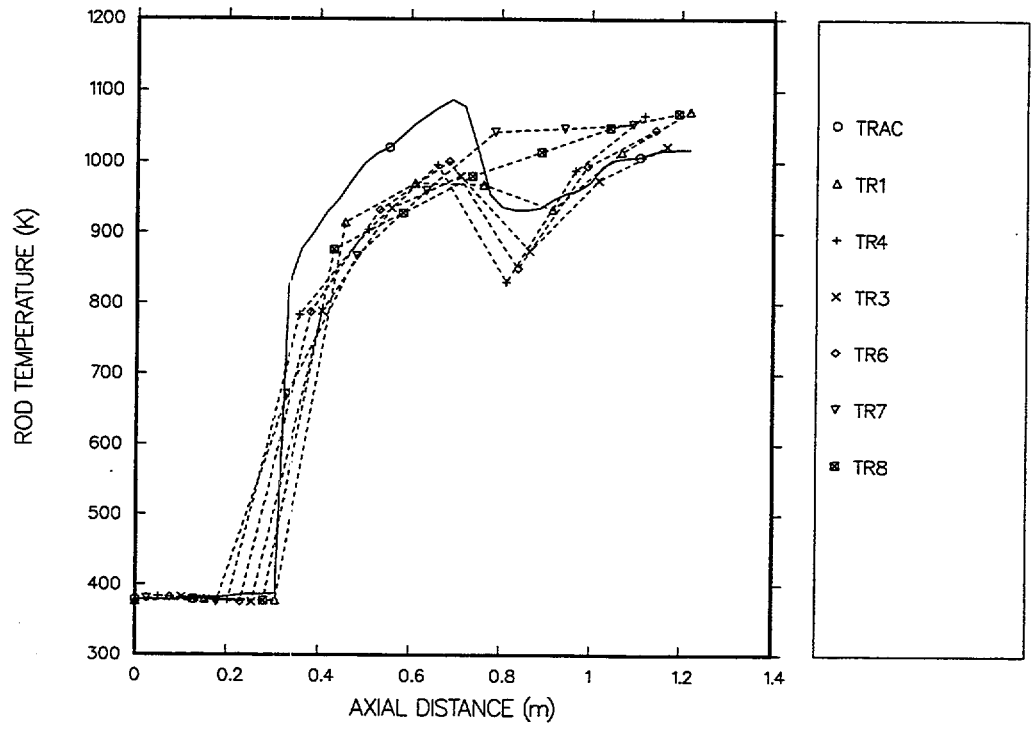

Fig. 4.4-19. Comparison of predicted and measured axial temperatures at 149 s.

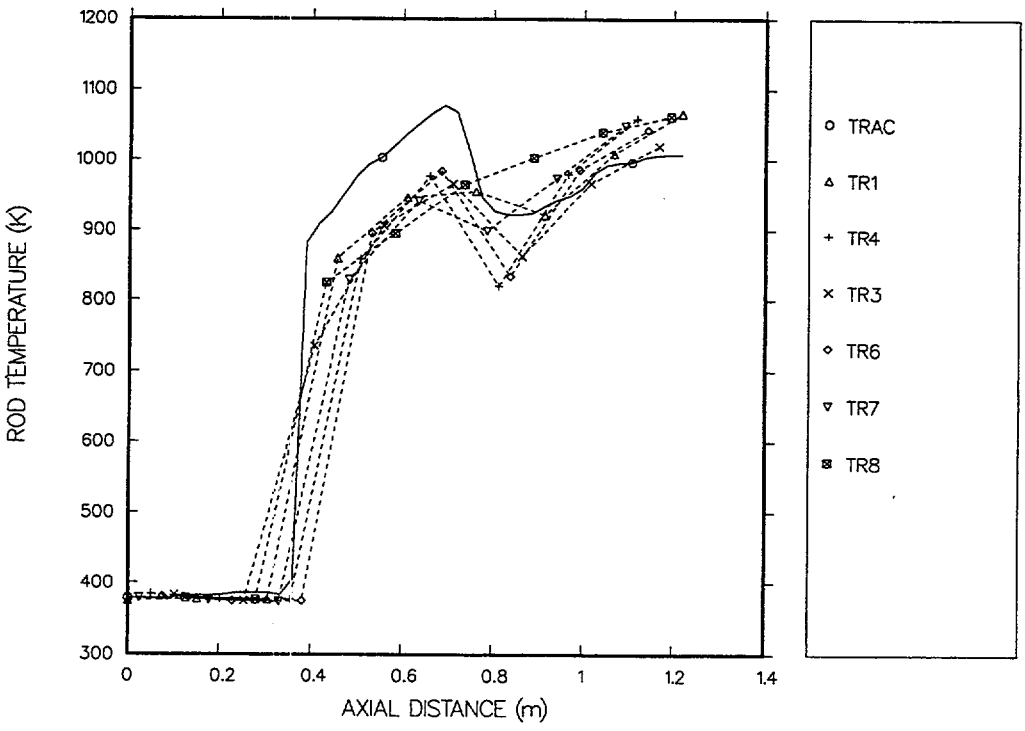

Fig. 4.4-20. Comparison of predicted and measured axial temperatures at 170 s.

This space is intentionally left blank.

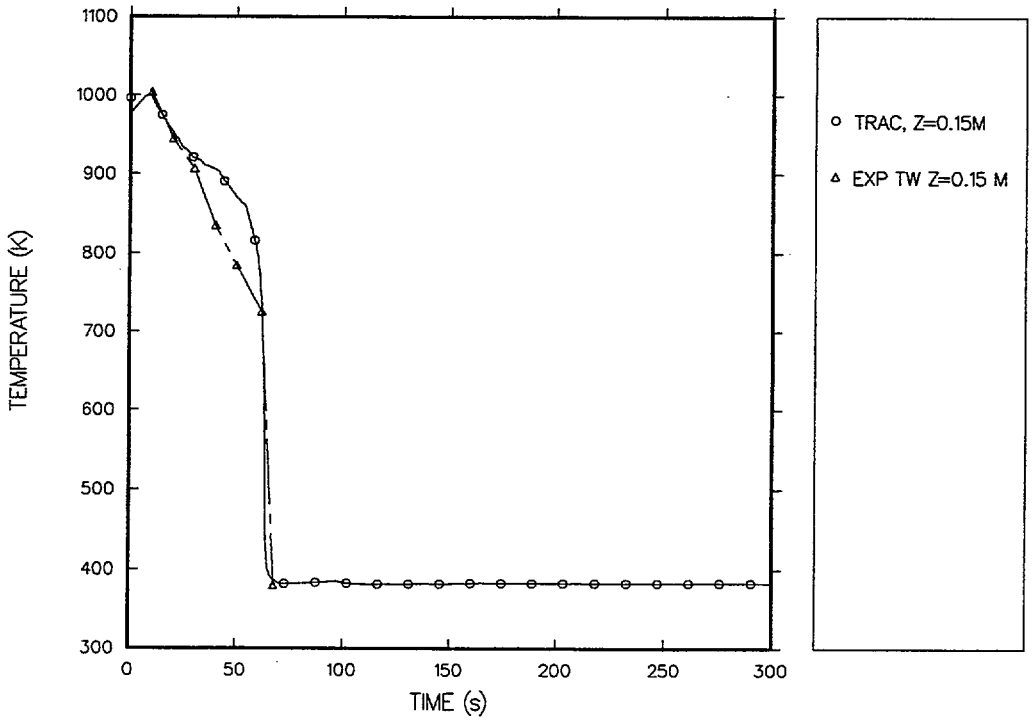

Fig. 4.4-21. Predicted and measured wall temperature, 15-cm elevation (without grid spacer model).

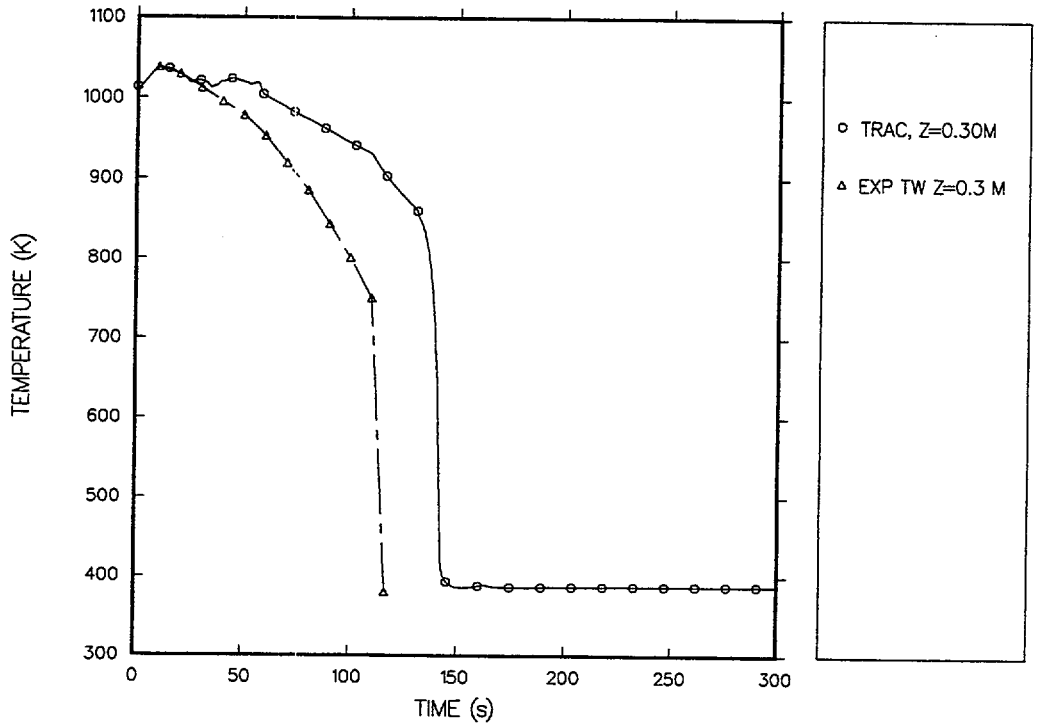

Fig. 4.4-22. Predicted and measured wall temperature, 30-cm elevation (without grid spacer model).

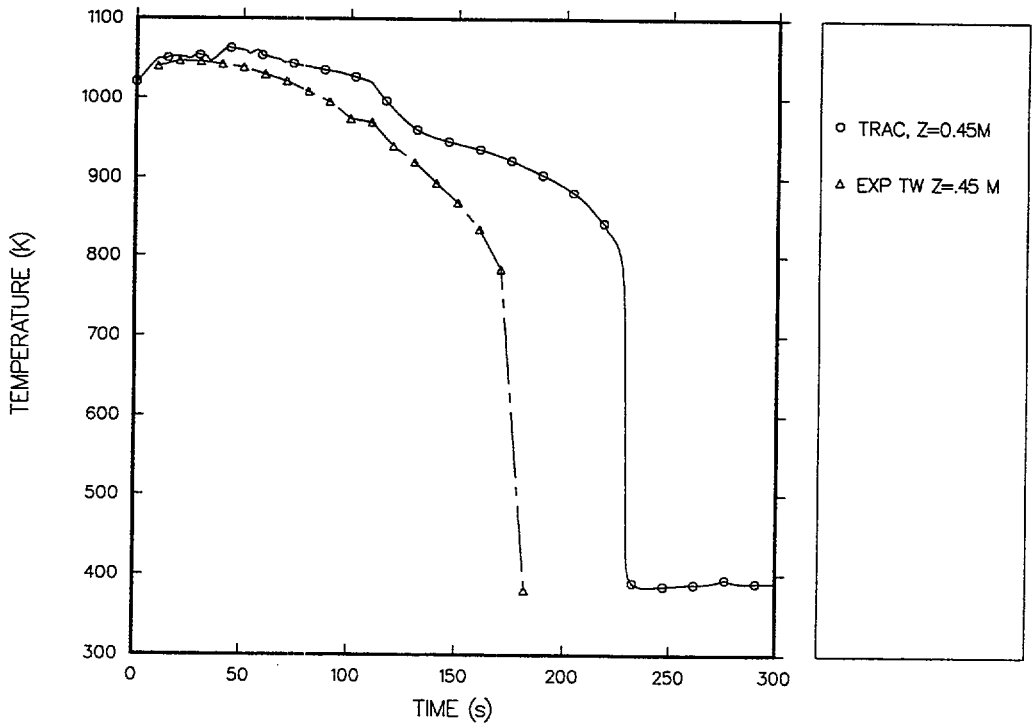

Fig. 4.4-23. Predicted and measured wall temperature, 45-cm elevation (without grid spacer model).

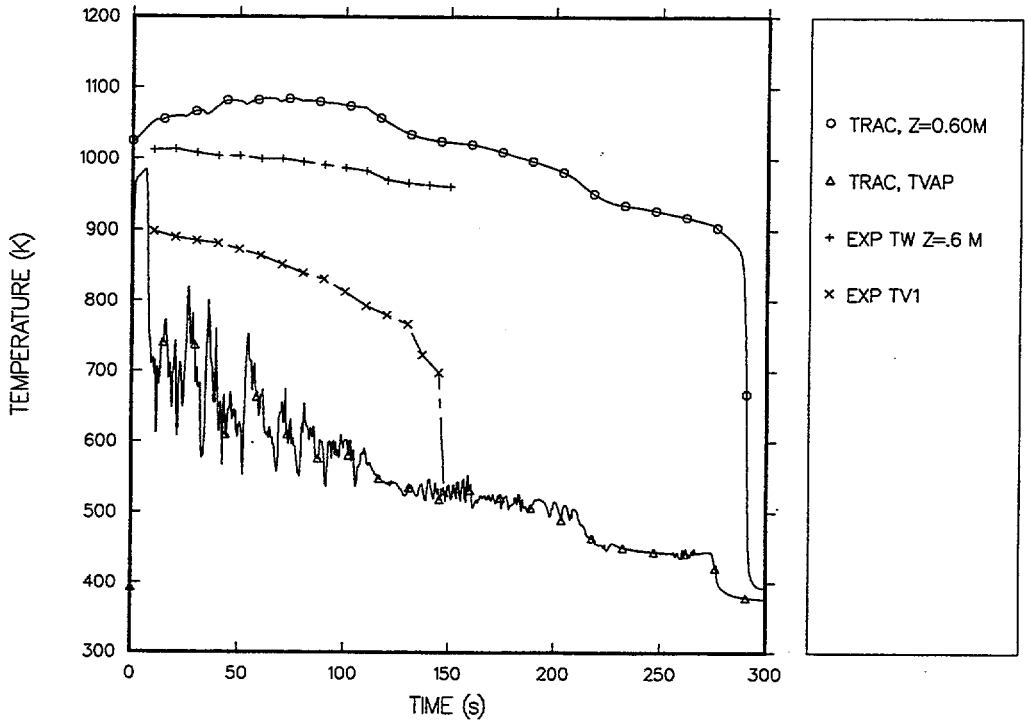

Fig. 4.4-24. Predicted wall and vapor-temperature histories at 60 cm (without grid spacer model).

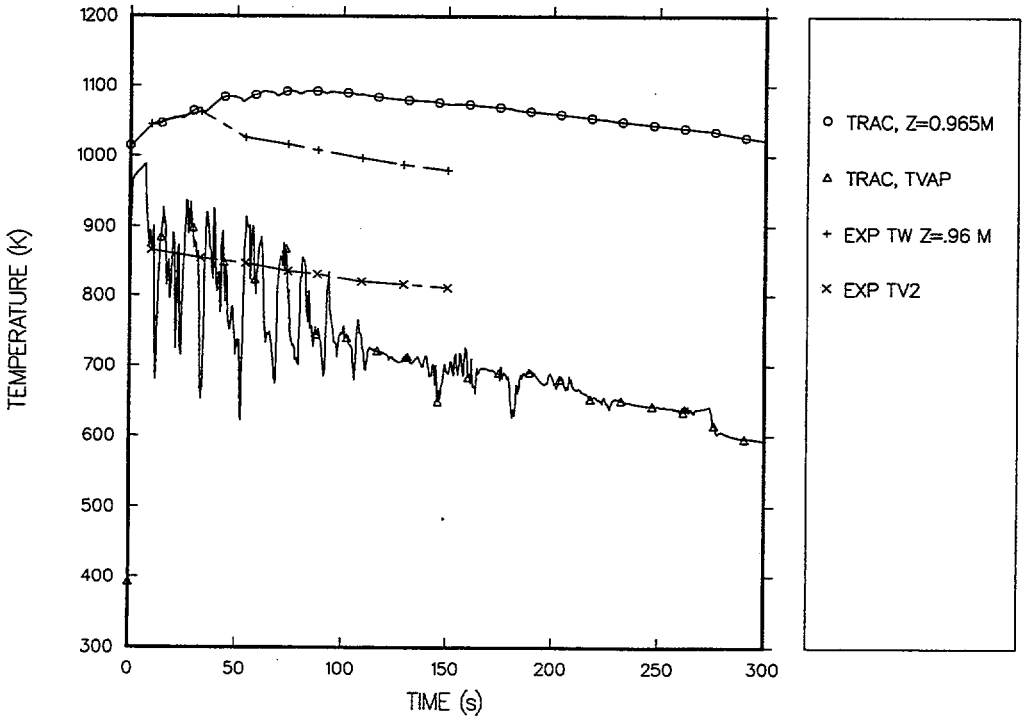

Fig. 4.4-25. Predicted wall and vapor-temperature histories at 96 cm (without grid spacer model).

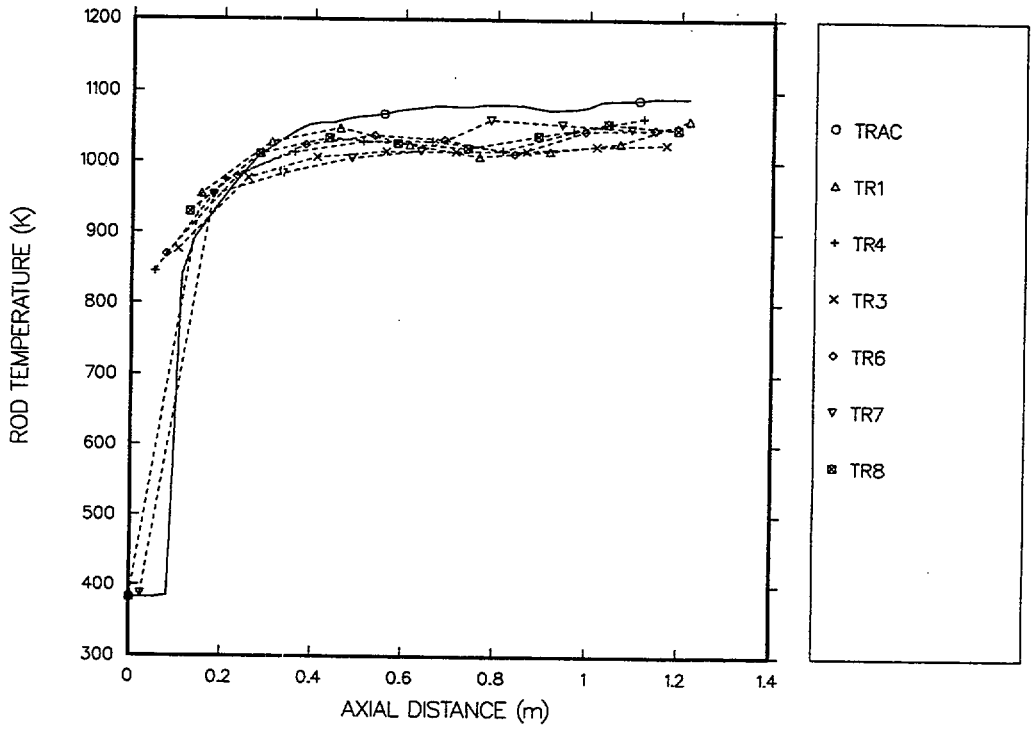

Fig. 4.4-26. Comparison of predicted and measured axial temperatures at 40 s (without grid spacer model).

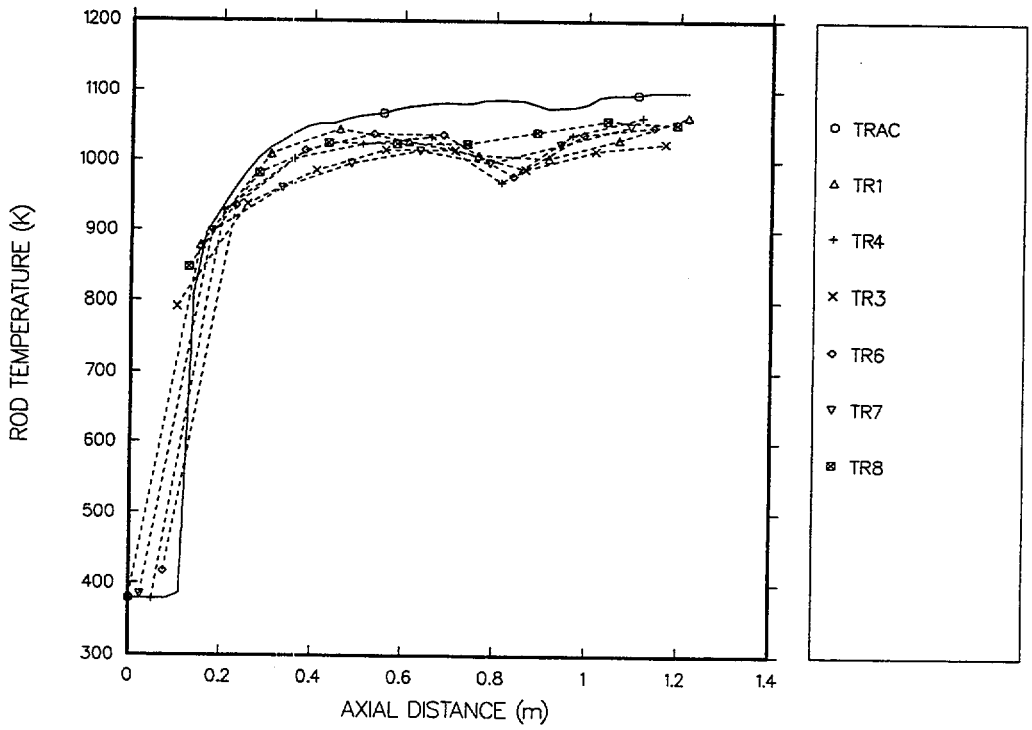

Fig. 4.4-27. Comparison of predicted and measured axial temperatures at 53 s (without grid spacer model).

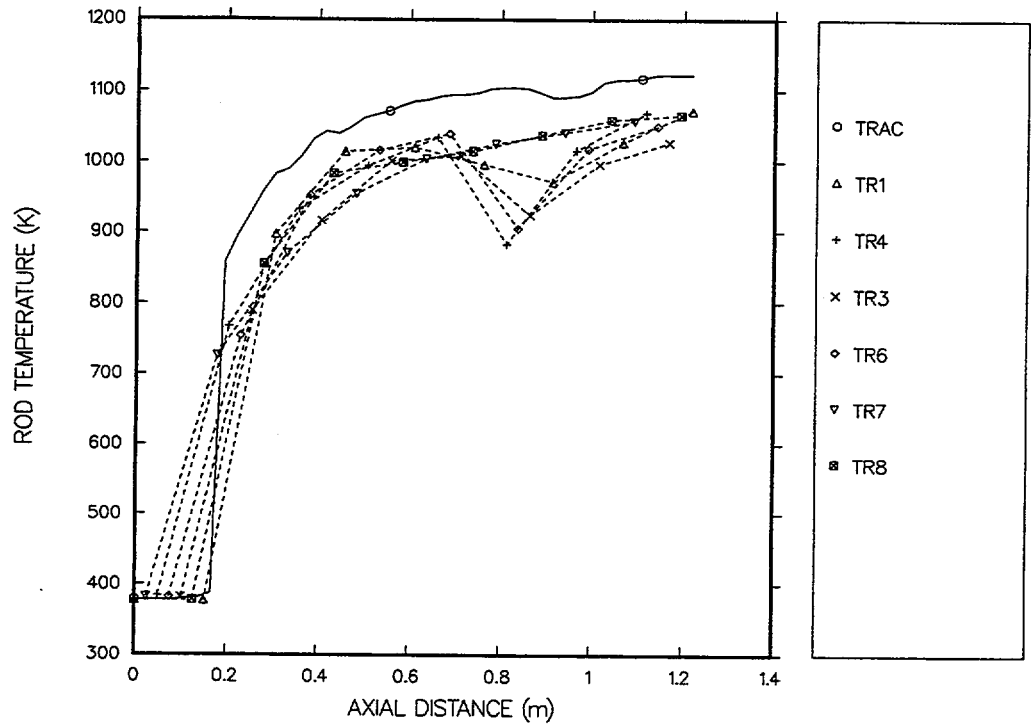

Fig. 4.4-28. Comparison of predicted and measured axial temperatures at 74 s (without grid spacer model).

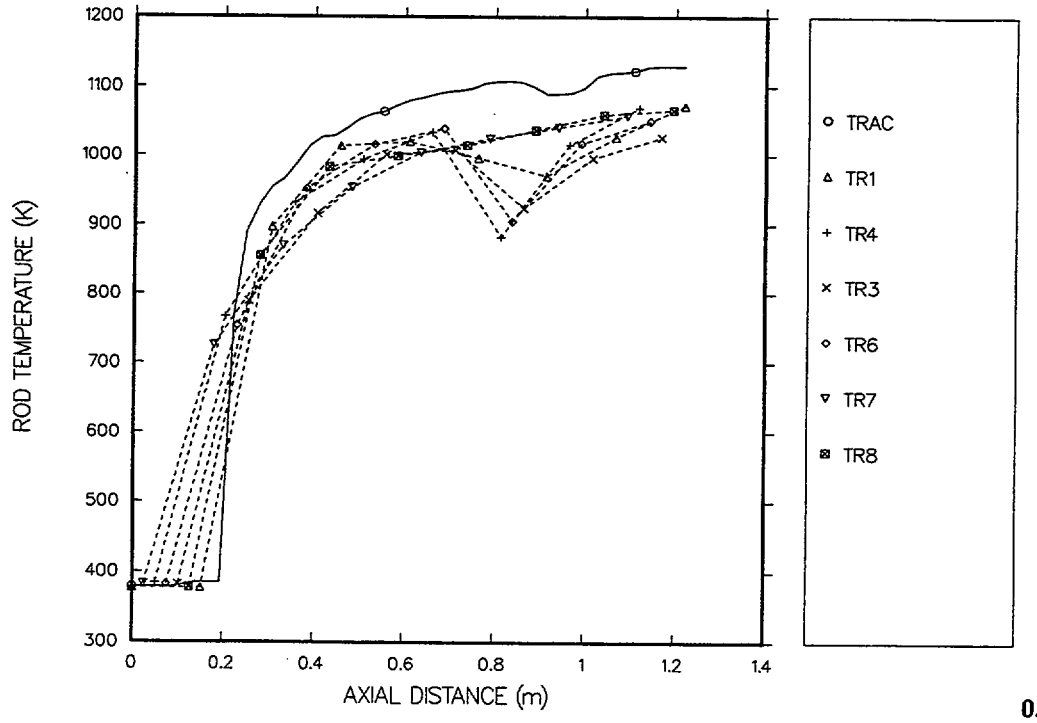

0.

Fig. 4.4-29. Comparison of predicted and measured axial temperatures at 94 s (without grid spacer model).

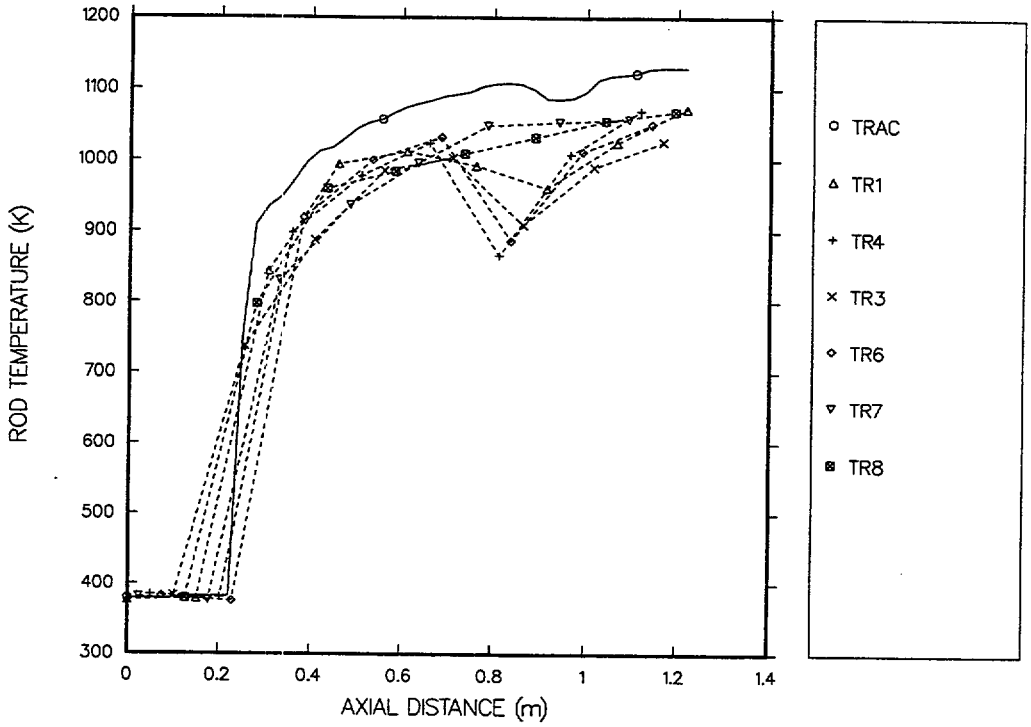

Fig. 4.4-30. Comparison of predicted and measured axial temperatures at 108 s (without grid spacer model).

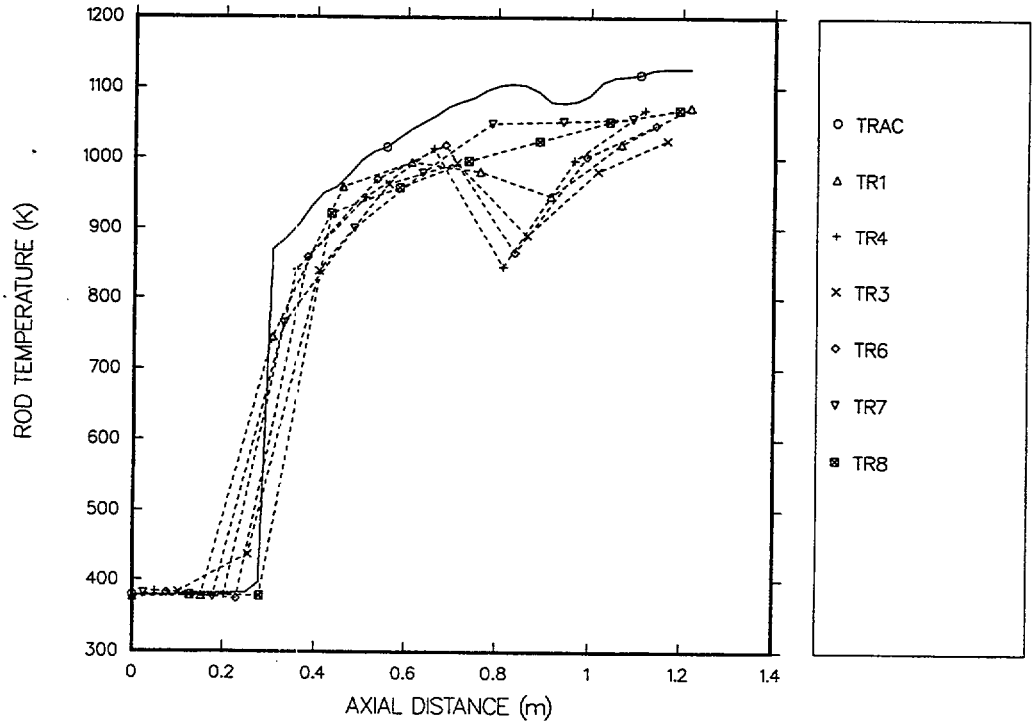

Fig. 4.4-31. Comparison of predicted and measured axial temperatures at 129 s (without grid spacer model).

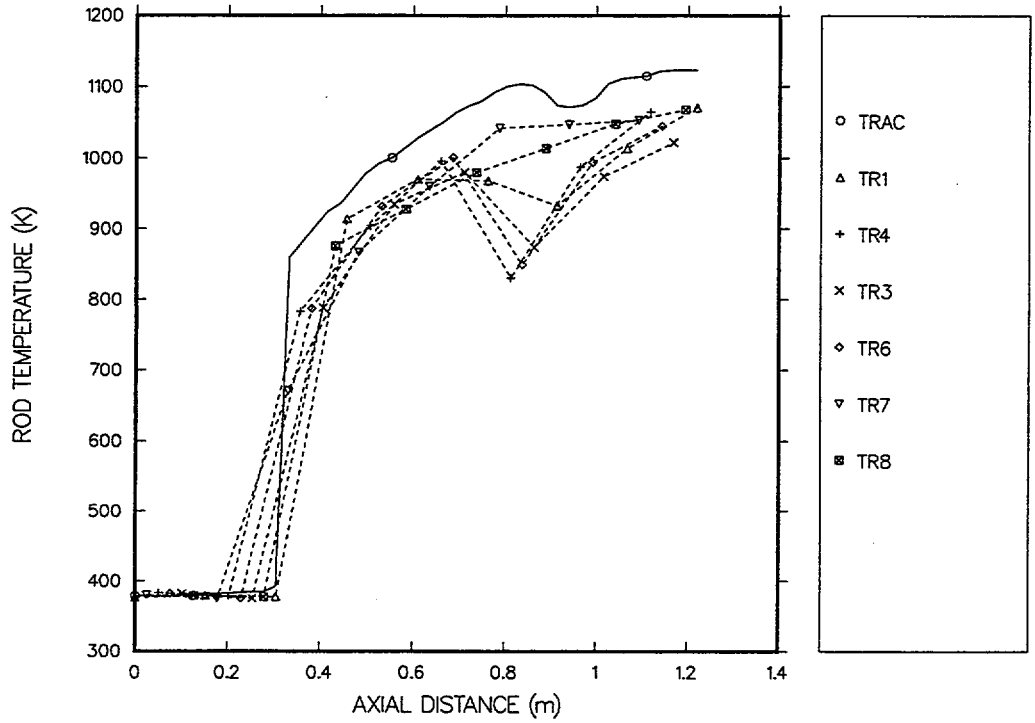

Fig. 4.4-32. Comparison of predicted and measured axial temperatures at 149 s (without grid spacer model).

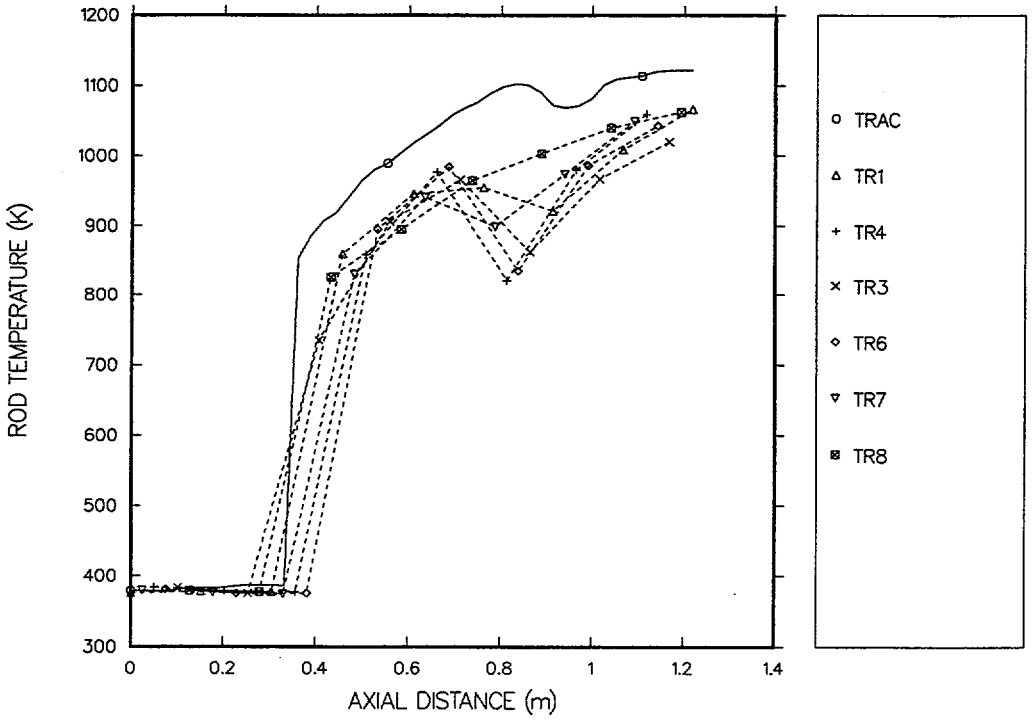

Fig. 4.4-33. Comparison of predicted and measured axial temperatures at 170 s (without grid spacer model).

4.5. Upper-Plenum Test Facility Cold-Leg Flow Test 8, Phase B, Part 1

4.5.1. Description of Test Facility

The Upper-Plenum Test Facility (UPTF), described in Ref. 4.5-1, is a full-scale model of a four-loop, 1300-MWe PWR, which includes the reactor vessel, downcomer, lower plenum, core simulation, upper plenum, and four loops with pump and steam-generator simulation. A flow diagram of the system and an overview of the test facility are shown in Figs. 4.5-1 and 4.5-2. Major dimensions of the facility are shown in Fig. 4.5-3 and a plan view of the test vessel is shown in Fig. 4.5-4. The thermal-hydraulic feedback of the containment is modeled using a containment simulator. The test vessel, core barrel, and internals are a full-size simulation of a PWR with four full-scale hot and cold legs modeling three intact loops and one broken loop. Both cold- and hot-leg breaks can be investigated with emergency core-coolant (ECC) injection into the intact- and broken-loop cold and/or hot legs and into the vessel downcomer. The steam produced in a real core and the liquid entrained by this steam flow are simulated by direct steam injection and by liquid presence in the core simulator. Steam production on the primary side of an intact steam generator is simulated by direct steam injection into each intact-loop steam-generator simulator.

4.5.2. Description of Test Procedures

UPTF Test 8 (Ref. 4.5-2) is a separate-effects test to investigate the thermal-hydraulic phenomena that occur in the loops of a PWR as a result of accumulator and low-pressure ECC liquid injection during end-of-blowdown, refill, and reflood phases of a postulated LOCA. Pressure and fluid oscillations can occur in the loops when induced by steam condensation on the ECC-injected subcooled liquid. In a reactor with cold-leg ECC injection, liquid plugs form in the cold leg when the ECC injection rate is large and when the liquid subcooling is large. The formation and movement of these plugs were predicted by TRAC before they were experimentally observed.

The goal of UPTF Test 8 was to investigate the loop flow pattern and to quantify the thermal-hydraulic boundary conditions that lead to pressure and flow oscillations in the loops where ECC liquid is injected. Test 8 consisted of two test runs or phases that differed only in the pump simulator flow resistance set in loop 2. In phase A (Run 112), the pump simulator K-factor was set to 10, and in phase B (Run 111), a K-factor of 18 was used; both referenced to a pipe diameter of 0.75 m. Each of the phases consisted of two parts: cold-leg ECC injection in Part 1 and hot-leg ECC injection in Part 2. The TRAC calculation presented herein models Part 1 of phase B, cold-leg ECC injection. The system test configuration for this test is depicted in Fig. 4.5-5. The flow parameters that determine liquid-plug formation and oscillation in loop 2 are of special interest in this test.

The hot-leg and cold-leg break valves of broken-loop 4 were both open. The loop-1 pump simulator was closed to model full blockage and no flow. The loop-2 and loop-3 pump simulators were set to a stroke of 108 mm (K factor of 18.0 for a 0.750-m pipe diameter) in an attempt to model partial blockage and to establish a 0.25-bar differential pressure between the upper plenum and downcomer. Broken-loop 4 had a throttle plate with an inner diameter of 0.411 m (K factor of 18.2 for a 0.750-m pipe diameter) installed in the 0.750-m diameter hot-leg pipe between the steam/water separator and break valve to simulate the flow resistance of a partially blocked pump.

Core-simulator steam injection was initiated at 23 s into the test with a 2-s ramp to 115.3 kg/s where it was then held constant at 115.3 kg/s for 200 s. No steam-generator-simulator steam injection took place during this test. The loop-2, cold-leg ECC injection was initiated at 27 s into the test with a 4-s ramp to 600 kg/s, where it was then varied through a series of 30-s time-interval steps shown in Table 4.5-1, starting at 600 kg/s and decreasing to 80 kg/s.

The transient conditions of UPTF Test 8, Phase B, Part 1, Run 111 (hereafter referred to as UPTF-8B) are shown in Table 4.5-2. Saturated steam was present throughout the primary system initially, except for liquid in the lower plenum, core, and downcomer of the vessel at a height of 4.2 m from the vessel bottom and in the intact-loop, steam-generator simulator, and broken-loop steam/water separator drains. Liquid was drained from the vessel shortly after core steam injection started to prevent the core from reflooding.

4.5.3. Description of the UPTF-8B Model

The TRAC model of the UPTF-experiment primary system used in this assessment is the TRAC-PF1/MOD1 code scalability, applicability, and uncertainty (CSAU) model. The vessel model for the MOD1 assessment contained 2 radial rings, 4 azimuthal sectors, and 13 axial levels. Several changes were made in the flow areas of the cells in the vessel for the MOD2 assessment. These changes were necessary because MOD2 requires that the user follow certain noding practices.

Noding diagrams for the TRAC model of the UPTF are shown in Figs. 4.5-6 to 4.5-14. The vessel axial noding is shown in Fig. 4.5-6. The vessel model consists of 13 axial levels, 4 azimuthal sectors, and 2 radial rings for a total of 104 computational cells. The azimuthal and radial noding distribution for the vessel is shown in Fig. 4.5-7. The core is represented by the inner ring, and the downcomer is represented by the outer ring.

Figures 4.5-8 to 4.5-10 show the noding for loops 1, 2, and 3. In each loop the hot leg is modeled with a Tee component; the steam-generator simulator is modeled with a combination of four Tee components and one Valve component; the crossover pipe, pump simulator, and cold leg are modeled with another Tee component. Steam injection into the top of the steam-generator simulator is modeled with Tee and Fill components. This Fill component can be controlled by the mass flow of liquid in the hot leg. The drain line from the bottom of the secondary side of the middle Tee to the steam-generator simulator inlet plenum is modeled with another Tee and Valve component. The pump simulator is modeled with a flow-area restriction and the correct volumes associated with the pump simulator component. ECC injection is modeled in both the hot and cold legs with the Tee and Fill components. The Fill components can invoke a time-dependent programmed ECC flow if desired. Loop-1 and loop-3 noding are identical. In loop 2, the pressurizer in the hot leg required the addition of an extra Tee component. This Fill also may use a preprogrammed-type steam flow.

Figures 4.5-11 and 4.5-12 show the broken-loop-4 hot- and cold-leg noding. The broken-loop cold-leg model is composed of a Valve component to model the main break Valve, a Tee component to model the bottom of the steam-generator simulator, and another Tee component to model the steam/water separator and piping to the

containment. The bottom of the steam-generator-simulator drain line is modeled to the drain tank Valve. This drain line drains off accumulated liquid during the course of the transient. The broken-loop hot leg is modeled with a Tee component for the hot leg, another Tee component for the steam-generator simulator, and a Valve component for piping run out to the containment tank. The containment tank is modeled with two Break components. These components provide a transient pressure boundary condition. Drain lines from the bottom of the vessel to the drain tank were completely modeled and are shown in Fig. 4.5-13.

The core steam/water injection sources are modeled by four individual Tee components shown in Fig. 4.5-14, each of which is connected to one of the four core cells at the vessel level 6. The Tee components are able to combine the steam input from a feedback injection with the preprogrammed steam/water input. The preprogrammed steam/water input was provided to Los Alamos National Laboratory (LANL) by Kraftwerk Union Atiengesellschaft (KWU). The walls between the UPTF injection zones are solid; therefore, TRAC incorporates a zero flow area in the radial and azimuthal direction at level 6. Because the steam is injected in the radial direction at this level, it will impact the walls and lose its radial momentum. To model this effect in the TRAC input, we directed the steam/water injection sources radially.

The feedback steam injection is calculated using a complex feedback logic controller shown in Fig. 4.5-15. Each of the four calculational vessel cells incorporates a separate feedback logic controller, as shown in the figure. A total of eight separate control blocks is required to calculate the amount of feedback steam to inject. These controllers calculate the steam flow generated based on a breakthrough at the tie plate above the particular cell. The effects of the decay heat and the remaining stored energy in the simulated bundle also are taken into account.

The UPTF-8B input model was updated to correct the vessel drainage simulation. In the previous TRAC UPTF-8B model, an attempt was made to control and modulate the vessel drain valve opening so that the calculated core liquid level would match the measured core liquid level. This approach was not successful in that the calculated liquid level did not match the measured core liquid level; also, it was not correct in simulating the actual drain valve operation because it depended on knowing beforehand the measured core liquid level. We do not know how the vessel drain valve was operated or controlled during the test. However, judging from the measured vessel drain mass flow data that are given in Ref. 4.5-2 and shown in Fig. 4.5-16, it appears that the drain valve was ramped open at a linear rate from 25 to 40 s, kept open at a constant position from 40 to 160 s, and then ramped closed at a linear rate from 160 to 190 s. To simulate the measured vessel drain flow, the UPTF-8B model was modified by replacing the vessel drain valve and its pressure boundary with a Fill component that modeled the measured mass flow drained from the vessel (Fig. 4.5-16). The void fraction input for the downcomer also was adjusted so that the predicted downcomer liquid level would match the measured downcomer liquid level at the start of the transient calculation.

A listing of the input model used for this developmental assessment calculation is found in Appendix G. Archival storage information for this input model is found in Section 4.5-8.

4.5.4. Comparison of Predicted and Measured Results

During the initial high ECC injection period of the test, a liquid plug is formed in the loop-2 cold leg. The liquid plug is located in the pipe between the loop-2 ECC injection port and the vessel downcomer. The liquid plug has sufficient liquid-steam interfacial area because the plug breaks up into slugs of liquid to condense the upstream steam flowing through loop 2 from the vessel upper plenum to the downcomer. An oscillation occurs as the plug moves to cover and uncover the ECC injection port. When the injection port is covered, the liquid-steam interfacial area and the steam-condensation rate are significantly reduced in the vicinity of the injection port. With a reduced steam-condensation rate in the cold leg, the approximate 30-kPa differential pressure between the upper plenum and downcomer moves the liquid plug toward the downcomer. This uncovers the ECC injection port, significantly increasing the liquid-steam interfacial area and the steam-condensation rate near the injection port. This reduces the upstream steam pressure in the vicinity of the ECC injection port, causing the liquid plug to move back and cover the injection port, which then starts this oscillatory cycle over again.

As the ECC injection rates are reduced, the liquid-steam interfacial area and liquid subcooling become insufficient to condense all the steam flowing toward the downcomer. When this situation occurs, the flow regime in the cold leg switches from a plug flow regime with highly dispersed ends to a stratified flow regime with significantly reduced liquid-steam interfacial area. The data indicate that an oscillatory-plug flow regime occurs in the loop-2 cold leg only for the injection rate of 600 kg/s during which period large amplitude oscillations are predicted. For the reduced injection rates, there is little or no oscillatory flow behavior predicted.

The TRAC-predicted and -measured vessel-downcomer pressures are shown in Fig. 4.5-17. These pressures are in agreement partly because this measured pressure was used to define the approximate time-dependent average behavior of the containment pressure given in Table 4.5-3. The initial pressure pulse from 23 to 30 s is due to the core-simulator steam injection occurring before ECC injection. The TRAC-predicted and measured pressures are oscillatory from 30 to 60 s during the ECC injection rate of 600 kg/s. The amplitude of the TRAC-predicted pressure oscillations are larger than that observed in the data. The pressure rise after 125 s is due to the core-simulator steam injection that is not fully condensed by the ECC liquid in stratified flow at injection rates below 250 kg/s.

The TRAC-predicted and -measured vessel-upper-plenum pressures are shown in Fig. 4.5-18. For the 600 kg/s ECC injection rate from 30 to 60 s, the TRAC-predicted vessel-upper-plenum pressure decreases, whereas the measured vessel-upper-plenum pressure remains approximately constant. At this high ECC injection rate, it appears that TRAC predicts a higher condensation rate of steam in the loop-2 cold leg than when measured. Thereafter at lower ECC injection flow rates, both pressures rise together. At ECC injection flow rates of 250 kg/s and below, during stratified flow of ECC liquid, it appears that the TRAC-predicted steam-condensation rate is slightly lower than measured, causing a slightly higher pressure difference between the vessel upper plenum and downcomer, as shown in Fig. 4.5-19.

The TRAC-predicted and -measured steam flows in loops 2 and 3, at the top of the loop

seal component just after the steam-generator simulator, are shown in Figs. 4.5-20 and 4.5-21. The flow at this loop location is steam that comes from the core-simulator steam injection into the vessel. At the 600-kg/s ECC injection rate, the TRAC-predicted flows appear to oscillate with a larger amplitude but with a frequency similar to that of the measured data. At ECC injection rates of 400 kg/s and 250 kg/s, the TRAC oscillatory amplitude is smaller than exhibited by the data. At ECC injection rates of 150 kg/s and below, both TRAC and the data indicate no significant oscillations. The TRAC-predicted mass flows for both loops are larger than the measured mass flow. This may be due to higher condensation rates predicted by TRAC.

Figure 4.5-22 shows the TRAC-predicted steam volume fraction in cells 17 to 21 of component 24 in the loop-2 cold leg between the ECC injection port and the vessel downcomer, respectively. During oscillatory-plug flow from 30 to 60 s, we observe that TRAC predicts only momentary filling of these mesh cells with liquid (when the void fraction goes to zero). That repeatedly filled condition occurs only for a fraction of a second in cell 17 where ECC liquid is injected, the time that subsequent cells are filled increases to as much as 10 s for cells 20 and 21. This indicates that TRAC predicts that the liquid that fills the cold-leg pipe cross section is made up of liquid slugs after injection where the length is no longer than the respective 1.5-m and 1.9-m lengths of mesh cells 17 and 18. As these liquid slugs with trapped steam between them oscillate in the pipe, they move progressively toward cell 21 and the vessel downcomer. Steam trapped between the slugs continues to condense and, when fully condensed, results in adjacent slugs combining into a longer liquid slug. The net effect is for ECC injected at cell 17 to flow down the loop-2, cold-leg pipe to the vessel downcomer in an oscillatory chugging fashion with liquid-slug lengths becoming longer as trapped steam condenses.

ECC liquid flows into the vessel downcomer and raises the liquid level in both the downcomer and core regions of the vessel. The ~30 kPa pressure difference between the downcomer and upper plenum of the vessel keeps the liquid level in the downcomer ~3.3 m above the liquid level in the core. To keep the vessel from reflooding, the vessel is drained. The TRAC-predicted liquid level and the actual liquid-height data in the core region are shown in Fig. 4.5-23. The predicted and actual liquid levels in the downcomer are shown in Fig. 4.5-24. The predicted liquid levels in the core region followed the measured liquid levels reasonably well but at a higher level because the calculated initial decrease in the liquid level did not match the measured decrease. There is closer agreement between the predicted and measured levels for the downcomer.

The initial decrease in the core liquid level cannot be accounted for by the measured drain mass flow given in the data report. The calculated core liquid level should have matched the measured core liquid level because the measured vessel drain mass flow was modeled. The initial decrease in core liquid level also occurs a few seconds earlier than what is predicted using the measured drain mass flow. One plausible explanation for this difference is that there may be some air trapped in the vessel drain lines at the start of the test. The initial opening of the vessel drain valve then would have allowed the vessel to drain very rapidly in the first few seconds, but without any indication from the mass-flow measurement system until the liquid reached the valve.

Another loss-of-coolant inventory from the system is the steam-mass flow into the containment simulator (modeled by two Break components on the ends of the hot and cold legs of broken-loop 4). Figure 4.5-25 shows the TRAC-predicted steam-mass flow exhausted into those Break components. It also shows the measured and TRAC input-specified steam-mass flows injected into the vessel by the core simulator. The difference between the injected and exhausted steam-mass flows approximately represents the steam-condensation rate that occurs primarily in the loop-2 cold leg.

In Fig. 4.5-26, the loop-2, cold-leg, Stalk 6 thermocouple fluid temperatures are plotted with the TRAC-predicted liquid and vapor temperatures. On the stalk, six thermocouples extend from the top to the bottom of the cold-leg pipe. Stalk 6 is located on the pump-loop-seal side of the ECC injection port. The thermocouple and TRAC temperatures are oscillatory during the 600-kg/s ECC injection rate from 30 to 60 s, respectively. The amplitude of the TRAC temperature oscillations appears to be larger than that of the measured data. We should not expect the same dynamic response from the measurement and the calculation because the data essentially are measurements of the fluid temperature in a small volume located a finite distance upstream from the ECC injection port and TRAC is the volume-averaged fluid temperature of the entire mesh cell on the pump-loop-seal side of the injection port.

In Fig. 4.5-27, the loop-2, cold-leg, Stalk 5 thermocouple fluid temperatures are plotted with the TRAC-predicted liquid and vapor temperatures. Stalk 5 is located on the downcomer side of the ECC injection port. The amplitude and frequency of the temperature oscillations at the 600- to 400-kg/s ECC injection rates from 30 to 90 s compare quite well with the data. The TRAC oscillatory amplitude at the 250-kg/s ECC injection rate from 90 to 120 s is smaller than that of the data. The TRAC subcooled liquid temperature is ~20 K below the measured temperatures when the ECC injection rates changed from 600 to 250 kg/s. This indicates that the loop-2, cold-leg TRAC condensation rate is too low at these high ECC injection rates. At 200 kg/s, the flow has become stratified and the top five thermocouples measure the steam temperature. The sixth thermocouple appears to measure the liquid temperature at the bottom of the pipe. At the last two hold points of 150- to 80-kg/s ECC injection rates, the TRAC-predicted liquid temperature and the sixth-thermocouple measured temperature are somewhat consistent, indicating that TRAC and the data exhibit a stratified-flow condition.

In Fig. 4.5-28, the Stalk 4 thermocouple fluid-temperature data are plotted with the TRAC-predicted liquid and vapor temperatures. Stalk 4 is between Stalk 3 (next to the downcomer) and Stalk 5 (next to the ECC injection port). The TRAC subcooled-liquid temperature is ~10 K above the measured temperatures from 30 to 90 s. As the liquid slugs flowed from the Stalk 5 to Stalk 4 location, the thermocouple temperatures cooled by ~5 K, whereas the TRAC-predicted liquid temperature warmed by ~5 K because of condensation of the trapped steam. The Stalk 4 sixth-thermocouple measured temperature in the bottom of the pipe is comparable to the TRAC-predicted liquid temperature during the last four hold points of 250- to 80-kg/s ECC injection rates from 90 to 210 s, indicating a stratified-flow condition.

In Fig. 4.5-29, the Stalk 3 thermocouple fluid-temperature data are plotted with the TRAC-predicted liquid and vapor temperatures. Stalk 3 is in the loop-2 cold leg nearest

to the downcomer/cold-leg connection. The Stalk 3, as well as Stalk 4, thermocouple data support the earlier observations that at high ECC injection rates of 250 to 600 kg/s, TRAC predicts more condensation than measured because its liquid subcooled temperatures are 5 to 10 K above the measured temperatures. At the low ECC injection rates of 80 to 200 kg/s, both TRAC and the data indicate stratified flow in the loop-2, cold-leg pipe with subcooled liquid at the bottom and saturated steam at the top of the pipe. In stratified flow, the lowest thermocouple temperatures are comparable to the TRAC-predicted liquid temperature, indicating that the TRAC condensation rate in the cold leg is consistent with the UPTF-8B experiment under stratified-flow conditions.

4.5.5. Lessons Learned and User Guidelines

Although the model used in TRAC for liquid-plug formation and movement is relatively simple, it apparently captures the dominant phenomena. However, we expect it to be sensitive to changes in spatial noding of the TRAC input-data model. Therefore, because the UPTF is a full-scale experimental facility, we recommended that all US PWR calculations use node sizes similar to the 1 to 2-m cell lengths used to analyze the loop-2 cold leg of this test. The general guideline used for noding the cold legs of the UPTF-8 TRAC model was to keep the length-to-diameter (L/D) ratio for cells between the ECC injection port and the vessel downcomer at ~2.0. However, the last cold-leg pipe cell that connects to the downcomer should have an L/D of ~0.8..

4.5.6. Conclusions

We compared the measured data from UPTF Test 8B part 1 and the predicted results from a TRAC-M/F77 transient calculation. The results of that comparison indicate that TRAC does a reasonable job of predicting cold-leg plugging and thermal-hydraulic oscillation, which in the test were driven by core-simulator steam injection and cold-leg ECC injection. The TRAC-predicted vessel upper-plenum pressure agreed reasonably well with the measured pressure, which indicated that the cold-leg steam-condensation rate is approximately correct. For high ECC injection rates, the frequency and amplitude of the oscillations in pressure, mass flow, and temperature were predicted reasonably well by TRAC. Whereas the plotted data show oscillations with less amplitude, the data are suspect and may have been time averaged because Ref. 4.5-4 shows the data in Fig. 4.5-19 oscillating with an amplitude four times greater. For low ECC injection rates of 80 to 400 kg/s, the transition to stratified flow was accurately predicted by TRAC. At the ECC injection rate of 400 kg/s, TRAC made the transition to stratified flow somewhat earlier than indicated by the measured data so that the TRAC-predicted amplitude of the oscillation was lower than the data during that transition.

4.5.7. Code Performance

The corrected UPTF Test 8B part 1 problem was calculated with TRAC-M/F77 code Version 5.5. The run performance information plus other pertinent comments are

Code Version 5.5

Platform	Sun Enterprise 3000
Total CPU time (s)	16164
Archive location of input model	CFS /tida/f77da/task4.4bdecks/inuptf8b.corr
Archive location of calculation	CFS /trac-da/F77DA/task4.4b/uptf8b.corr.tar.gz

REFERENCES

4.5-1. SIEMENS AG, UB KWU, "UPTF: Program and System Description," Report No. U9 414/88/023 (November 1988).

4.5-2. SIEMENS AG, UB KWU, "Upper Plenum Test Facility (UPTF) Test No. 8 Cold/Hot Leg Flow Pattern Test U9 316/88/11," Quick-Look Report (September 1988).

4.5-3. H. J. Stumpf, "Posttest Analysis of UPTF Test 08 Using TRAC-PF1/MOD2," Los Alamos National Laboratory document LA-CP-90-373 (September 6, 1990).

4.5-4. SIEMENS AG, "2D/3D Program Upper Plenum Test Facility, Test No. 6, Downcomer Countercurrent Flow Test U9 316/89/2," Quick-Look Report (March 1989).

TABLE 4.5-1

LOOP-2 ECC LIQUID-INJECTION BOUNDARY CONDITIONS

TIME (s)	LIQUID-INJECTION MASS FLOW (kg/s)
0–27	0.0
31–61	600.0
62–91	400.0
92–121	250.0
122–151	200.0
152–181	150.0
182–211	80.0
212–225	0.0

TABLE 4.5-2

TRANSIENT CONDITIONS

PARAMETERS	VALUE
Vessel and containment initial pressure	375.0 kPa
Vessel lower-plenum liquid level	2.4–4.2 m
Steam-generator-simulator steam injection	0.0 kg/s
Core-simulator steam injection	0.0–115.3 kg/s
Core-simulator steam temperature	416.1 K
Loop-2, cold-leg ECC liquid injection	0.0–600.0 kg/s
Loop-2, cold-leg ECC liquid temperature	311.0 K
Loops 1 and 3 cold-leg ECC liquid injection	0.0 kg/s
Loops 1, 2, 3, and 4 hot-leg ECC liquid injection	0.0 kg/s
Loop-1 fully blocked pump K factor	infinity
Loop-2 partially blocked pump K factor	18.0
Loop-3 partially blocked pump K factor	18.0
Broken-loop-4, throttle-plate K factor	18.2
Broken-loop-4, hot- and cold-leg break valves	open

TABLE 4.5-3

CONTAINMENT-SIMULATOR PRESSURE BOUNDARY CONDITIONS

TIME (s)	PRESSURE (kPa)
23.0	375.0
24.0	375.0
26.0	405.0
32.0	390.0
88.0	390.0
225.0	400.0

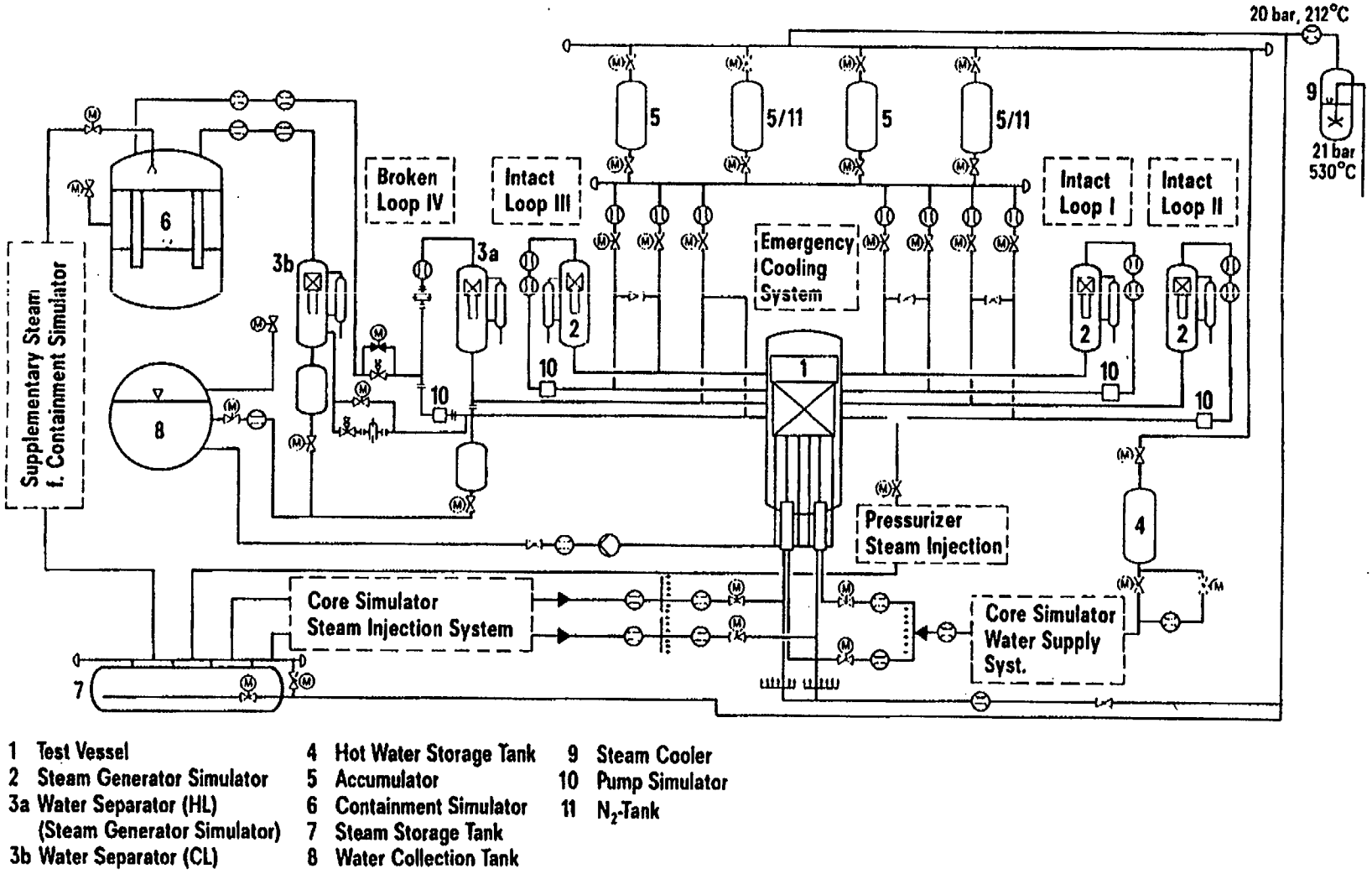

Fig. 4.5-1. UPTF flow diagram.

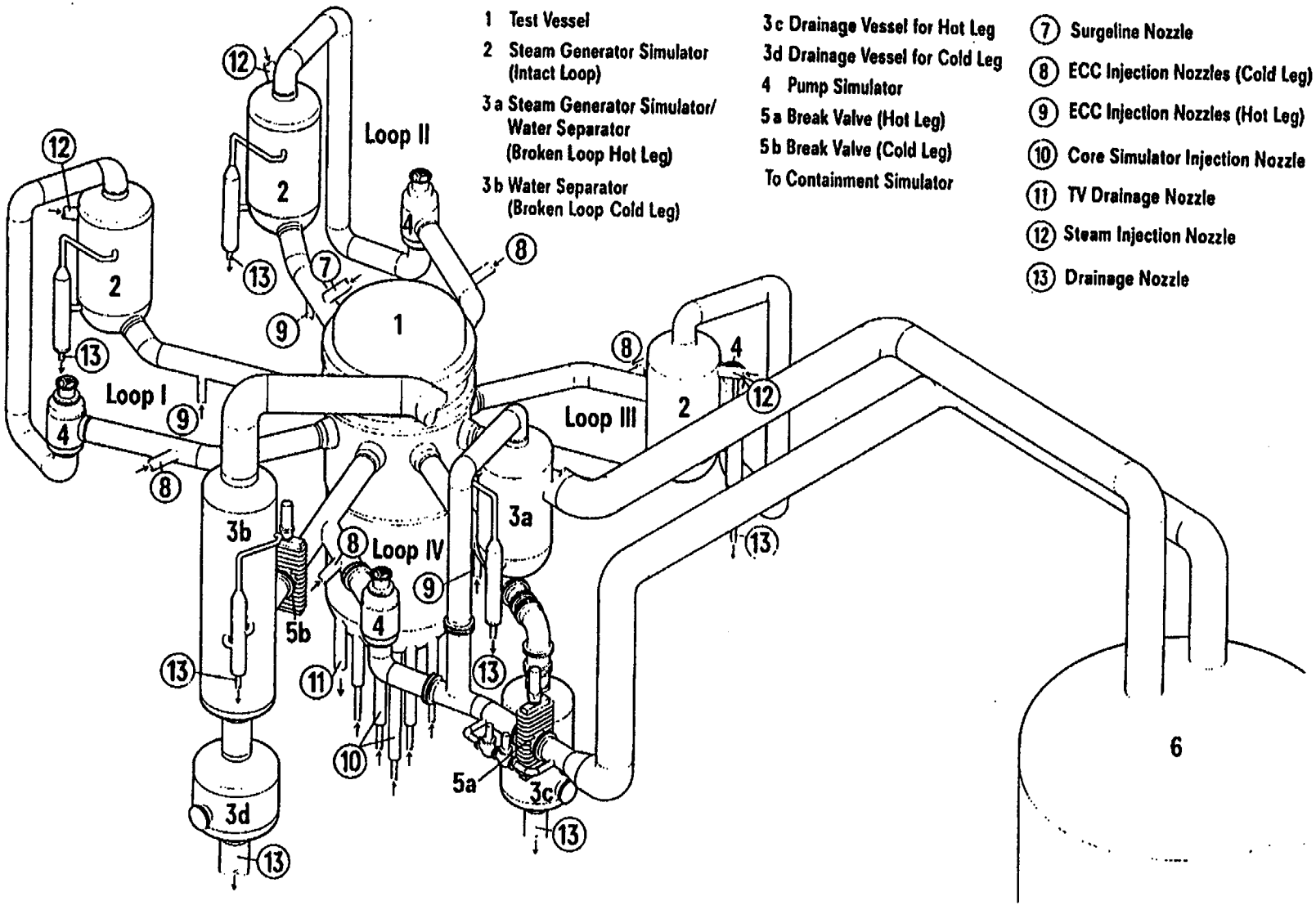

Fig. 4.5-2. Overview of UPTF primary system.

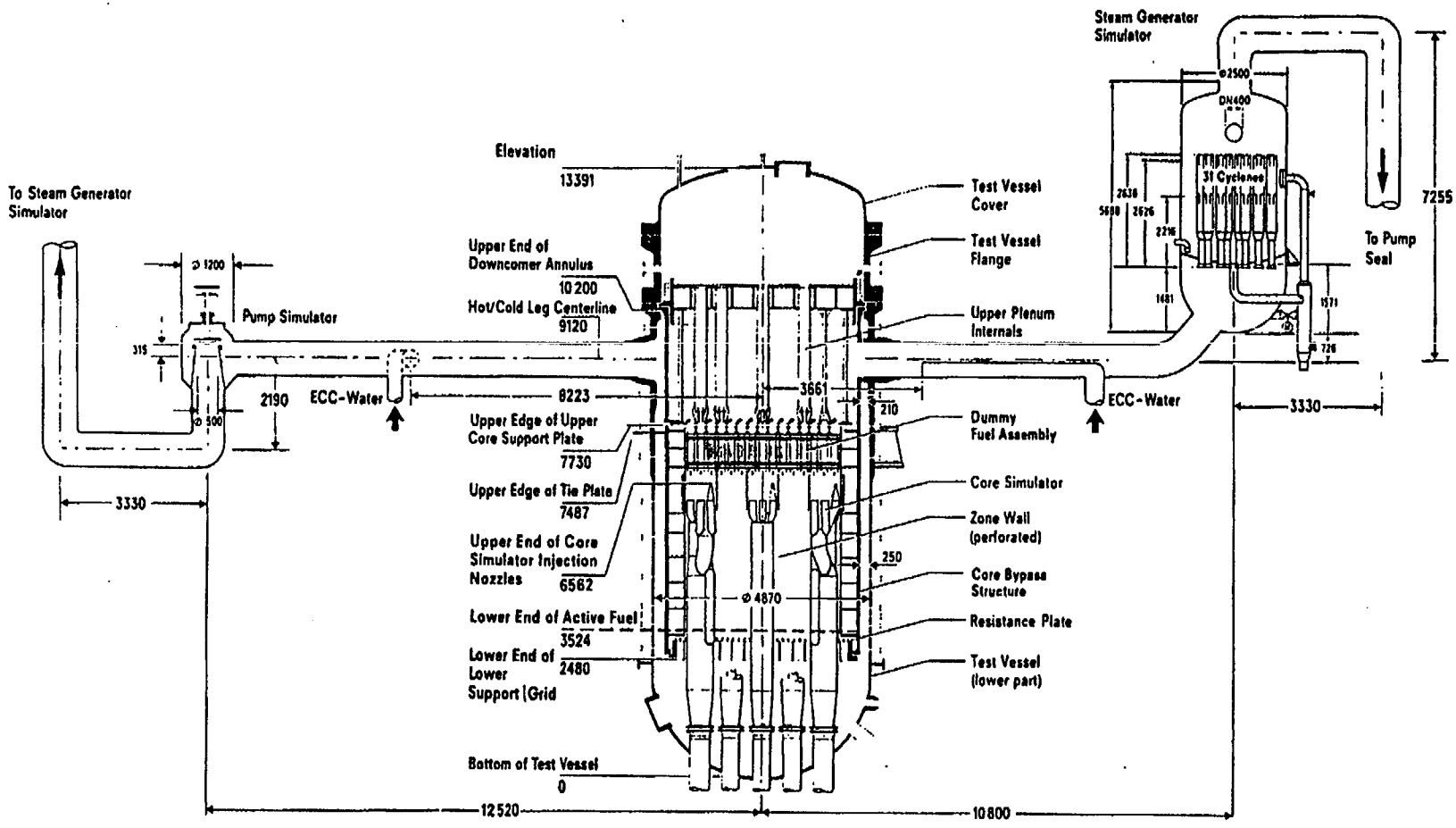

Fig. 4.5-3. Major dimensions of the UPTF primary system.

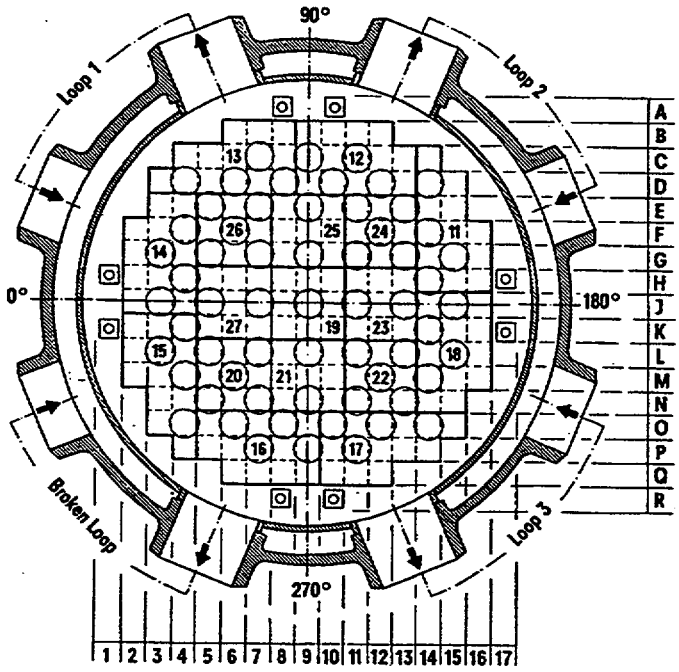

Fig. 4.5-4. Plan view of UPTF test vessel.

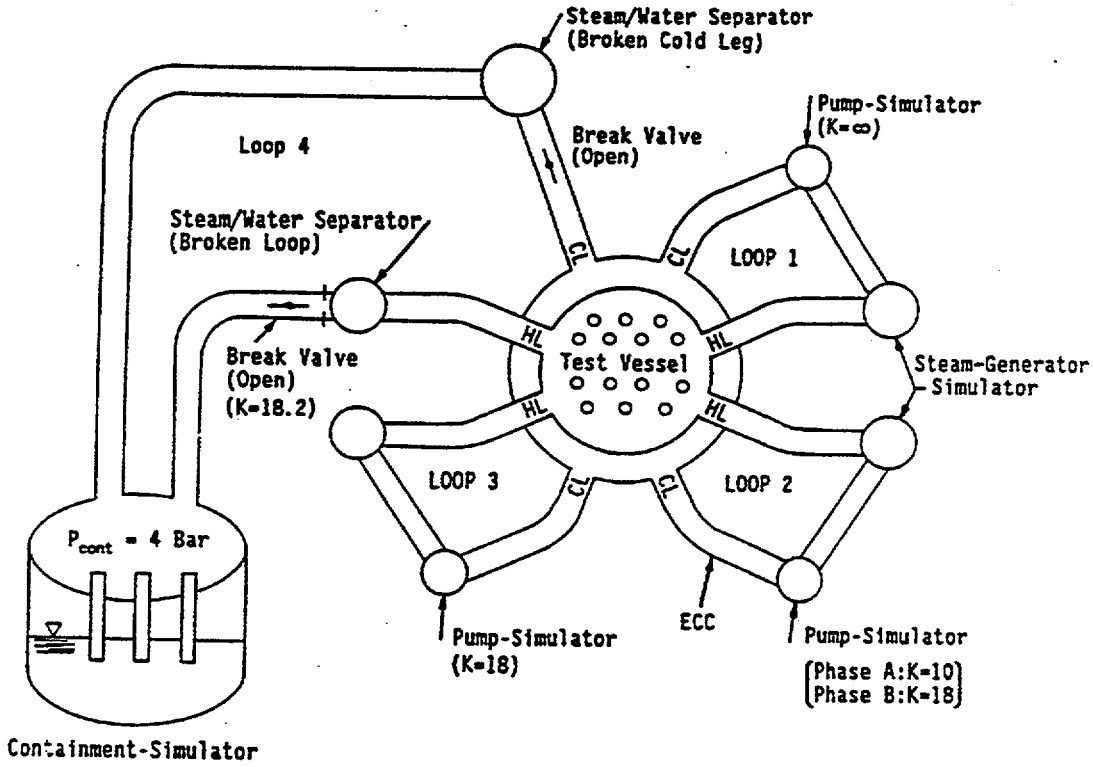

Fig. 4.5-5. System configuration for UPTF Test 8, Part 1.

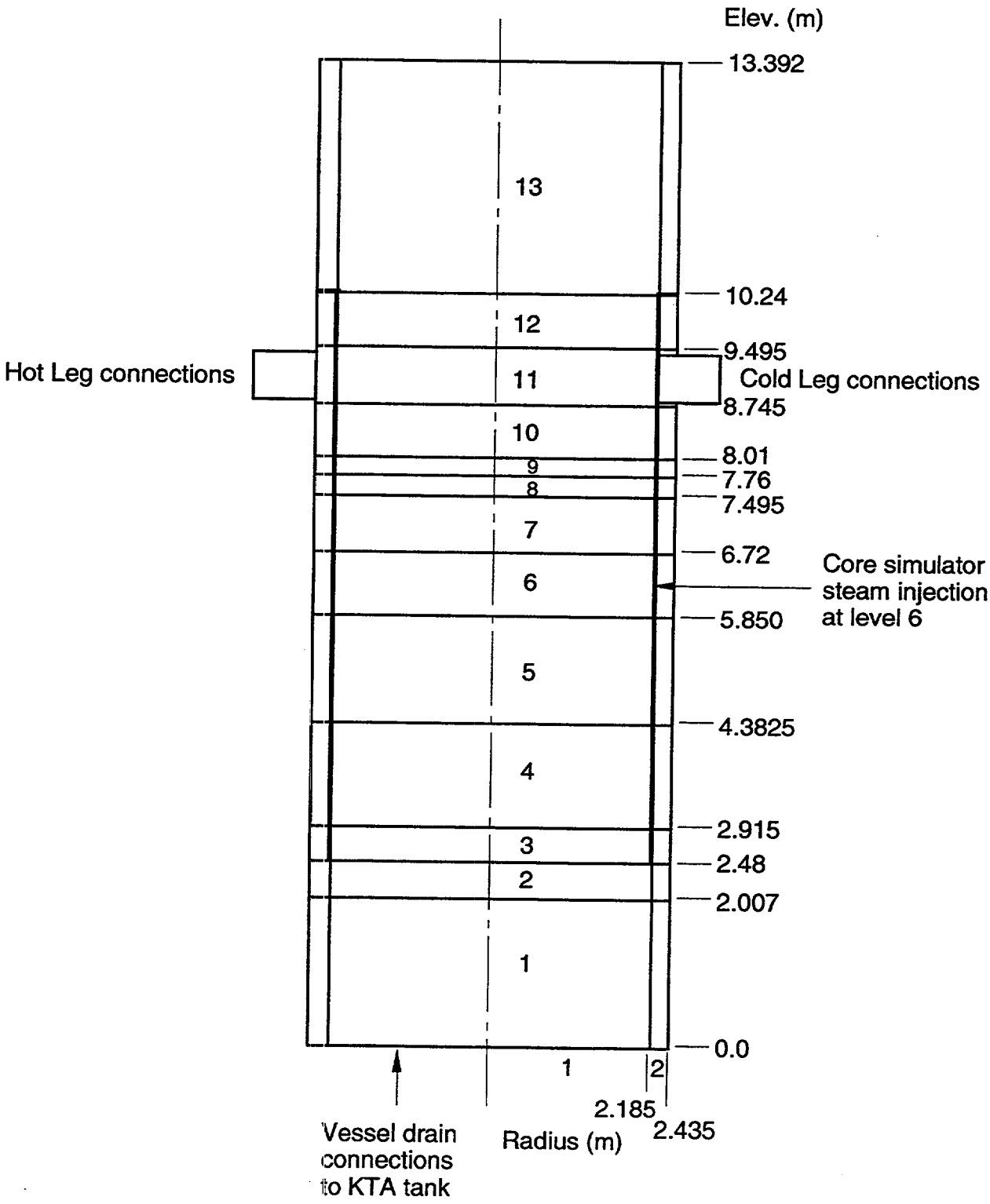

Fig. 4.5-6. UPTF-8B vessel model elevation view.

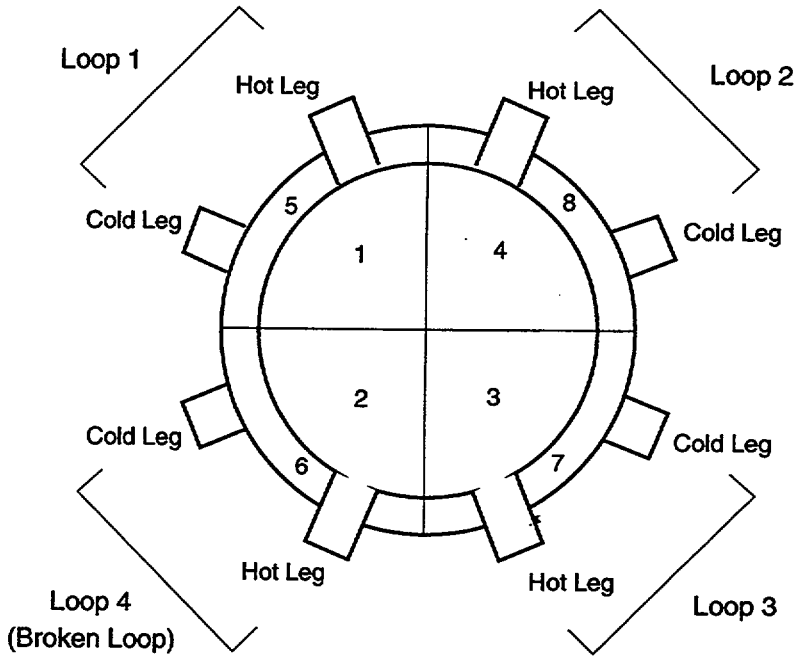

Fig. 4.5-7. UPTF-8B vessel model plan view.

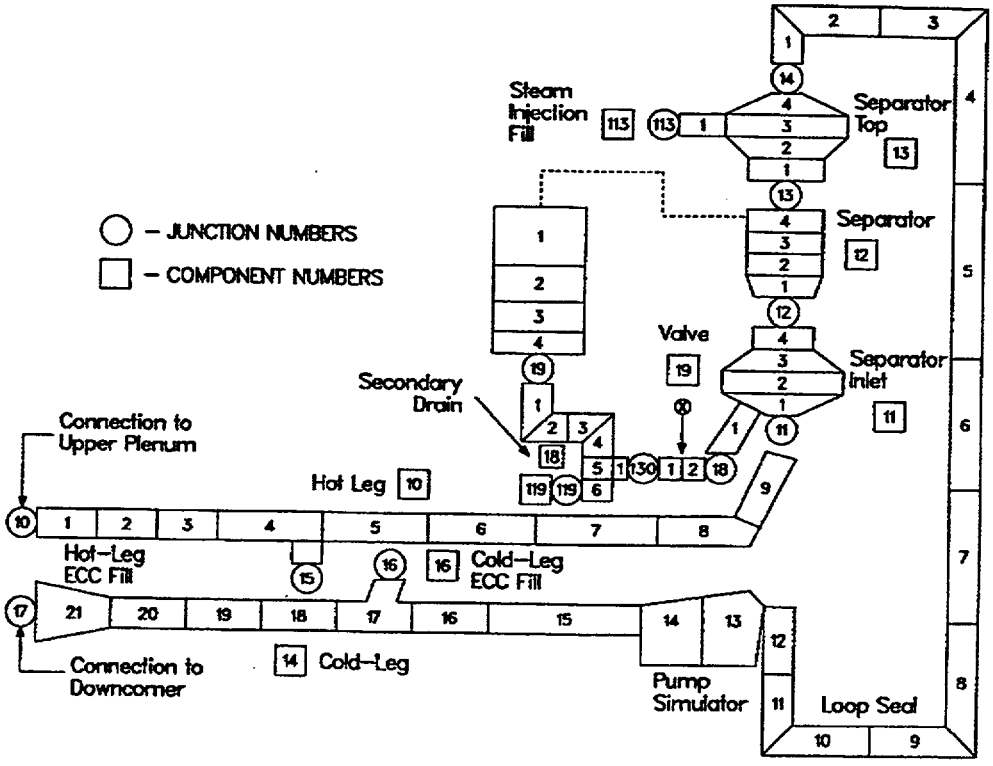

Fig. 4.5-8. UPTF loop-1 noding diagram.

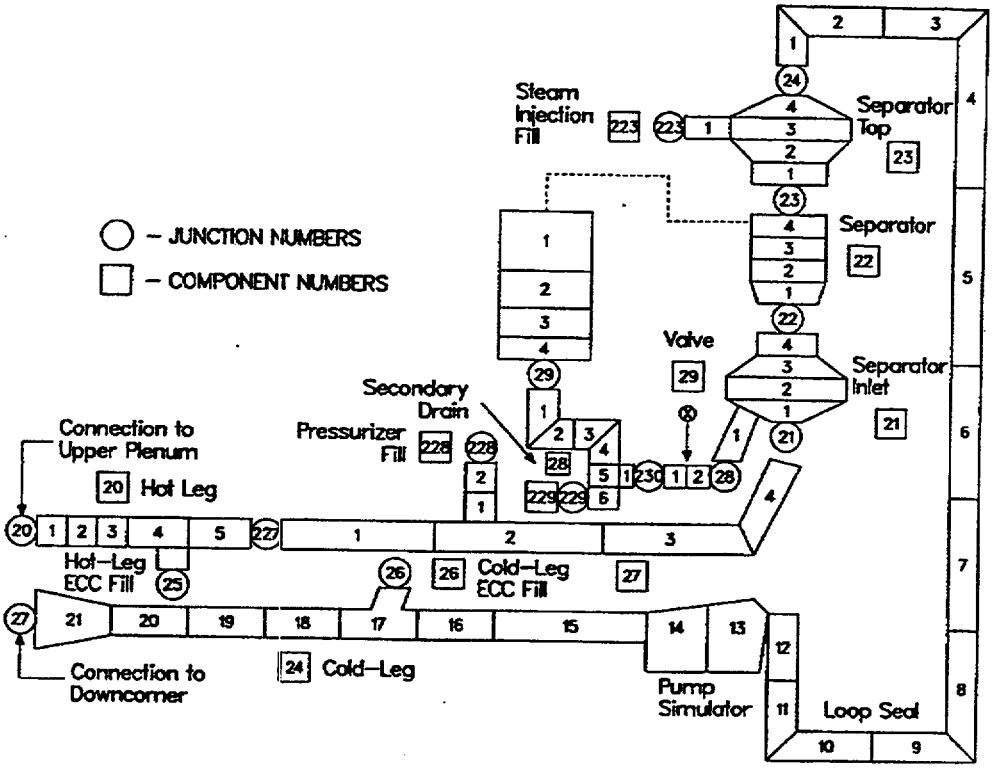

Fig. 4.5-9. UPTF loop-2 noding diagram.

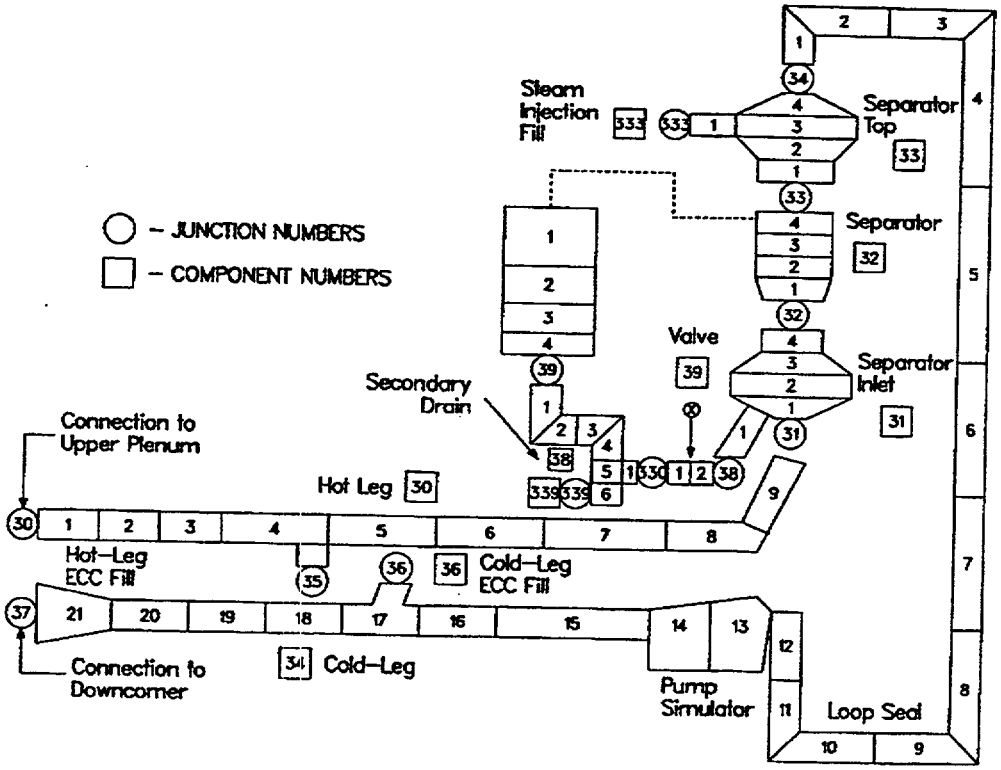

Fig. 4.5-10. UPTF loop-3 noding diagram.

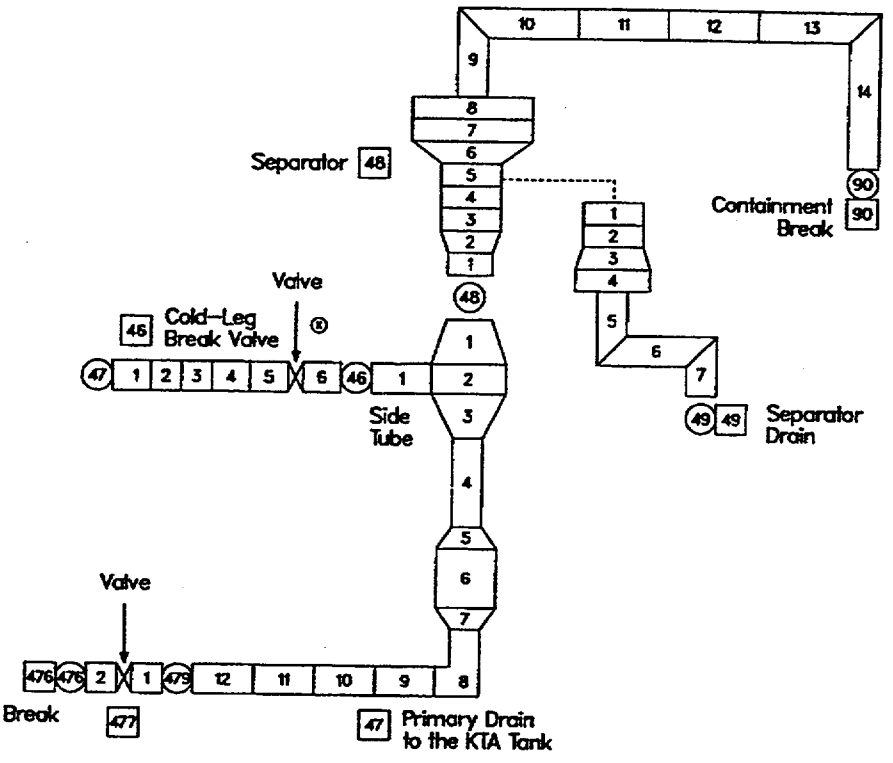

Fig. 4.5-11. UPTF broken-loop-4, cold-leg noding diagram.

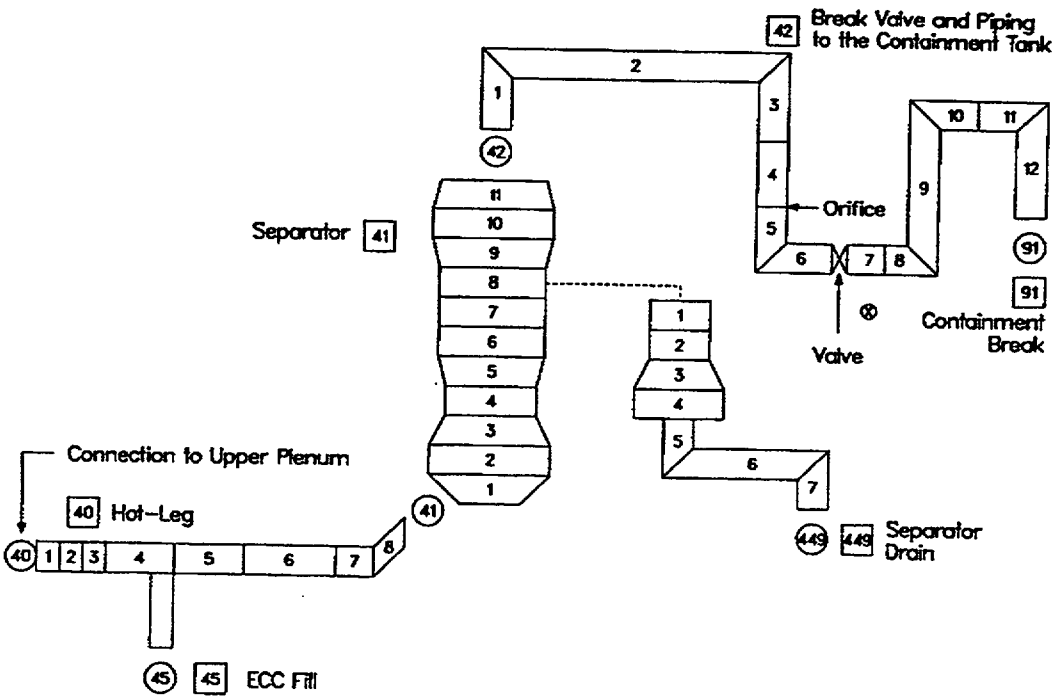

Fig. 4.5-12. UPTF broken-loop-4, hot-leg noding diagram.

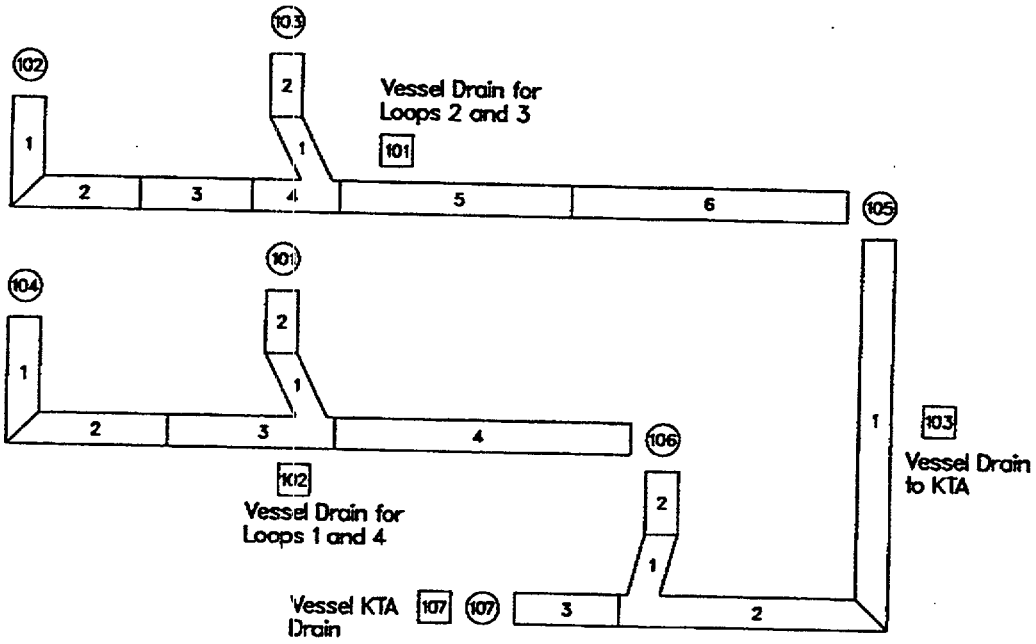

Fig. 4.5-13. UPTF water drainage system noding diagram.

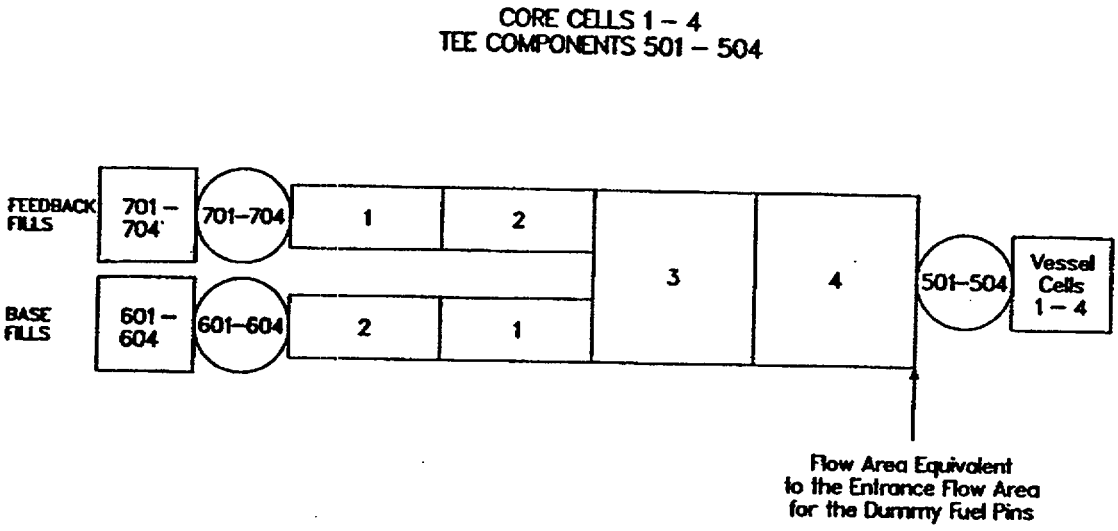

Fig. 4.5-14. UPTF core-simulator-injection noding diagram.

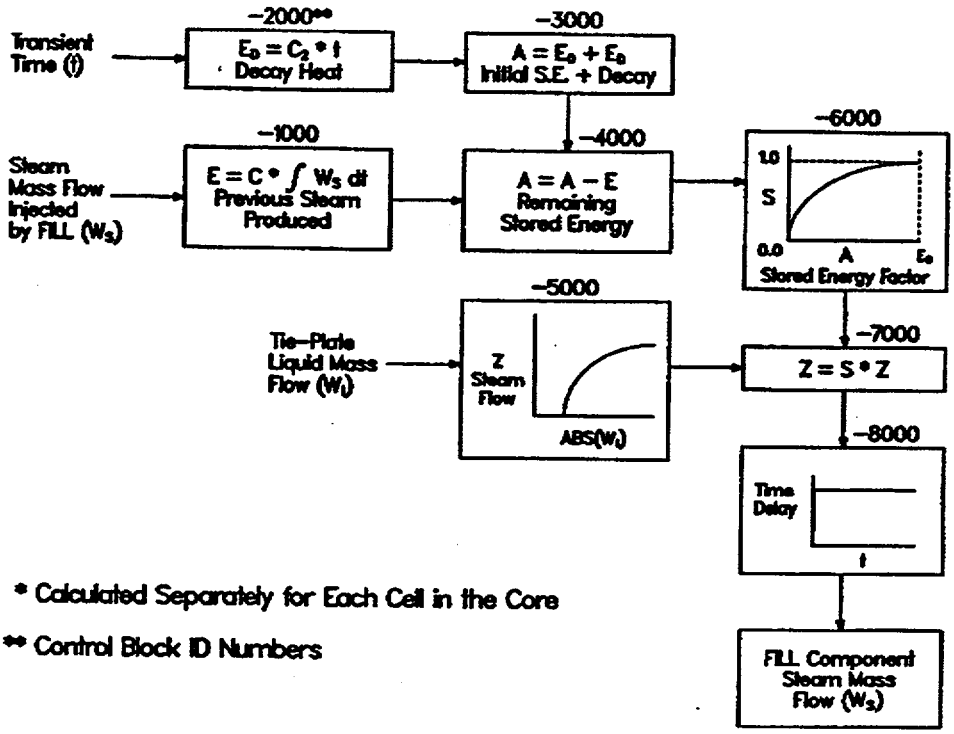

Fig. 5.4-15. Steam feedback logic-controller model.

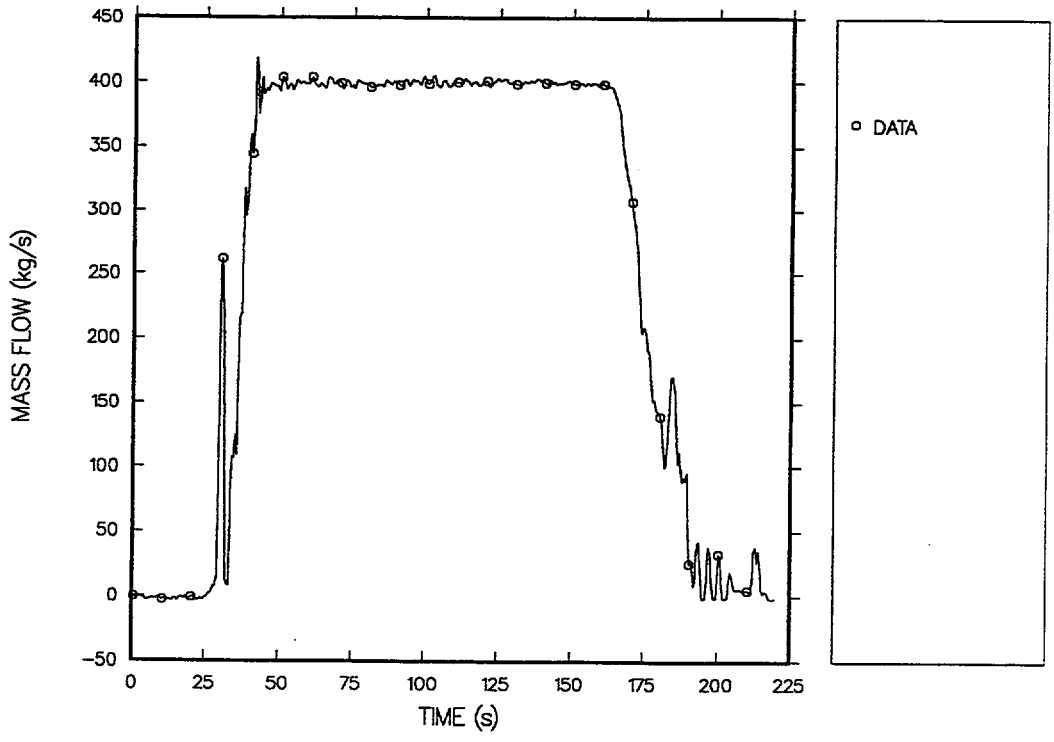

Fig. 4.5-16. Measured liquid mass flow drained from the vessel.

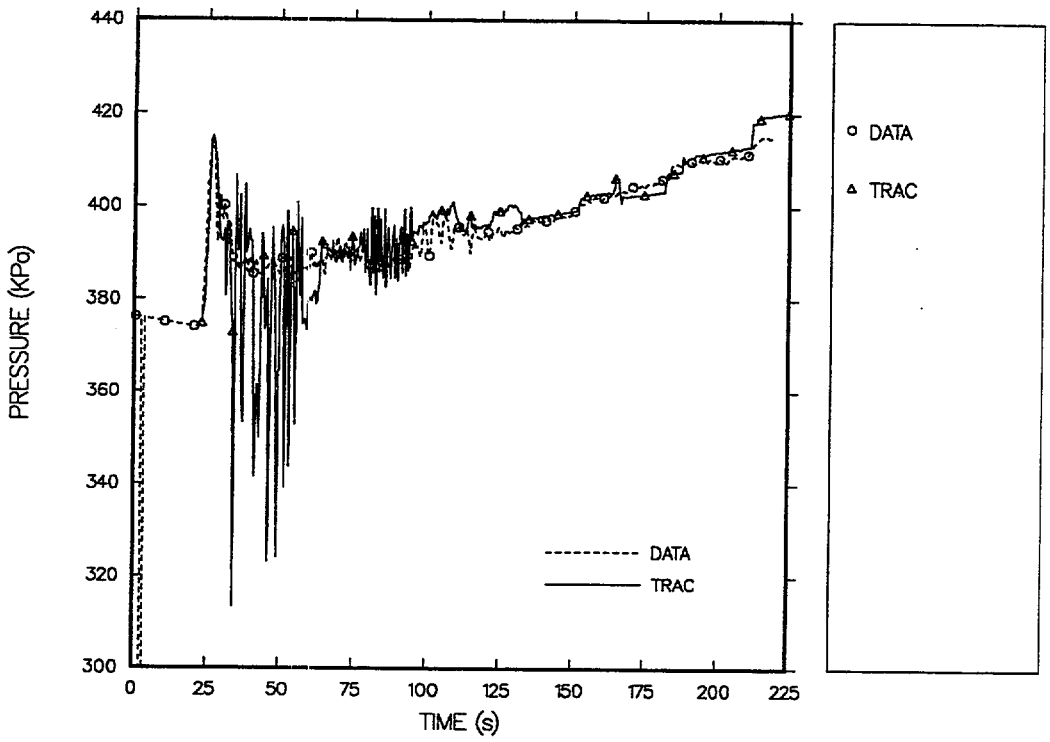

Fig. 4.5-17. Vessel downcomer pressure.

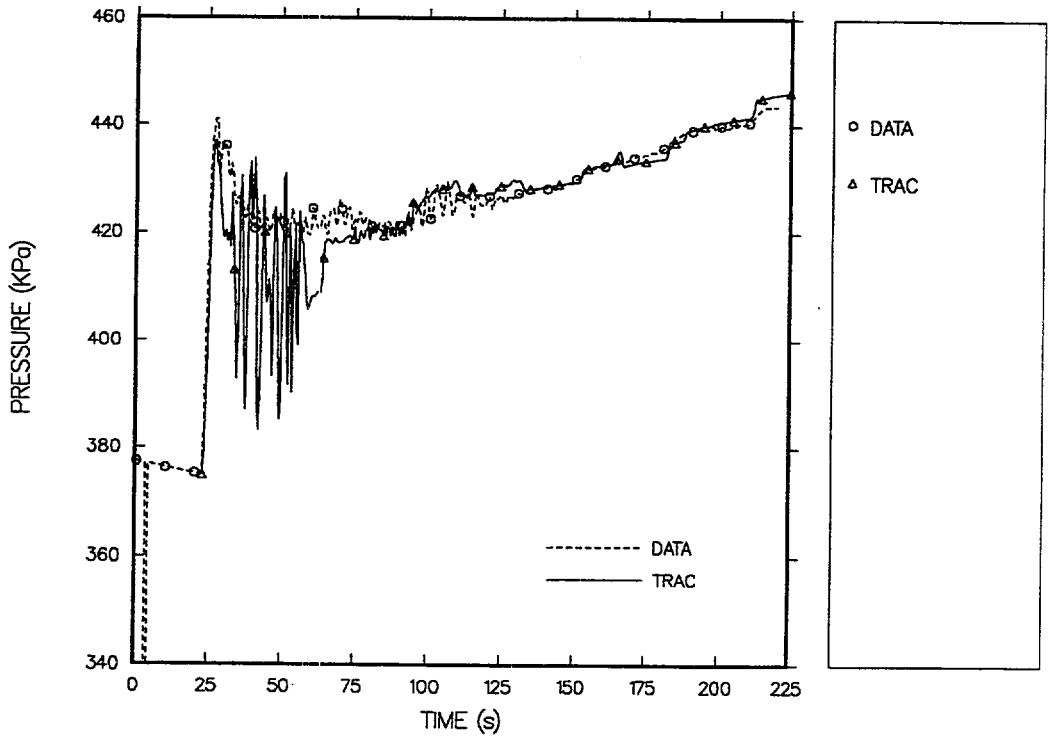

Fig. 4.5-18. Vessel upper-plenum pressure.

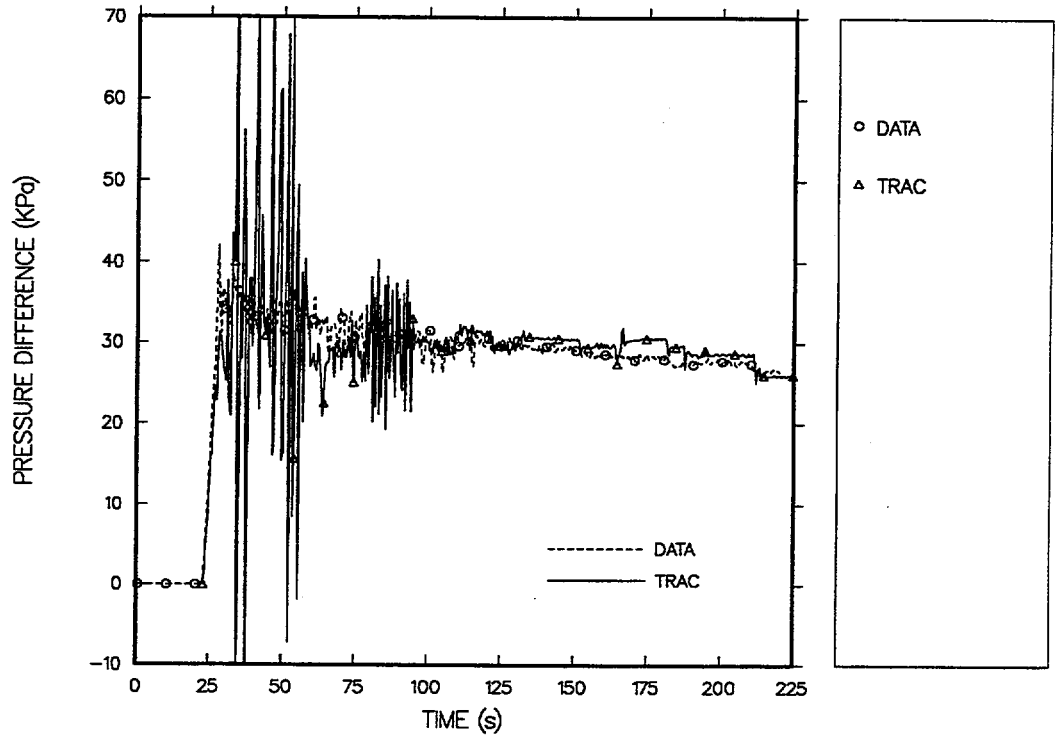

Fig. 4.5-19. Pressure difference between vessel upper plenum and downcomer.

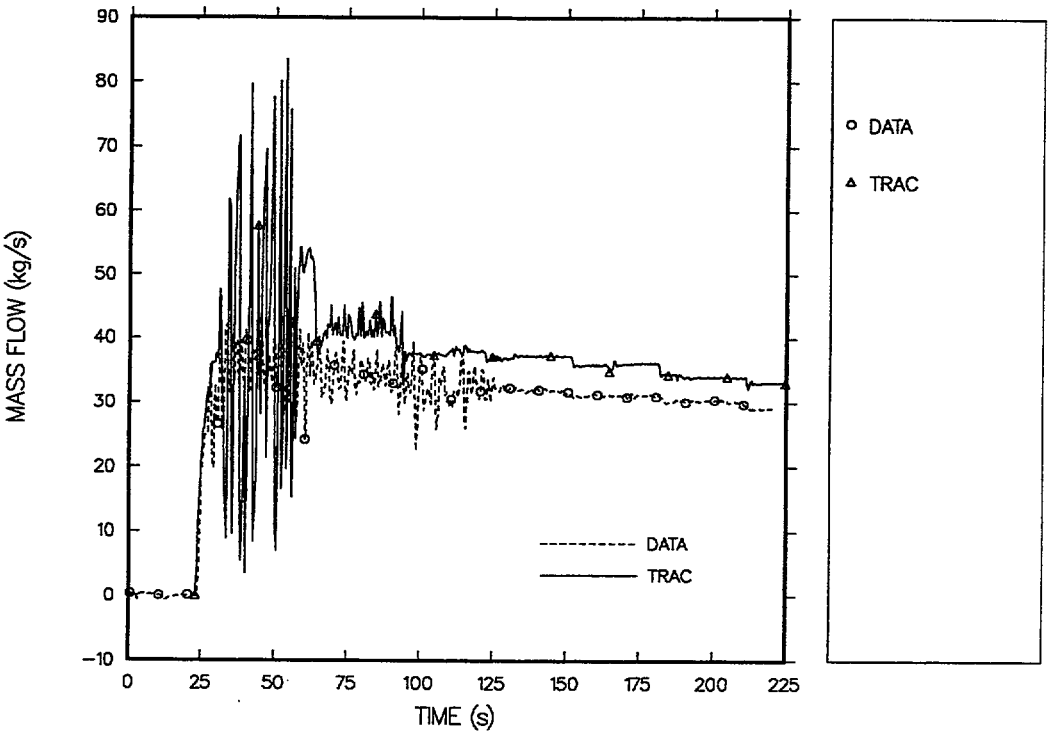

Fig. 4.5-20. Steam flow in loop 2 at the top of the loop seal downstream of the steam generator simulator.

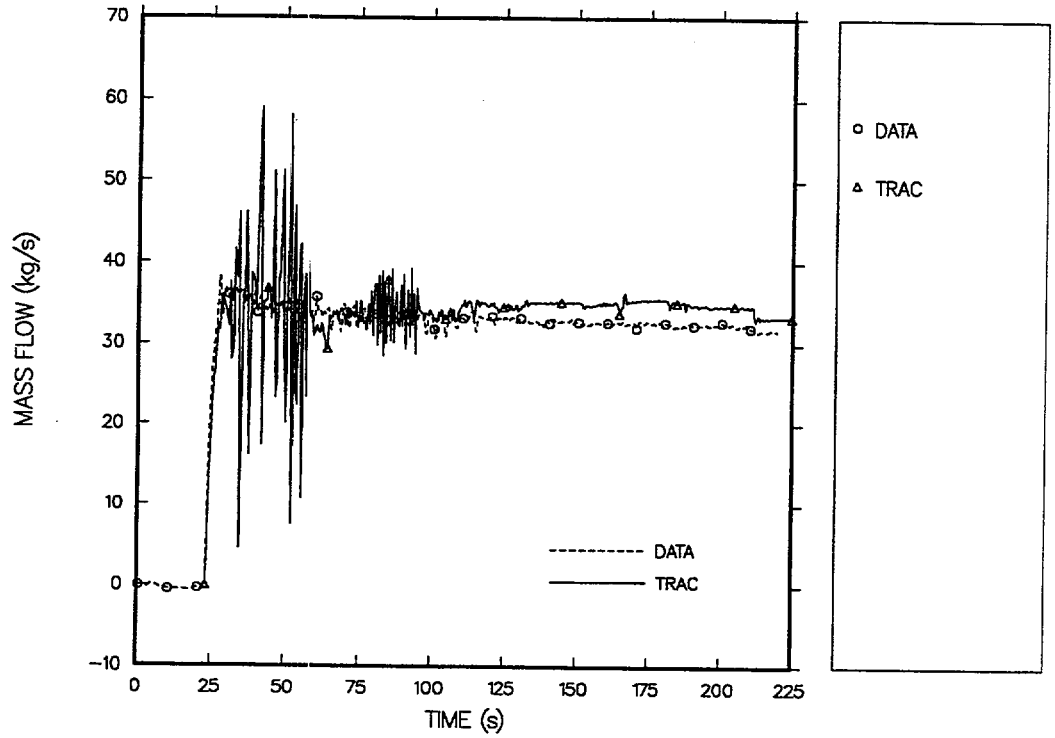

Fig. 4.5-21. Steam flow in loop 3 at the top of the loop seal downstream of the steam generator simulator.

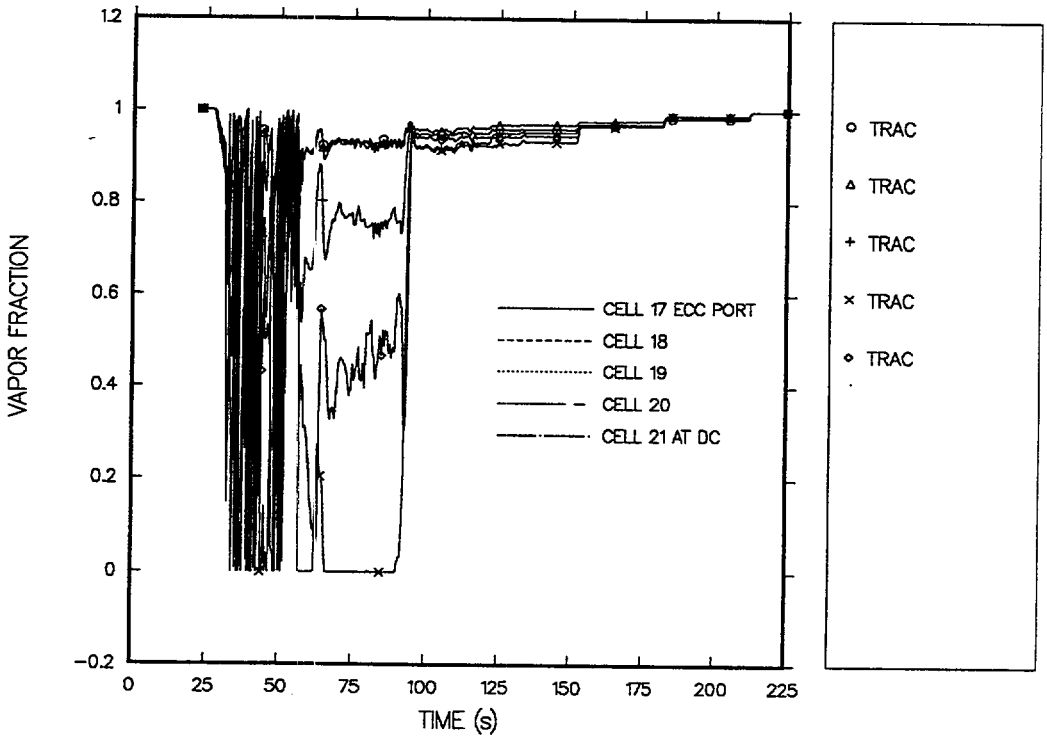

Fig. 4.5-22. Loop-2, cold-leg pipe: TRAC-predicted steam volume fraction between the ECC injection port and vessel downcomer.

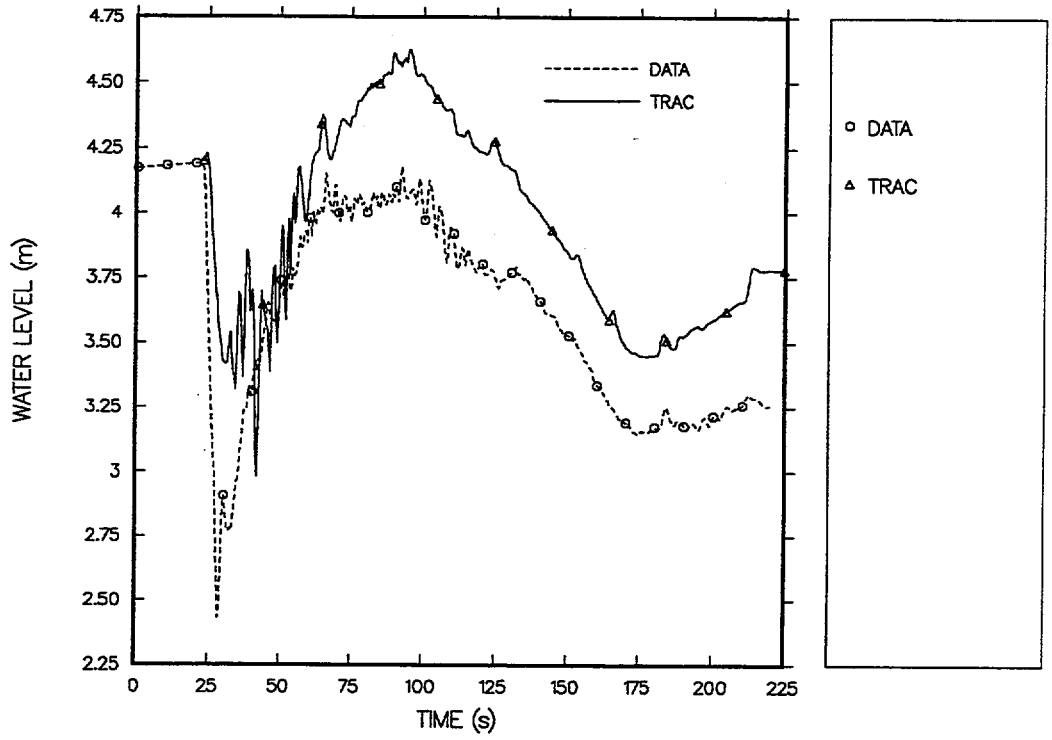

Fig. 4.5-23. Liquid height in the core region of the vessel from UPTF-8B data and TRAC.

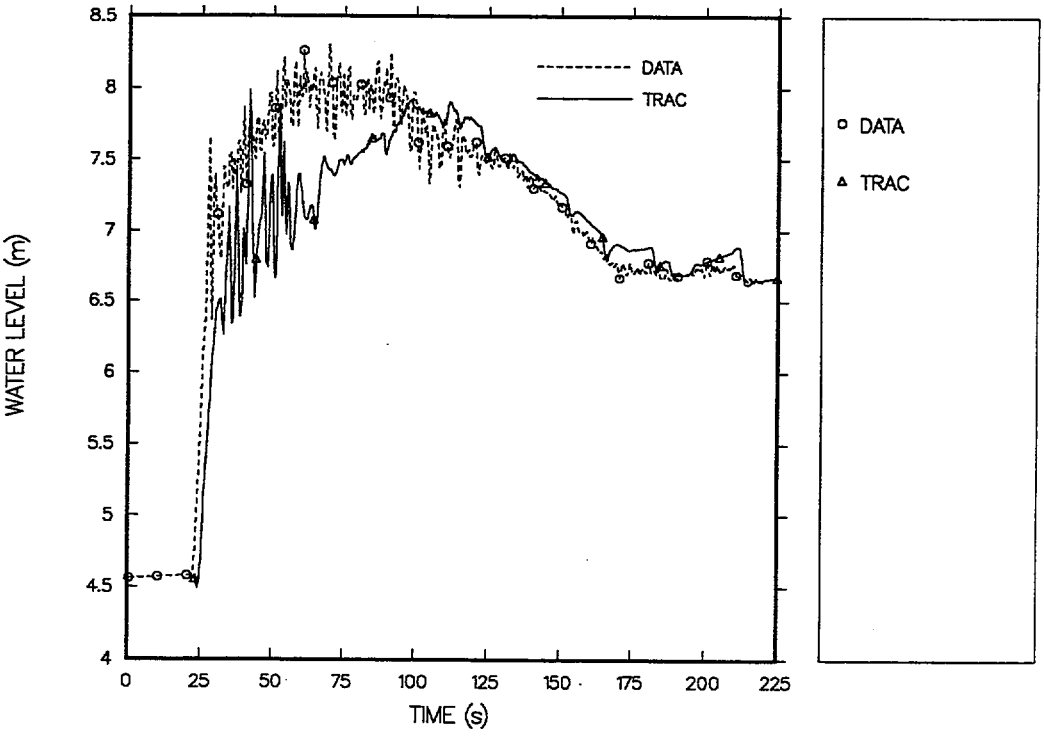

Fig. 4.5-24. Liquid height in the downcomer region of the vessel from UPTF-8B data and TRAC.

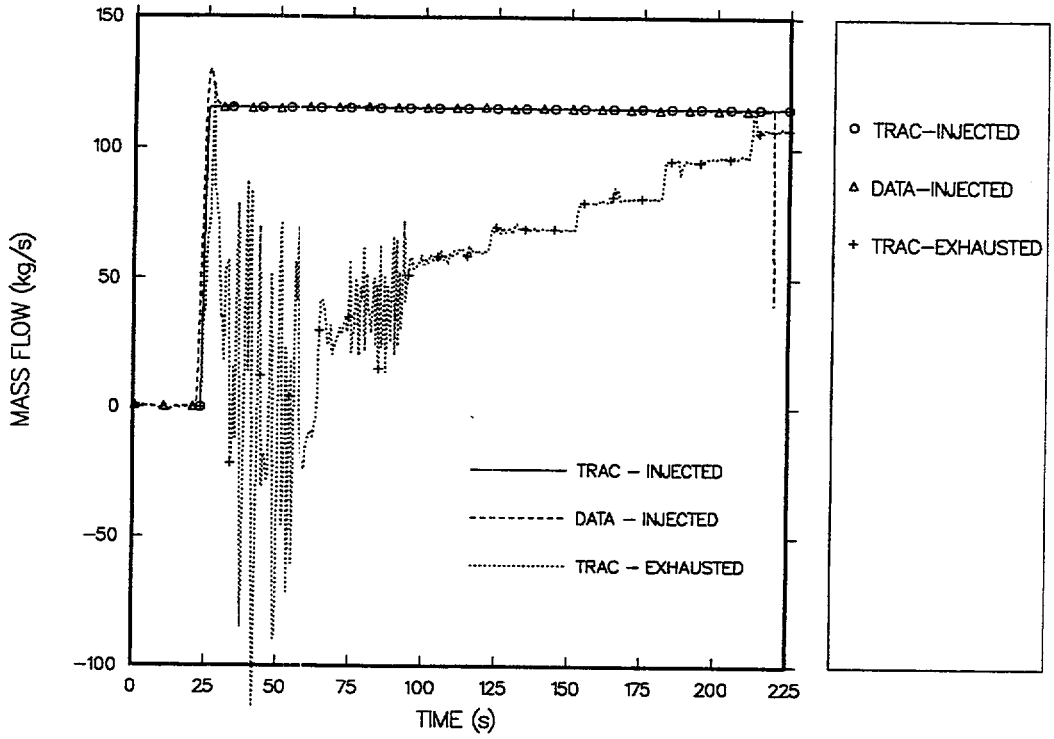

Fig. 4.5-25. Steam mass flow injected into and exhausted from the experiment.

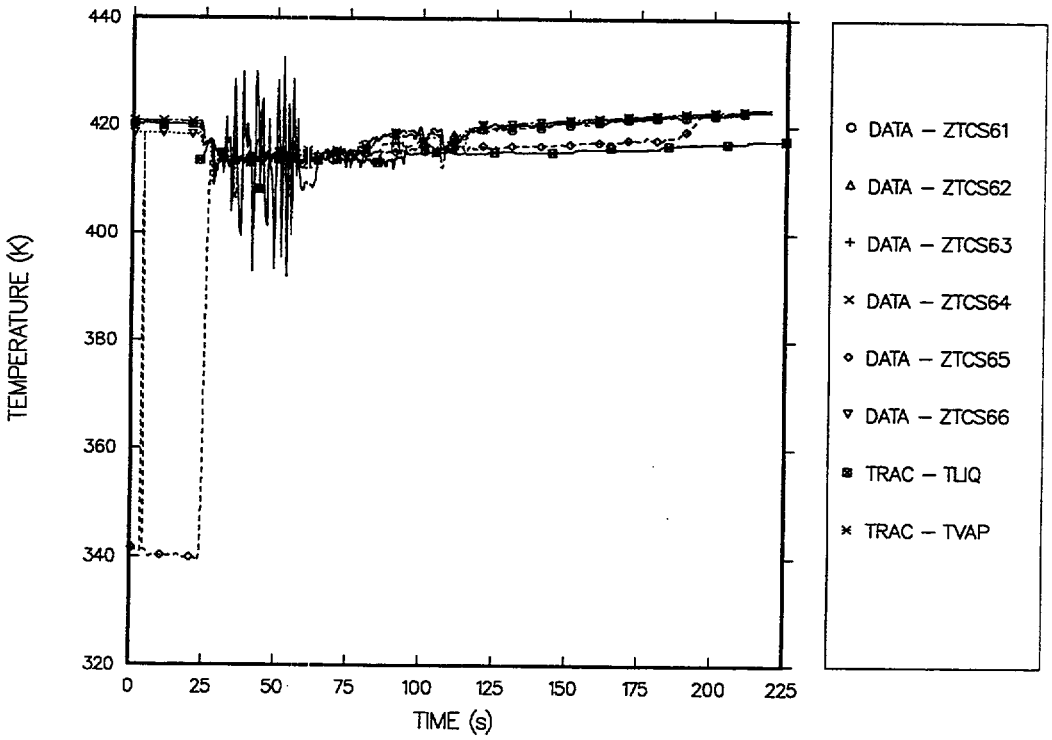

Fig. 4.5-26. Loop-2, cold-leg temperatures from Stalk 6 thermocouple data and TRAC.

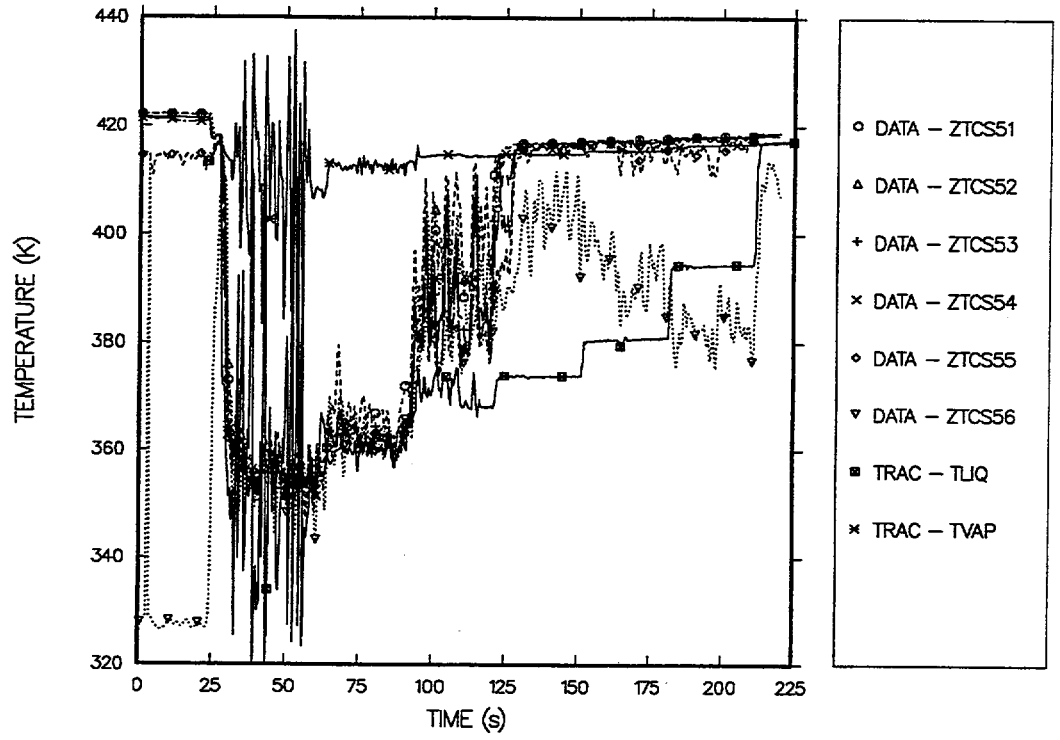

Fig. 4.5-27. Loop-2, cold-leg temperatures from Stalk 5 thermocouple data and TRAC.

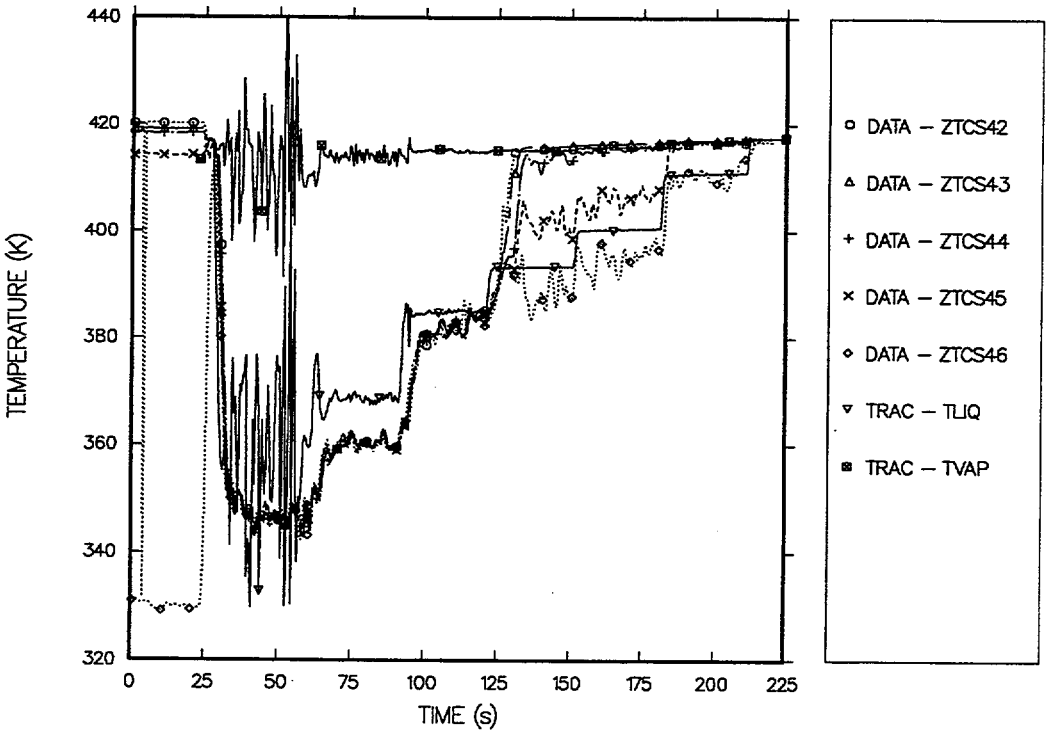

Fig. 4.5-28. Loop-2, cold-leg temperatures from Stalk 4 thermocouple data and TRAC.

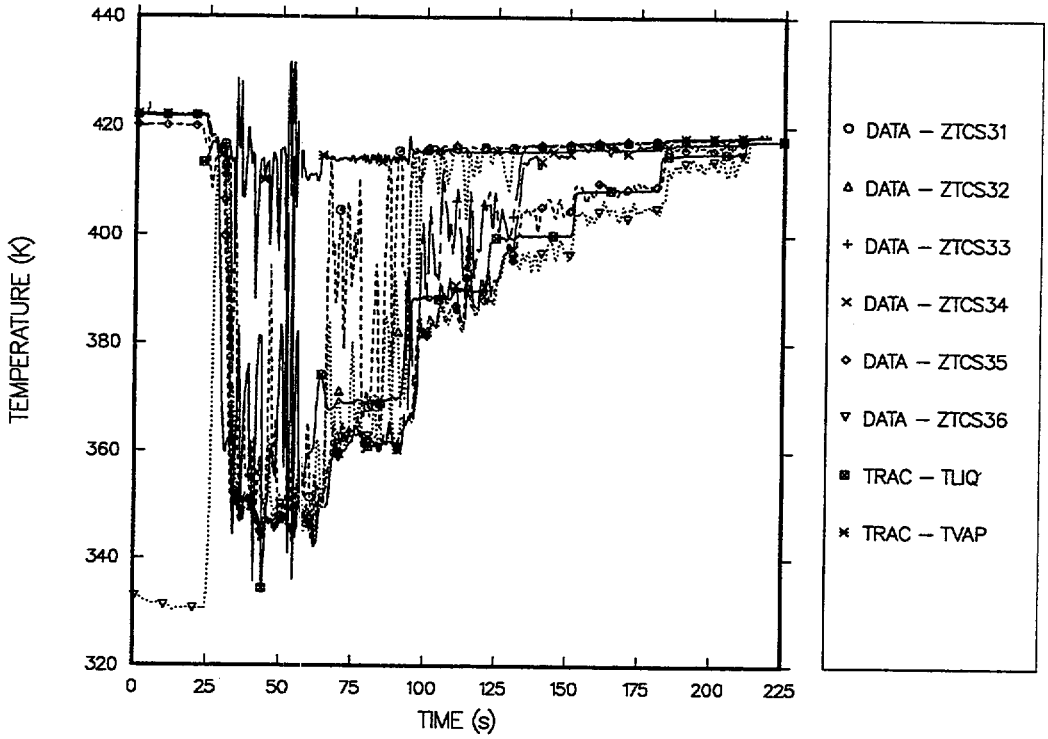

Fig. 4.5-29. Loop-2, cold-leg temperatures from Stalk 3 thermocouple data and TRAC.

4.6. Upper-Plenum Test Facility Downcomer Test 6, Run 133

4.6.1. Description of Test Facility

The UPTF, described in Ref. 4.6-1, is a full-scale model of a four-loop 1300-MWe PWR, which includes the reactor vessel, downcomer, lower plenum, core simulation, upper plenum, and four loops with pump and steam-generator simulation. A flow diagram of the system and an overview of the test facility are shown in Figs. 4.6-1 and 4.6-2. Major dimensions of the facility are shown in Fig. 4.6-3, and a plan view of the test vessel is shown in Fig. 4.6-4. The thermal-hydraulic feedback of the containment is modeled using a containment simulator. The test vessel, core barrel, and internals are a full-size simulation of a PWR with four full-scale hot and cold legs modeling three intact loops and one broken loop. Both cold- and hot-leg breaks can be investigated with ECC injection into the intact- and broken-loop cold and/or hot legs and into the vessel downcomer. The steam produced in a real core and the liquid entrained by this steam flow are simulated by direct steam injection and by liquid presence in the core simulator. Steam production on the primary side of an intact steam generator is simulated by direct steam injection into each intact-loop steam-generator simulator.

4.6.2. Description of Test Procedure

UPTF Test 6 is a separate-effects test to investigate the steam-water flow phenomenon in the lower plenum and downcomer of a US/Japan PWR during the end-of-blowdown and refill portions of a cold-leg LBLOCA. A series of five steady-state runs was made under similar boundary conditions to investigate the steam/water CCFL behavior in the full-scale downcomer of a PWR. The goals of this test were to establish test points on a flooding curve, to determine scale and geometry effects on downcomer ECC bypass behavior, and to provide full-scale test data for code assessment. ECC injection flow rate was held constant at 1500 kg/s, 500 kg/s from each intact cold leg, whereas steam injection flow rates ranged from 100 to 500 kg/s.

The system configuration for all five tests in this series (see Fig. 4.6-5) was as follows:

- closed intact-loop pump simulators,
- closed hot-leg break valve, and
- fully open cold-leg break valve.

At the start of each test, the primary system is filled with steam only. There is no water in the lower plenum. The primary system pressure corresponds to the containment pressure, and the primary structures are heated to the saturation temperature of the maximum pressure expected during the test. ECC water is injected into the intact-loop cold leg, and nitrogen is injected into the ECC water. Steam is injected into the core simulator and the intact-loop steam-generator simulators.

A TRAC analysis was performed for Run 133, which corresponded to a steam-injection flow rate of 110 kg/s. The test conditions for Run 133 are as follows:

Initial pressure in downcomer	257 kPa
Downcomer wall temperature	460 K
Lower-plenum water inventory	0 kg
Pressure in drywell	256 kPa
ECC temperature	388–390 K
Total ECC-injection rate	1473 kg/s
Total nitrogen-injection rate	1 kg/s
Total core simulator steam mass flow rate	110 kg/s
Steam-generator simulators steam mass flow rate (each)	29–33 kg/s

The intact loops are blocked at the pump simulators, so the steam flow from the steam-generator simulators is forced to flow through the hot legs, down into the vessel, and up the downcomer. Therefore, the total amount of steam that flows up the downcomer is ~200 kg/s for this test. The steam flow is held fairly constant throughout the test.

4.6.3. Description of the TRAC Model

The TRAC-PF1/MOD2 model used in this assessment is a revision of the CSAU model previously used in an assessment using TRAC-PF1/MOD1, Version 14.3. The vessel model for the MOD1 assessment contained 13 axial levels, 3 radial rings, and 4 azimuthal sectors. The MOD2 version was extended to 8 azimuthal sectors. In flow areas of cells in the vessel, several changes were necessary because the MOD2 code requires that the user follow certain noding practices.

The UPTF Test 6 model used for the assessment of TRAC, Version 5.5, is the same as that used for the assessment of TRAC, Version 5.4. Noding diagrams for the TRAC model of UPTF Test 6 are shown in Figs. 4.6-6 to 4.6-14. The vessel axial noding is shown in Fig. 4.6-6. The vessel model consists of 13 axial levels, 8 azimuthal sectors, and 3 radial rings. The azimuthal and radial noding distribution for the vessel is shown in Fig. 4.6-7. The core is represented by the inner two rings, and the downcomer is represented by the outer ring.

Figures 4.6-8 to 4.6-10 show the noding for loops 1, 2, and 3. In each loop the hot leg is modeled with a Tee component; the steam generator simulator is modeled with a combination of four Tee components and one Valve component; and the crossover pipe, pump simulator, and cold leg are modeled with another Tee component. Steam injection into the top of the steam-generator simulator is modeled with Tee and Fill components. This Fill component can be controlled by the mass flow of liquid in the hot leg. The drain line from the bottom of the secondary side of the middle Tee to the steam-generator simulator inlet plenum is modeled with another Tee and Valve

component. The pump simulator is modeled with a flow-area restriction and the correct volumes associated with the pump simulator component. ECC injection is modeled in both the hot and cold legs with the Tee and Fill components. The Fill components can invoke a time-dependent programmed ECC flow if desired. The loop 1 and loop 3 noding are identical. In loop 2, the pressurizer in the hot leg required the addition of an extra Tee component. This Fill also may use a preprogrammed-type steam flow.

Figures 4.6-11 and 4.6-12 show the broken-loop-4 hot- and cold-leg noding. The broken-loop cold-leg model is composed of a Valve component to model the main break Valve, a Tee component to model the bottom of the steam-generator simulator, and another Tee component to model the steam/water separator and piping to the containment. The bottom of the steam-generator-simulator drain line is modeled to the drain tank Valve. This drain line drains off accumulated liquid during the course of the transient. The broken-loop hot leg is modeled with a Tee component for the hot leg, another Tee component for the steam generator simulator, and a Valve component for piping run out to the containment tank. The containment tank is modeled with two Break components. These components provide a transient pressure boundary condition. Drain lines from the bottom of the vessel to the drain tank were completely modeled and are shown in Fig. 4.6-13.

The core steam/water injection sources are modeled by 16 individual Tee components each having the same noding shown in Fig. 4.6-14. Each component is connected to one of the 16 core cells at the vessel level 6. The Tee components are able to combine the steam input from a feedback injection with the preprogrammed steam/water input. For UPTF Test 6, there is no feedback injection flow. The walls between the UPTF injection zones are solid; therefore, TRAC incorporates a zero flow area in the radial and azimuthal direction at level 6. Because the steam is injected in the radial direction at this level, it will impact the walls and lose its radial momentum. To model this effect in the TRAC input, the steam/water injection sources are directed radially.

A listing of the input model used for this developmental assessment calculation is found in Appendix H. Archival storage information for this input model is found in Section 4.6-7.

4.6.4. Comparison of Predicted and Measured Results

Figure 4.6-15 shows a comparison of TRAC predictions and experimental measurements of the mass of liquid in the vessel as a function of time. The agreement is good. The liquid mass inventory in the downcomer and lower plenum predicted by TRAC is shown in Fig. 4.6-16. The liquid mass inventory in the core and upper plenum is negligible.

An important aspect of the test results is the accuracy of the mass balance that accounts for the distribution of the injected mass. Figure 4.6-17 shows the overall mass balance for the time period ~30 s after the beginning of ECC injection.[4.6-2] From this figure it can be seen that >10 000 kg of mass is not accounted for. This discrepancy mainly is caused by transient effects after the start of ECC injection, some level measurements influenced by high pressure, and some water inventories that may not be detectable, such as water flowing into the containment simulator.

From Fig. 4.6-17, we can see that in the test, mass rapidly accumulates in the cold legs at the start of ECC injection as liquid plugs form. As water is delivered to the downcomer, the cold-leg inventory reaches a relatively steady value of ~7200 kg ~15 s after the start of ECC injection. The mass flow out of the cold-leg break shows a relatively steady increase. Initially the liquid inventory in the vessel increases slowly; the rate of increase becomes greater when the cold-leg liquid inventory reaches a fairly steady value.

The mass balance predicted by TRAC is shown in Fig. 4.6-18. The mass in the intact cold legs was determined by summing the fluid-cell masses in each of the intact cold legs, cells 14 through 21 of components 14, 24, and 34 of the TRAC loop models (Figs. 4.6-8 to 4.6-10). At 25 s after start of ECC injection, the predicted total cold-leg mass is about 7% higher than measured, an excellent agreement. However, the predicted break flow is about 60% higher than the measured value. The overall agreement is satisfactory considering the large uncertainty in the experimental mass balance.

A few measurements of liquid temperature and pressure were also reported in Ref. 4.6-2. The data were measured 60 s after the beginning of the run at a time when the pressures and temperatures were varying slowly. The corresponding values predicted by TRAC are shown for comparison in Fig. 4.6-19. The calculated temperatures agree with the data reasonably well. The calculated pressure difference across the reactor (from the downcomer near cold-leg 2 to the break in cold-leg 4) is 17% higher than the measured value. This may be partly caused by changes made in flow areas within the reactor. The MOD2 version of the code does not allow flow areas greater than the ratio of the cell volume to length. It was necessary to decrease some flow areas with a resulting increase in pressure drop.

4.6.5. Lessons Learned and User Guidelines

The vessel noding for the final simulation contained eight azimuthal sectors. A previous calculation using only four azimuthal sectors gave much lower downcomer penetration by the ECC water and vessel inventories that were much too low. If only four 90° sectors are used and a cold leg is connected to each, the system is not accurately simulated because the azimuthal extent of the cold-leg connections is actually <45°. Using eight sectors provides an area for steam upflow in the downcomer in regions where there is little or no downflow of water, a condition closer to reality for this case. It is recommended that at least eight azimuthal sectors be used for four-loop systems.

The initial simulations included nitrogen fills with no moisture, which resulted in a large number of warning messages for these fills. Adding a small amount of moisture (PAIN < PIN) eliminated this problem with no noticeable effect on the computational results. It is recommended that some moisture be included with nitrogen injection.

4.6.6. Conclusions

A comparison of data from the UPTF-6, Run 133 test with calculations performed using TRAC-PF1/MOD2 was completed. The results of that comparison indicate that the code does a reasonable job of predicting downcomer penetration of ECC flow. The predicted vessel liquid-mass inventory is in good agreement with the data. The break flow is somewhat overpredicted, but the differences are not large compared with the uncertainty in the experimental mass balance.

4.6.7. Code Performance

UPTF Test 6 was run on code Version 5.5. The run performance information plus other pertinent comments follow.

Code Version 5.5

Platform	Sun Enterprise 3000
Total CPU time (s)	18308.0
Archive location of input model	CFS /tida/f77da_decks/inuptf6
Archive location of calculation	CFS /trac-da/F77DA/nonreflood/ uptf6.tar.gz

REFERENCES

4.6-1. SIEMENS AG, UB KWU, "UPTF: Program and System Description," Report No. U9 414/88/023 (November 1988).

4.6-2. SIEMENS AG, UB KWU, "2D/3D Program Upper Plenum Test Facility, Test No. 6, Downcomer Countercurrent Flow Test U9 316/89/2," Quick-Look Report (March 1989).

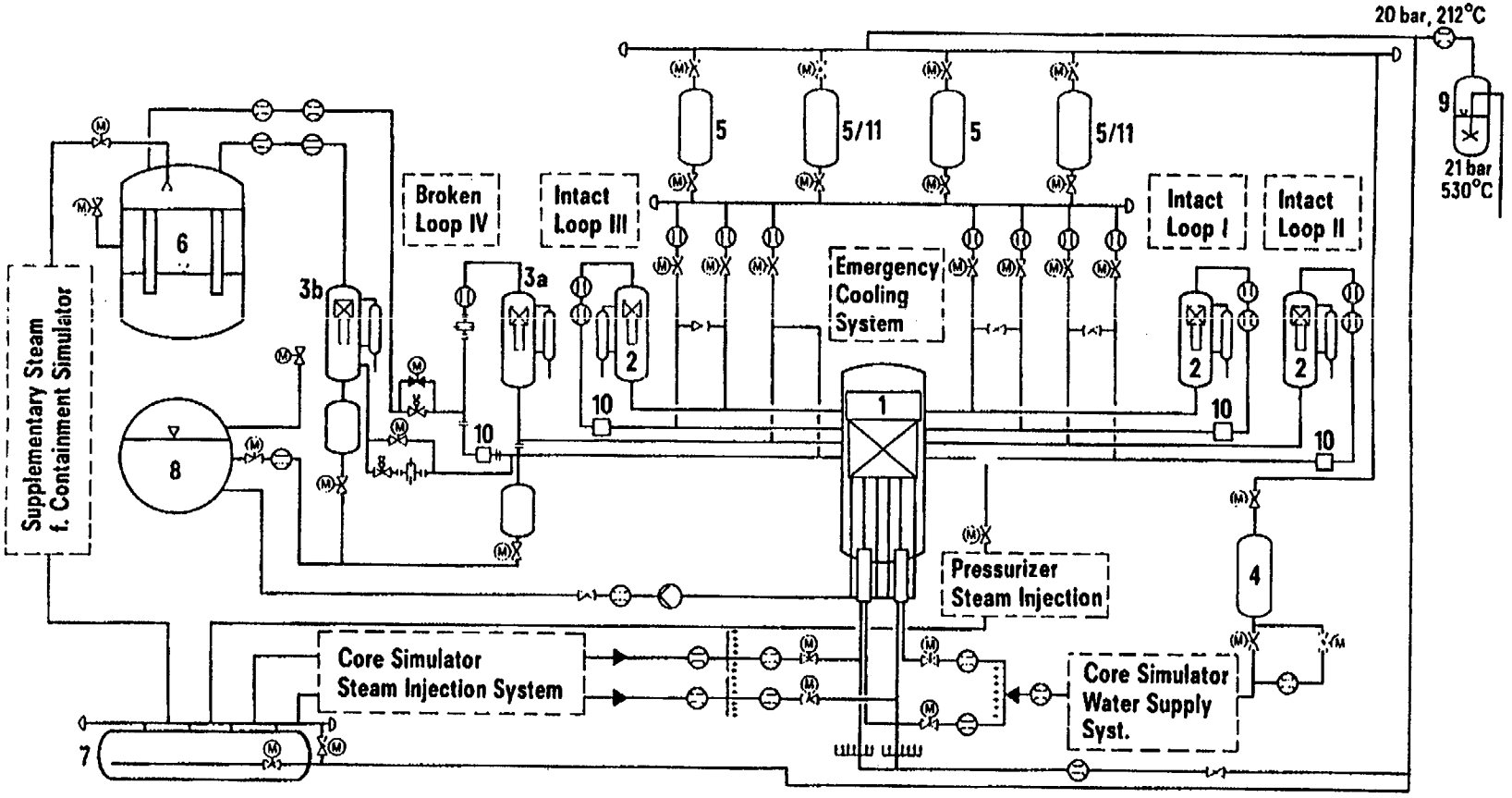

1 Test Vessel
2 Steam Generator Simulator
3a Water Separator (HL)
(Steam Generator Simulator)
3b Water Separator (CL)
4 Hot Water Storage Tank
5 Accumulator
6 Containment Simulator
7 Steam Storage Tank
8 Water Collection Tank
9 Steam Cooler
10 Pump Simulator
11 N_2-Tank

Fig. 4.6-1. UPTF flow diagram.

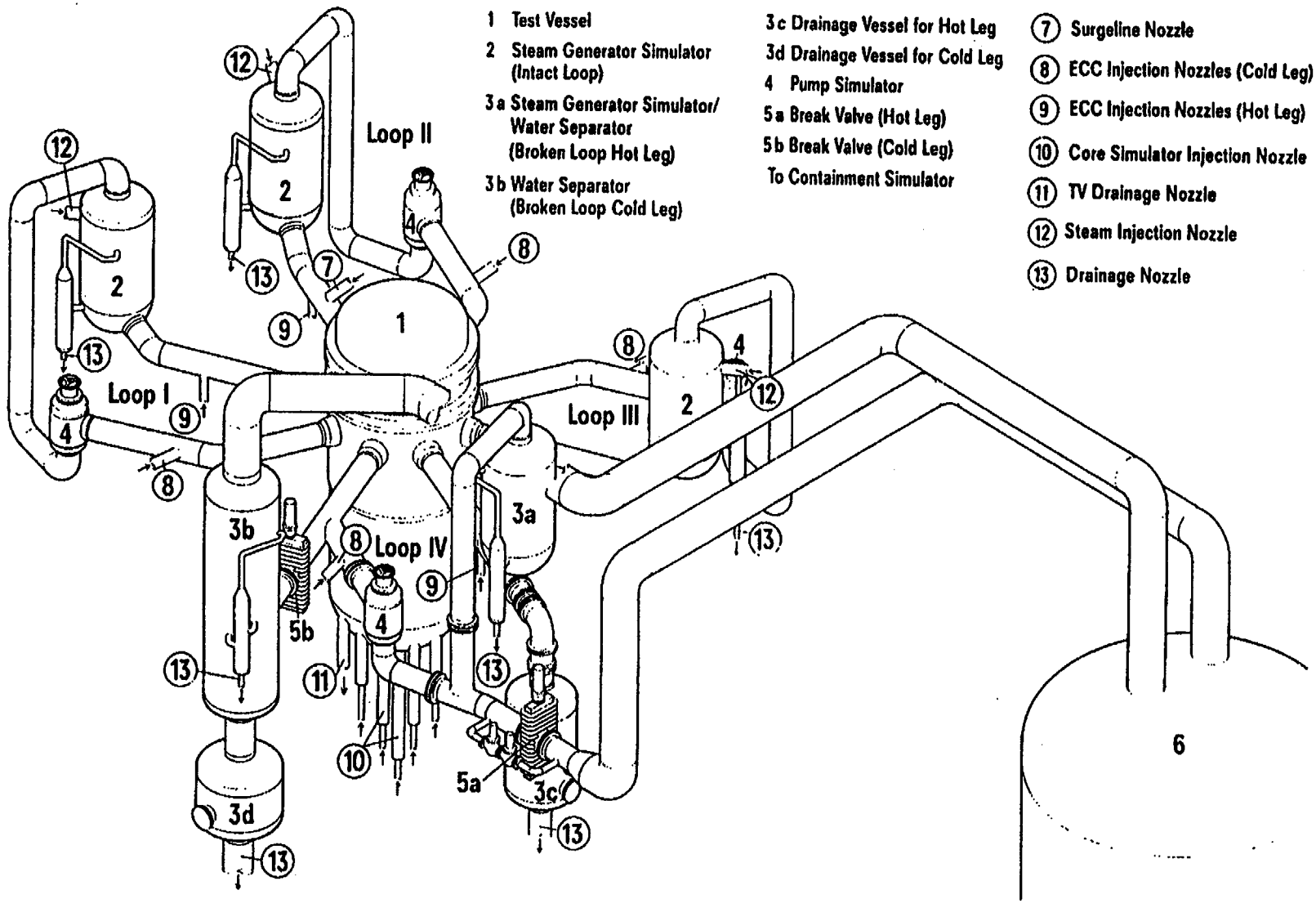

Fig. 4.6-2. Overview of UPTF primary system.

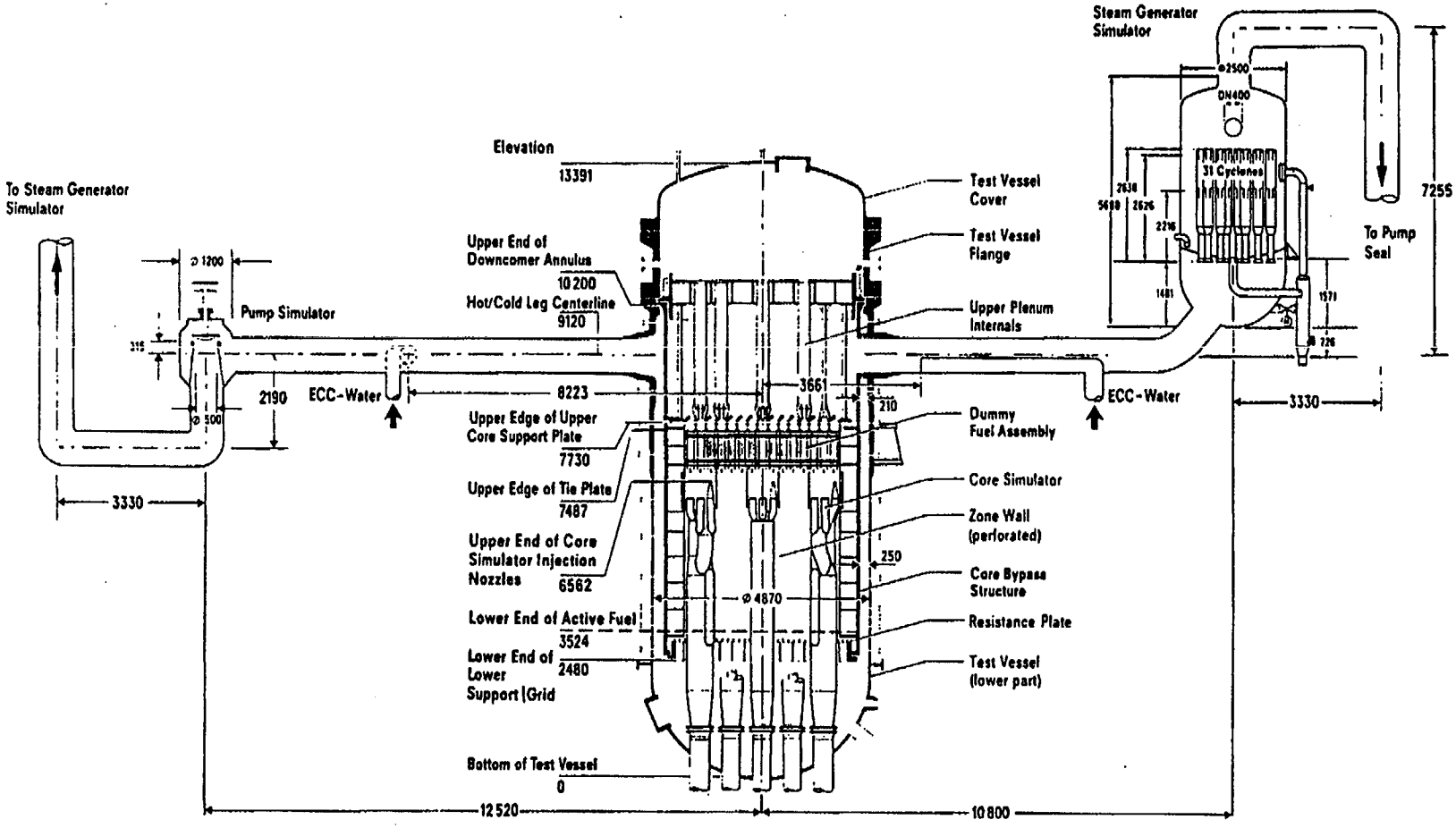

Fig. 4.6-3. Major dimensions of the UPTF primary system.

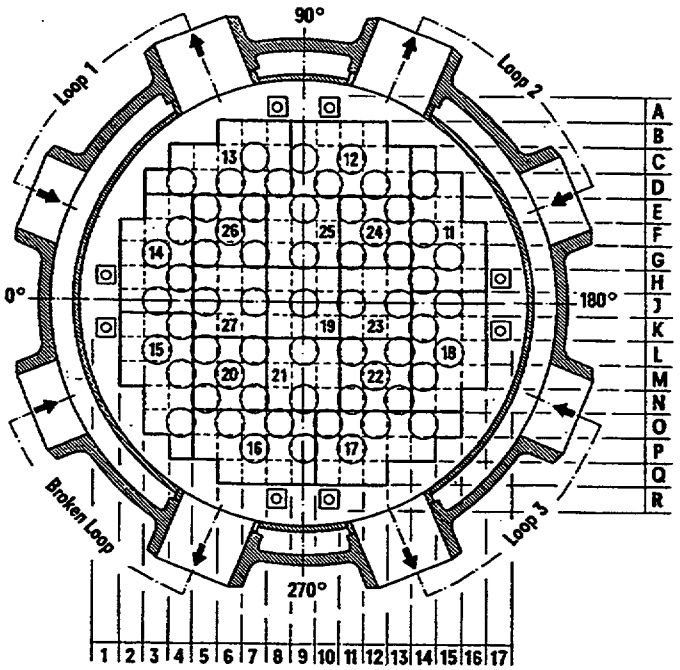

Fig. 4.6-4. Plan view of UPTF test vessel.

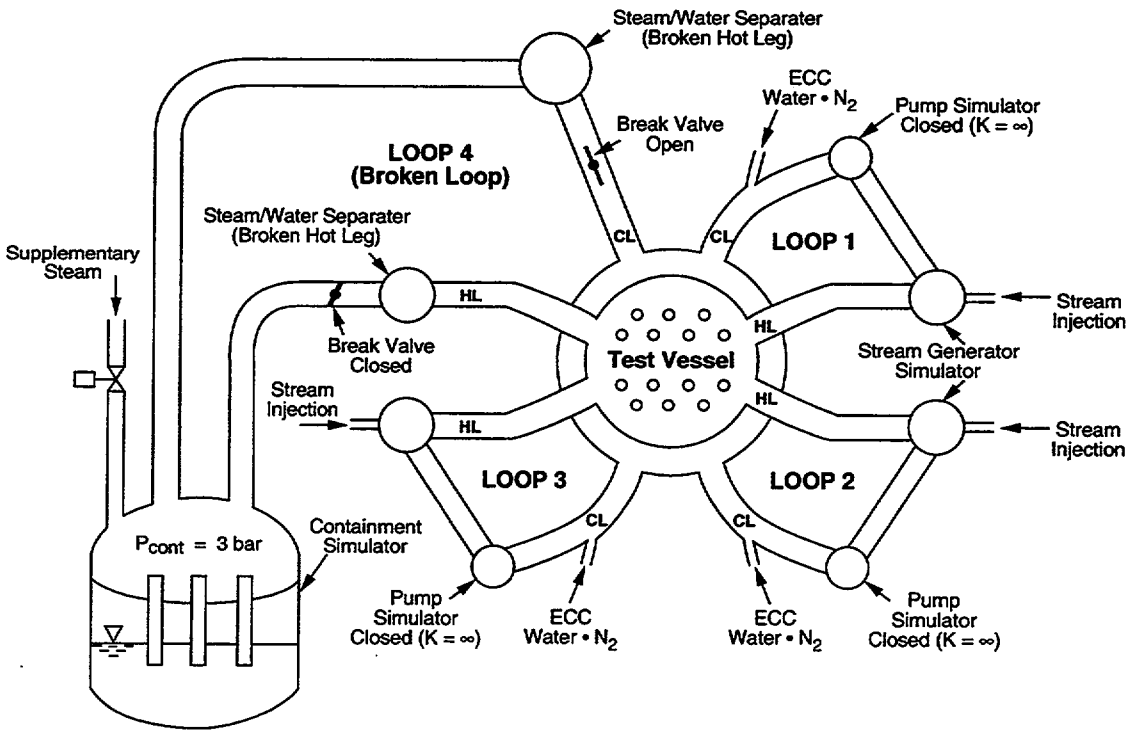

Fig. 4.6-5. System configuration for UPTF Test 6.

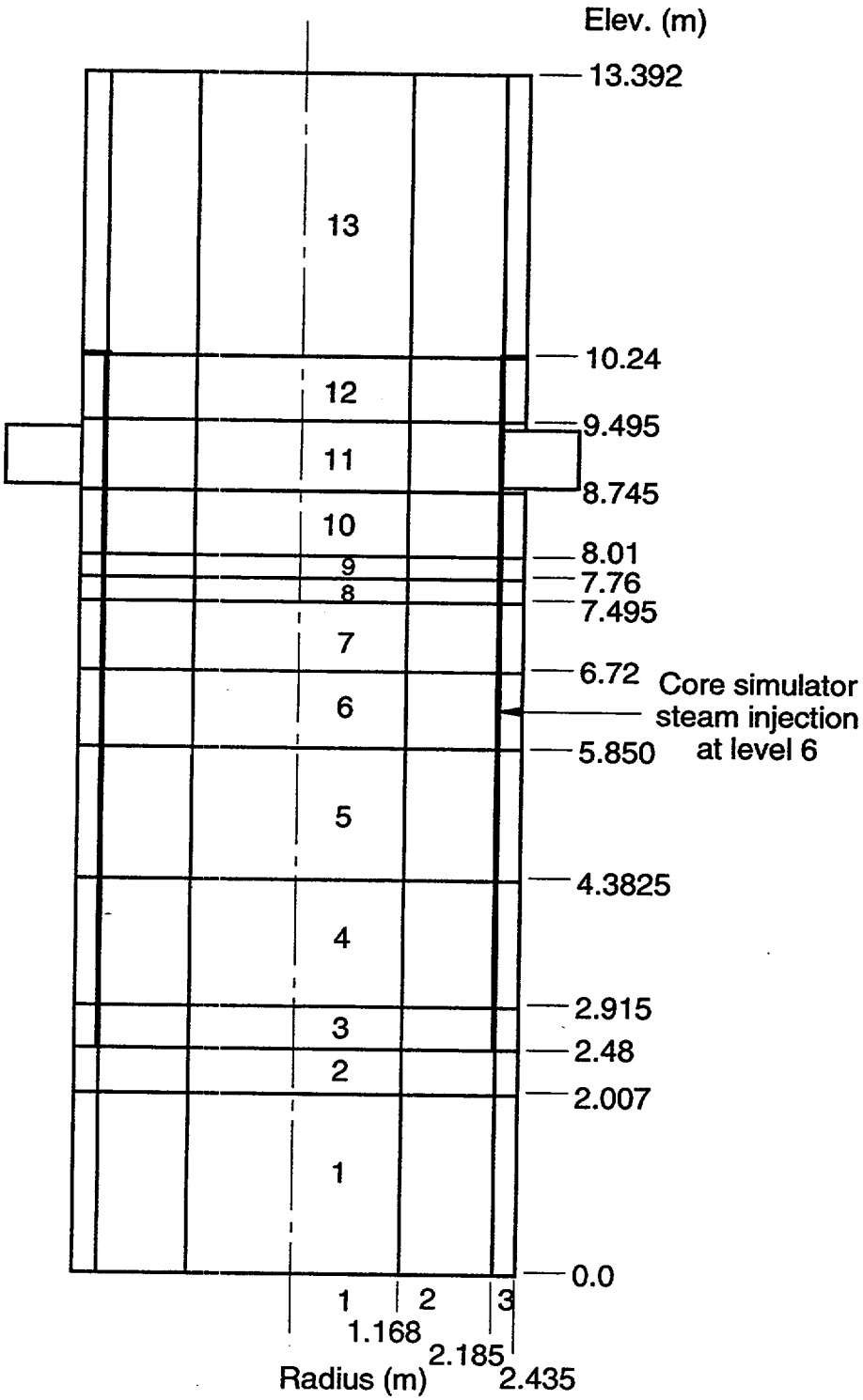

Fig. 4.6-6. Vessel model elevation view for UPTF Test 6.

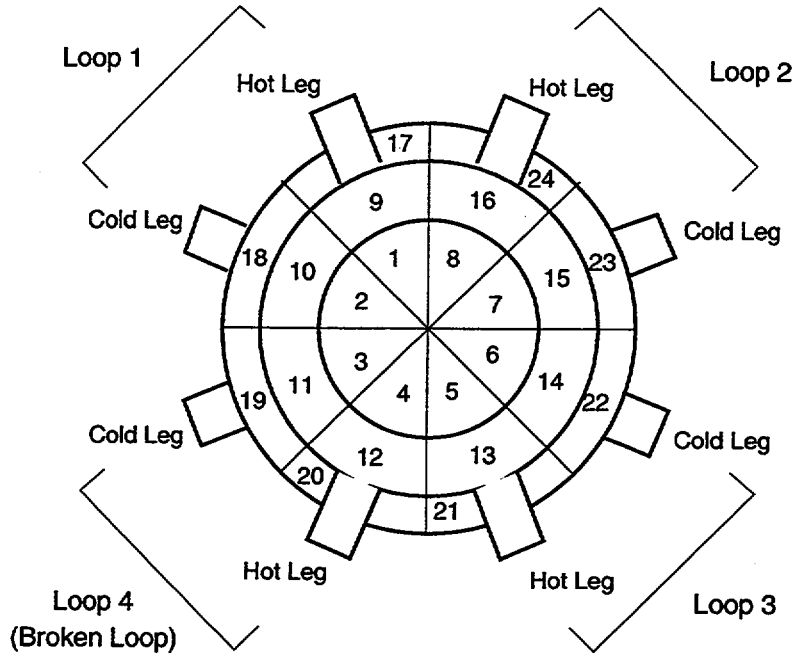

Fig. 4.6-7. Vessel model plan view for UPTF Test 6.

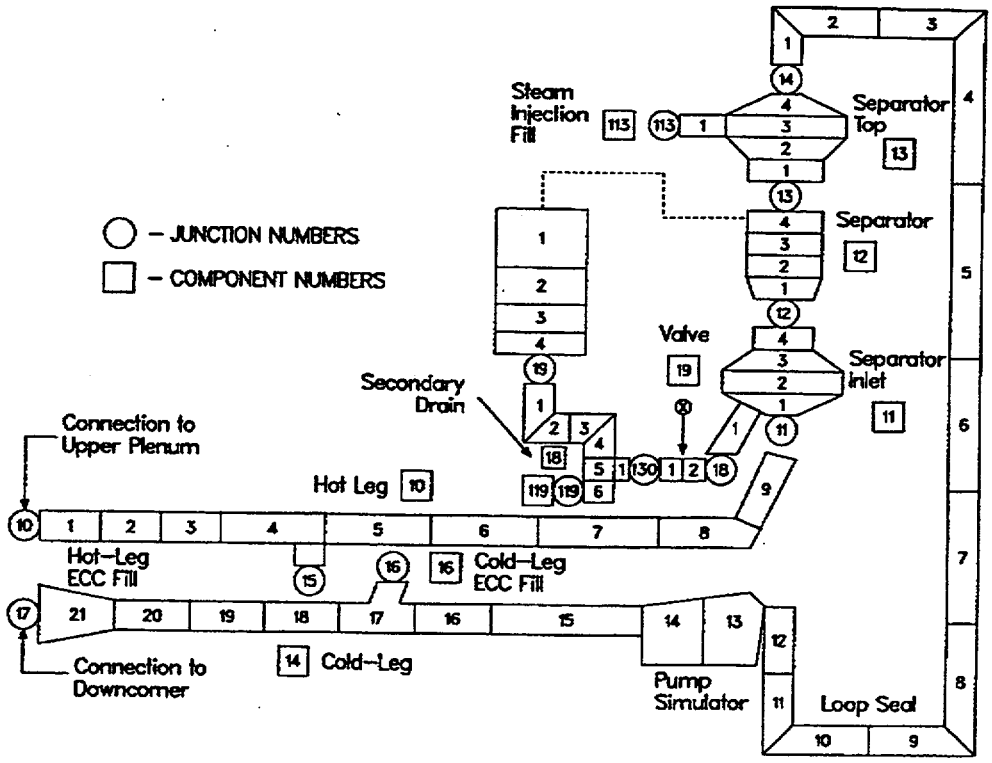

Fig. 4.6-8. UPTF loop-1 noding diagram.

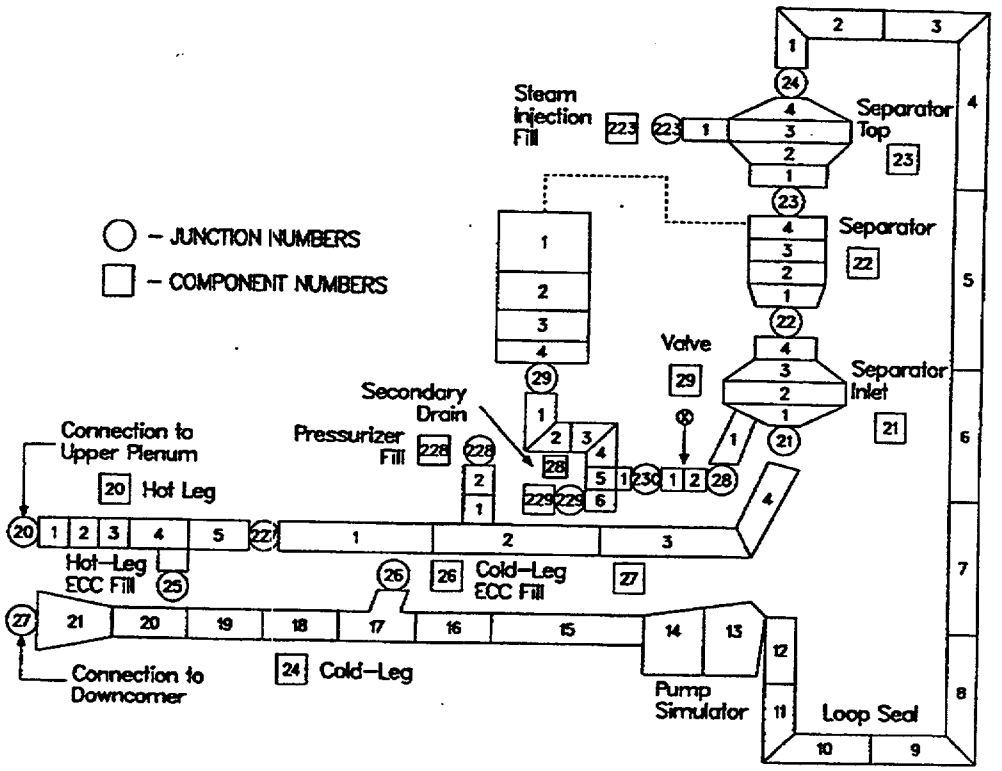

Fig. 4.6-9. UPTF loop-2 noding diagram.

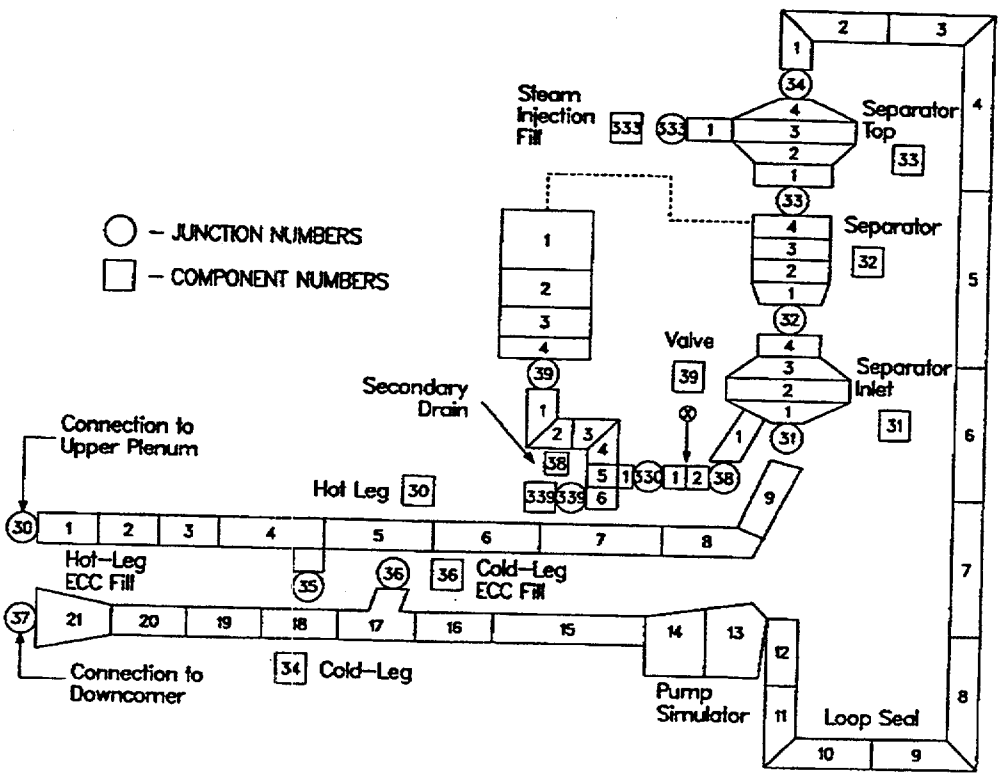

Fig. 4.6-10. UPTF loop-3 noding diagram.

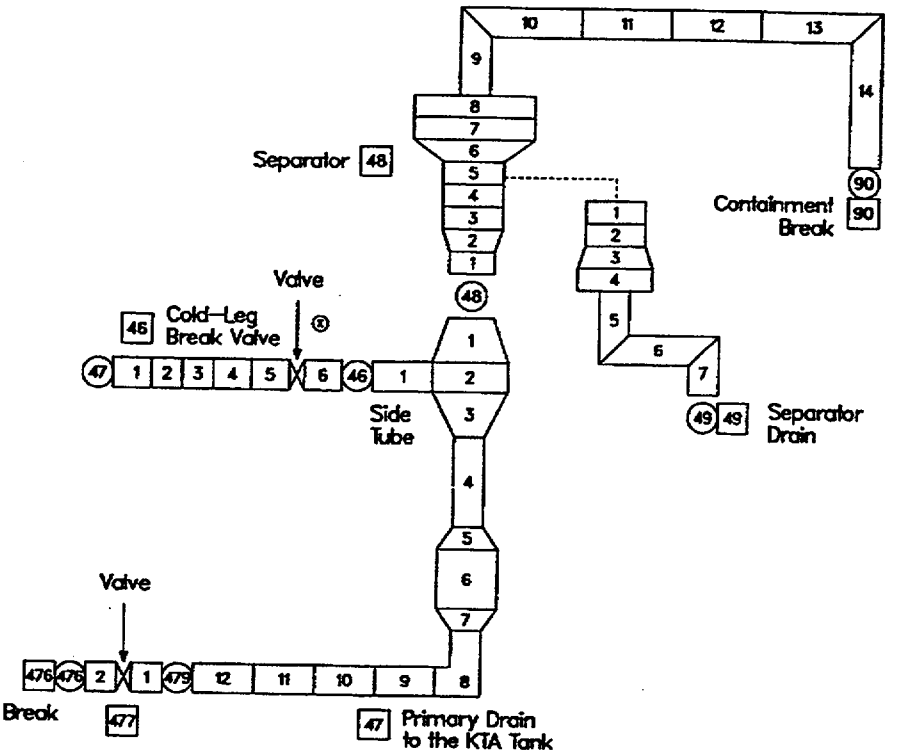

Fig. 4.6-11. UPTF loop-4 broken-cold-leg noding diagram.

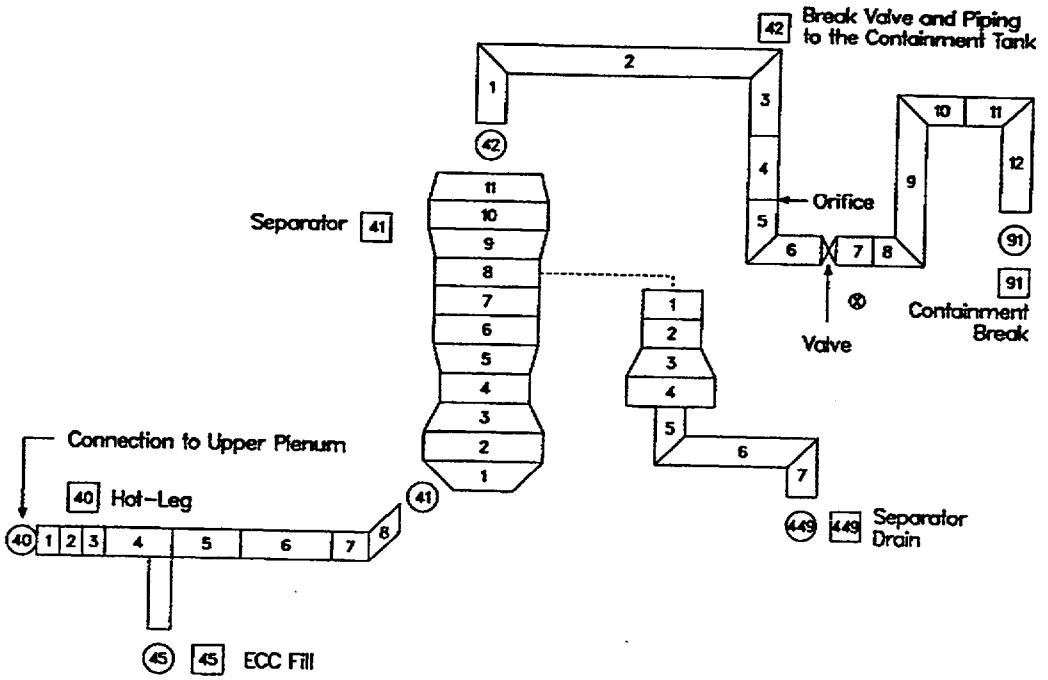

Fig. 4.6-12. UPTF loop-4 broken-hot-leg noding diagram.

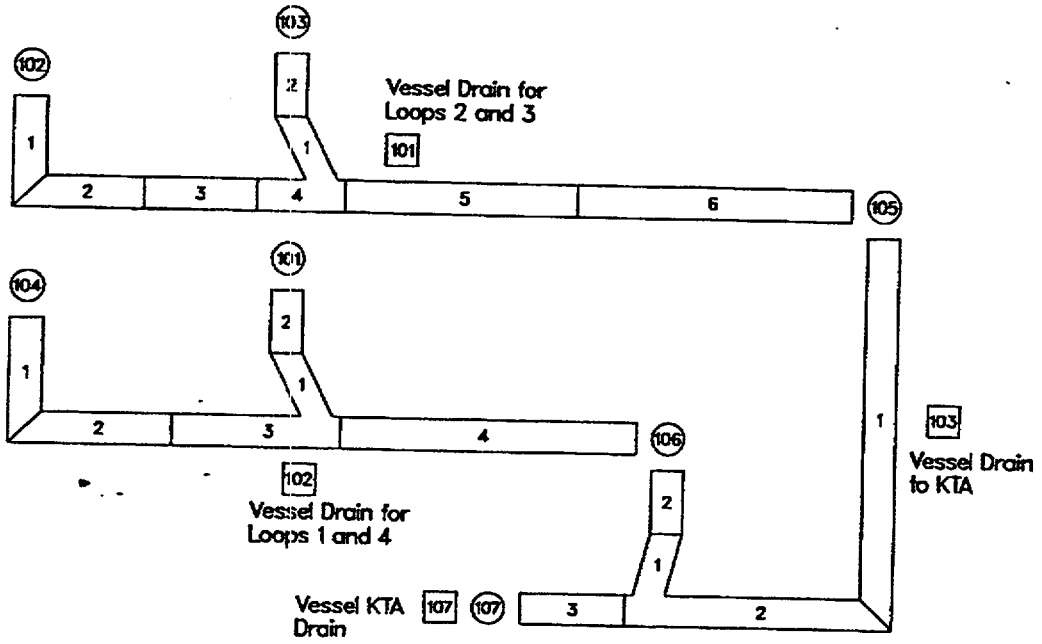

Fig. 4.6-13. UPTF water drainage system noding diagram.

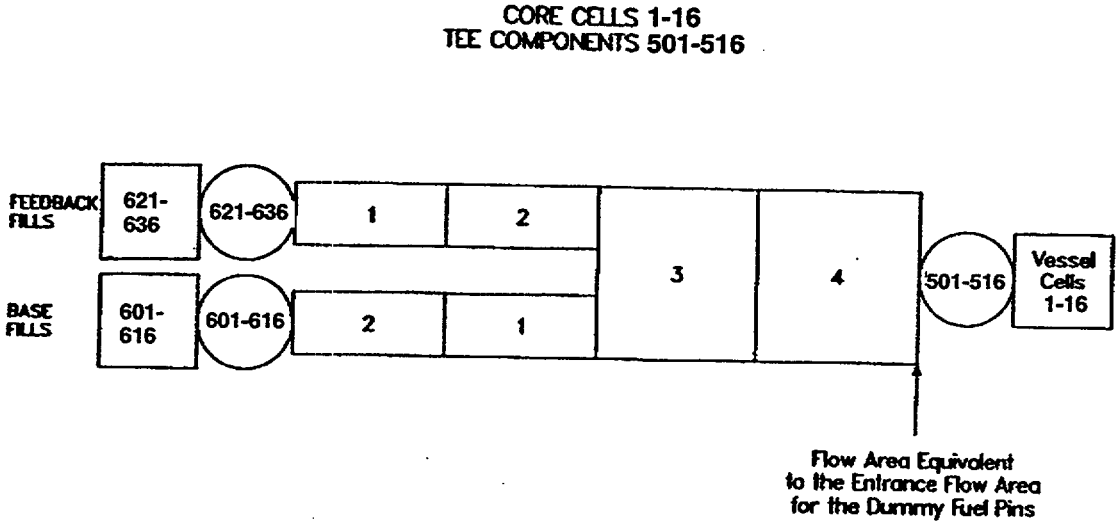

Fig. 4.6-14. UPTF core-simulator-injection noding diagram.

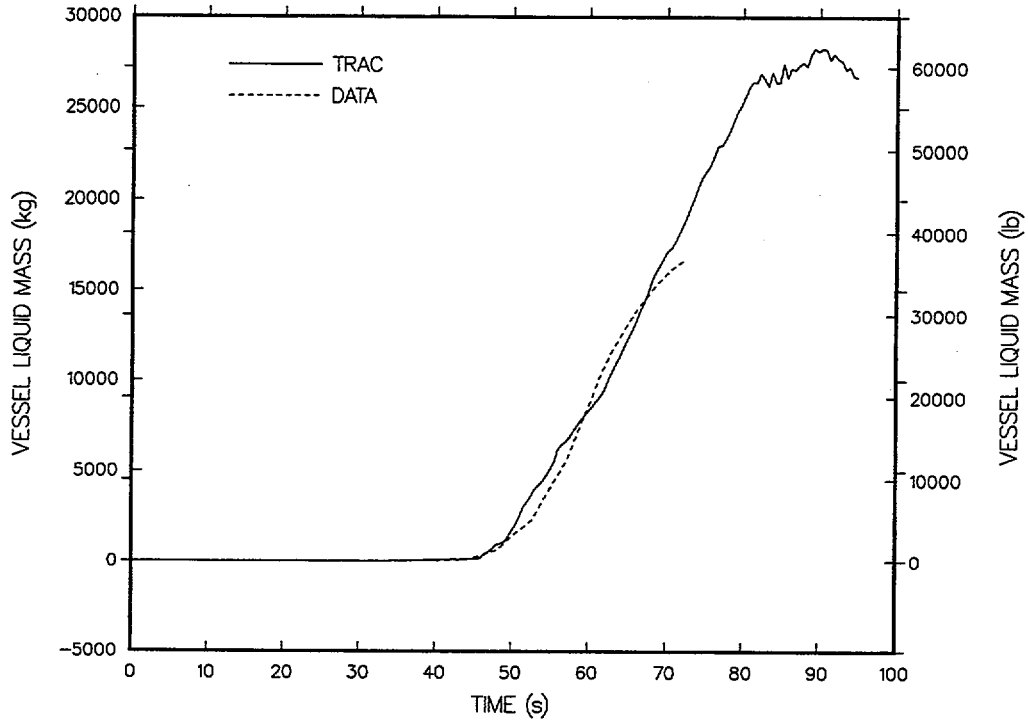

Fig. 4.6-15. Vessel liquid mass vs time.

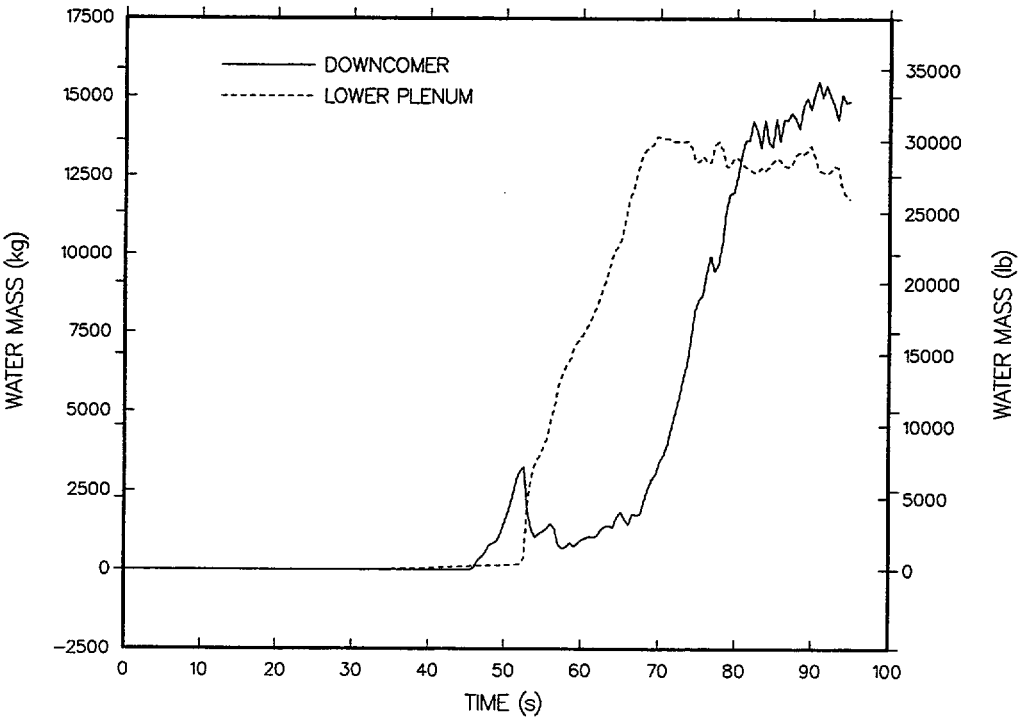

Fig. 4.6-16. Calculated downcomer and lower-plenum liquid-mass inventories

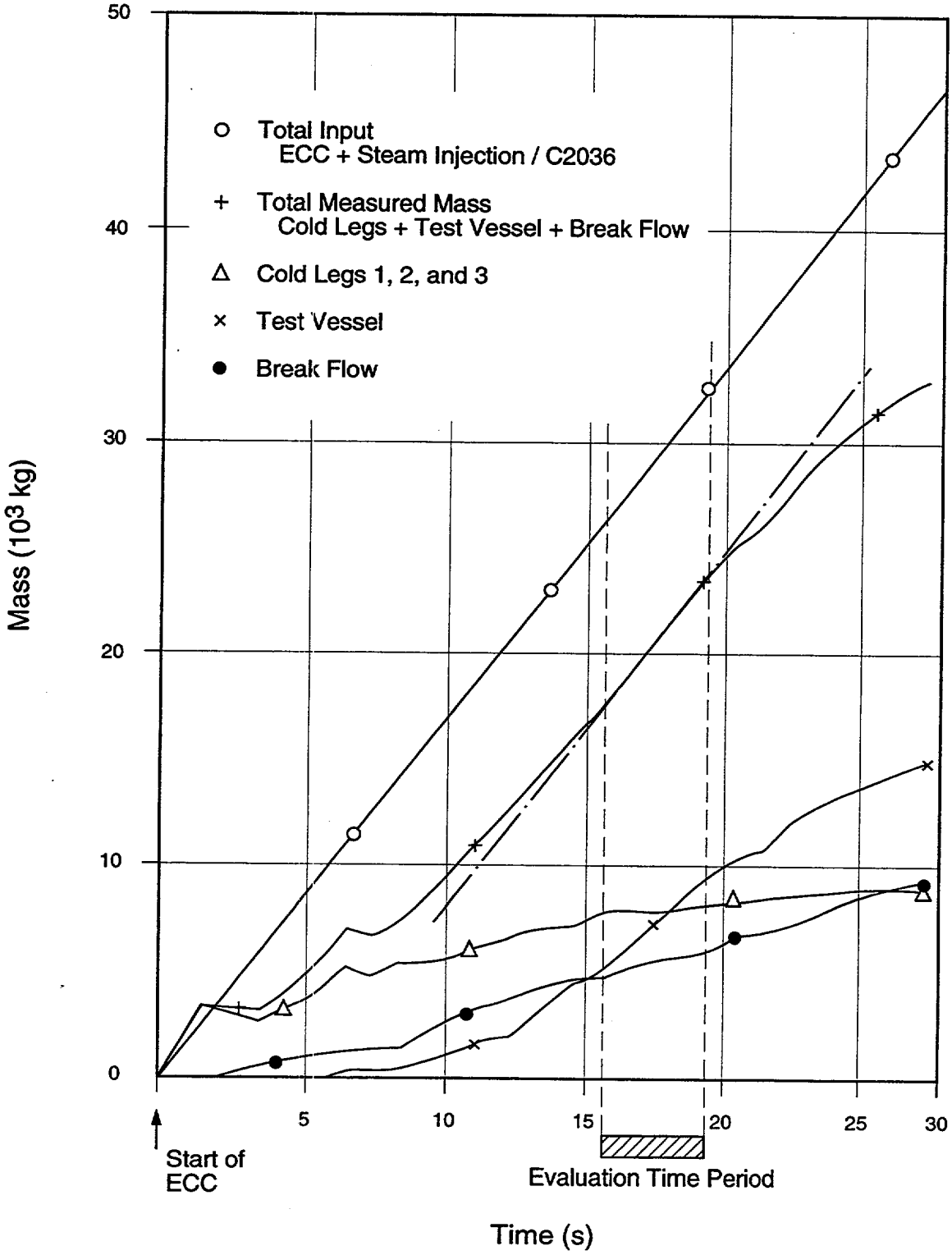

Fig. 4.6-17. Overall mass balance (experimental).

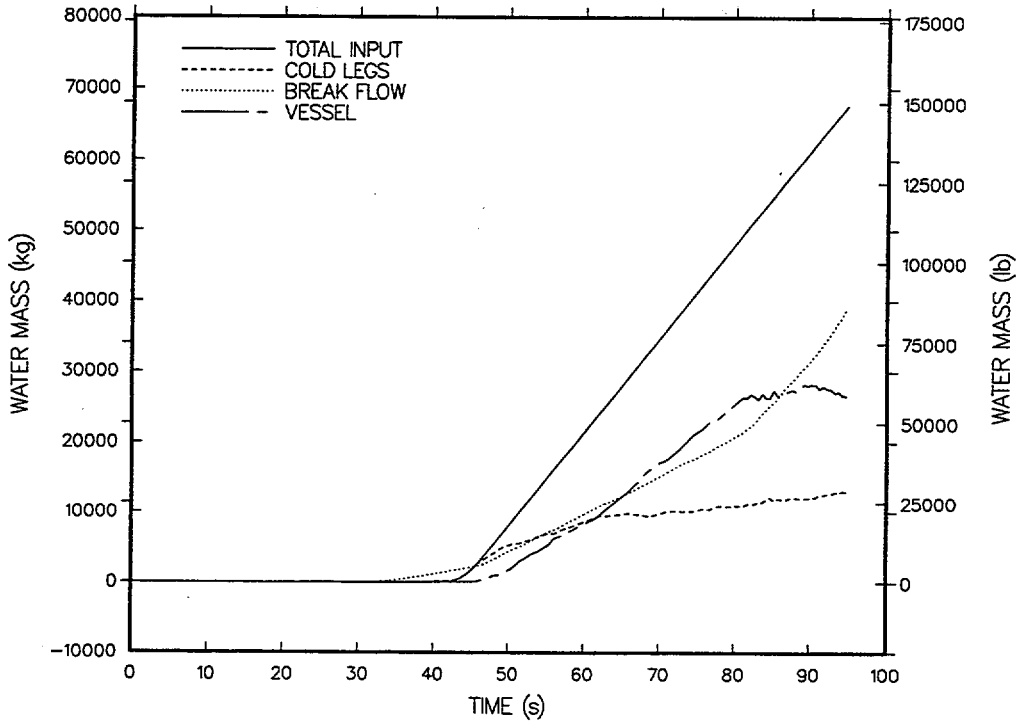

Fig. 4.6-18. Overall mass balance (calculated).

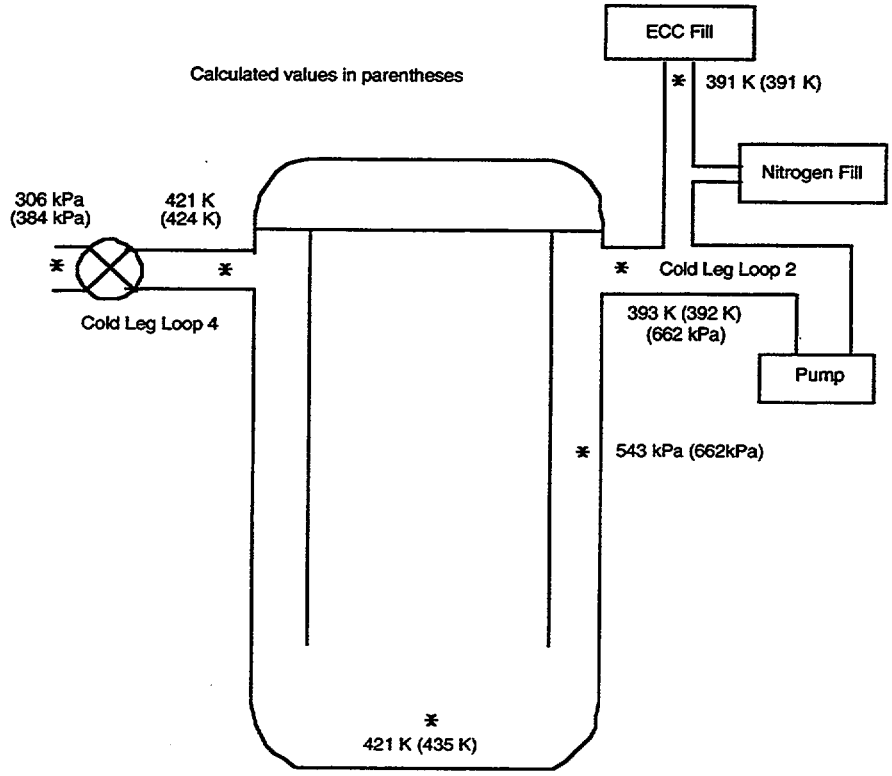

Fig. 4.6-19. Pressures and liquid temperature at t = 60 s.

4.7. CCTF Core I Test C1-5 (Run 14)

The Cylindrical Core Test Facility (CCTF) was designed, built, and operated by the Japan Atomic Energy Research Institute (JAERI). The CCTF was designed to provide information on thermal-hydraulic behavior during the refill and reflood phases of a LOCA in a PWR; the blowdown period is not simulated. Two test series were run in the CCTF, and the facility configuration was modified slightly (CCTF-II) for the second series relative to the initial facility configuration, CCTF-I.

4.7.1. Facility Description

The CCTF is a full-height, experimental facility designed to model a four-loop 1100-MWe PWR. Figures 4.7-1 and 4.7-2 show a schematic of the CCTF facility and a top view of the primary system piping, respectively. Figure 4.7-3 shows a top view of the pressure vessel. Additional facility descriptive information can be found in Refs. 4.7-1 and 4.7-2. All pertinent PWR components have been modeled, and most major vessel and primary-loop dimensions are volume scaled in a ratio of 1/21.4, as compared with a 1100-MWe PWR. The pressure-vessel downcomer annulus is larger than the width that results from an exact 1/21.4 scaling because the scaled core bypass area is included as part of the downcomer area. The upper-plenum internals model those used in the reference plant but are reduced in size by a ratio of 8/15. This approach of using a larger number of internal structures that are smaller than scaled size was chosen because the use of larger structures would have resulted in only a few structures in the upper plenum and thus the possibility of strong asymmetries and unrealistic flow distributions. Depending on facility configuration and operation, tests in the CCTF have been variously defined as either SET[4.7-3] or integral effect tests (IETs).

The CCTF vessel contains a core, an annular downcomer, and upper and lower plena. The CCTF core contains 32 8 x 8 bundles, each containing 57 electrically heated rods and 7 nonheated rods (a total of 1824 heated rods and 224 nonheated rods). Each bundle includes rods with three different power densities. The heated rods are held in place by grids, as in a PWR. Each heated rod consists of a nichrome heating element, magnesium oxide and boron nitride insulators, and an Inconel sheath. The heated length and the outer diameter of the heater rods are 3.66 m and 10.7 mm, respectively. The axial power profile is simulated by a 17-step chopped cosine profile, as shown in Fig. 4.7-4. The axial peaking factor is 1.492. The nonheated rods simulated the guide and instrument thimble tubes in PWR fuel assemblies.

The primary loops consist of three intact loops and a broken loop. Each loop consists of hot-leg and cold-leg piping, a steam-generator simulator, and a pump simulator. The 200% cold-leg break is simulated in the broken loop. The two ends of the broken loop are connected to two containment tanks through blowdown valves. The steam-generator simulators are of the U-tube and shell type. Each steam generator simulates two loops that are housed in a single-shell assembly having two compartments, one simulator for each loop in a single compartment. The primary coolant passes through the tube side, and the secondary coolant is stagnant in the shell side. The steam-generator tubes are 25% shorter than those in a commercial reactor.

The ECCS consists of two accumulators and a low-pressure coolant injection (LPCI) system. The instrumentation consists of detectors, signal conditioners, signal

processors, recording equipment, and display equipment. Temperature measurements are made with alumel chromel thermocouples having an expected error of 0.5%. Pressure and differential pressure measurements are made with differential pressure cells, with an expected error of 0.3%. Pressure-vessel, liquid-level measurements are made in two ways. Differential pressure measurements are used to determine the collapsed liquid level. The liquid level is also measured directly using conductivity or optical detectors. ECC water mass-flow-rate measurements are made with electromagnetic flow meters, with an expected error of 0.5%. Mass-flow-rate measurements in the outlet nozzles of the steam generators are made with Pitot tubes. Mass-flow-rate measurements from the downcomer into the core are made with four drag disks. The steam mass-flow rate from containment tank II is measured with a venturi tube. Two-phase-flow measurements in the primary loops are made with spool pieces. A spool piece is installed in each hot and cold leg. Each spool piece consists of a three-beam gamma densitometer, a full-flow turbine flowmeter, three drag transducers attached to a drag screen, fluid and metal temperature thermocouples, an absolute pressure transducer, and a differential pressure transducer across the drag screen. The fluid densities, velocities, mass-flow rates, and void fraction can be obtained by using data-processing software. Velocimeters were installed in the lower plenum to measure the core-flooding rate.

4.7.2. Test Procedure and Description

CCTF Test C1-5 (Run 14), hereafter referred to as CCTF Run 14, was the CCTF Core-I facility base case.[4.7-1] The facility configuration, test conduct, and data were documented by JAERI.[4.7-2]

CCTF Run 14 does not directly correspond to either a best-estimate (BE) or evaluation-model (EM) condition. The power level for this test is 7% greater than the value used in current EM licensing analyses and 35% higher than a realistic BE case. ECC flows are 25% lower than the scaled ECC flow that is expected in a PWR. Pump-simulator orifices are sized to provide an equivalent locked-rotor pump resistance. The 0.2-MPa containment pressure chosen for this test is lower than that used in most licensing calculations.

In preparing for the test, the accumulator tank, LPCI tank, saturated water tank, and secondary sides of the steam-generator simulators were filled with purified water. The instruments were checked for their zero points and sensitivities.

After these preparatory operations, the primary system was heated with the preheaters to its specified temperatures (downcomer wall, core internals, and primary-loop piping wall) and was pressurized to the specified pressure using steam. The water in the accumulator tank was electrically heated to its specified temperature and pressurized with nitrogen gas to provide sufficient head to drive the injection flow required. The water in the LPCI tank was also heated to its specified temperature and was circulated through the delivery lines to preheat the lines to the same temperature as the water. The water in the secondary side of each steam-generator simulator was also heated and pressurized to the specified temperature and pressure. The water in the saturated water tank was heated to approximately the saturation temperature as the expected primary pressure.

After establishing the initial conditions of the test, the electric power for preheating was turned off and the lower plenum was filled to the specified level from the saturated water tank. When the proper water level in the lower plenum was reached (0.9 m) and other initial conditions of the test stabilized at the allowable tolerance, electric power was applied to the heater rods in the core and the data recording was started. The temperature rises in the rods were monitored by a computer. When a specified initial cladding temperature was reached, direct injection of the accumulator water into the lower plenum was initiated. The system pressure was maintained at the specified initial pressure throughout the test by controlling the outlet valve of containment tank II. The decay power input to the rods was programmed to begin when the water reached the bottom of the heated region of the core. The specified initial cladding temperature of the heater rods was predetermined by interpolation between the cladding temperature after preheating and the cladding temperature assumed for the time of bottom of core recovery (BOCREC). When the water reached the specified level below the core, the injection port for the accumulator water was switched from the lower plenum to the three intact cold-leg ECC ports. The accumulator (ACC)-injection flow rate was then reduced during the cold-leg injection. At a specified time after BOCREC, the valves in the accumulator lines and the LPCI circulation lines were closed and the valves in the LPCI injection lines were opened. These actions transferred the ECC injection from the accumulator mode (high flow rate) to the LPCI mode (lower flow rate). The steam and entrained water flowed via the broken and intact loops to the containment tanks. The steam was then vented to the atmosphere to maintain a constant pressure in the containment tanks. The test was terminated after all the thermocouples on the surface of the heater rods indicated quenching of the rods.

CCTF Run 14 proceeded as described in the previous paragraph. Direct injection of accumulator water into the previously filled lower plenum began after power was applied to the core and after the cladding temperature at a specified location reached 506°C. When the lower plenum filled and the water level reached the bottom of the heated core, the core power followed a programmed transient to simulate decay power. The injection port was changed from the lower plenum to the three intact cold-leg ECC ports 14 s after the start of ACC injection. As specified, 22 s after the initiation of ACC injection, ECC injection was transferred from the accumulator ACC injection mode (high flow rate) to the LPCI mode (lower flow rate). The operating parameters for CCTF Run 14 are presented in Table 4.7-1.

4.7.3. TRAC Model

Several TRAC-PF1/MOD1 input models have been developed for simulation of CCTF Run 14. These include (1) a finely noded, 3D vessel model with 16 axial levels, 4 radial sectors, and 4 azimuthal sectors; (2) a coarsely noded, 3D vessel model with 16 axial levels, 2 radial sectors, and 2 azimuthal sectors; and (3) a finely noded 1D vessel model with 24 axial levels, 1 radial sector, and 1 azimuthal sector. Of these three versions of the CCTF Run 14 input model, only the latter has been updated so that it can be run using TRAC-PF1/MOD2 and modernized, FORTRAN 77 (TRAC-M/F77) codes. Therefore, by default, this model was selected for this reflood developmental assessment activity. The CCTF Run 14 1D vessel model has also been used for assessment of an earlier code version by JAERI.[4.7-4] The use of a 1D vessel model is justified based on this assessment, as well as on an evaluation by JAERI of the CCTF

Core-I Reflood Test C1-5 (Run 14),[4.7-6] which basically concludes that the core thermo-hydraulic behavior is nearly 1D.

The CCTF Run 14 1D-TRAC input model used in this assessment directly models only the core and upper plenum of the CCTF-I facility. The boundaries of the model have been reduced by artificially limiting the model to a limited region of the larger test facility, i.e., not modeling the downcomer and cold legs, thereby permitting a more direct assessment of the core thermal-hydraulic modeling. In effect, the added degrees of freedom associated with the downcomer and cold legs have been eliminated. However, this approach requires that appropriate boundary conditions be applied if the simplified model is to be acceptable. To this end, the core-inlet boundary conditions are specified by a Fill component with time-dependent, core-inlet mass flow and fluid temperature. The core-outlet boundary conditions are specified by a single Break component, with the time-dependent pressure specified. The total power supplied to the heater rods is also provided.

The noding diagram for the input model is shown in Fig. 4.7-5. The CCTF core and upper plenum are modeled with 24 axial levels. The core is modeled with 18 axial levels. The axial power profile of Fig. 4.7-4 is modeled. The fine axial noding used in the core of the CCTF Run 14 model (~0.2-m-high axial levels) is not consistent with the noding used in standard full-plant models. For example, core nodes in an AP600 model are ~0.6 m high. To see the effect of core noding, a parametric noding calculation in which the core is coarsely noded into six axial levels is presented in Sec. 4.7.5.

The inlet Fill (component 1) is connected via the Pipe (component 2) to axial cell 1. The Break (component 5) is connected to axial cell 23 via the Pipe (component 4). The core extends axially from levels 2 through 19. Figure 4.7-6 shows the modeled core inlet mass flow, which is based on the mass flow measured at the lower plenum. The previous CCTF Run 14 TRAC input model used a mass-flow input to the lower plenum based on flow measurements taken upstream of the core. This was not an accurate representation of the flow entering the lower plenum. The CCTF Run 14 model was corrected to model the flow entering the lower plenum accurately. The high initial flow between 63 and 78 s is from ACC injection flow. The flow thereafter is from the low-pressure ECC injection flow. The specified input tables for core-inlet coolant temperature, upper-plenum pressure, and core power also reflect measured values. Figure 4.7-7 shows the time-averaged core flooding rate, defined as the time-averaged core inlet mass flow divided by the core inlet flow area and the density of the core inlet flow.

A listing of the input model used for this developmental assessment calculation is found in Appendix I. Archival storage information for this input model is provided in Section 4.7.7.

4.7.4. Comparison of Predicted and Measured Results

The calculation was performed with TRAC-M/F77, Version 5.5. These results are for newrfd=3, which activates the reflood model with an explicit top-down reflood modeling. An identical set of graphical code-data comparisons for Version 5.5 with newrfd=1 is presented without analysis in Appendix J. Setting newrfd=1 activates the bottom-up reflood model as it existed for TRAC-PF1/MOD2 developmental assessment

calculations. We have run CCTF Run 14 calculations both with and without the grid-spacer model. We have determined that the grid-spacer model should not be used because it results in excessive and nonphysical heat-transfer processes in the upper portions of the core. Therefore, the base-case assessment results for CCTF Run 14 do not use the TRAC grid-spacer model (see Section 4.4-5 for details).

The cladding thermal response during an LBLOCA transient, whether measured or predicted, is carefully analyzed because of the associated safety implications. Three cladding thermal-response-related parameters of importance are (1) the PCT, (2) the PCT time (the time at which the PCT is reached), and (3) the time at which the cladding at a given axial position is quenched. One of the challenges we have faced is the need to access and acquire the experimental database for each of the experiments used for TRAC assessment. We have not completed this effort for CCTF Run 14. Therefore, to develop several important comparisons of predicted and measured results, we resorted to extracting experimental data from Ref. 4.7-4. This is a secondary source; thus, we have identified all such uses of secondary-source data for the CCTF Run 14 in the applicable figure caption.

A comparison of the predicted and measured PCTs as a function of elevation within the core is shown in Fig. 4.7-8. Measured PCTs at only five elevations were presented in Ref. 4.7-4. The predicted and measured PCTs are in excellent agreement up to an elevation of ~1.75 m. The predicted PCTs are higher than measured in the upper portions of the core.

A comparison of the predicted and measured PCT times as a function of elevation within the core is shown in Fig. 4.7-9. The two data traces identify the range of PCT times observed during the test at each axial level within the core. The TRAC-predicted PCT times are always later than measured but are in reasonable agreement with the PCT times observed in the test in the lower 40% of the core (1.5-m level). However, at higher elevations the predicted PCT time is much later than observed in the test.

A comparison of the predicted and measured quench times as a function of elevation within the core is shown in Fig. 4.7-10. Quench times are improved with the revised mass flow input. The predicted quench times are in excellent agreement to an elevation of 2.0 m. The calculated transient was run to only 450 s. The transient should be rerun until the quenching is predicted at the 3.1-m level to complete the comparison with the measured quench-time results.

The overall trends observed in Figs. 4.7-8 through 4.7-10 also can be seen by comparing predicted and measured cladding temperatures at a given axial level as a function of time. Predicted and measured wall-temperatures at elevations of 0.38, 1.105, 1.83, 2.44, and 3.05 m are shown in Figs. 4.7-11 through 4.7-13, respectively. At the 0.38-m level, there is an almost exact agreement between the predicted results and the measured data. At the 1.105-m level, the predicted PCT is ~30 K higher than measured and the predicted PCT time is ~30 s later than measured, but the predicted quench time is within 1 s of the measured quench time.

At the 1.83-m level or core midplane (Fig. 4.7-12), the predicted PCT is ~50 K higher than measured and the predicted PCT time is ~90 s later than measured, but the quench

time is within 5 s of the measured quench time. The agreement is judged to be reasonable.

The agreement between predicted and measured PCTs degrades in the upper portions of the core; the agreement is judged to be minimal. The predicted and measured PCTs at the 2.44- and 3.05-m levels are shown in Fig. 4.7-13. Clearly, TRAC underpredicts the cooling of the heater rods in the upper portions of the core. At the 2.44-m level, the PCT is 102 K higher than measured and the PCT time is 95 s later than the measured time. At the 3.05-m level, the PCT is 107 K higher than measured and the PCT time is 167 s later than the measured time. Predicted and measured quench times and quench front velocities in the bottom half of the core are summarized in Table 4.7-2. For the lower half of the core, the predicted and measured quench front velocities are in reasonable agreement.

The underlying cause for the reasonable prediction of cladding temperature response in the lower half of the core and the degraded prediction in the upper half of the core can be inferred from Figs. 4.7-14 through 4.7-16. These figures compare the predicted and measured core-axial, void-fraction profiles at three different times: 37, 137, and 237 s. These times are defined from the start of reflood. With the revised mass flow input model, the calculated void fraction profile at 37 s matches the data better than before. The void fraction profiles at 137 and 237 s are about the same as before. Clearly, at higher elevations in the core, TRAC underpredicts the liquid content of the two-phase flow.

The overall trends observed in Figs. 4.7-14 through 4.7-16 also can be seen by comparing predicted and measured core-ΔP values across four levels of the core as a function of time. Predicted and measured core-ΔP histories between the 0- and 0.61-, 0.61- and 1.22-, 1.22- and 1.83-, and 1.83- and 2.44-m elevations are shown in Figs. 4.7-17 through 4.7-20, respectively. The solid lines show the predicted pressure-drop history, and the dotted lines show the measured data. The reference point for these elevations is the bottom of the core. These elevations can be cross-referenced to the facility model by referring to Fig. 4.7-4. An offset of 0.2 m must be addressed (i.e., the 0.61-m level of the ΔP plot is offset by an additional 0.2 m in Fig. 4.7-4 and therefore appears as 0.810 m). The corresponding vapor fraction plots (i.e., average void fraction between the same elevations for which core ΔP are plotted) are shown in Fig. 4.7-21.

Progressing upward through the core, reasonable agreement between the predicted and measured core-ΔP traces is observed between 0.0 and 0.61 m (Fig. 4.7-17). Between 60 and 150 s, there is a slight underprediction of the core-ΔP, but thereafter, there is good agreement between the predicted and measured values.

There is minimal-to-reasonable agreement between the predicted and measured core-ΔP traces between 0.61 and 1.22 m (Fig. 4.7-18). There is a sharp overprediction at 100 s, followed by a sharp underprediction at 120 s. The underprediction continues out to about 180 s, but thereafter, the core ΔP is overpredicted. The corresponding predicted vapor fraction for the portion of the core between 0.61 and 1.22 m is presented in Fig. 4.7-21. Because the core ΔP is directly translatable to the amount of liquid at these elevations, undercooling of the core at the 1.105-m level is consistent (see Fig. 4.7-11).

The comparison of predicted and measured core-ΔP traces between 1.22 and 1.83 m (Fig. 4.7-19) shows that the trend of underpredicting the pressure drop at higher core elevations is accelerating. Because the core ΔP is directly translatable to the amount of liquid at these elevations, undercooling of the core is consistent (see Fig. 4.7-12). The corresponding predicted vapor fraction for the portion of the core between 1.22 and 1.83 m is presented in Fig. 4.7-21.

The comparison of predicted and measured core-ΔP traces between 1.83 and 2.44 m (Fig. 4.7-20) shows that the prediction of pressure drop at higher core elevations continues to degrade. As the core ΔP is directly translatable to the amount of liquid at these elevations, undercooling of the core is consistent (see Fig. 4.7-13). The corresponding predicted vapor fraction for the portion of the core between 1.83 and 2.44 m is presented in Fig. 4.7-21.

Finally, a comparison of predicted and measured core mass is shown in Fig. 4.7-22. The predicted core mass consistently is lower than measured. In earlier code versions,[4.7-4] reasonable agreement was obtained between the predicted and measured core mass. However, the liquid mass below the quench front was overpredicted, and the liquid mass above the quench front was underpredicted. For the current calculation, the predicted liquid mass below the quench front is in reasonable agreement with the measured liquid mass, whereas a deficiency of liquid above the quench front is predicted (Figs. 4.7-14 through 4.7-16). Because the total (integrated) predicted and measured core-inlet mass flows are in close agreement throughout the test (Fig. 4.7-6), too much coolant is predicted to exit the core. This suggests that the root cause may lie with either the interfacial drag model (the transport rate of liquid through the core above the quench front is too rapid) or the interfacial heat-transfer model (too much liquid-to-steam transformation).

4.7.5. Renoding Sensitivity Study

A renoding sensitivity study was performed where the core was noded more coarsely. The 18 levels of the core were combined into 6 levels for an average cell height of ~0.6 m. However, the 17-step axial power profile modeled in the 18-level core was retained. The renoded CCTF-14 model is shown in Fig. 4.7-38. The renoded model input listing is presented in Appendix W.

A comparison of the 18- and 6-level, core-model calculated results to measured data is presented in Figs. 4.7-39 through 4.7-51. These figures are the same set of plots presented in Figs. 4.7-8 through 4.7-20 but with the 6-level, core-model calculated results added. The comparison is for the calculation where newrfd=3 and grid spacers are not modeled.

In general, the coarser noding results in lower PCTs, later PCT times, and later quench times than the finely noded model. Figure 4.7-39 shows that the 6-level, core-model calculated PCTs are slightly higher than the 18-level, core-model PCTs at the lower elevations but are higher at rod elevations of ~2 m. Figure 4.7-40 shows slightly later PCT times for the 6-level core at the rod elevations below 1.4 m and above 2 m. Figure 4.7-41 shows earlier quench times for the 6-level core below 1 m and later quench times at rod elevations of ~1 m.

In Fig. 4.7-42, the calculated rod temperatures for the two core models are almost the same at 0.38 m; however, at the 1.105-m elevation, the 6-level core shows a higher PCT, a later PCT time, and a later quench time than the 18-level core. At the 1.83-m elevation shown in Fig. 4.7-43, the 6-level core shows a lower PCT and later quench time than the 18-level core. In Fig. 4.7-44, the 6-level core shows lower calculated PCTs than the 18-level core.

The void fraction profiles of Figs. 4.7-45 through 4.7-47 show that the 6-level, core-model profiles are not as good as the 18-level, core-model profiles. Figures 4.7-48 through 4.7-51 show that the ΔPs calculated with the 6-level core are not as good as the ΔPs calculated with the 18-level core.

A full set of calculations was performed for the renoded model, which was the same set performed for the finely noded model: (1) newrfd=3 without grid spacers, (2) newrfd=3 with grid spacers, (3) newrfd=1 without grid spacers, and (4) newrfd=1 with grid spacers. A full set of calculation plots for the coarsely noded model, corresponding to Figs. 4.7-8 through 4.7-37 for the finely noded model, is presented in Appendix X for the newrfd=3 calculations (with and without grid spacers) and in Appendix Y for the newrfd=1 calculations (with and without grid spacers).

4.7.6. Conclusions

A developmental assessment of TRAC-M, Version 5.5, has been completed using data from CCTF Run 14. There was minimal-to-reasonable agreement between the predicted and measured cladding temperatures for the lower half of the core. However, above the midplane, the agreement between predicted and measured cladding temperatures is minimal. These results are consistent with both predicted and measured core-axial, void-fraction distributions at specified times and with time-varying, void-fraction traces at a given elevation.

The predicted vapor fraction above the core midplane consistently approaches a value of 1.0 (fully voided), whereas the data show a vapor fraction between 0.8 and 0.9 at these same elevations. A long-standing issue remains about cold surfaces in the upper portion of the core, which are hypothesized to condense vapor and collect a thin liquid film. This film is thought to increase the pressure drop but is otherwise inferred as the presence of increased liquid in the two-phase mixture flowing through the upper elevations of the core. The cold-wall effect may be real and may account for part of the liquid inferred to exist in the coolant stream. However, the underprediction of clad cooling in the upper portions of the core clearly is consistent with the presence of more liquid at these elevations than predicted.

The predictions of PCT times are in reasonable agreement with the measured values for the lower part of the core but are in only minimal agreement in the upper part of the core. This outcome is consistent with the underprediction of liquid in the upper portions of the core. The predictions of cladding quench times are in reasonable agreement with the measured times in the lower two-thirds of the core. Higher in the core, the predicted quench times are later than measured. Again, this outcome is consistent with the underprediction of liquid in the upper portions of the core.

For the current calculation, the predicted liquid mass below the quench front is in reasonable agreement with the measured liquid mass, whereas a deficiency of liquid above the quench front is predicted. Because the total (integrated) predicted and measured core-inlet mass flows are in close agreement throughout the test, too much coolant is predicted to exit the core. This suggests that the root cause of the differences between measured and predicted core-inlet mass flows may lie with either the interfacial drag model (because the transport rate of liquid through the core above the quench front is too rapid) or the interfacial heat-transfer model (too much liquid-to-steam transformation).

In general, a coarser noding of the core results in a less accurate calculation. Lower PCTs, later PCT times, and later quench times are calculated with a coarsely noded core model rather than with a finely noded core model. Void fraction profiles and core ΔPs also are less accurate.

CCTF Run 14 was conducted differently than that modeled. The test featured a more integral nature than modeled in that there was ECCS injection into the cold legs during a portion of the test; however, the test was modeled as a separate-effects test with no downcomer. Use of this approach required that time-varying boundary conditions be provided at the core inlet (coolant mass-flow rate and temperature) and upper-plenum outlet (pressure).

4.7.7. Code Performance

CCTF Core-I Run 14 was calculated on code Version 5.5. The calculation performance information plus other pertinent comments follow.

Finely Noded 18-Level Core Input Model

Platform	Sun Sparc 20
Total CPU time (s)	2844
Archive location of input model	CFS /tida/f77da/task4.4bdecks/incctf14.corr
Archive location of calculation	CFS /trac-da/F77DA/task4.4b/cctf14.corr.tar.gz

Coarsely Noded 6-Level-Core Input Model

Platform	Sun Sparc 20
Total CPU time (s)	1616
Archive location of input model	CFS /tida/f77da/task4.4bdecks/incctf14.renode
Archive location of calculation	CFS /trac-da/F77DA/task4.4b/cctf14.renode.tar.gz

REFERENCES

4.7-1. P. S. Damerell and J. W. Simons, Eds., "2D/3D Program Work Summary Report," US Nuclear Regulatory Commission document NUREG/IA-0126 (June 1993).

4.7-2. K. Hirano, et. al., "Data Report on Large Scale Reflood Test-14—CCTF Test C1-5 (Run 014)," Japan Atomic Energy Research Institute document JAERI-Memo-57-214 (August 1982).

4.7-3. "Separate Effects Test Matrix for Thermal-Hydraulic Code Validation, Volume I—Phenomena Characterization and Selection of Facilities and Tests," Organization for Economic Co-operation and Development Nuclear Energy Agency document NEA/CSNI/R(93)/Part. 1/Rev. and "Volume II—Facility and Experiment Characteristics," Organization for Economic Cooperation and Development Nuclear Energy Agency document NEA/CSNI/R(93)/Part 2/Rev. (September 1993).

4.7-4. H. Akimoto, "Analysis of TRAC-PF1 Calculated Core Heat Transfer for a CCTF Test," *Nuclear Engineering and Design* **88**, 215–227 (1985).

4.7-5 Y. Murao, H. Akimoto, T. Sudoh, and T. Okubo, "Evaluation Report on CCTF Core-I Reflood Test C1-5 (Run 14)," Japan Atomic Energy Research Institute document JAERI-M-83-027 (February 1983).

TABLE 4.7-1

OPERATING PARAMETERS FOR CCTF RUN 14

System Pressure	2.02 kg/cm^2
Total Power	9.36 MW_t
Radial Power Distribution	1.07:1.0:0.82
Downcomer Wall Temperature	182°C
Primary Piping Wall Temperature	120°C
Steam-Generator Secondary-Side Liquid Temperature	262°C
Peak Clad Temperature at ECC Injection Initiation	502°C
ECC Liquid Temperature	114°C
Lower-Plenum Liquid Level	0.87 m
ACC Injection Rate	278 m^3/h
Low-Pressure Coolant Injection Rate	30.2 m^3/h

TABLE 4.7-2

PREDICTED AND MEASURED QUENCH TIMES AND QUENCH-FRONT VELOCITIES FOR CCTF RUN 14

Location (m)	Quench Time (s)		Quench-Front Velocity (mm/s)	
	Experiment	Calculation	Experiment	Calculation
0.38	70	79	5.4	4.7
1.105	151	133	9.0	13.4
1.83	332	298	4.0	4.4

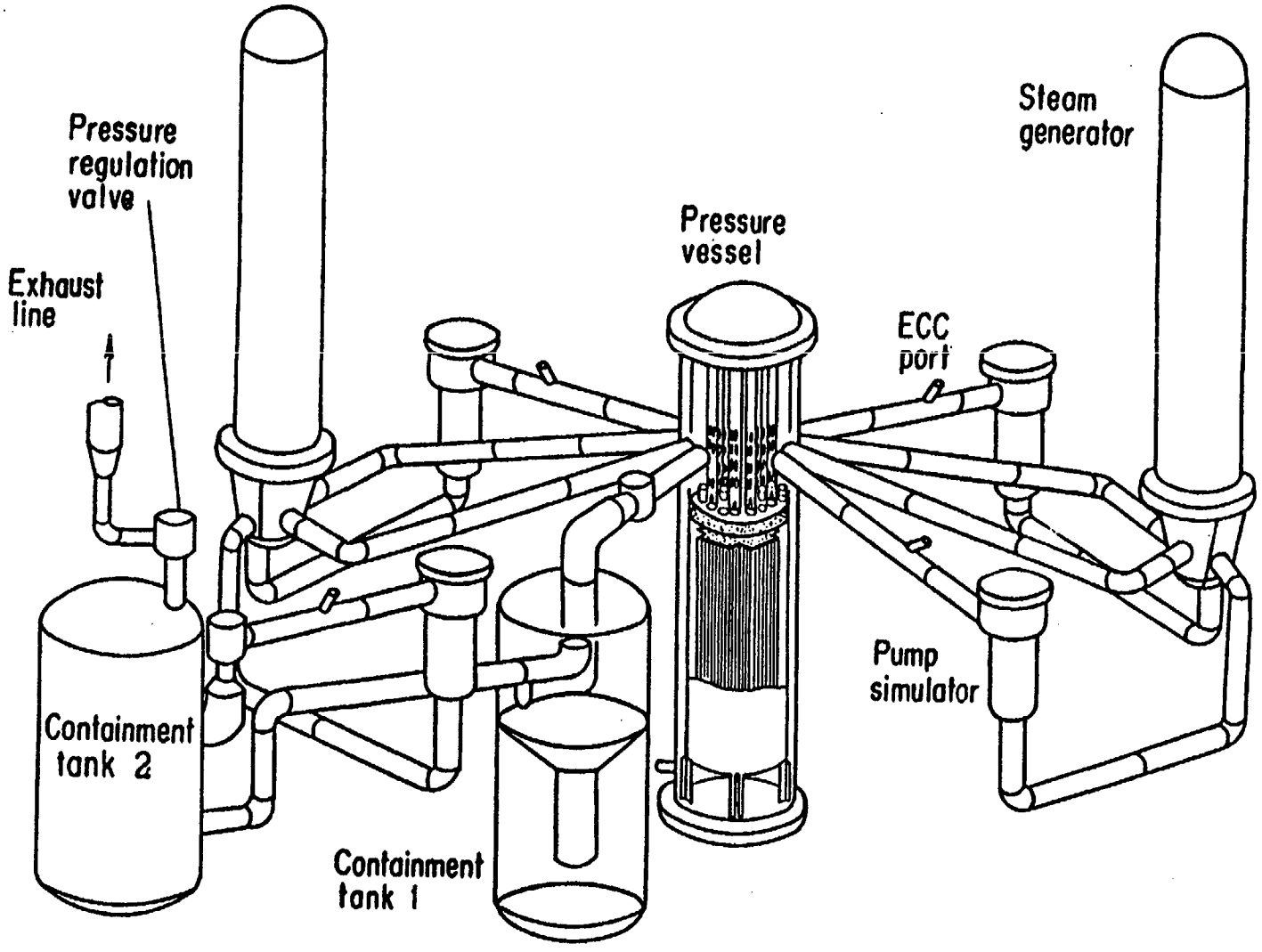

Fig. 4.7-1. Isometric view of CCTF.

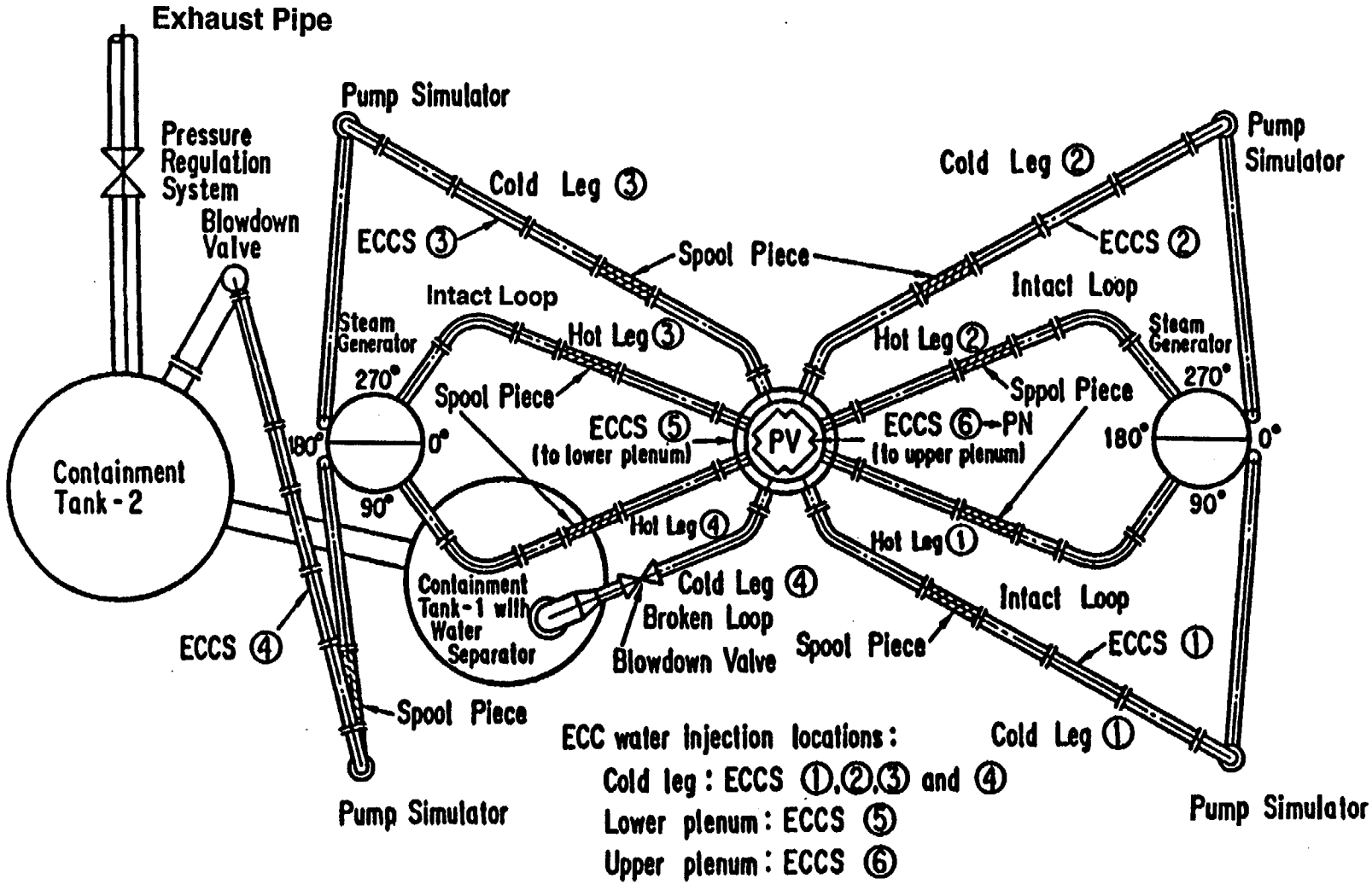

Fig. 4.7-2. Top view of primary-loop piping layout.

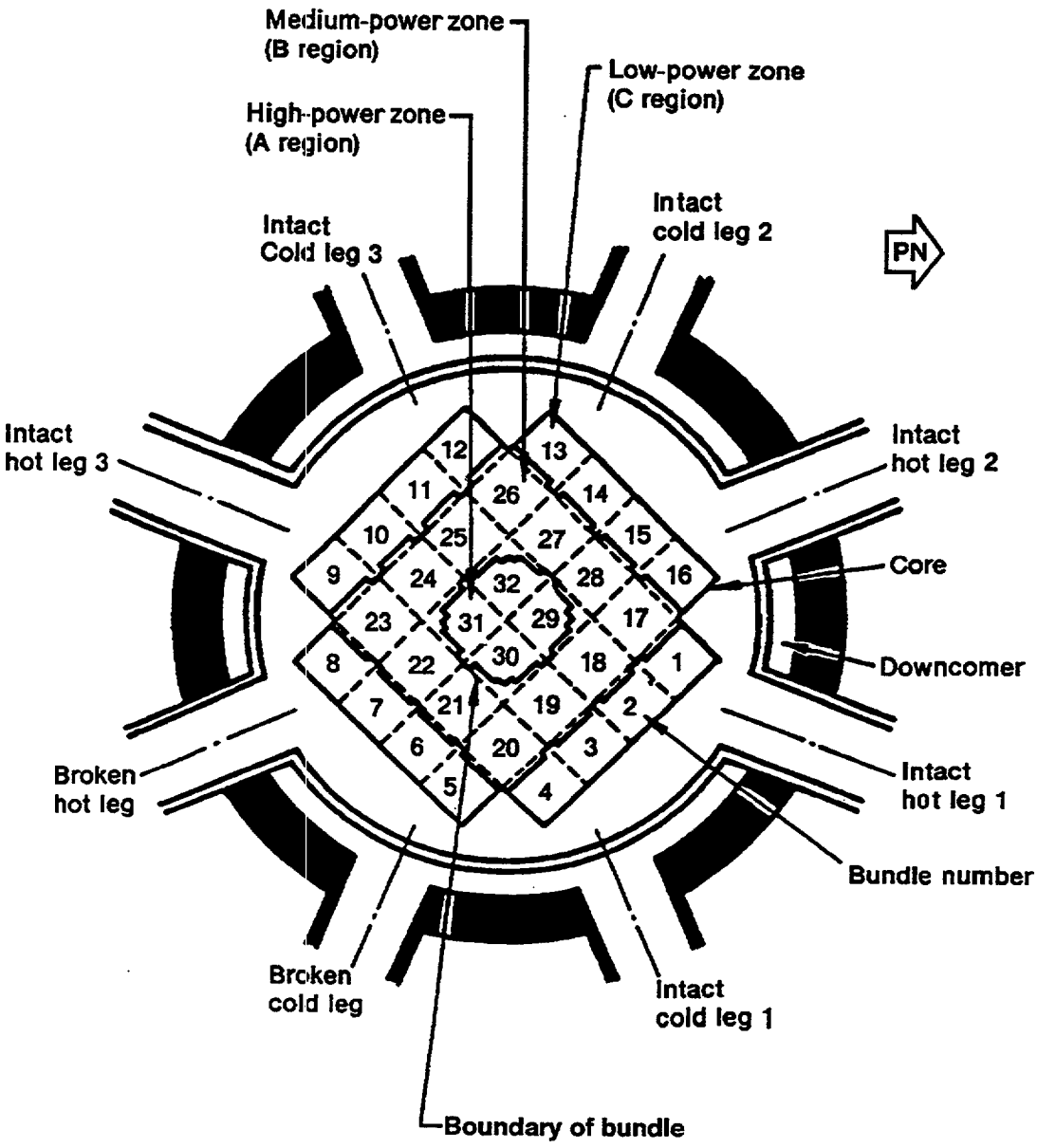

Fig. 4.7-3. Cross section of the CCTF pressure vessel through the Core-I vessel core and primary-loop nozzles.

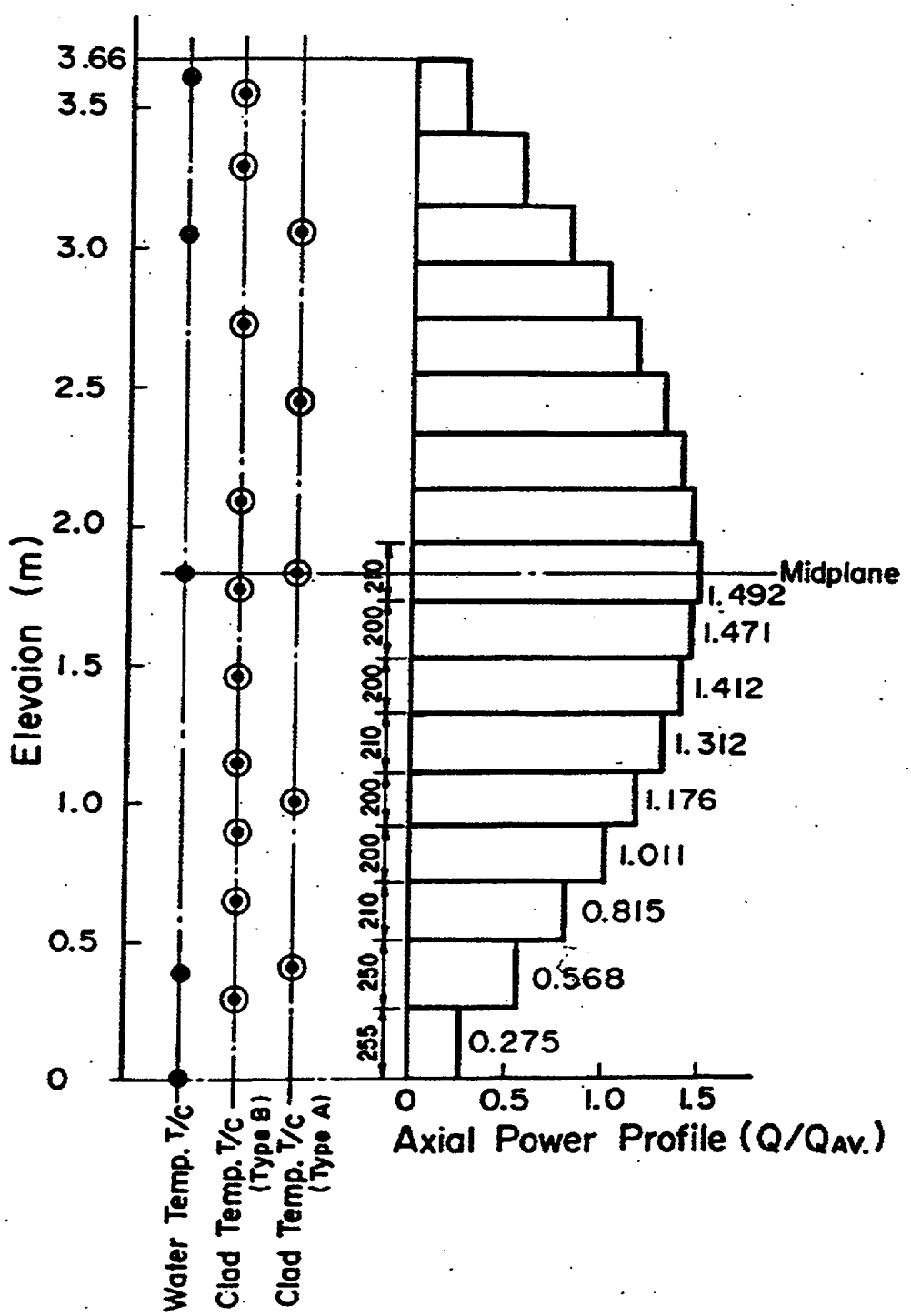

Fig. 4.7-4. CCTF Core-1 axial power profile.

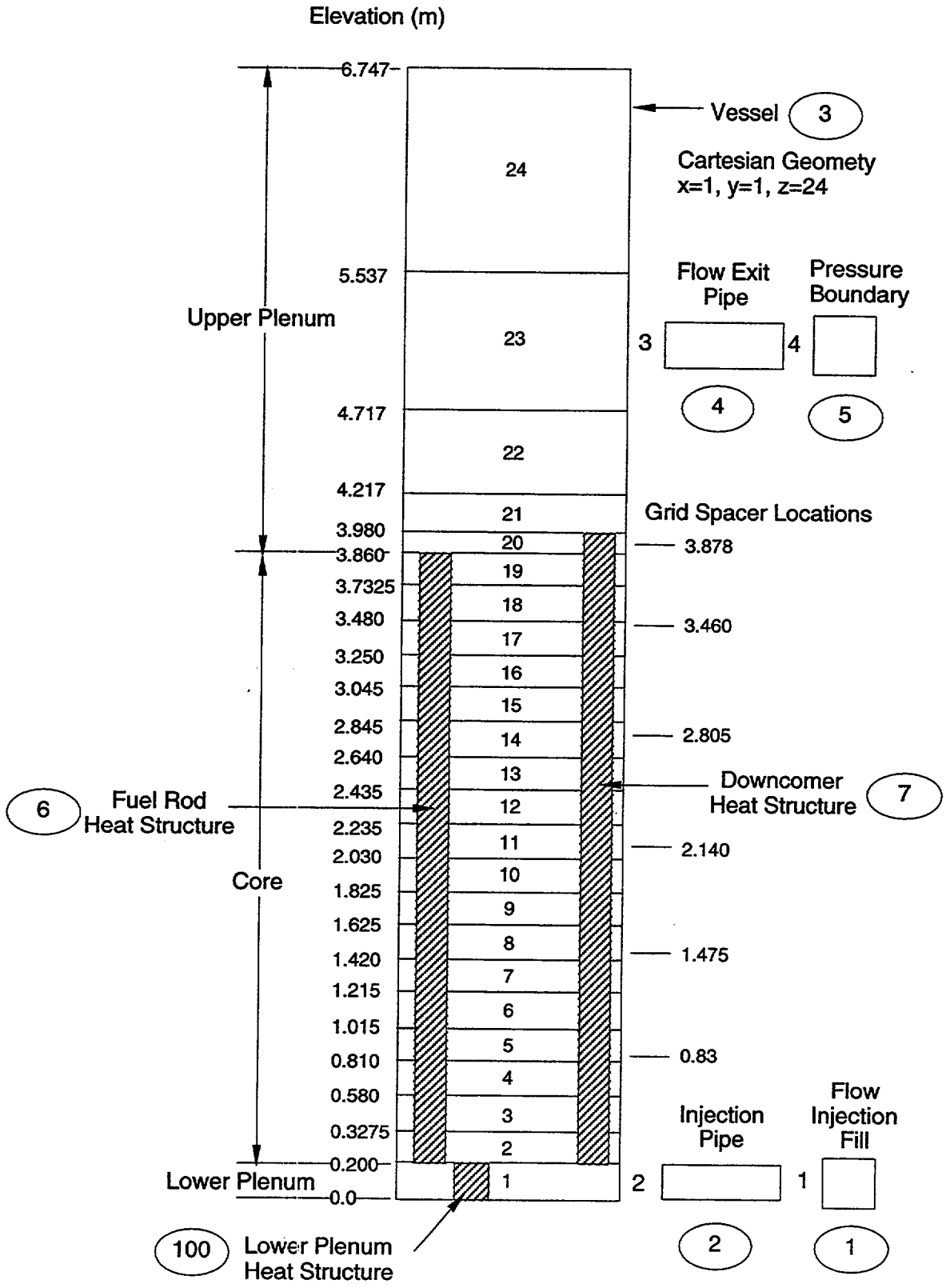

Fig. 4.7-5. CCTF Run 14 input model noding diagram.

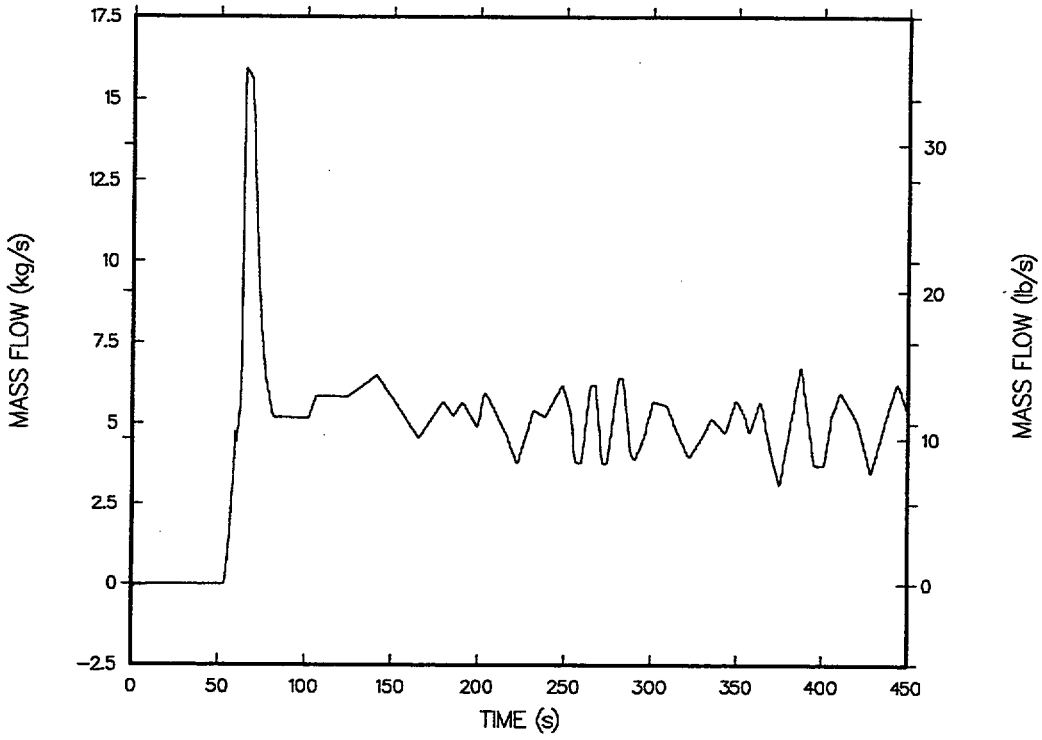

Fig. 4.7-6. Measured core-inlet mass flow.

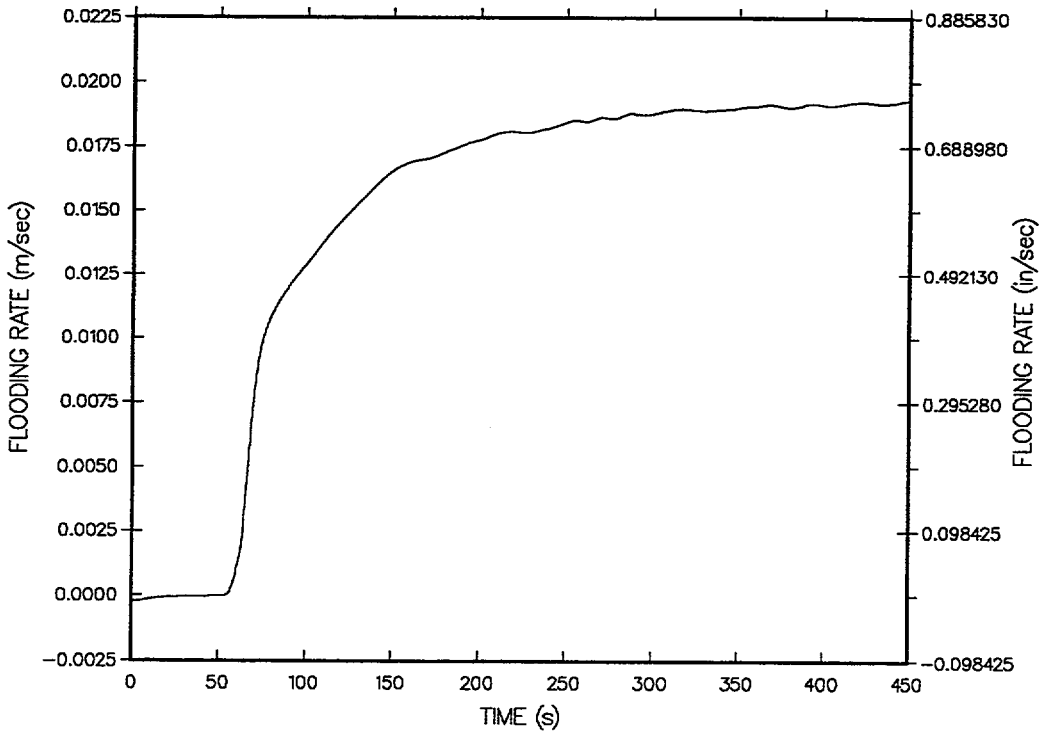

Fig. 4.7-7. Time-averaged core flooding rate.

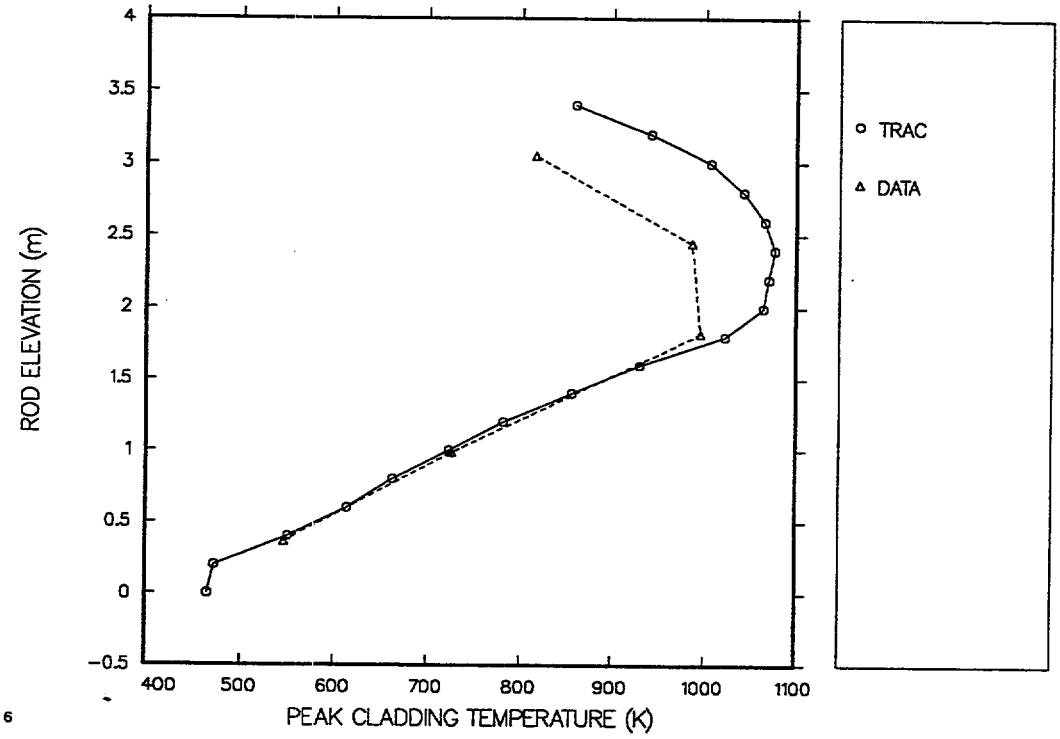

Fig. 4.7-8. Comparison of predicted and measured PCTs (experimental data from Ref. 4.7-6).

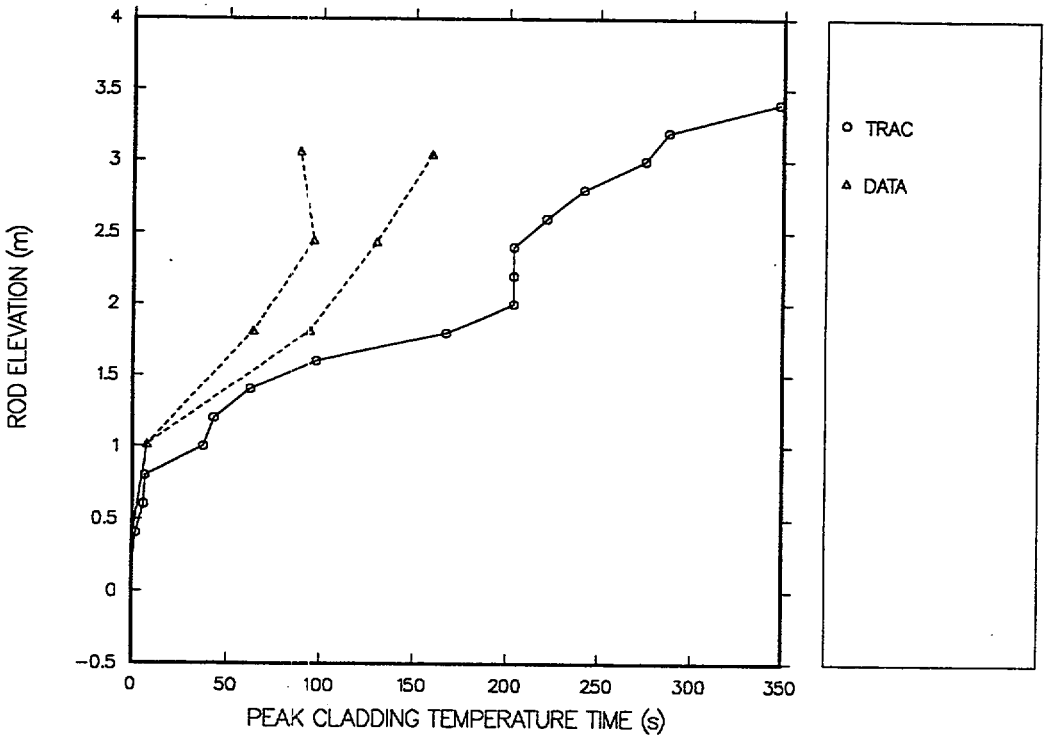

Fig. 4.7-9. Comparison of predicted and measured PCT times (experimental data from Ref. 4.7-6).

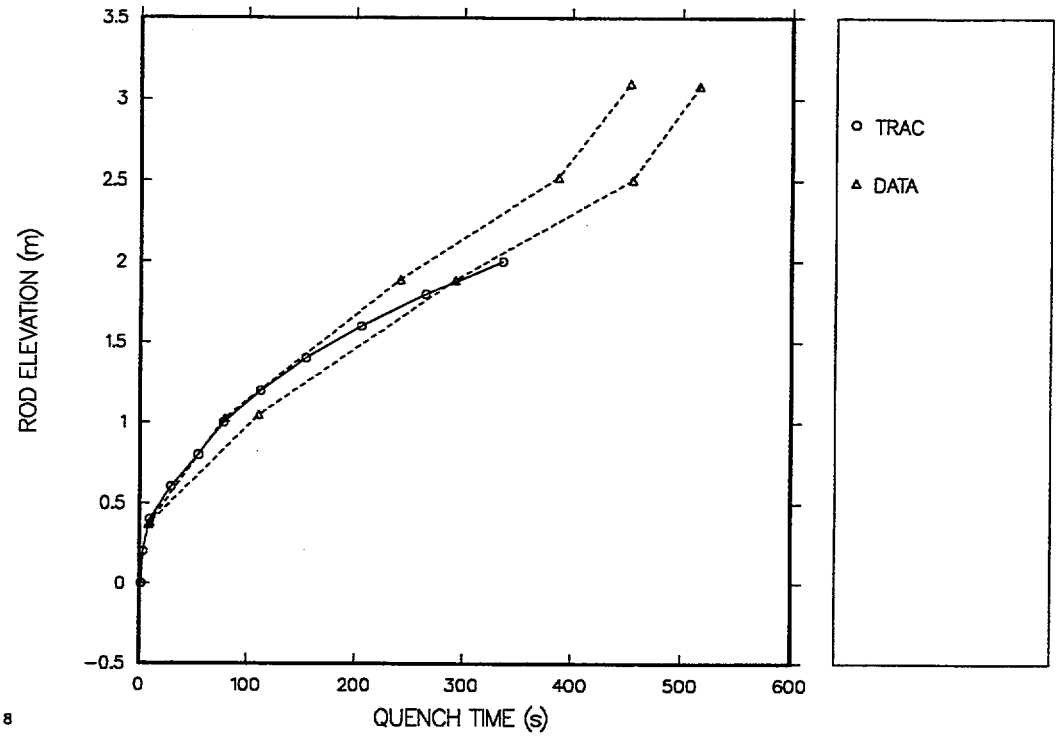

Fig. 4.7-10. Comparison of predicted and measured quench times (experimental data from Ref. 4.7-6).

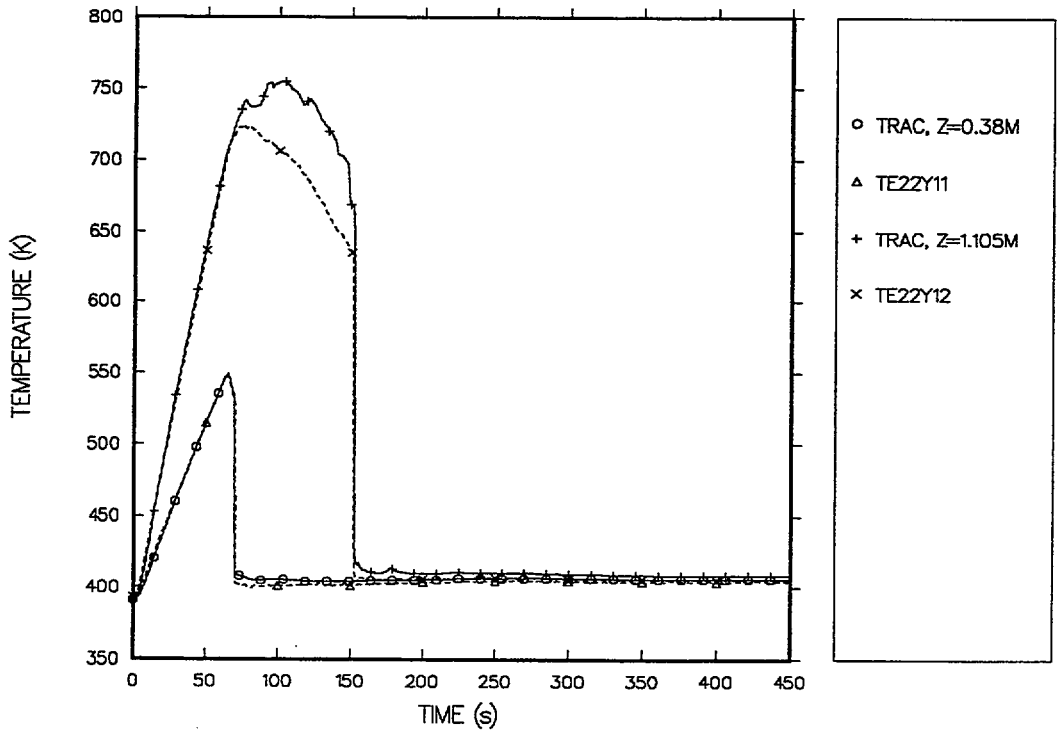

Fig. 4.7-11. CCTF-14 run: Wall-temperature histories at 0.38- and 1.105-m elevations.

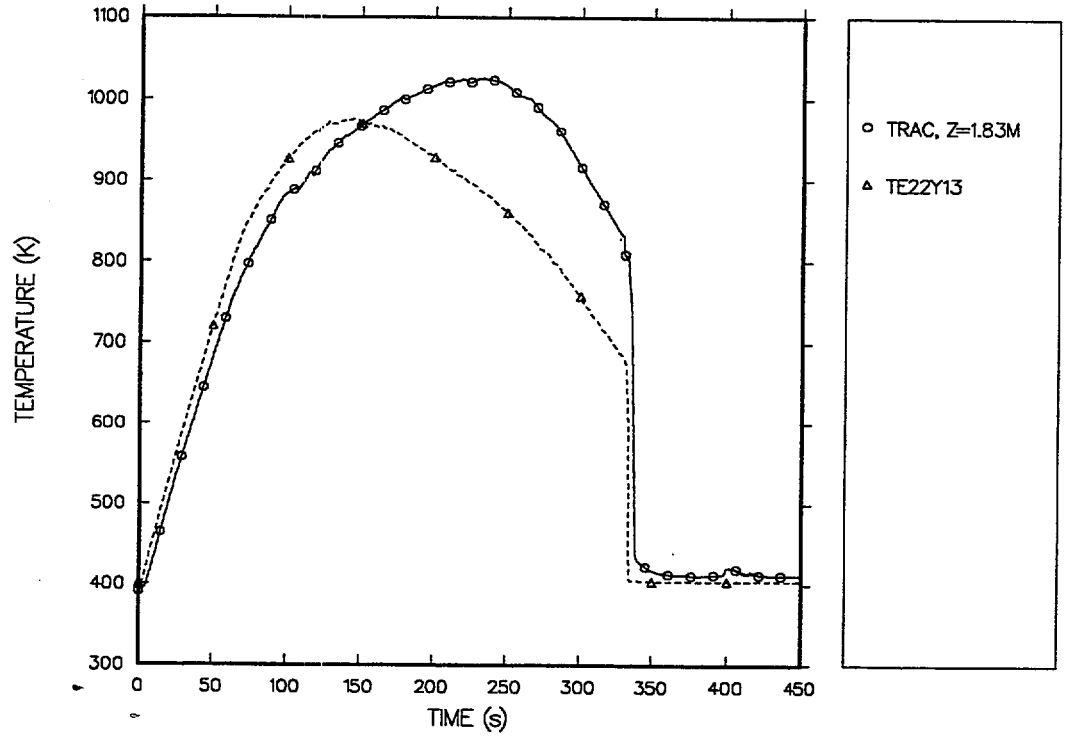

Fig. 4.7-12. CCTF-14 run: Wall-temperature histories at 1.83-m elevations.

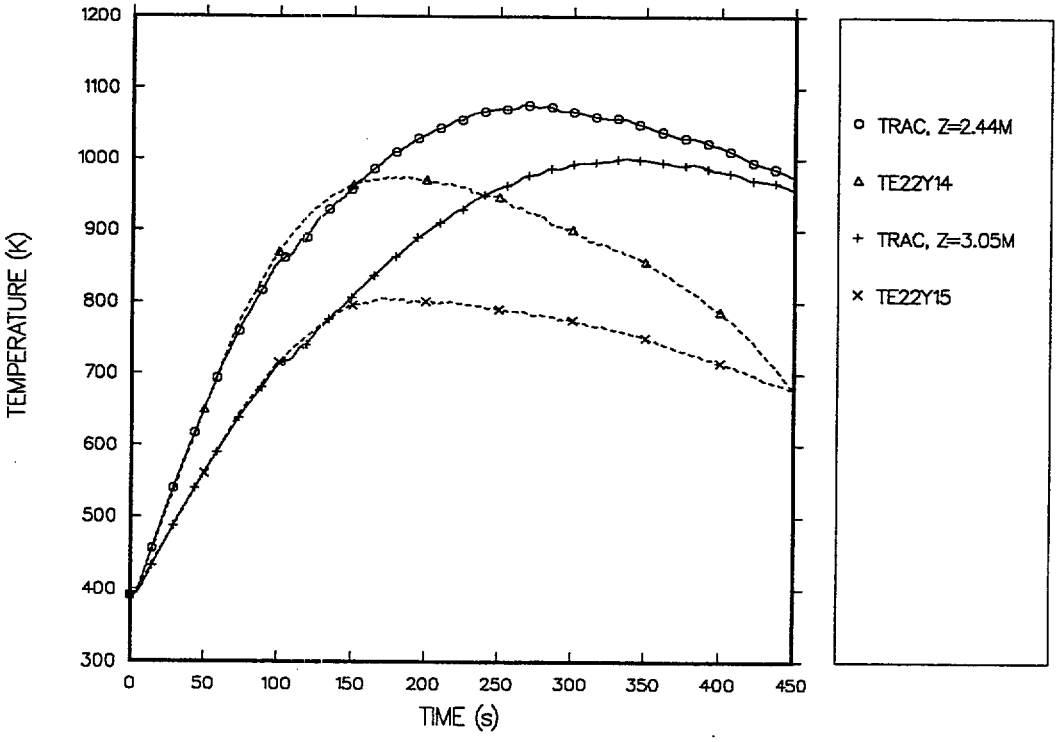

Fig. 4.7-13. CCTF-14 run: Wall-temperature histories at 2.44- and 3.05-m elevations.

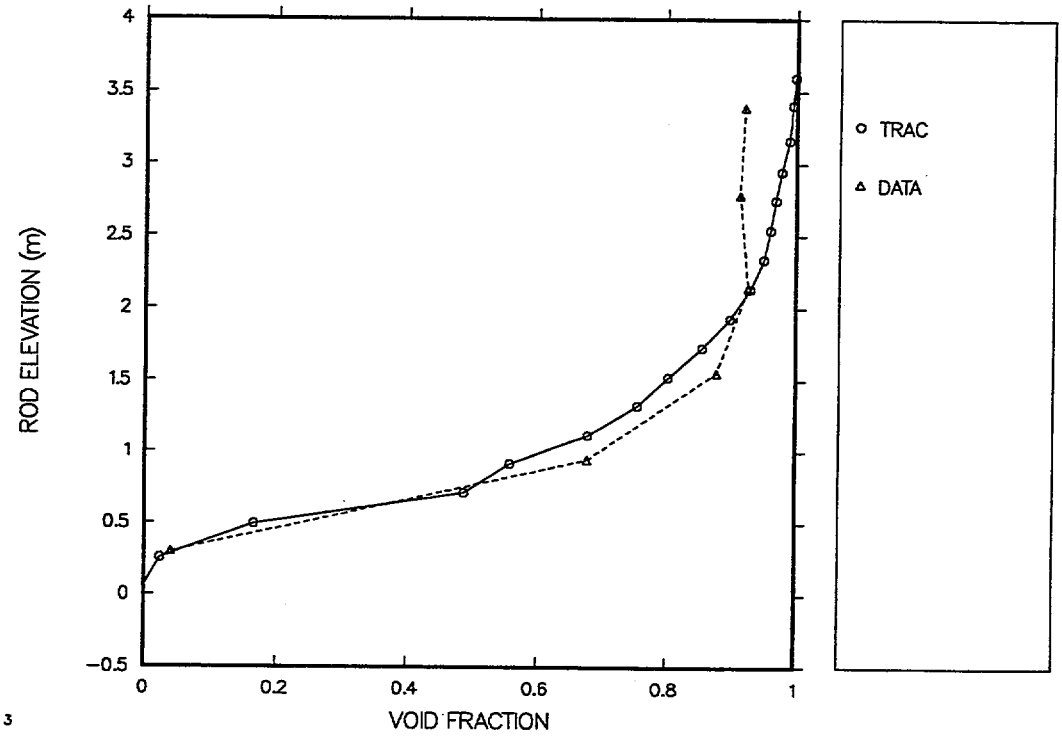

Fig. 4.7-14. Comparison of predicted and measured core-axial void-fraction profiles at 37 s (experimental data from Ref. 4.7-6).

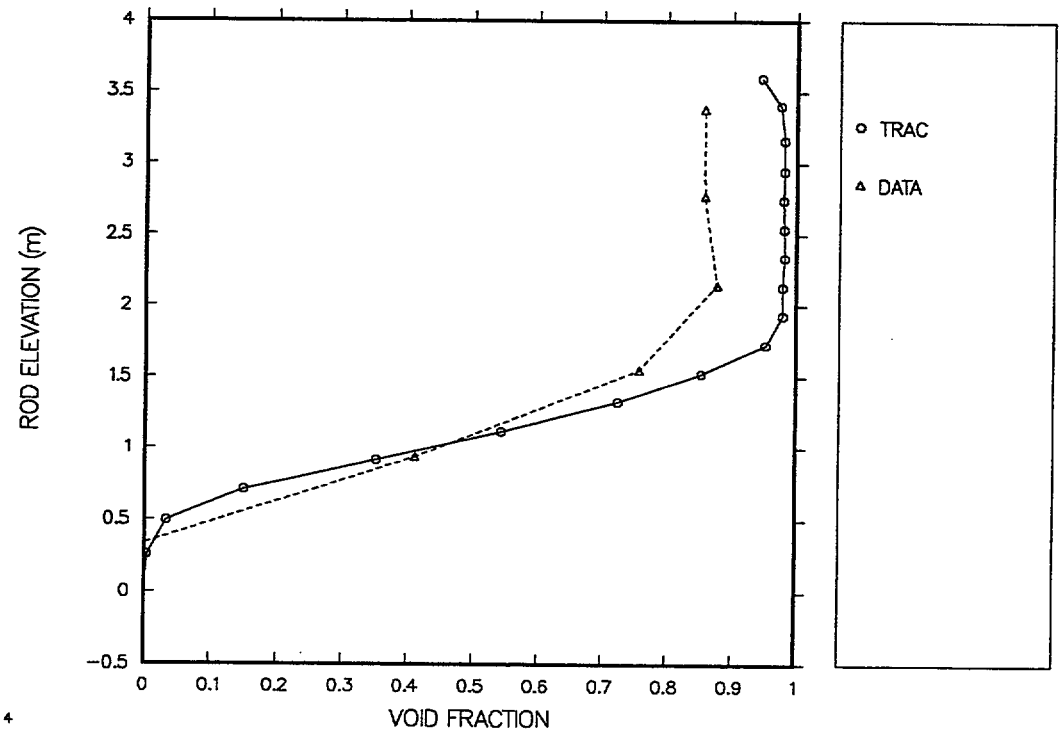

Fig. 4.7-15. Comparison of predicted and measured core-axial void-fraction profiles at 137 s (experimental data from Ref. 4.7-6).

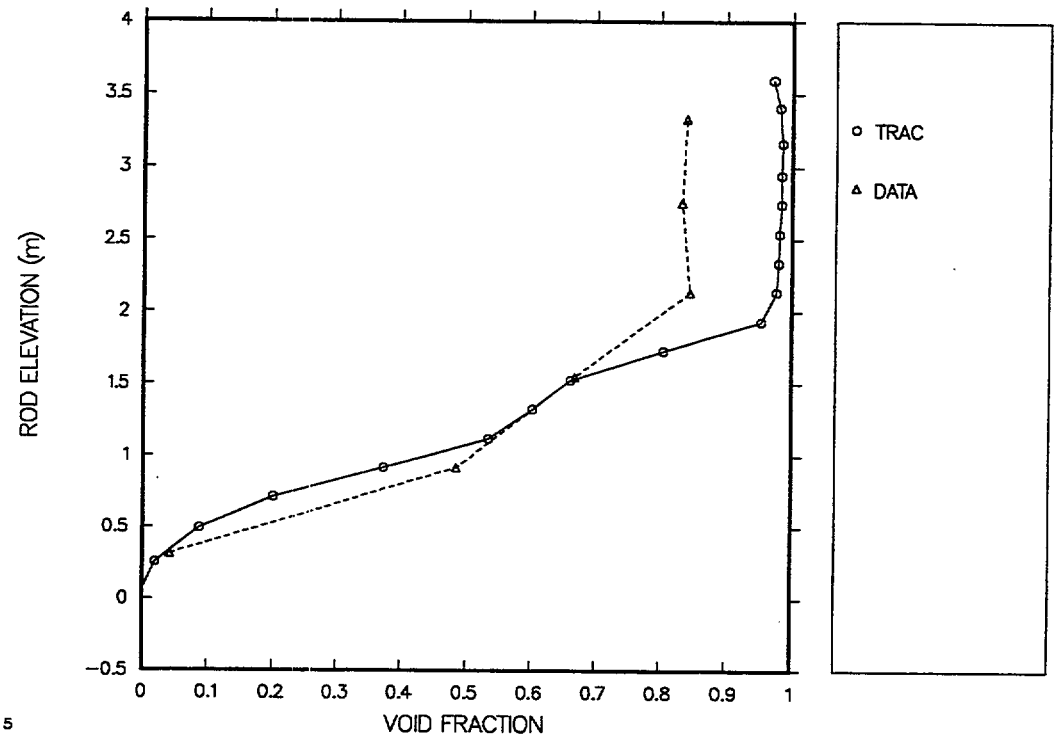

Fig. 4.7-16. Comparison of predicted and measured core-axial void-fraction profiles at 237 s (experimental data from Ref. 4.7-6).

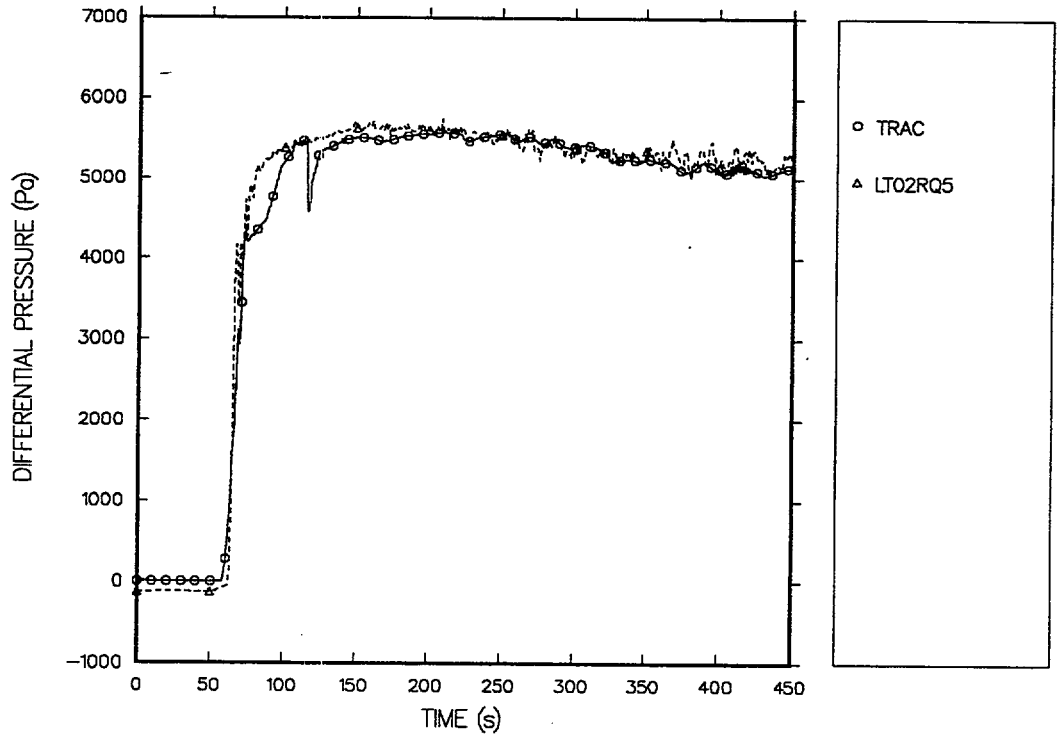

Fig. 4.7-17. CCTF-14 run: Core ΔP history between the 0.0- and 0.61-m elevations.

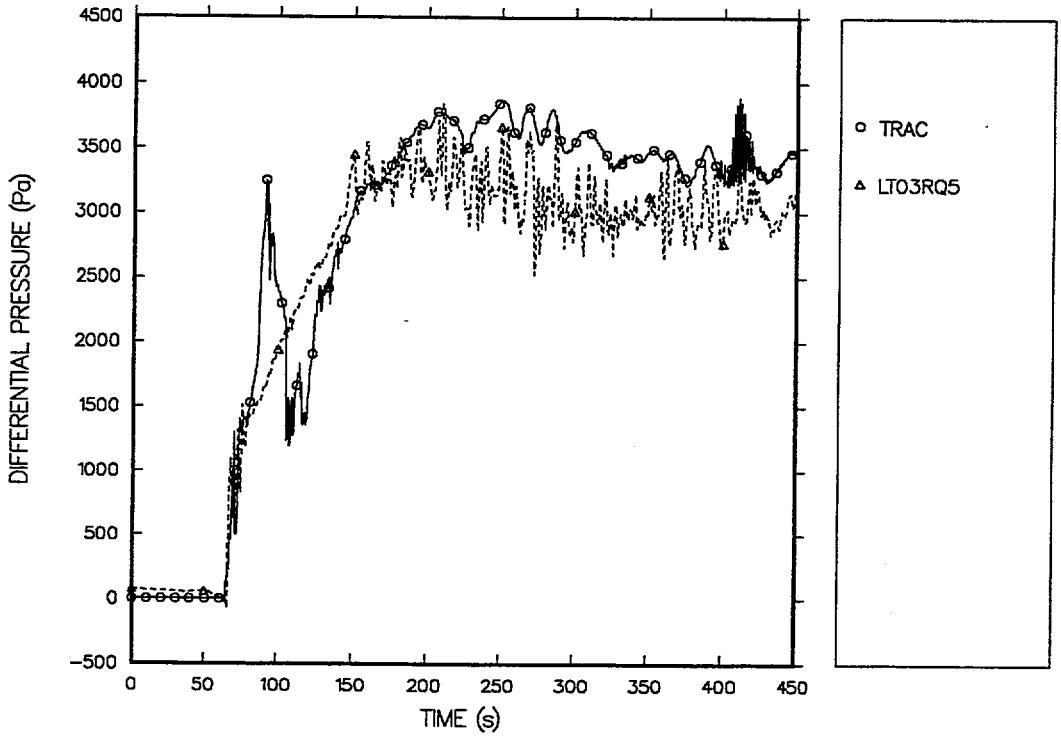

Fig. 4.7-18. CCTF-14 run: Core ΔP history between the 0.61- and 1.22-m elevations.

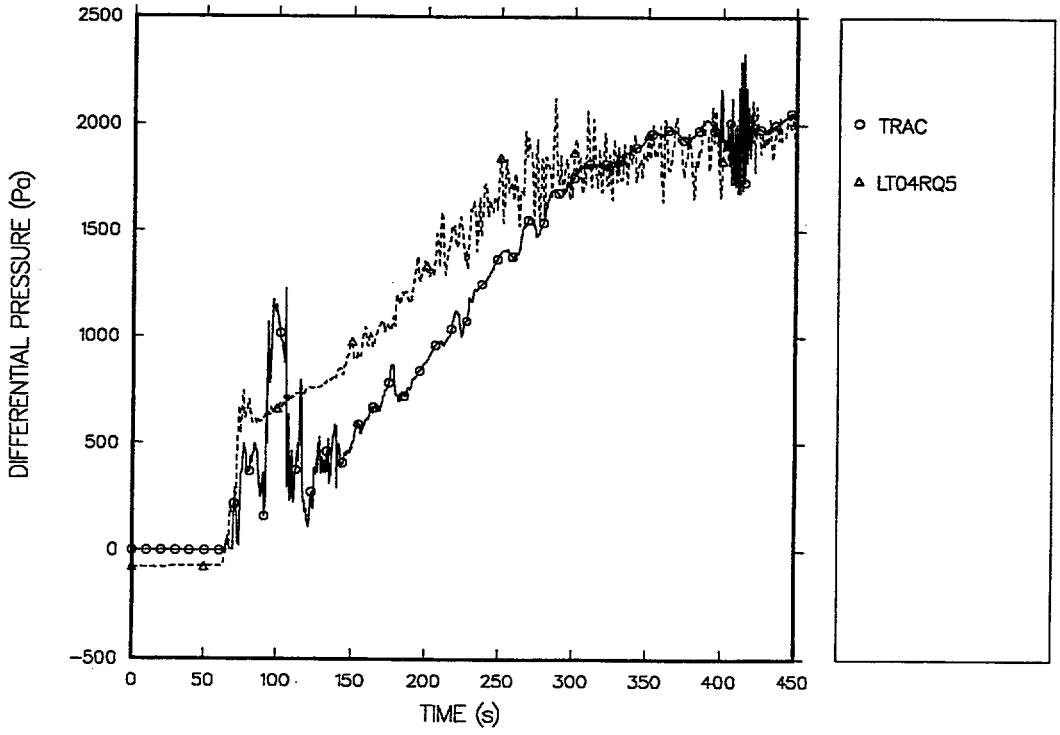

Fig. 4.7-19. CCTF-14 run: Core ΔP history between the 1.22- and 1.83-m elevations.

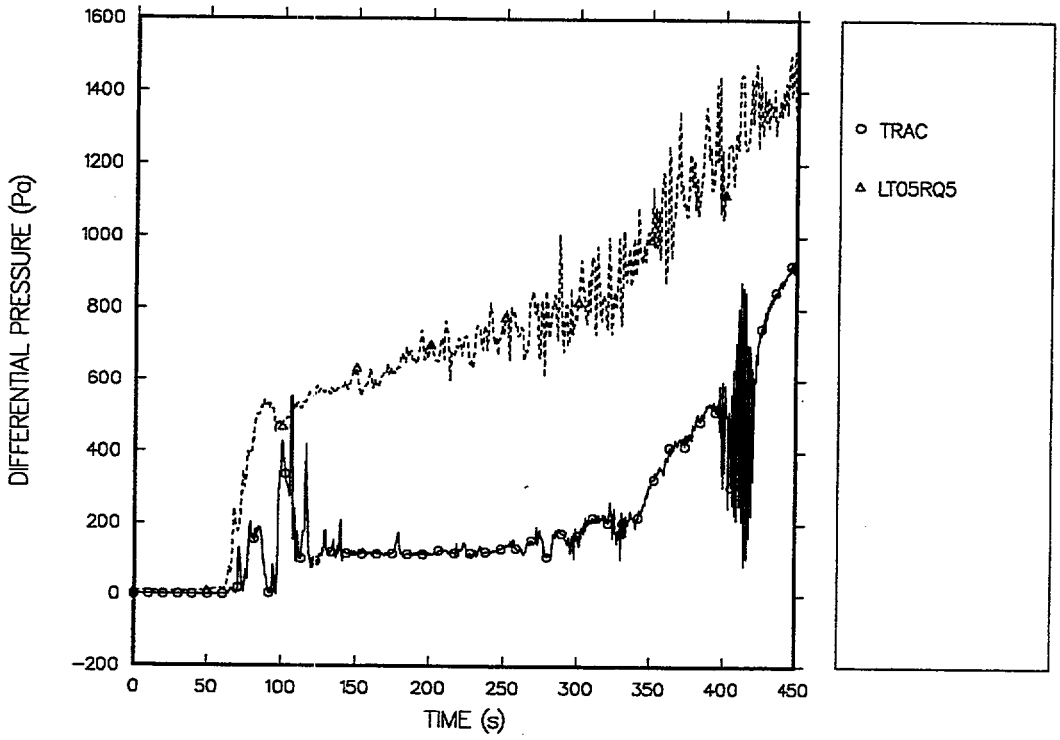

Fig. 4.7-20. CCTF-14 run: Core ΔP history between the 1.83- and 2.44-m elevations.

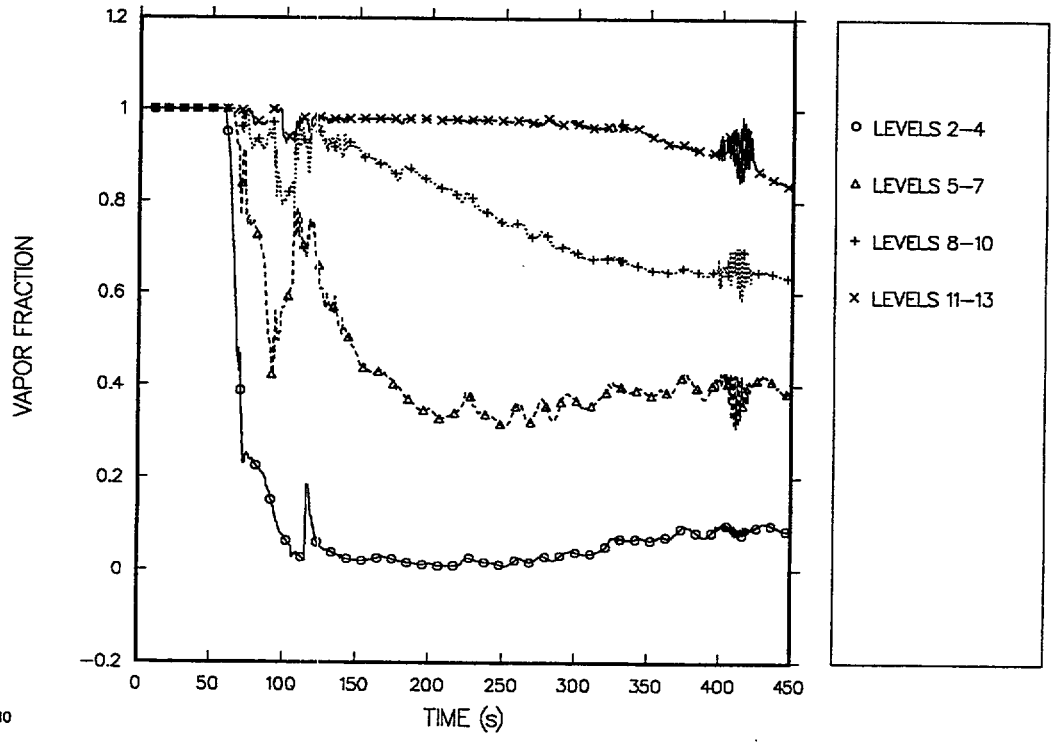

Fig. 4.7-21. CCTF-14 run: Predicted void-fraction histories within the core.

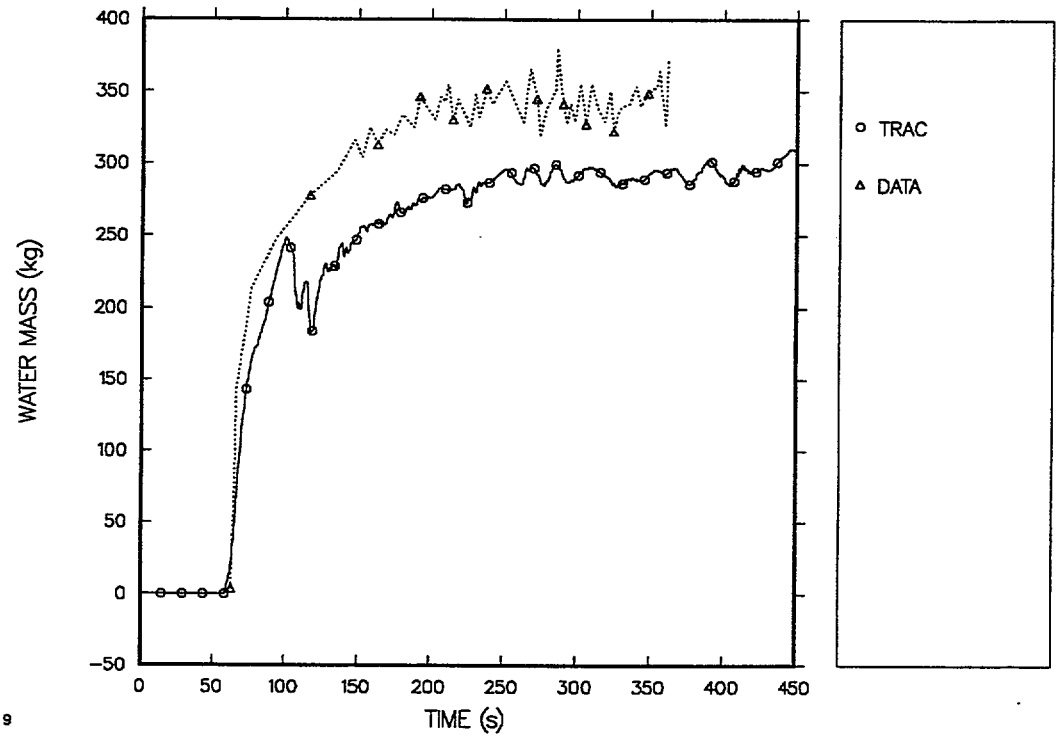

Fig. 4.7-22. CCTF-14 run: Comparison of predicted and measured core mass.

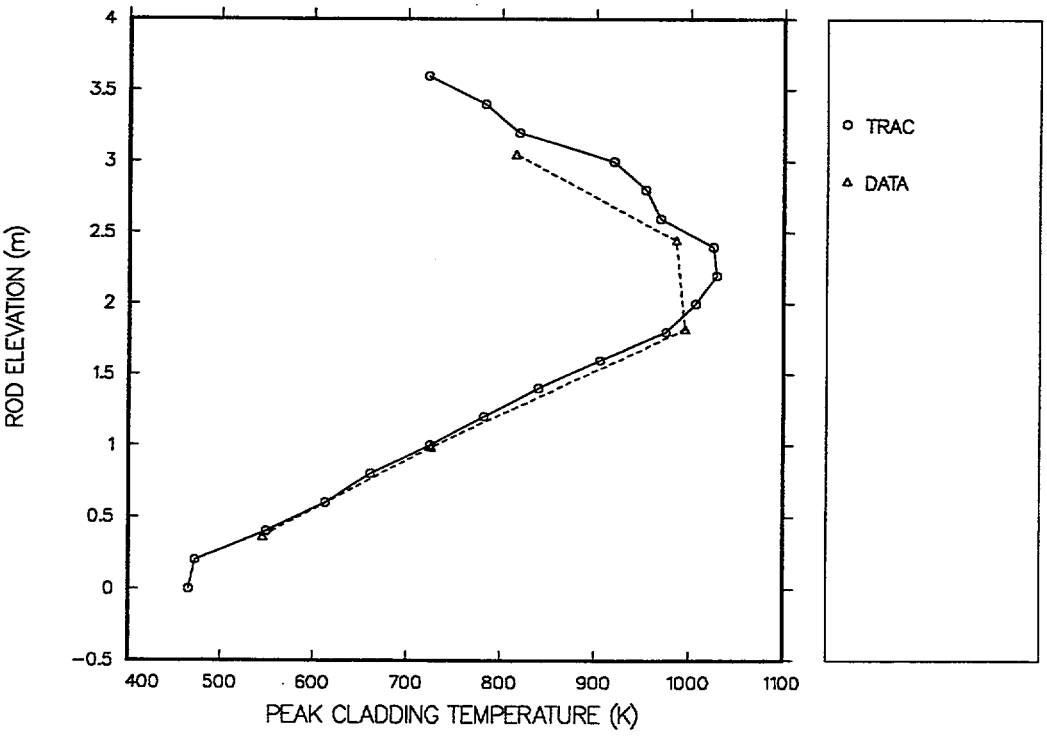

Fig. 4.7-23. Comparison of predicted and measured PCTs with the grid-spacer model (experimental data from Ref. 4.7-6).

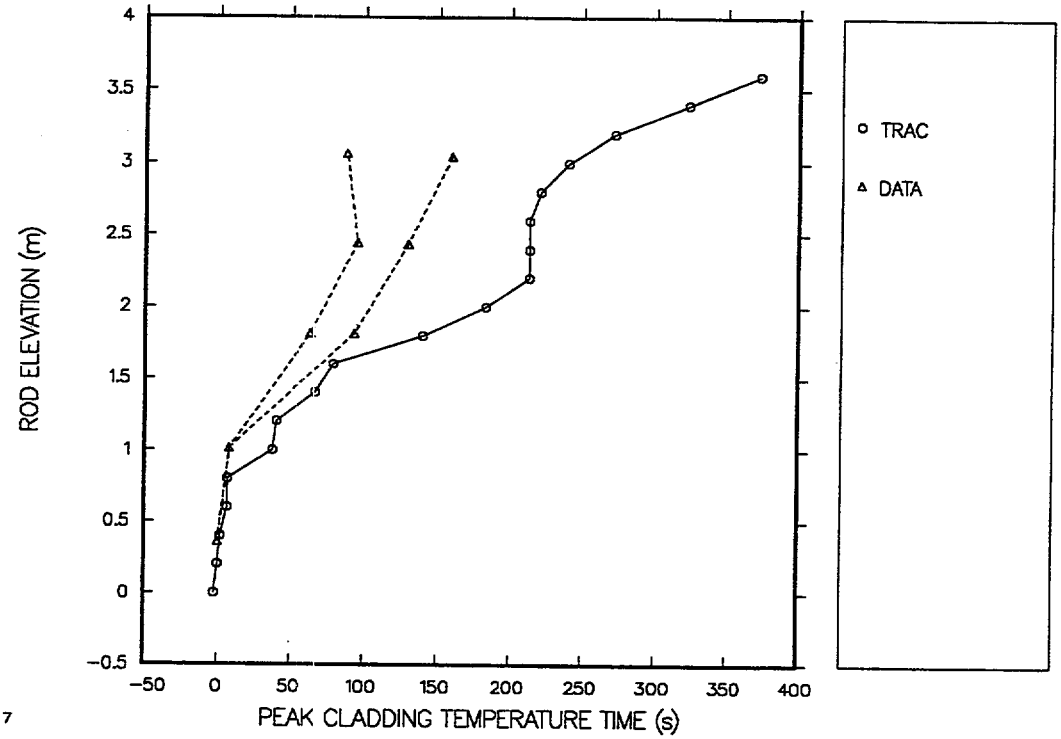

Fig. 4.7-24. Comparison of predicted and measured PCT times with the grid-spacer model (experimental data from Ref. 4.7-6).

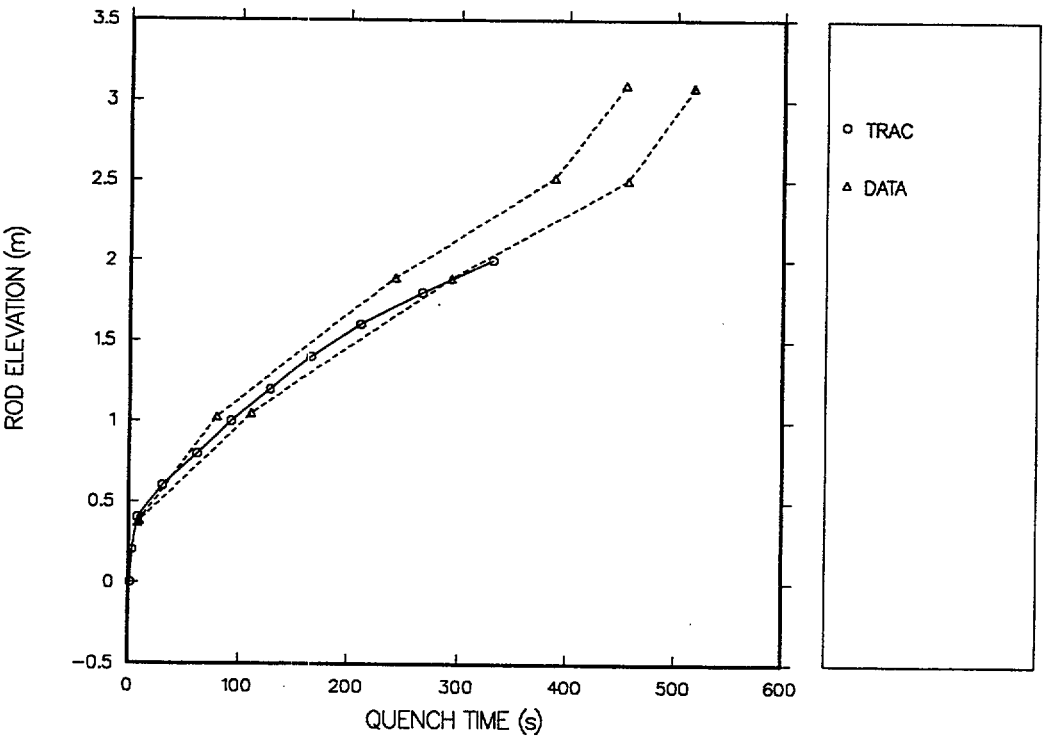

Fig. 4.7-25. Comparison of predicted and measured quench times with the grid-spacer model (experimental data from Ref. 4.7-6).

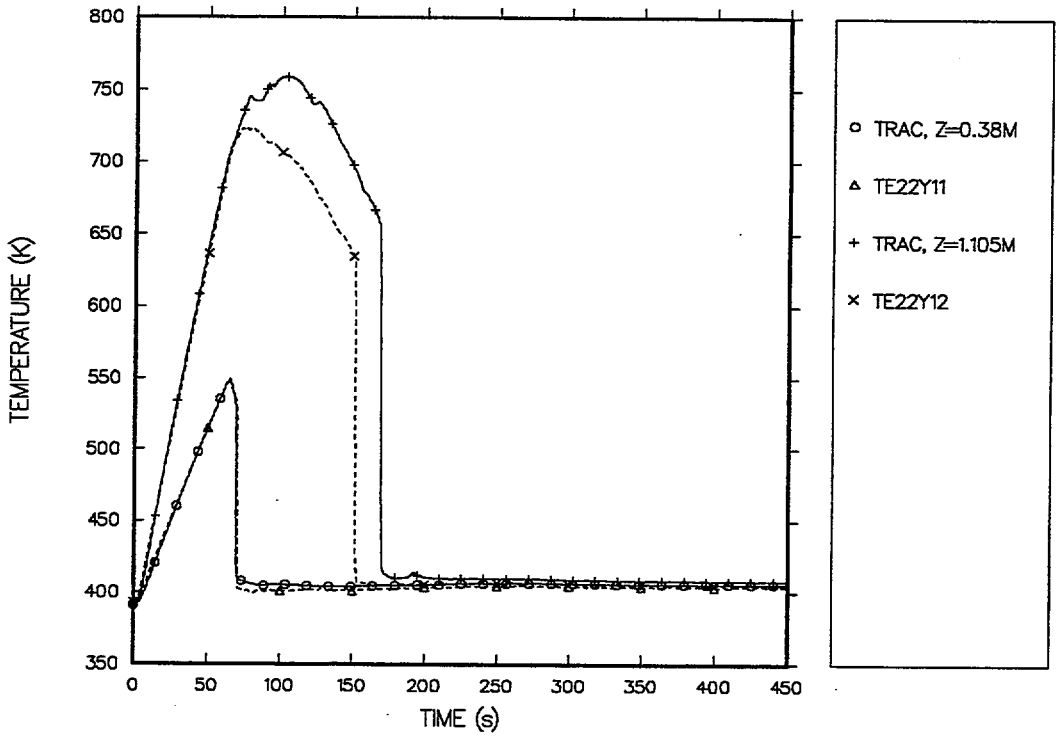

Fig. 4.7-26. CCTF-14 run: Wall-temperature histories at 0.38- and 1.105-m elevations with the grid-spacer model.

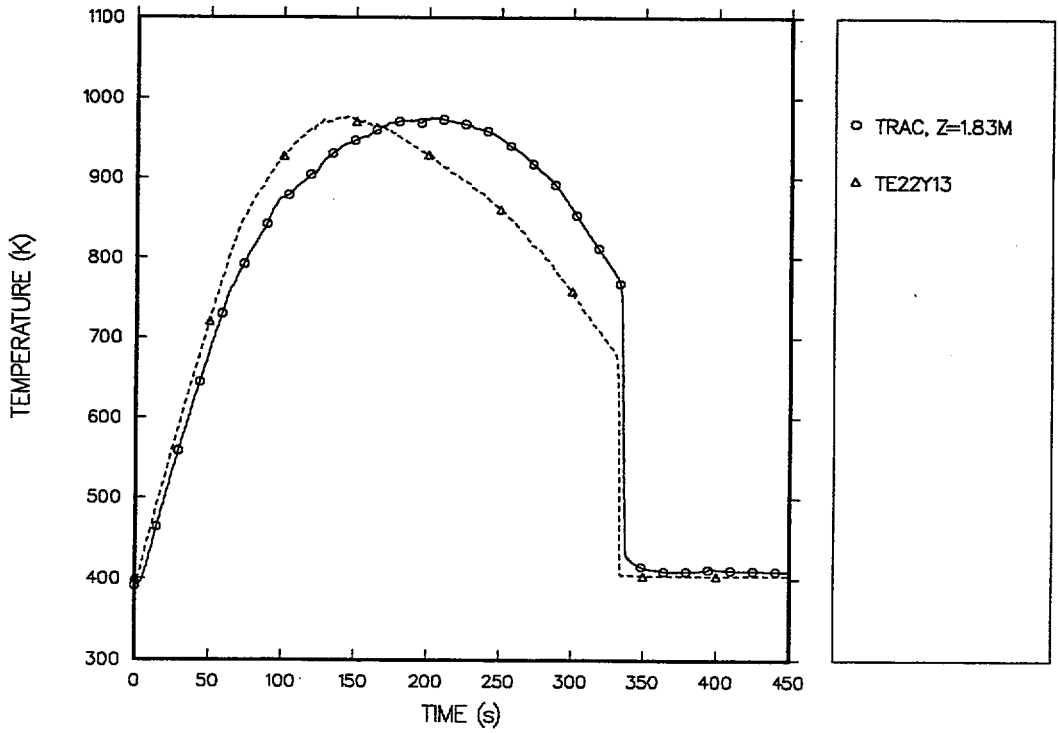

Fig. 4.7-27. CCTF-14 run: Wall-temperature histories at 1.83-m elevations with the grid-spacer model.

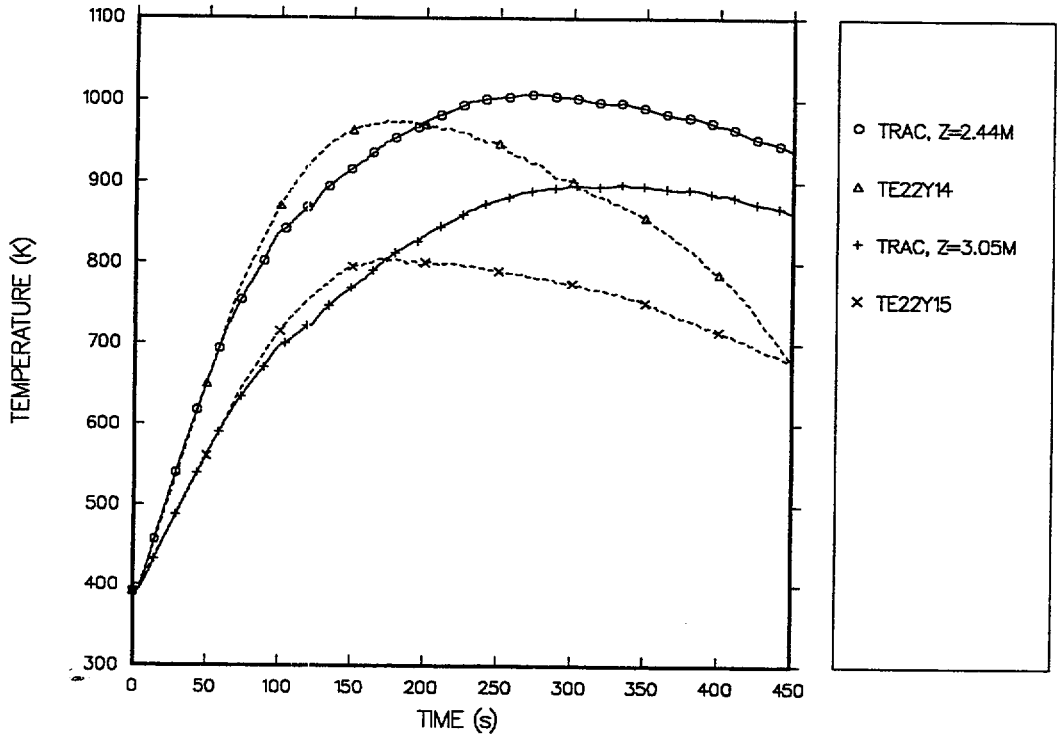

Fig. 4.7-28. CCTF-14 run: Wall-temperature histories at 2.44- and 3.05-m elevations with the grid-spacer model.

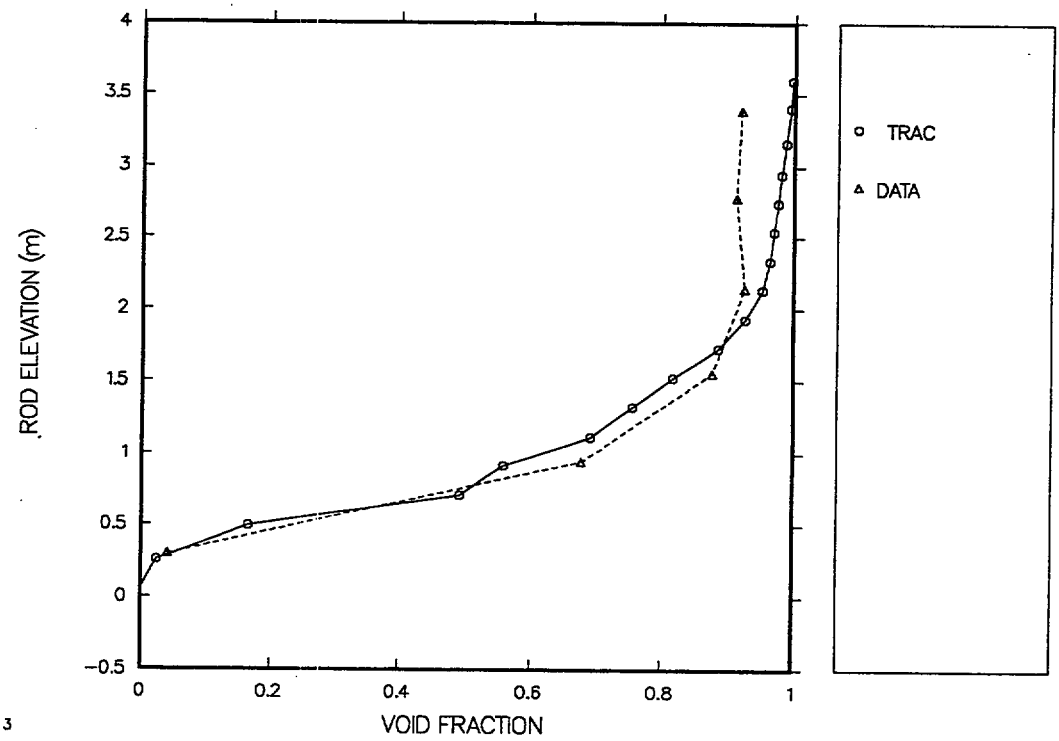

Fig. 4.7-29. Comparison of predicted and measured core-axial void-fraction profiles at 37 s with the grid-spacer model (experimental data from Ref. 4.7-6).

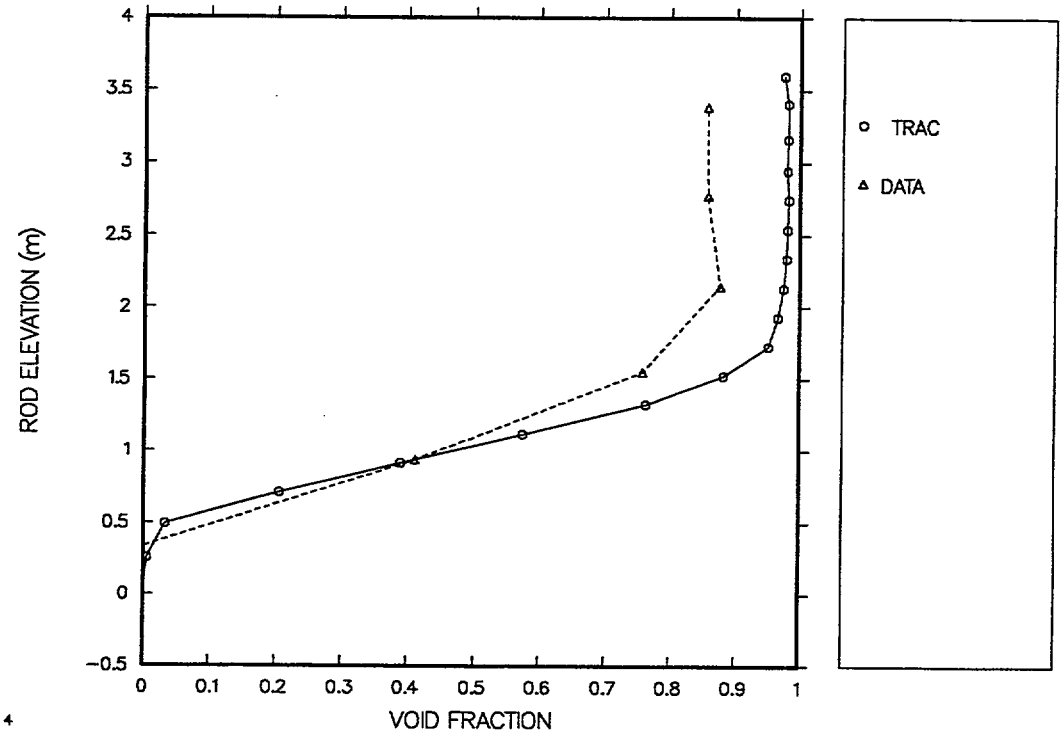

Fig. 4.7-30. Comparison of predicted and measured core-axial void-fraction profiles at 137 s with the grid-spacer model (experimental data from Ref. 4.7-6).

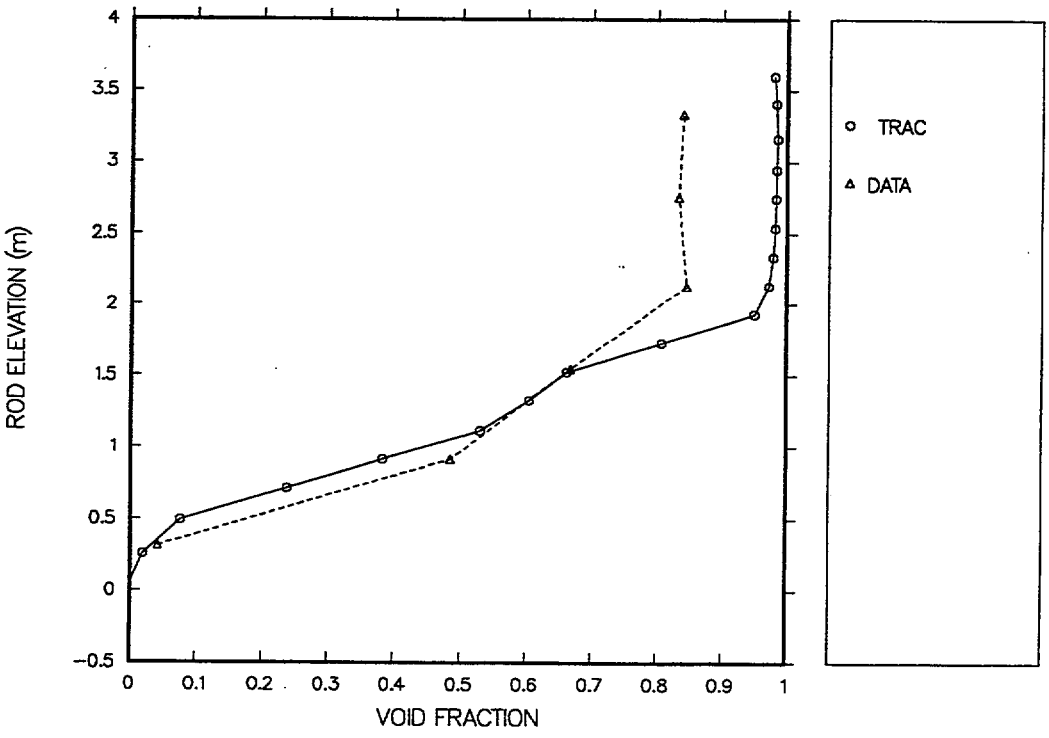

Fig. 4.7-31. Comparison of predicted and measured core-axial void-fraction profiles at 237 s with the grid-spacer model (experimental data from Ref. 4.7-6).

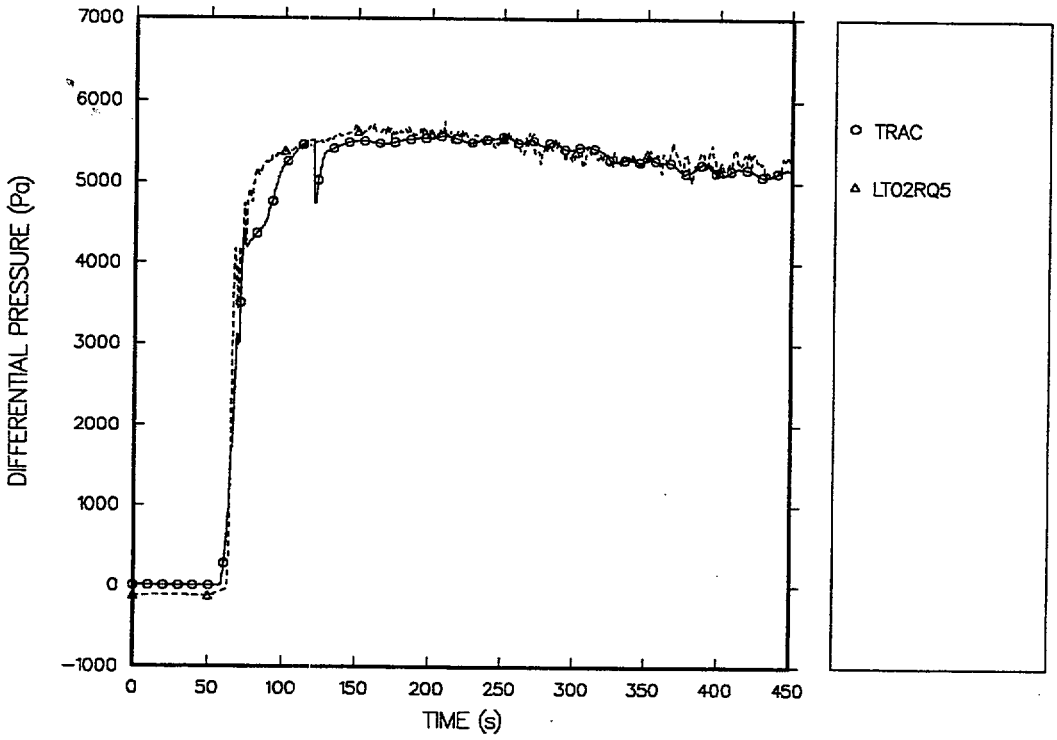

Fig. 4.7-32. CCTF-14 run: Core-ΔP history between the 0.0- and 0.61-m elevations with the grid-spacer model.

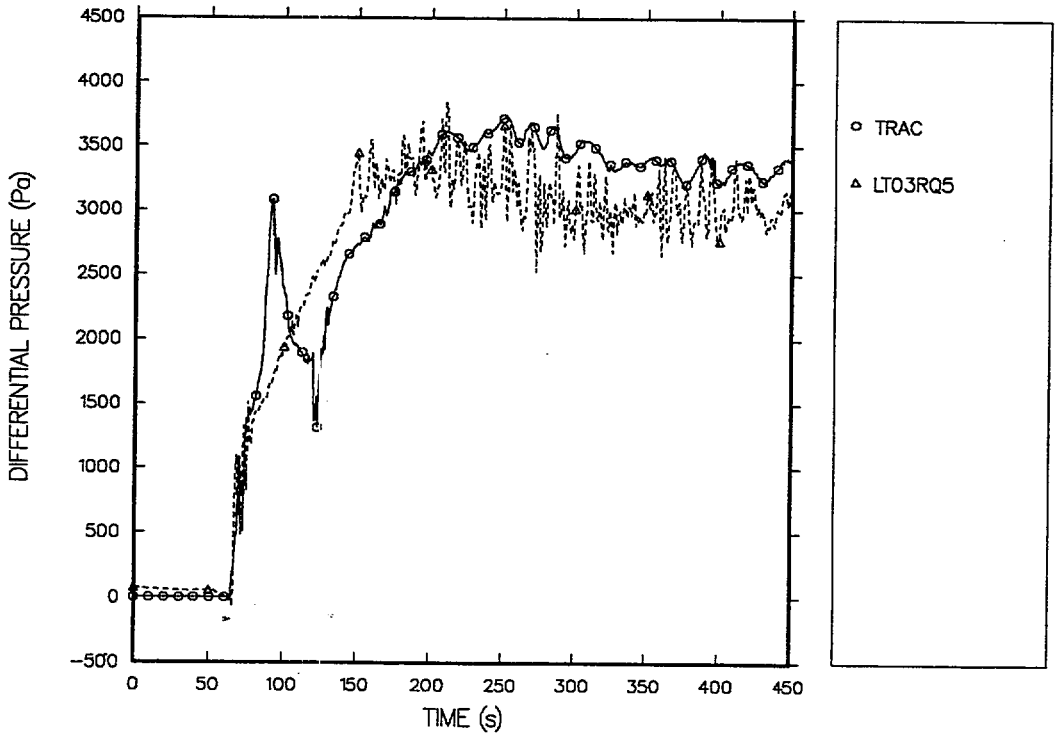

Fig. 4.7-33. CCTF-14 run: Core-ΔP history between the 0.61- and 1.22-m elevations with the grid-spacer model.

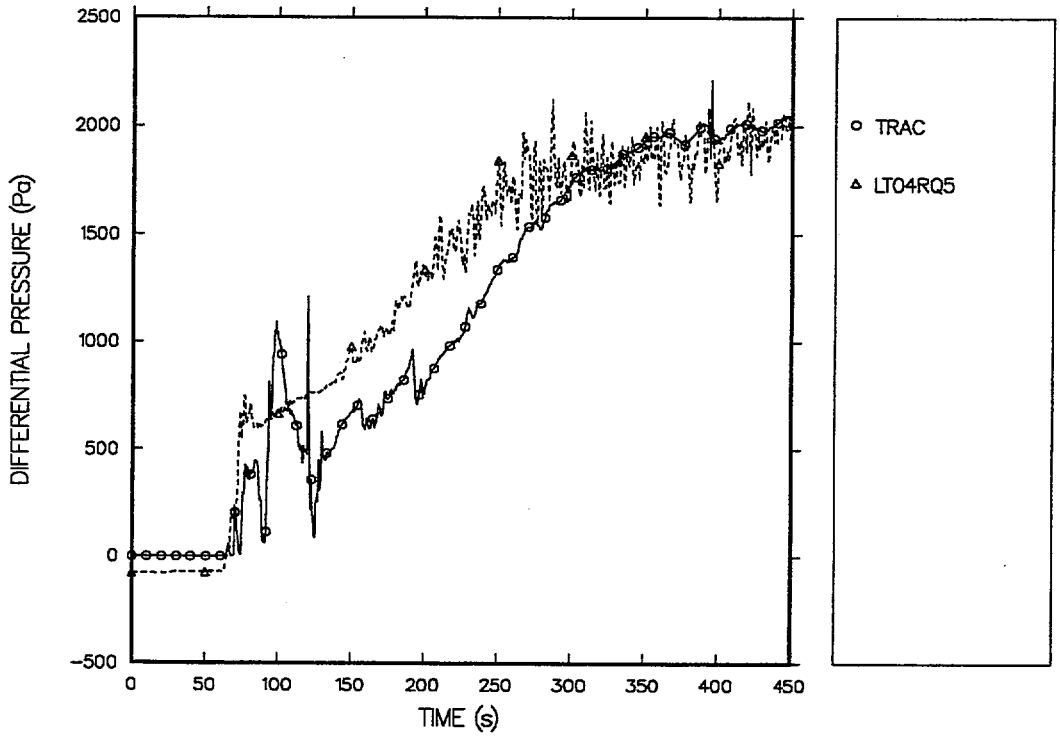

Fig. 4.7-34. CCTF-14 run: Core-ΔP history between the 1.22- and 1.83-m elevations with the grid-spacer model.

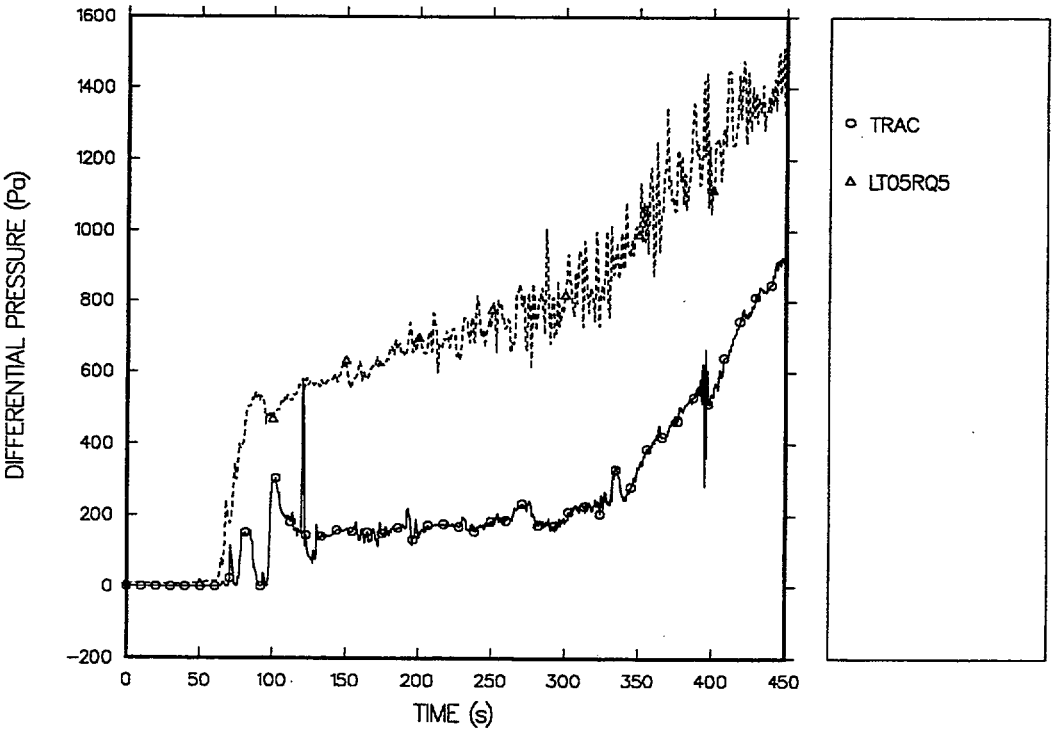

Fig. 4.7-35. CCTF-14 run: Core-ΔP history between the 1.83- and 2.44-m elevations with the grid-spacer model.

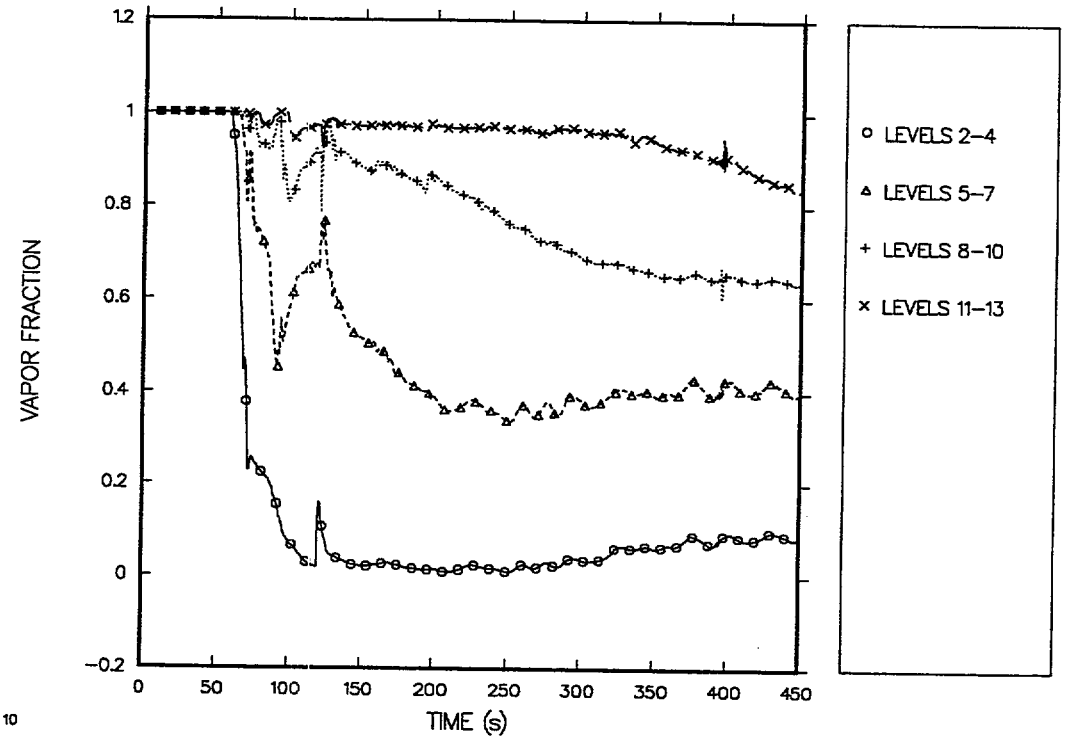

10

Fig. 4.7-36. CCTF-14 run: Predicted void-fraction histories within the core with the grid-spacer model.

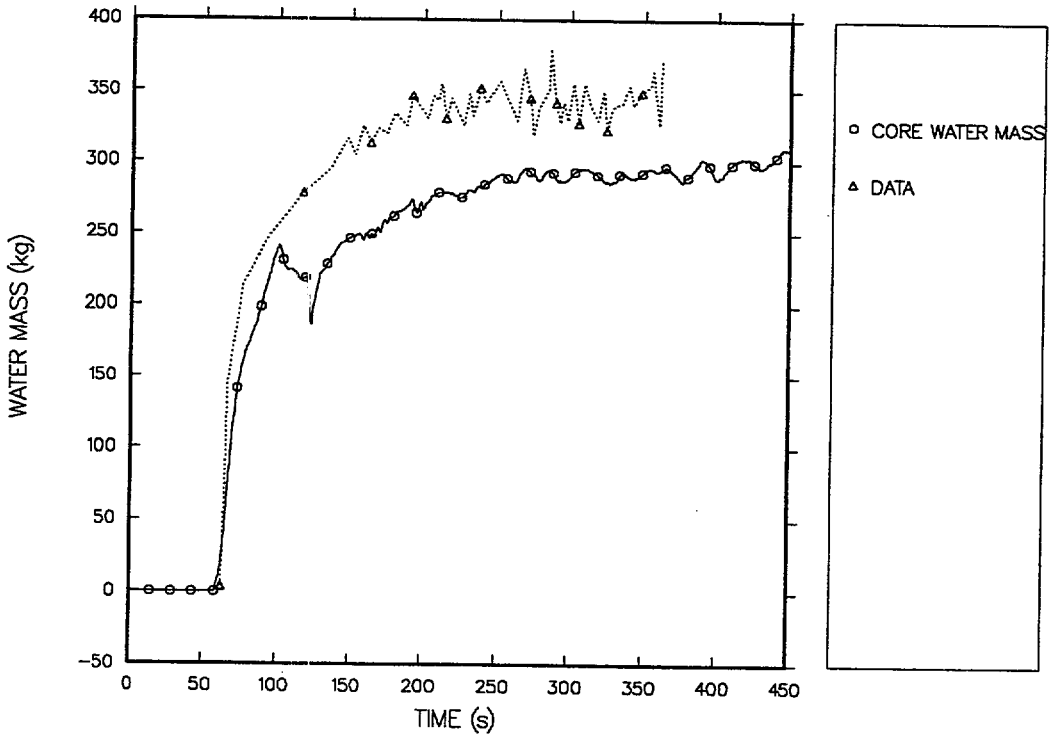

9

Fig. 4.7-37. CCTF-14 run: Comparison of predicted and measured core mass with the grid-spacer model.

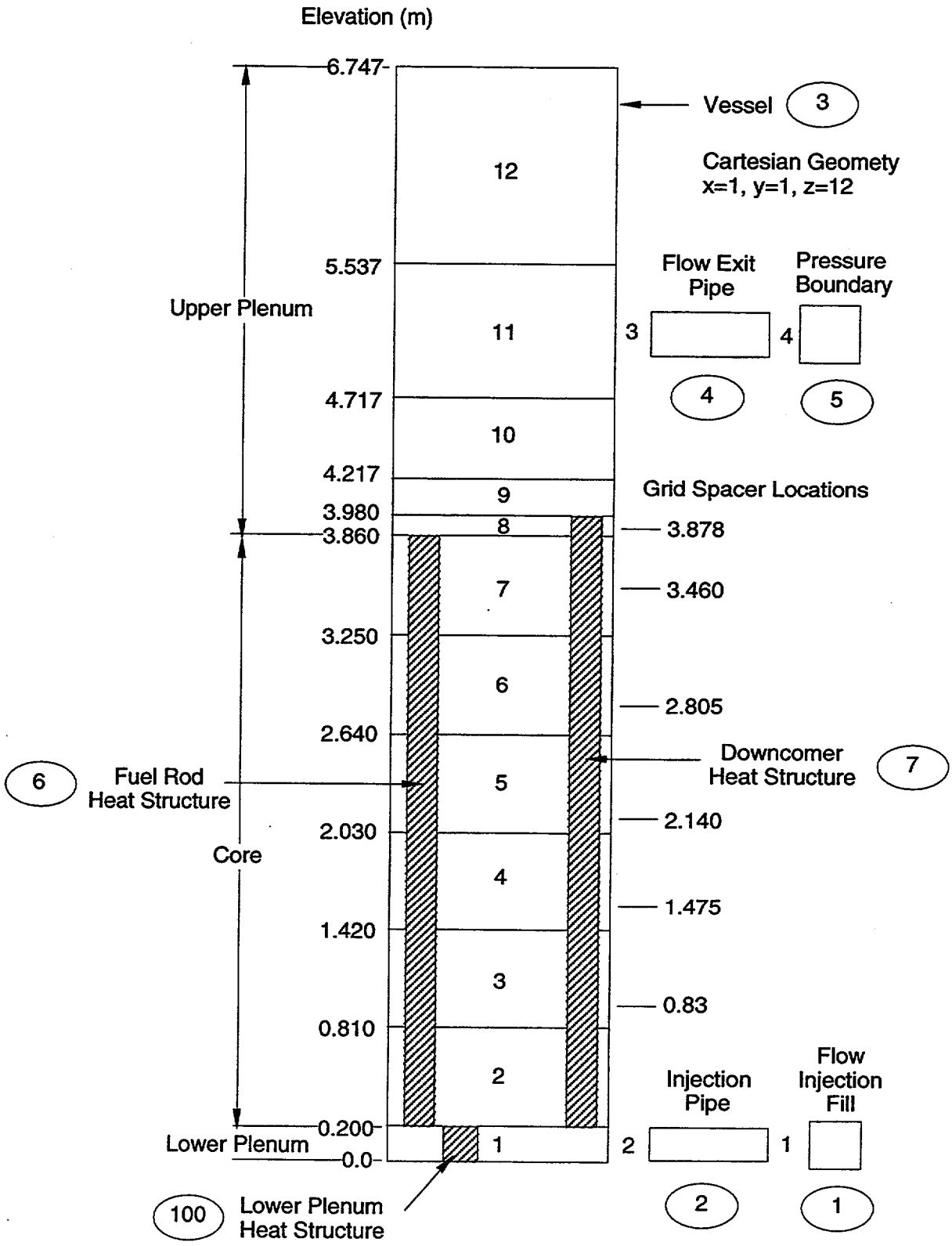

Fig. 4.7-38. Renoded 6-level core CCTF input model.

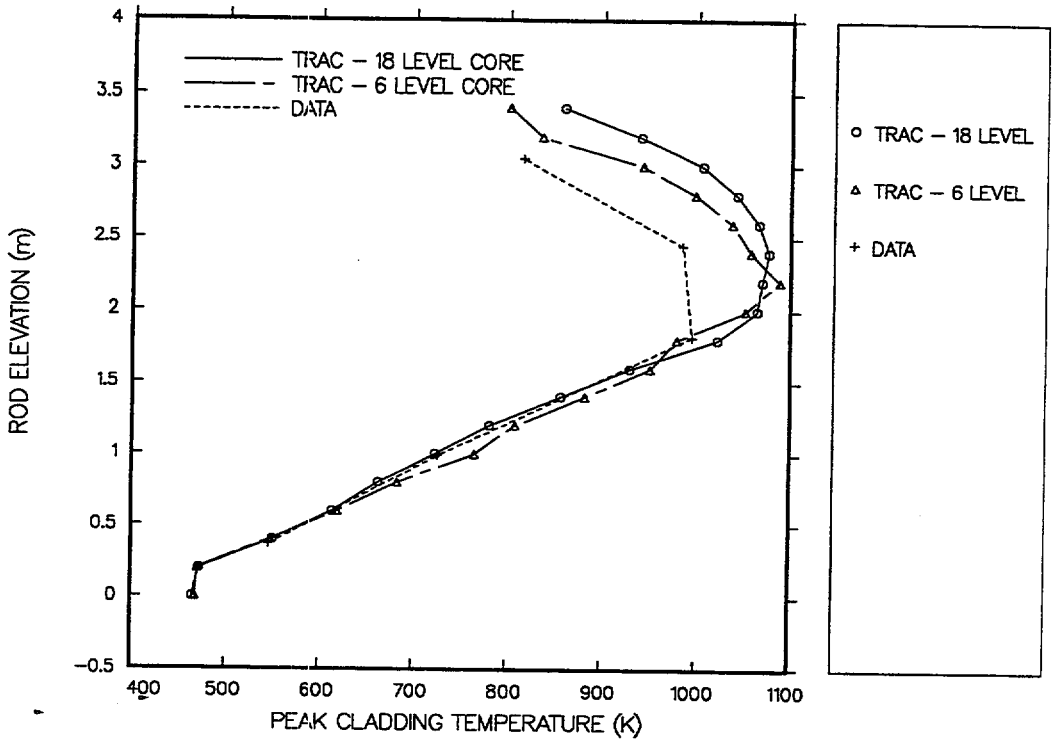

Fig. 4.7-39. Calculated PCTs for the 18- and 6-level core models compared to measured data.

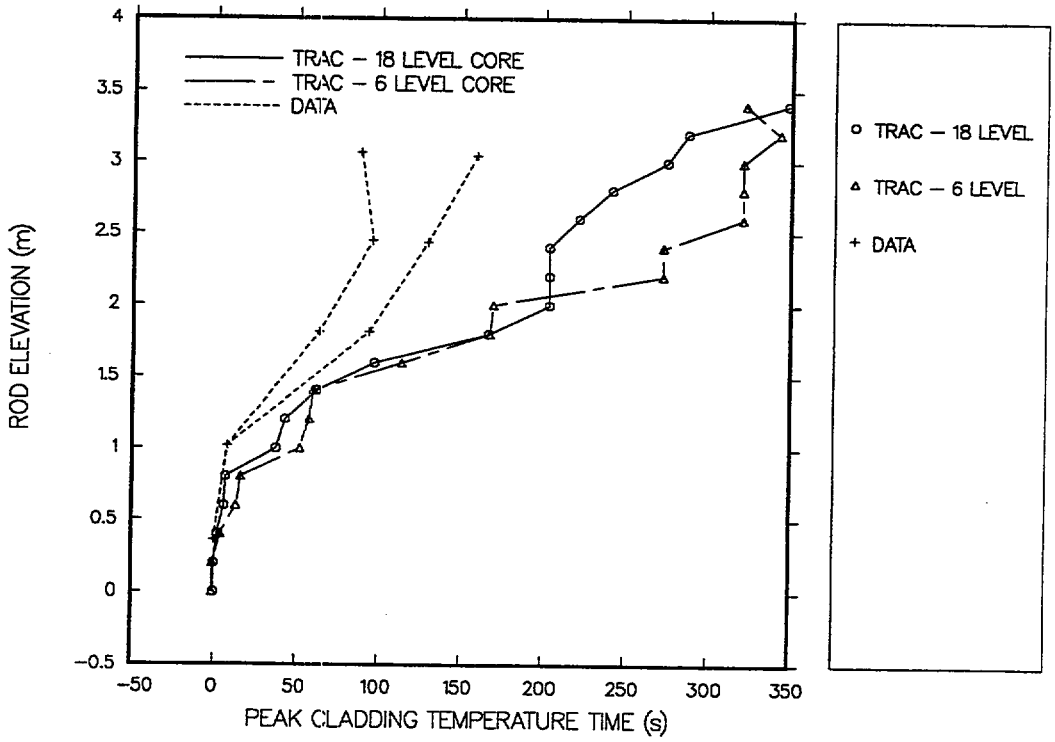

Fig. 4.7-40. Calculated PCT times for the 18- and 6-level core models compared to measured data.

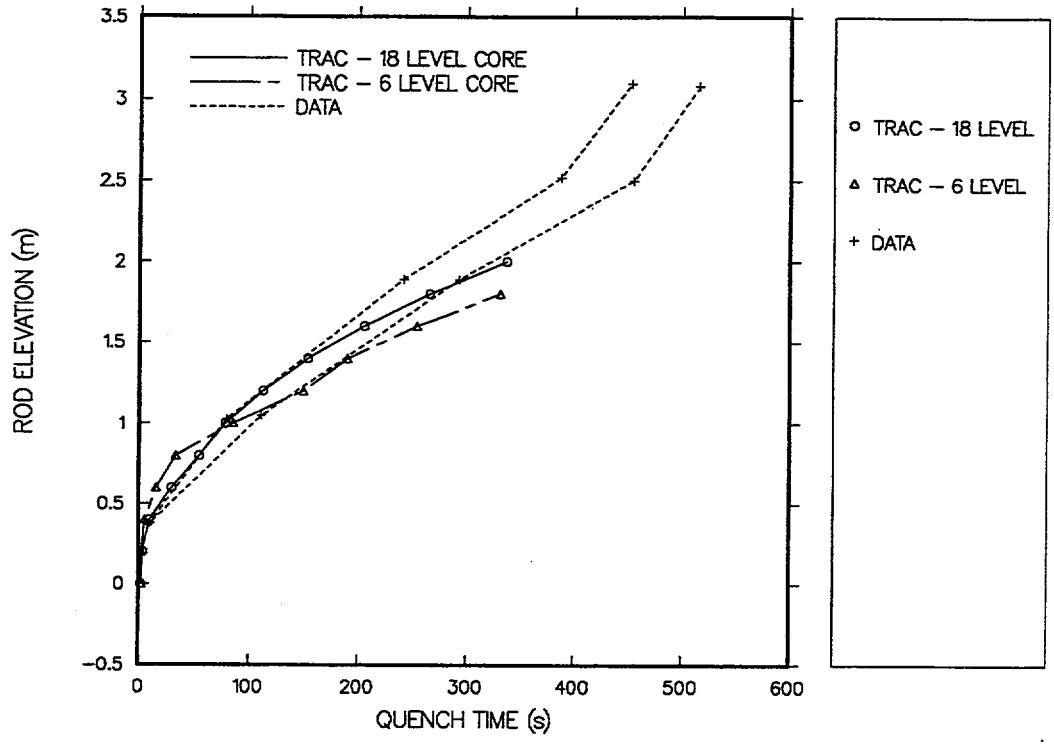

Fig. 4.7-41. Calculated quench times for the 18- and 6-level core models compared to measured data.

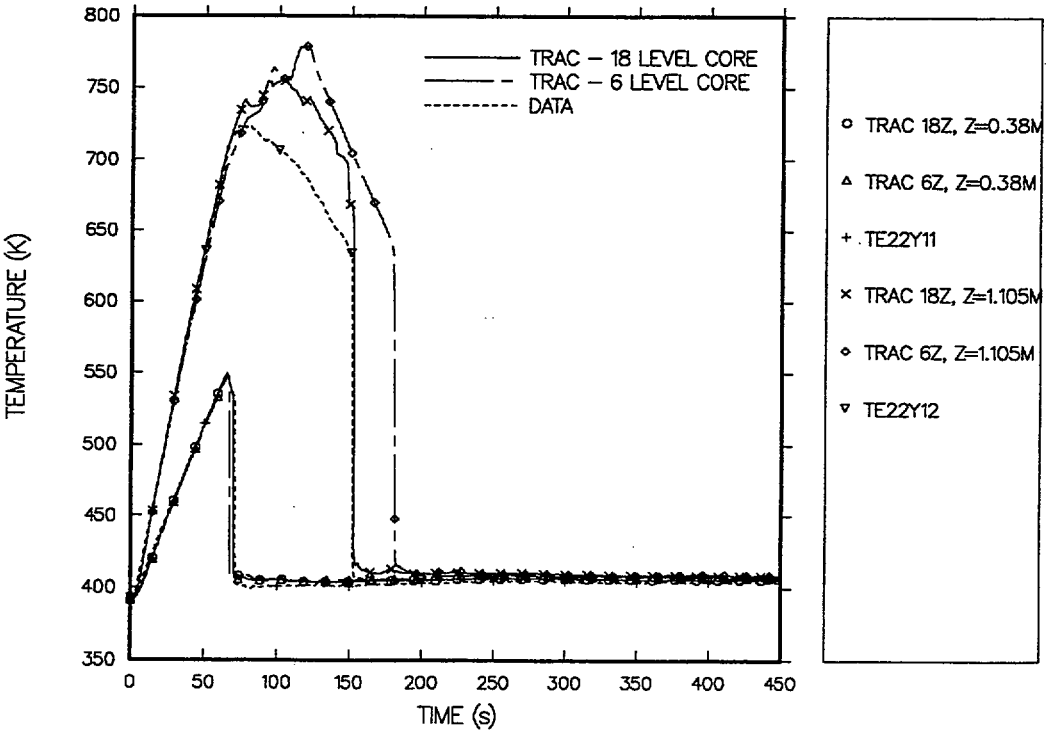

Fig. 4.7-42. Calculated rod temperatures at 0.38- and 1.105-m elevations for the 18- and 6-level core models compared to measured data.

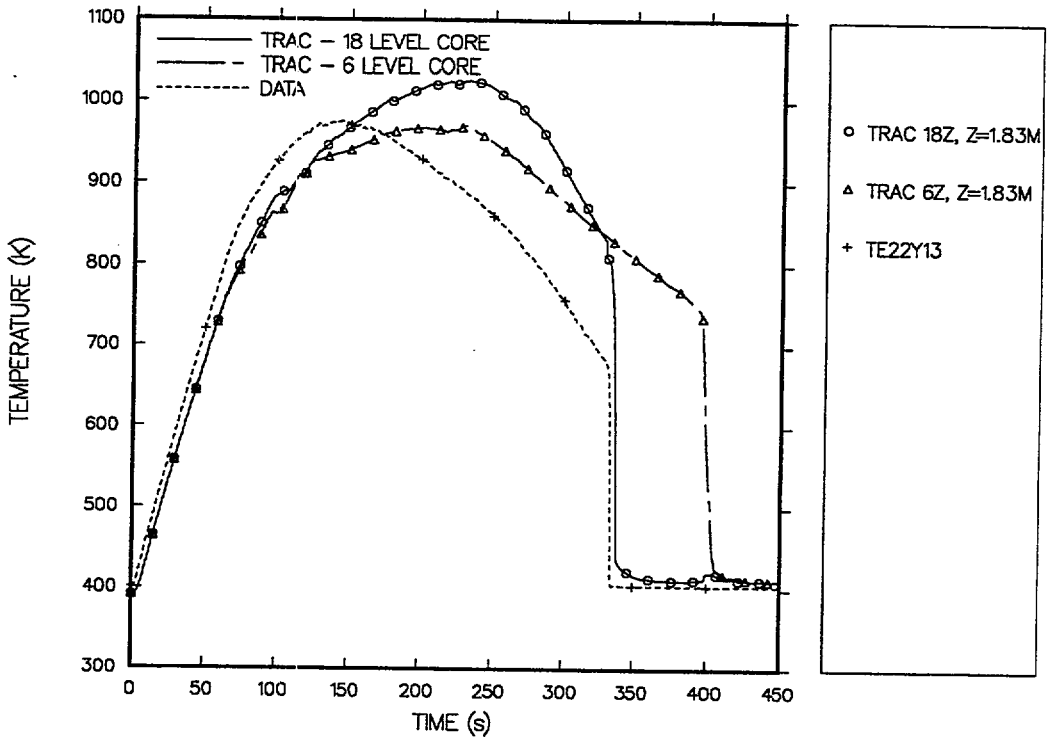

Fig. 4.7-43. Calculated rod temperatures at the 1.83-m elevation for the 18- and 6-level core models compared to measured data.

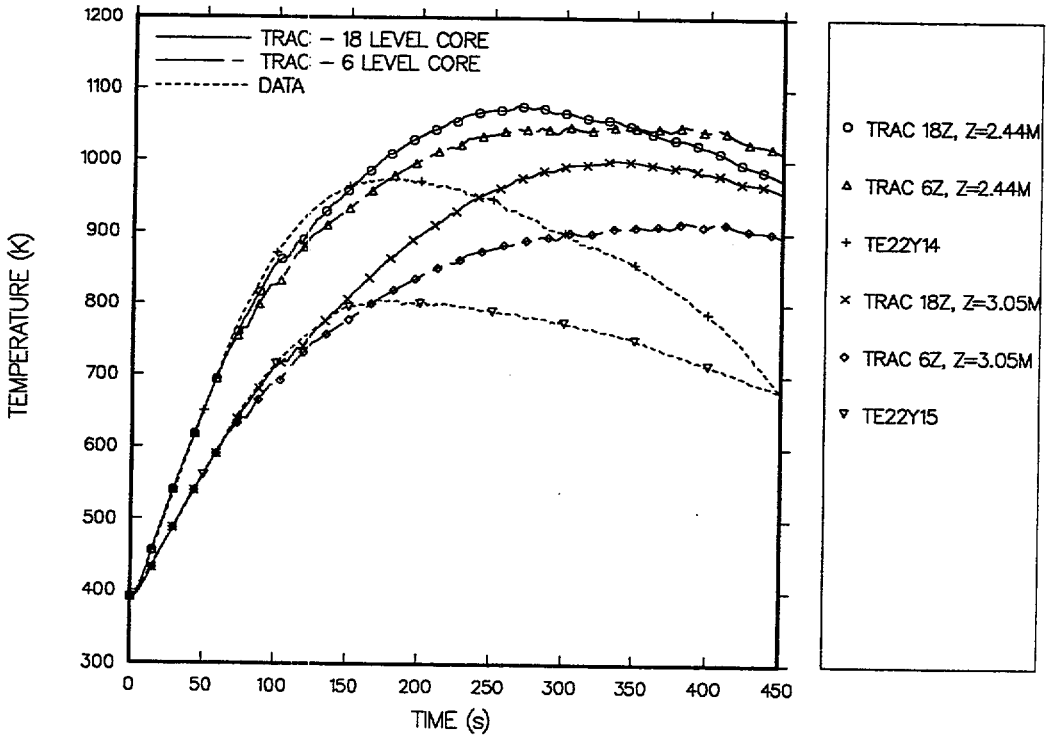

Fig. 4.7-44. Calculated rod temperatures at 2.44- and 3.05-m elevations for the 18- and 6-level core models compared to measured data.

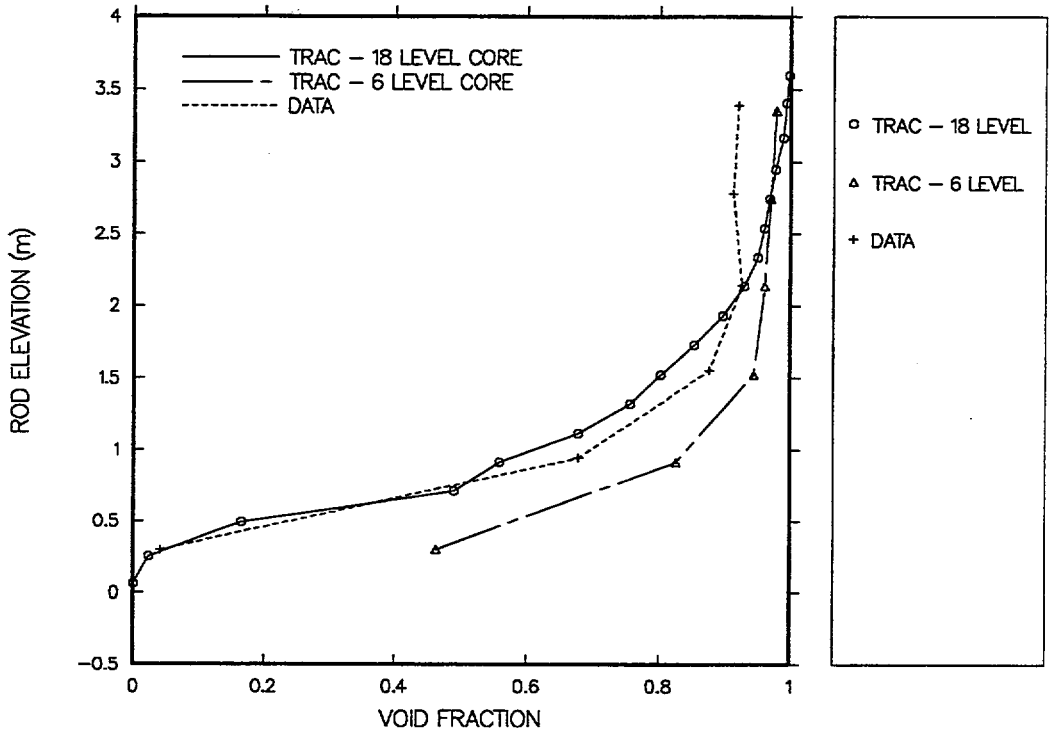

Fig. 4.7-45. Calculated core-axial void-fraction profiles for the 18- and 6-level core models at 37 s compared to data.

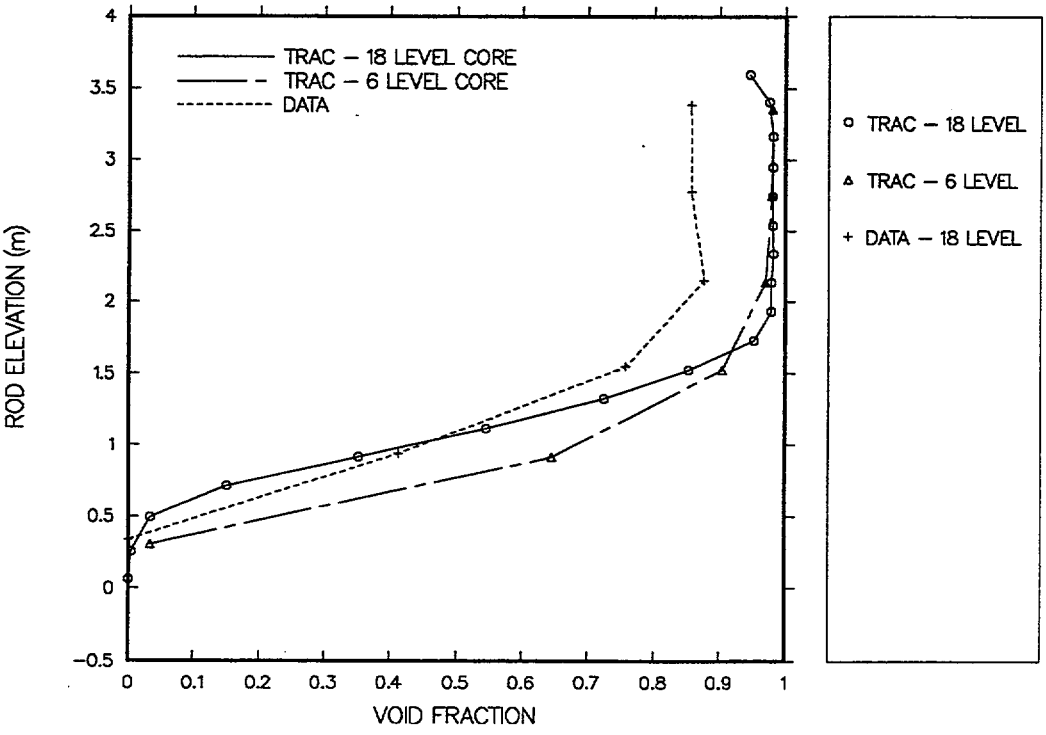

Fig. 4.7-46. Calculated core-axial void-fraction profiles for the 18- and 6-level core models at 137 s compared to data.

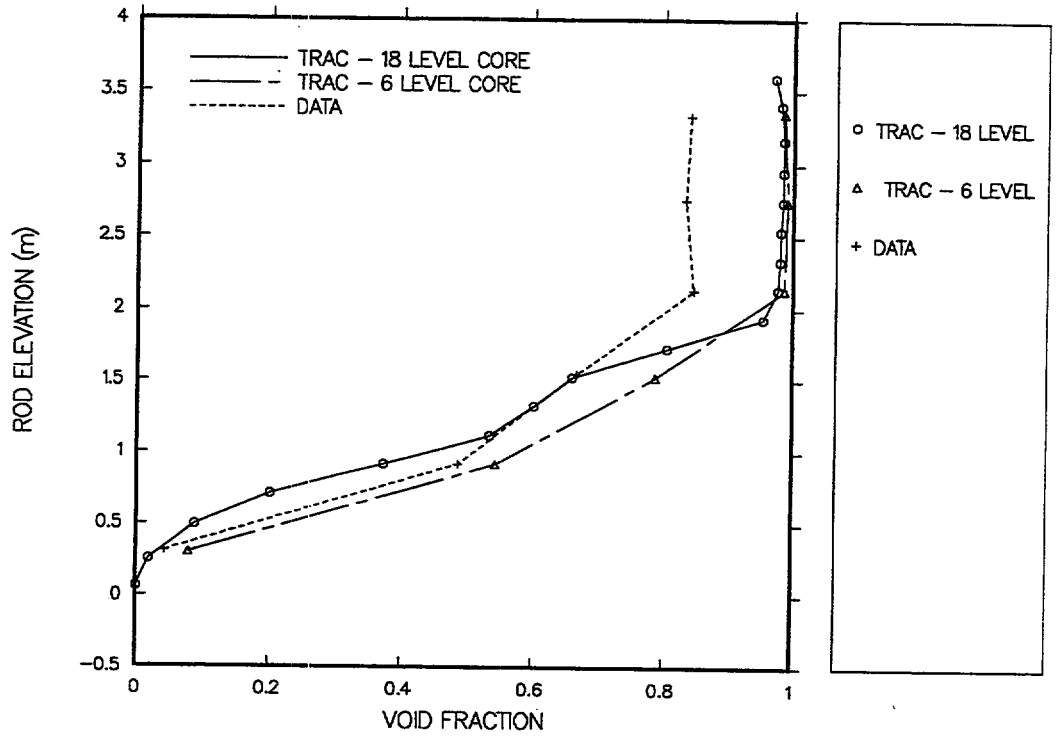

Fig. 4.7-47. Calculated core-axial void-fraction profiles for the 18- and 6-level core models at 237 s compared to data.

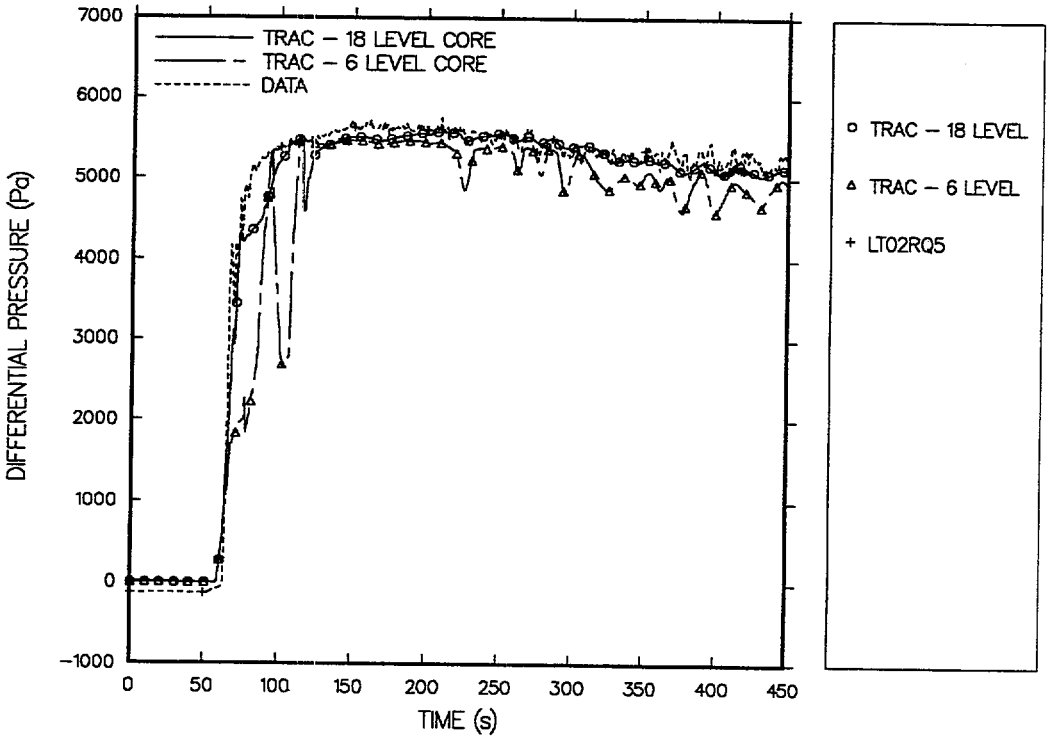

Fig. 4.7-48. Calculated core ΔP between the 0.0- and 0.61-m elevations for the 18- and 6-level core models compared to data.

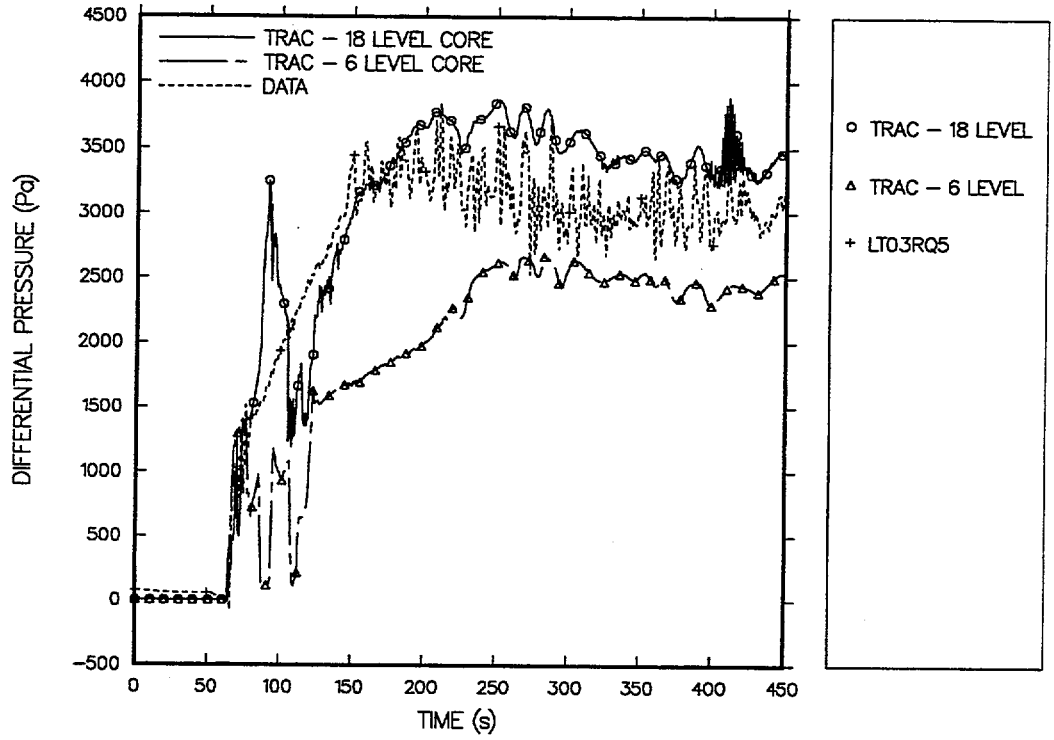

Fig. 4.7-49. Calculated core ΔP between the 0.61- and 1.22-m elevations for the 18- and 6-level core models compared to data.

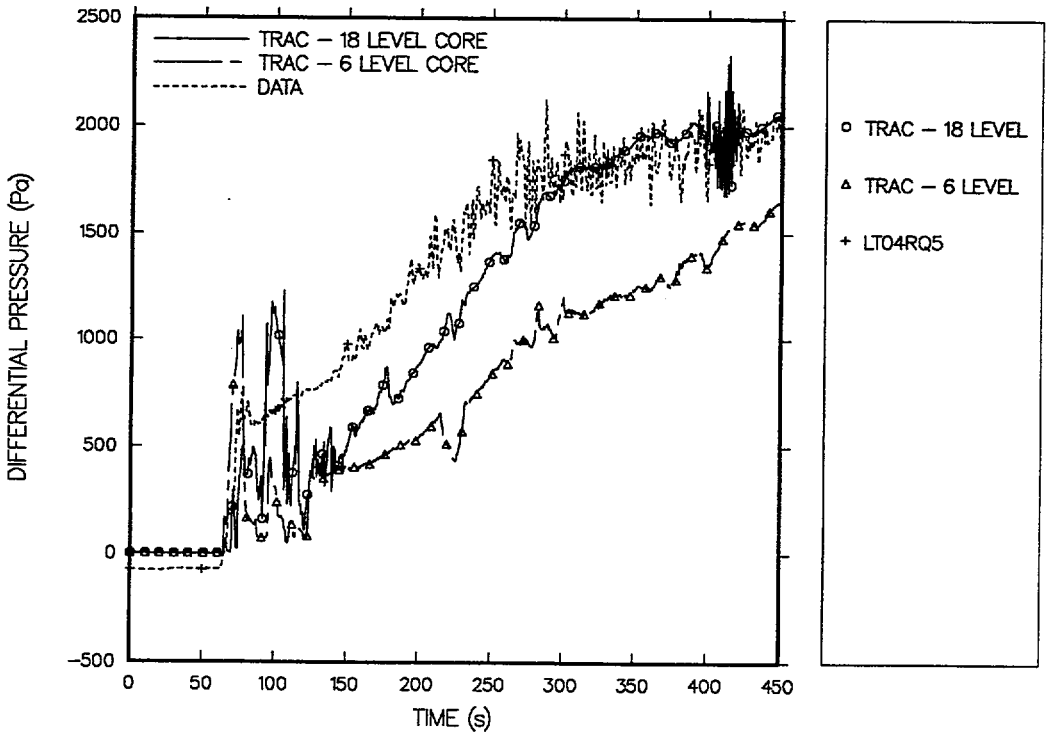

Fig. 4.7-50. Calculated core ΔP between the 1.22- and 1.83-m elevations for the 18- and 6-level core models compared to data.

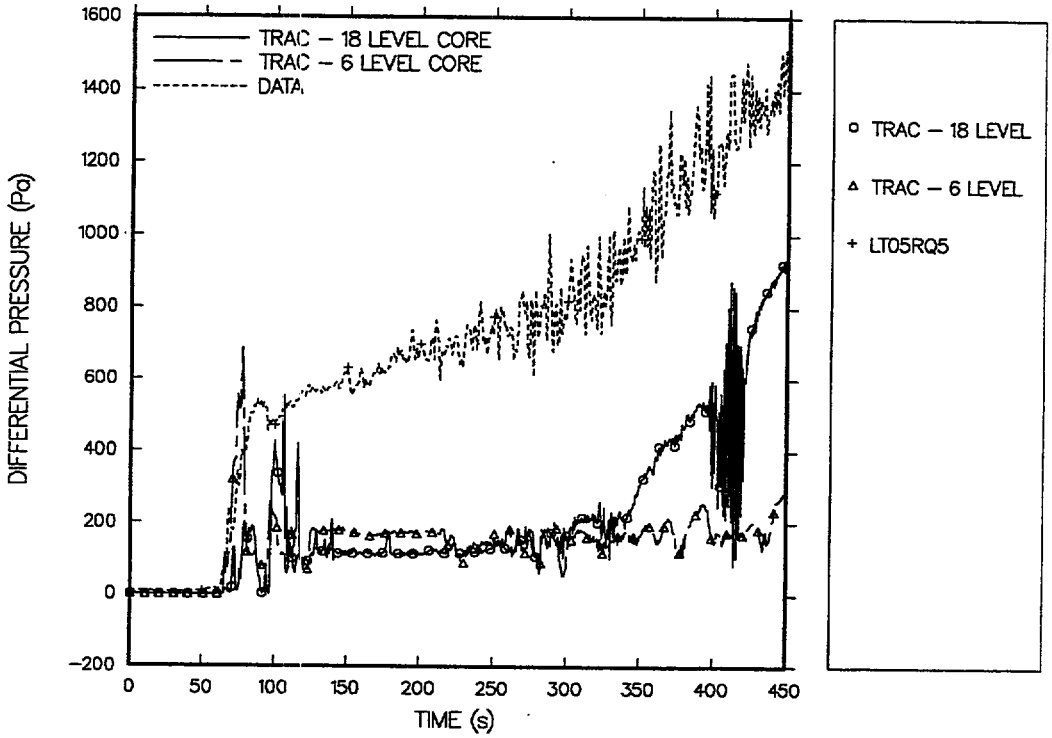

Fig. 4.7-51. Calculated core ΔP between the 1.83- and 2.44-m elevations for the 18- and 6-level core models compared to data.